Interface Investigations of the Si | Cu and Si | Ag Contact with Respect to the Photoelectrochemical Performance

Schäfer, Céline

(2020)

Interface Investigations of the Si | Cu and Si | Ag Contact with Respect to the Photoelectrochemical Performance

Zur Erlangung des akademischen Grades Doktor-Ingenieur (Dr.-Ing.)
Vorgelegte Dissertation von M. Sc. Céline Schäfer aus Miltenberg

1. Gutachten: Prof. Dr. W. Jaegermann
2. Gutachten: Jun. Prof. Dr. U. Kramm

TECHNISCHE UNIVERSITÄT DARMSTADT

Interface Investigations of the Si | Cu and Si | Ag Contact with Respect to the Photoelectrochemical Performance

Vorgelegte Dissertation von Céline Schäfer aus Miltenberg

1. Gutachten: Prof. Dr. W. Jaegermann

2. Gutachten: Jun. Prof. Dr. U. Kramm

Tag der mündlichen Prüfung: 08.06.2020

Darmstadt

„Wir müssen Ausdauer und vor allem Vertrauen in uns selbst haben. Wir müssen glauben, dass wir begabt sind und dass wir etwas erreichen können.“

-Marie Curie-

Contents

1 Introduction 3

2 Fundamentals 7

2.1 Material Classes 7

2.2 Semiconductor Interfaces 9

2.3 Solar Cells 12

2.4 Photoelectrochemical Cells 17

2.5 CO_2 Reduction 21

3 Experimental Methods 25

3.1 Electron Beam Deposition 25

3.2 Photoelectron Spectroscopy 26

3.2.1 Physical Basics 26

3.2.2 Interface Experiments 29

3.3 Photoelectrochemical Measurements 30

3.4 Scanning Electron Microscopy 31

4 Experimental Procedure 33

4.1 Sample Preparation 34

4.2 Electron Beam Deposition 34

4.3 XPS Measurements 37

4.4 Interface Experiments 38

4.5 Film Thickness 39

4.6 Photoelectrochemical Measurements 39

5 Characterization of the Si | Cu Interface 41

5.1 p-Si | Cu Interface 41

5.1.1 Energy Band Alignment 41

5.1.2 Electrochemistry 45

5.1.3 XPS after Electrochemistry 46

5.2 pn^+-Si | Cu Interface 47

5.2.1 Energy Band Alignment 47

5.2.2 Electrochemistry 58

5.2.3 Characterization after Electrochemistry 59

5.3 p-Si | µcn-Si | Cu Interface..... 64
5.3.1 Energy Band Alignment..... 64
5.3.2 Electrochemistry 76
5.3.3 Characterization after Electrochemistry..... 79
5.4 pin-Si | Cu Interface..... 83
5.4.1 Energy Band Alignment..... 84
5.4.2 Electrochemistry 87
5.4.3 Characterization after Electrochemistry..... 91
5.5 a-Si | a-Si | µc-Si | Cu Interface..... 94
5.6 Comparison of all Si | Cu Interfaces..... 95
6 Characterization of the Si | Ag Interface 99
6.1 pn^+-Si | Ag Interface..... 99
6.1.1 Energy Band Alignment..... 99
6.1.2 Electrochemistry 102
6.1.3 Characterization after Electrochemistry..... 105
6.2 p-Si | µcn-Si | Ag Interface..... 107
6.2.1 Energy Band Alignment..... 107
6.2.2 Electrochemistry 109
6.2.3 Characterization after Electrochemistry..... 112
6.3 a-Si:H | a-Si:H | µcn-Si:H | Ag Interface 113
6.3.1 Energy Band Alignment..... 113
6.3.2 Electrochemistry 116
6.3.3 Characterization after Electrochemistry..... 118
6.4 Comparison of all Si | Metal Interfaces..... 120
7 Summary and Outlook 123
Appendix 129
Important Symbols and Abbreviations 135
List of Figures 137
Bibliography 145
Publications and Conferences 155
Résumé 157

1 Introduction

The industrial revolution from 1760 to 1830 was the starting point of our today's modern world. Mankind has developed a variety of new techniques to facilitate and extend daily work as well as quality of living.[1] Since the last three centuries mankind faces a substantial progress. Besides great industrial achievements, on the other hand our planet suffers from harmful environmental effects caused by growing industry impacts. The large population density as well as our living standard is responsible for a drastically increase of energy demand, especially within the last decades. It cannot be denied that the temperatures all over the world are rising, which is related to global warming and climate change.[2] The availability of fossil fuels such as coal, crude oil and natural gas, which are our main energy supplies, will be exhausted in the future. The reason for this is the amount and rapidity of their consumption in relation to the time consuming natural evolution of fossil fuels. Fossil fuels originate from organic remains, which emerged millions of years ago from CO_2 by natural photosynthesis.[3] The industrialization has emitted an increased amount of CO_2 in our atmosphere, which is too large to be converted by natural photosynthesis. As a consequence global warming caused by the greenhouse gas CO_2 enhances the scarcity of fossil fuels. Therefore, it is our duty to reconsider our worldwide energy supply and convert our energy system to renewable energies.

The best-known renewable energies are wind and solar power. However, these techniques suffer from their inherent volatility with strongly variable energy fluxes with time, which are not in phase with the social consumption needs. It is necessary to develop storable and transportable fuels from renewable energies. One solution for that challenge can be found in nature. The natural photosynthesis, which is the most important and prototypical method of harvesting solar energy, acts as role model.[4] Here, CO_2 and water are converted to glucose and oxygen by using sun light. The idea is to develop an "artificial leaf", which is able to convert CO_2 and water into storable and reusable fuels (CO_2 reduction) as well as oxygen (water oxidation, oxygen evolution reaction). Storing chemical fuels is advantageous as they have up to 100 times higher energy and power densities compared to the best batteries. Moreover, large scale storage on unlimited timescale is possible.[5]–[7]

Figure 1 compares the natural photosynthesis with the artificial process on different size scales. Natural photosynthesis is performed by light absorption by biological entities that contain chlorophyll pigments. These pigments are responsible for the conversion of water to oxygen and adenosine triphosphate (ATP). In a second step, which is known as Calvin cycle atmospheric carbon dioxide and water is further converted to hydrocarbons, such as glucose ($C_6H_{12}O_6$). In the artificial photosynthesis the reactions should be induced by a photo catalyst, for example a copper thin film with the help of the photovoltage of a solar cell. Less complex hydrocarbons, such as carbon monoxide (CO), methane (CH_4), ethylene

(C_2H_4) or ethanol (C_2H_7OH) are formed. The following paragraph will address the realization of such an artificial leaf and its main components.[8]

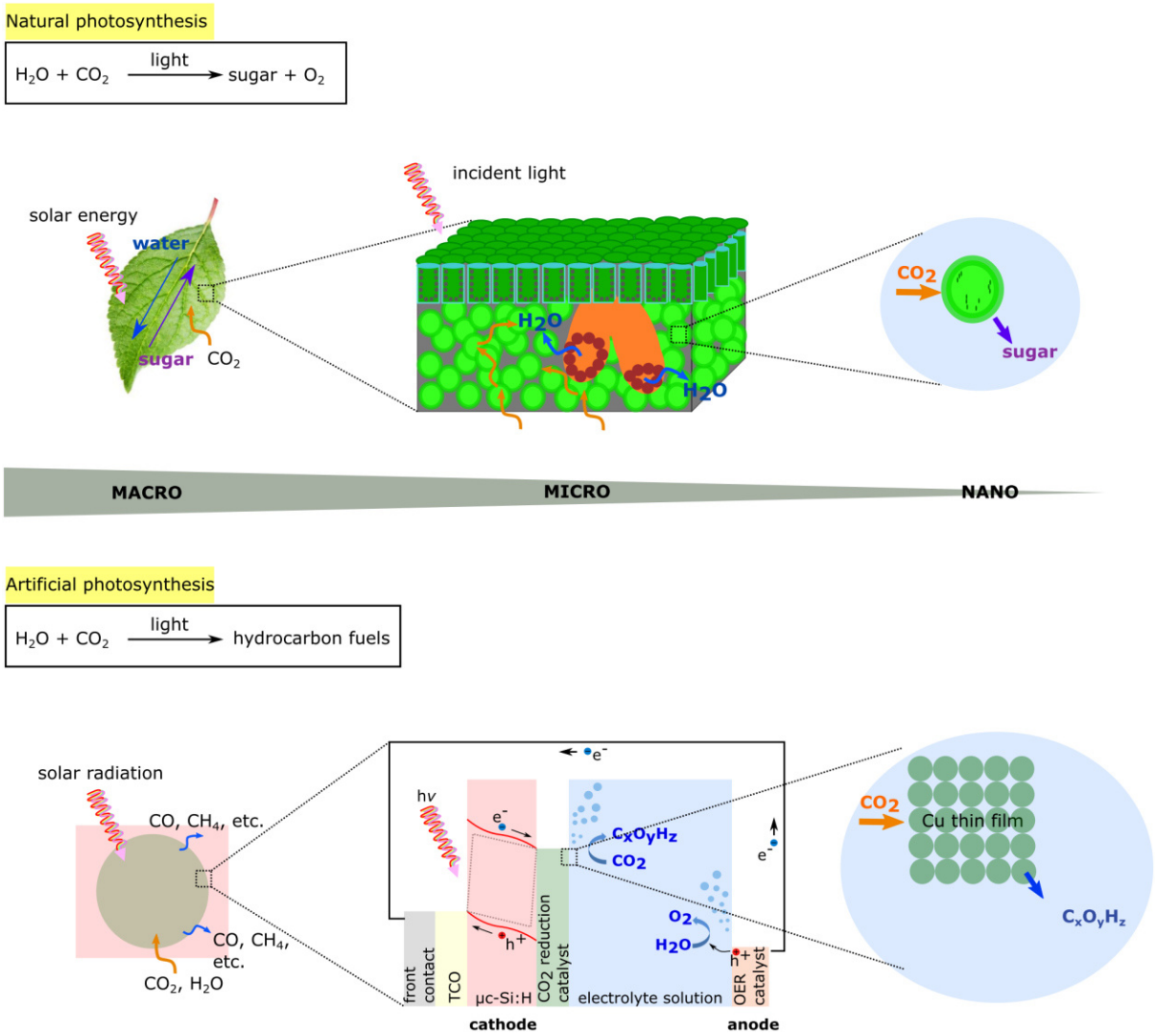

Figure 1: Schematic illustration and comparison of the natural and artificial photosynthesis from macroscopic to nanoscale.

For the realization of such an artificial leaf photoelectrochemical cells may develop to a key technology. One essential part of such a device is a photoabsorber, which has to drive both half-cell reactions (CO_2 reduction and oxygen evolution reaction). This photoabsorber material should be a cheap multijunction photoelectrode, which is able to transform sun light into an electrochemical potential difference, which is large enough to drive the desired reactions. The second important part of the artificial leaf are appropriate catalysts for the CO_2 reduction reaction and another one for the oxygen evolution reaction, which allow high current densities at low overpotentials. Here, thin layers or nanoparticles of metal or metal oxides are conceivable. The redox reaction should take place in an electrolyte (pH > 7) at moderate temperatures to achieve high stability and favorable kinetics of the involved materials. Last important part of the artificial leaf is an ion exchange membrane for the separation of gas, liquids and products.

Figure 2 schematically shows the architecture of an artificial leaf photoelectrochemical cell with its main parts.

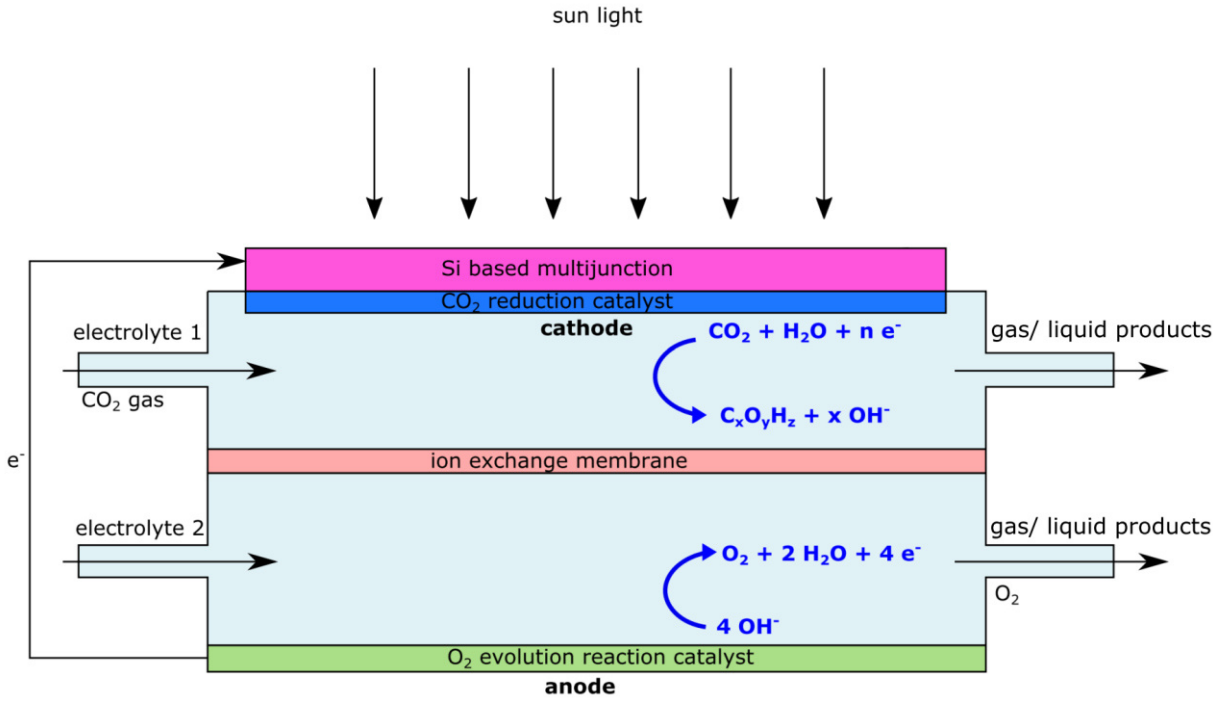

Figure 2: Scheme of an artificial leaf photoelectrochemical cell architecture including a Si based multijunction as photoabsorber, a CO_2 reduction catalyst as well as an oxygen evolution catalyst and an ion exchange membrane.

Objective of this work was the systematic investigation of the interface between the Si based multijunction and the CO_2 reduction catalyst. The electronic band alignment at the interface strongly influences the corresponding photoelectrochemical performance of the systems and therefore the efficiency of the CO_2 reduction. Hence it is necessary to characterize and optimize that interface. As photoabsorber material different Si substrates were used, starting from a very basic model system, which uses a p-Si wafer, coming to more advanced systems including pn^+-Si, p-Si | µcn-Si, µc-Si:H and a-Si:H | a-Si:H | µc-Si:H junctions. Furthermore, different Si surface terminations such as native silicon dioxide, hydrogen termination as well as thermally grown silicon dioxide were investigated with respect to the energetic band alignment and the resulting photoelectrochemical behavior when being in contact to the catalyst material. As CO_2 reduction catalyst thin films of metallic copper and silver were used, which were deposited to the Si support by a physical vapor deposition technique. Literature has shown that both materials can be successfully used as CO_2 reduction catalyst, which will be discussed more in detail in this work.

All material systems were investigated by photoelectron spectroscopy before and after electrochemical characterization as well as by scanning electron microscopy. The aim was to prove whether there is a

relation between the initial electronic band structure of the material system and the corresponding photoelectrochemical performance.

2 Fundamentals

In this chapter the fundamental properties of the different material classes are introduced. A special focus will be on semiconductors and semiconductor interfaces. Furthermore, the principles of solar cells as well as photoelectrochemical cells will be explained. Finally, the mechanism of the CO_2 reduction reaction is introduced.

2.1 Material Classes

The difference between metals, semiconductors and insulators is the interatomic bonding which effects the electronic properties. While in metals the electrons are delocalized in the lattice which result in a metallic bond, semiconductors have covalent or ionic bonds. Metals show partially occupied bands which results in high charge carrier density as well as electron mobility. The electrons which are close to the Fermi level are responsible for the electric conductivity. In a metal the Fermi level E_F can be described as electrochemical potential of the electrons. The work function (φ) is defined by the energetic distance of the Fermi level to the vacuum level (E_V) which is shown in Figure 3. In case of a semiconductor it has to be differentiated between the highest occupied state which is called valance band maximum and the lowest unoccupied state which is called conduction band minimum. These electronic states are separated by the energy band gap (E_G). Electrons of the valence band (VB) can be excited to the conduction band (CB) by applying a sufficiently high energy, for example in form of photons. This effect results in the ability of carrying electric current by electrons of the valence band leaving behind a hole and occupy a state in the conduction band. Here, the Fermi level can be described as the energy level below which all electronic states are occupied. For intrinsic semiconductors the Fermi level lies in the middle of the band gap and can be shifted by additional positive or negative charge carriers or other defects. Equivalent to metals the work function in semiconductors is defined by the distance between Fermi level and vacuum level. The distance between valence band maximum and vacuum level is the ionization potential (I_P) and E_A describes the electron affinity which is the distance from the conduction band minimum to the vacuum level. The electric transport properties within a semiconductor are defined by electrons in the conduction band and holes in the valence band. Additional charge carriers can be generated for example by optical excitation with visible light which is described by the inner photoelectric effect. This feature is the main difference between semiconductors and insulators (having large band gaps).

Compared to a semiconductor the energy band gap of an insulator is notably larger and therefore charge carriers cannot be generated by the excitation with visible light.[9][10] Well known values of energy

band gaps of semiconductors are for example E_G=1.12 eV for Silicon (Si) and E_G=1.42 eV for gallium arsenide (GaAs).[11][12] Furthermore, these two materials are popular examples for different types of semiconductors possessing either a direct or an indirect band gap. While the conduction band minimum and the valence band maximum of Si are not at the same position of the Brillouin zone in reciprocal space, which indicates an indirect band gap, GaAs has an direct energy band gap as here the conduction band minimum and the valence band maximum are at the same position in reciprocal space.[13][14] Whether a semiconductor has a direct or indirect energy band gap affects the way of exciting an electron from the valence band maximum to the conduction band minimum. In case of a direct energy band gap an electron can be excited by one incident photon which needs to have at least the same energy as the band gap. For an indirect semiconductor one incident photon with a sufficient high energy cannot result in an electron transfer to the conduction band as the valence band maximum and the conduction band minimum are at different positions in the reciprocal space. In that case an additional phonon excitation is required to fulfil momentum conservation.[10][15]

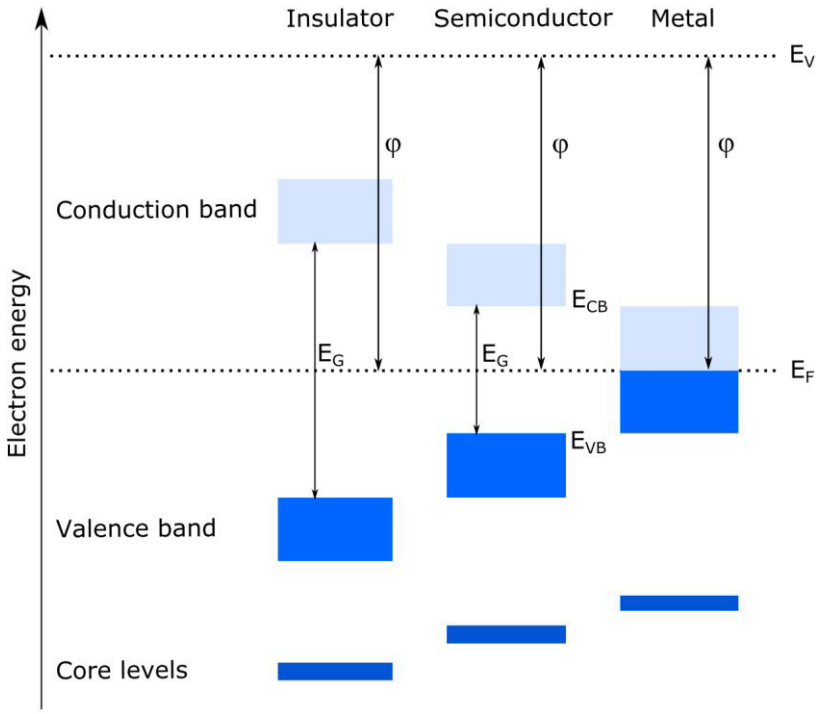

Figure 3: Energy band diagrams for a metal, a semiconductor and an insulator at a temperature of 0 K. The material class depends on the energy band gap E_G. The Fermi level E_F indicates the position below which all electronic states are fully occupied (dark blue bands are occupied, light blue bands are empty).

The Fermi level can be moved within the band gap of a semiconductor which is a result of the dopability of semiconductors. Doping means adding small amounts of a foreign substance which affects the electronic structure of the material. It can be distinguished between two kinds of doping. On the one hand acceptors can be added to the semiconductor which increases the number of holes. This doping

mechanism is called p-doping. On the other hand it is possible to add donors in order to increase the concentration of electrons which is known as n-doping. In both cases the mobility of the charge carriers μ play an important role and strongly affect the electric conductivity σ which is defined by

$$\sigma = |e|(n\mu_n + p\mu_p), \tag{1}$$

where e is the electrical charge, p the hole and n the electron concentration.

2.2 Semiconductor Interfaces

Solid state interfaces play a key role in many applications such as metal-oxide-semiconductors (MOS) and field effect transistors (MOS-FET), MOS capacitor, light emitting diodes (LED), semiconductor lasers as well as solar cells. Here, the solid state interface is between two semiconductors or between a metal and a semiconductor. The principle process of all solid state interfaces is the charge carrier equilibration across the junction which develops when different energetic levels are adjusted. Due to the Fermi level alignment electrons are transferred from the material with the lower work function to the one with the higher work function. As a result of this an electric field will evolve which leads to a bending of the electronic bands in the semiconductor. The band bending can be distinguished in three different ways: accumulation, depletion and inversion. These different possibilities of band bending will be explained by the example of an n-type semiconductor. In case of an accumulation, which is shown in Figure 4 a), the band bending is caused by an increase of majority charge carriers at the interface. The majority charge carriers of an n-semiconductors are electrons. When it comes to a depletion the electron concentration at the interface is decreased which causes an accumulation of holes. Holes are the minority charge carriers in an n-semiconductor. This effect can be seen in Figure 4 b). An extreme form of predominant majority charge carriers at the interface is the so called inversion which is shown in Figure 4 c). Here, the conduction band is strongly bend and therefore, intersects the Fermi level. Analogous to the example of an n-type semiconductor, the bands of a p-semiconductor bend in opposing way. Here, the majority charge carriers are holes and the minority charge carriers are electrons.

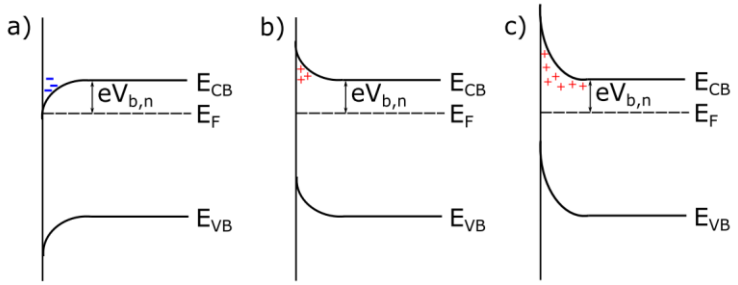

Figure 4: Possible energy band situations at an n-type semiconductor: a) accumulation, b) depletion and c) inversion.

When bringing two semiconductors into contact it is differentiated between a homocontact and a heterocontact. In case of a homocontact two semiconductors of the same material but different doping are brought into contact which can lead to a pn-homocontact. The most prominent example paragon for semiconductor homocontacts is silicon (Si) which is present with any kind of doping and hence available as pn-homojucntion as well as np-homojunction. For heterocontacts two semiconductors of different materials are brought into contact for example gallium arsenide (GaAs) and Si. As the pn-homocontact of Si plays an important role in this work, this situation is illustrated in Figure 5 a). It can be observed that near the interface the bands bend in order to adjust the Fermi levels of the p- and n-doped region of the semiconductor. This area is called space charge region (SCR) which is defined by the width of the SCR. The width of the SCR in the p-type semiconductor is indicated by $-W_p$ for the p- and W_n for the n-type semiconductor, respectively. If semiconductors with different band gaps are brought into contact (heterocontact), the situation at the interface becomes more complex which is shown in Figure 5 b). The difference in the size of energy band gap leads to an offset ΔE_{CB} in conduction band and ΔE_{VB} in valence band when adjusting the Fermi level.

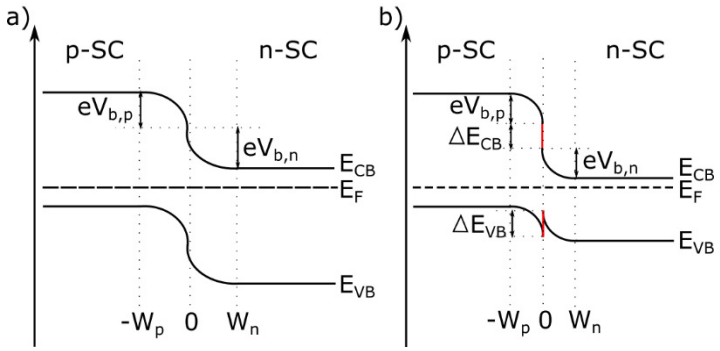

Figure 5: Band diagram of a a) p-n-semiconductor contact with differently doped regions but equal energy band gap which results in a band bending of eV_b in both regions; b) semiconductor contact with differently doped regions and different energy band gaps which causes an offset in valence and conduction band.

Another relevant contact situation is the so called Schottky-contact which is formed by the interface between a semiconductor and a metal. Figure 6 schematically illustrates the band diagram of such a Schottky-contact. Equally to the pn-contact the semiconductor bands at the interface bend in order to align to the Fermi level of the metal. The direction of the band bending is responsible for the charge carrier transport properties at the interface. An example which is relevant for this work is the Si | Cu Schottky-contact.[16]

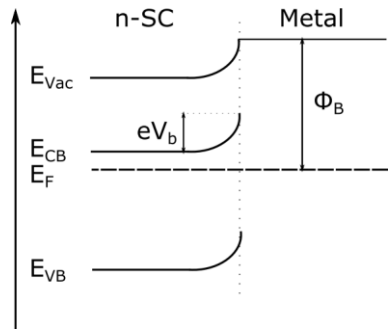

Figure 6: Schottky contact with an n-semiconductor and a metal which causes a band bending of eV_b in the energy bands of the semiconductor.

2.3 Solar Cells

A solar cell is a semiconductor device which is able to convert solar energy into electrical energy. A basic solar cell consists of a simple pn-junction, while thin film solar cells, which are used in this work are composed of different functional layers. Here, main part is the intrinsic absorber layer, which absorbs the sun light and therefore generate electron hole pairs. How much of the sun light can be absorbed depends on the energy band gap of the used semiconductor, which on the other hand defines the maximum value of photovoltages which can be produced. The optimum band gap which absorbs the most part of the solar spectrum has a size of E_G=1.1 eV.[17] Only photons which have an energy equal or larger the energy band gap of the semiconductor can be absorbed. Due to this reason Si with a band gap of E_G=1.12 eV is an ideal solar cell material. Besides the absorber layer, a solar cell needs to have an electron conductive layer as well as a hole conductive layer. In a semiconductor device these selective conductive layers are an n-doped semiconductor and a p-doped semiconductor. The solar cell current is generated depending on the photovoltage, according to the solar cell characteristics under illumination shown in Figure 7. The indicated values are characteristic for a solar cell. There are the short circuit current density J_{SC}, the open circuit voltage U_{OC} and the efficiency η. The efficiency is the relation of the voltage (U_{MPP}) at the maximum power point (MPP) and the current density at MPP (J_{MPP}) with respect to the power density of the light (P_{photon}). The efficiency is calculated by $\eta = (U_{MPP} * J_{MPP} / P_{photon})$.

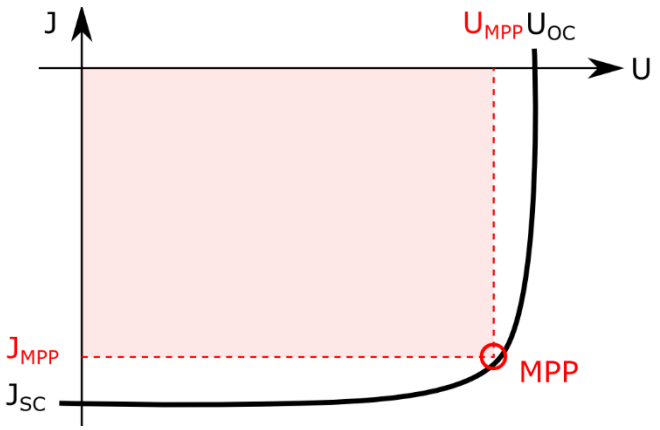

Figure 7: Solar cell characteristics under illumination including the typical values: M_{PP}, U_{MPP}, U_{OC}, J_{MPP} and J_{SC}.

Besides the limitation of the photovoltage caused by the size of the energy band gap the thickness of the absorber layer plays an important role for the photocurrent. In order to absorb the whole incoming light the absorber layer thickness should be larger than the reciprocal absorption coefficient. However, the absorption layer should be thin enough to prevent recombination as an enlarged distance to the contacts of the solar cell promote the effect of recombination of charge carriers. The optimum absorption layer thickness strongly depends on its optical and electrical properties such as absorption coefficient and

charge carrier mobility. The adjacent layers of the absorber material must exhibit a high conductivity for the present type of charge carriers. This is important because the charge carriers need to be transmitted to the external contacts. On the other hand it is crucial that the conductivity for the opposing type of charge carriers is very low. Furthermore, absorption of photons should not take place in these layers. A relevant example for a thin film solar cell is the p-i-n-Si structure. The corresponding band diagram is schematically shown in Figure 8. Here, the difference between the solar cell under illumination and in the dark is demonstrated. In case of an illuminated solar cell the charge carrier distribution cannot be explained by the Fermi level due to the additionally created electrons and holes. In fact, Quasi-fermi levels for both types of charge carriers form which is shown in Figure 8. The Quasi-fermi levels in the doped layers are equal to the Fermi levels in the dark as the change of the number of majority charge carriers is negligible. Whereas, the generation of charge carriers in the intrinsic absorber layer strongly influences the number of minority charge carriers and therefore affect the position of the Quasi-fermi level. The situation illustrated in Figure 8 represents an ideal model of a thin film solar cell which is not easy to realize.[18]

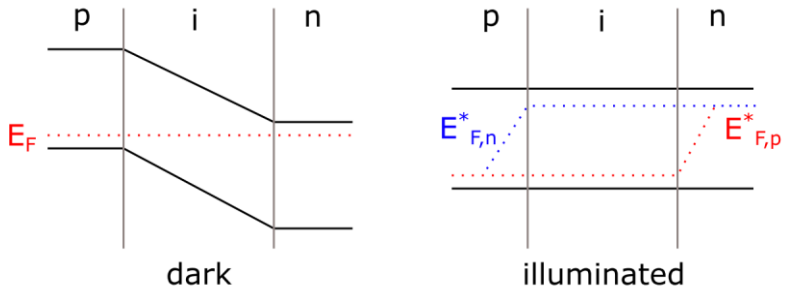

Figure 8: Schematic illustration of a p-i-n structured solar cell in the dark and under illumination.

For this work a-Si:H | a-Si:H | µc-Si:H and µc-Si:H solar cells with p-i-n structure were used. Contrary to crystalline Si, amorphous Si exhibits no long range order in the atomic positions. However, amorphous Si is principally also tetrahedrally coordinated with four bonds as it is the case for crystalline Si, but bond lengths as well as angles are different from the well-ordered crystalline structure. As a result structural defects such as strained bonds and three- or fivefold coordinated Si atoms exist within the amorphous Si, which leads to dangling bonds within the Si structure. As open bonds significantly reduce the electrical properties of Si, hydrogen is incorporated into the Si network in order to passivate the open bonds. With that the defect density can be reduced by three to four magnitudes from 10^{19} cm^{-3} to approximately 10^{15}-10^{16} cm^{-3}.[19] The amorphous structure of Si itself is not affected by the incorporation of hydrogen.[20] Besides the lattice structure, the electronic structure of amorphous Si is also different compared to crystalline Si. While crystalline Si exhibits the electronic structure of a classical semiconductor, amorphous Si exhibits so called band tails which result from more distorted bonds. In these band tails the mobility of charge carriers is reduced. However, they can be injected into

the conduction band with increased temperature enhancing their transport rate. In contrast to crystalline Si, which possesses a classical indirect band gap, the band gap of amorphous Si is defined as a mobility gap. Because of the presence of the band tails, an exact distinction between localized and extended states cannot be defined. Therefore, several values between 1.6 eV [21] to 1.9 eV [22] for the optical band gap are valid.

The used µc-Si:H p-i-n solar cell consists of a hydrogenated highly microcrystalline Si phase, which is embedded in an amorphous texture. Depending on the desired properties of the solar cell the structure can be designed exhibiting highly crystalline to mostly amorphous character. The structure can be adjusted by varying a number of deposition parameters, which is not part of this work.[23][24] The properties of microcrystalline Si are very similar to single crystalline Si. One important feature with respect to photovoltaic applications is the absorption spectrum which does not show crucial differences within a wide energy range for both materials. Furthermore, micro- and single crystalline Si show a similar optical band gap energy of 1.12 eV.[25][26] Within a photon energy range of approximately 1.0 eV to 1.85 eV the application of micro- or single crystalline Si does not influence the light absorption while amorphous Si absorbs much less photons within this range. However, above 1.85 eV the absorption coefficient of amorphous Si is very high followed by microcrystalline Si and then single crystalline Si. As a consequence, amorphous Si absorbs more light in the blue to ultraviolet (UV) region, while microcrystalline Si is favorably used to absorb photons with low energy in the infrared (IR) region. The spectrum of the visible light is absorbed by amorphous Si as well as microcrystalline Si. Figure 9 shows the absorption coefficient of crystalline Si (c-Si), µc-Si:H and a-Si:H as a function of the photon energy. In order to take advantage of these differences in the ability to absorb light, multijunction solar cells were developed. The stacking of a-Si:H and µc-Si:H solar cells leads to an nearly optimum exploitation of the solar spectrum and hence extends the range of achievable photovoltages.[19], [24], [25], [27], [28]

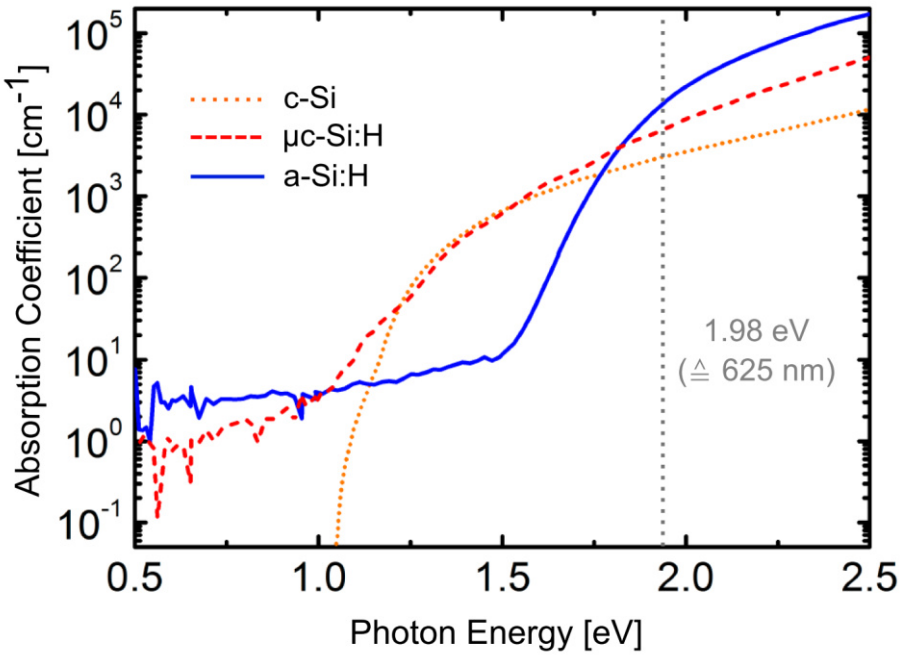

Figure 9: Absorption coefficient as a function of the photon energy. Orange: c-Si, red: µc-Si:H and blue a-Si:H. The figure is adapted from Ref. [24]

The used a-Si:H | a-Si:H | µc-Si:H and µc-Si:H solar cells with p-i-n structure are designed with a glass window and a transparent conductive oxide (TCO) to allow the light to enter the absorbing layer. Furthermore, a front as well as a back contact is needed which in this work is deposited afterwards within the experimental procedure. Exemplary schematic drawings of such solar cell structures are shown in comparison to a pn$^+$-Si single junction in Figure 10. Contrary to the simple case of a pn$^+$-Si single junction where the light enters the photoabsorber through the n-layer, in case of the used a-Si:H | a-Si:H | µc-Si:H and µc-Si:H solar cells it is necessary to illuminate the solar cells through the p-layer as especially in a-Si:H the hole mobility is much lower compared to electron mobility. As a consequence most of the photons are absorbed in the i-layer close to the p-i interface. Hence, the low mobility holes can easily travel to the p-layer as the distance is comparably short. Besides acting as absorber layer, the i-layer expands the space charge region of the solar cell, which allows the transport of photogenerated charge carriers by drift. This is crucial due to the reduced charge carrier lifetimes. [19], [24], [27]–[29] It can also be noticed from Figure 10 that the p-layer is much thinner in case of the solar cells. A thin p-layer in the pin-configuration of the solar cells allows more light to enter the absorber layer, which results in an increased photocurrent. However, a thicker p-layer enhances the electric field in the solar cell and hence, increases the photovoltage.[24]

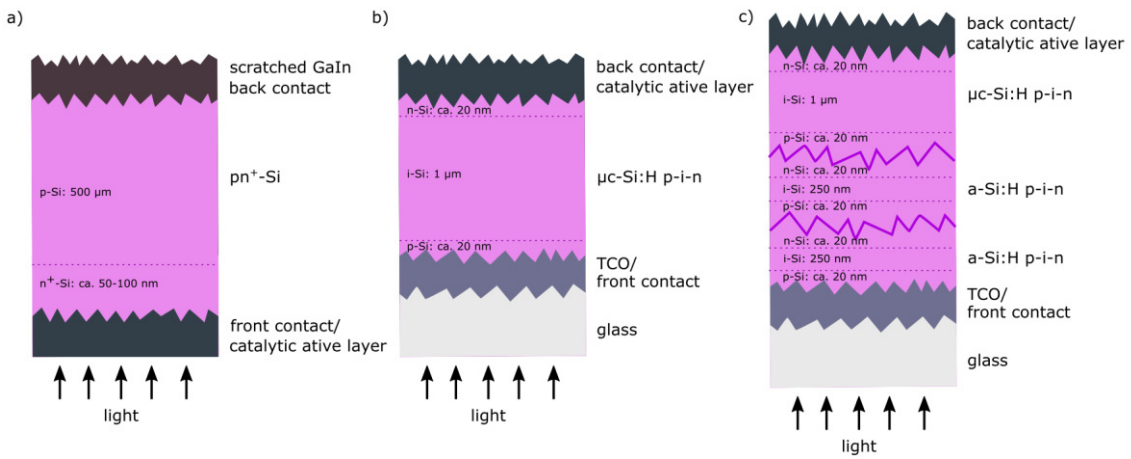

Figure 10: Schematic drawing of a) a pn$^+$-Si single junction, b) a µc-Si:H p-i-n solar cell with glass window, TCO, front and back contact and c) an a-Si:H | a-Si:H | µc-Si:H solar cell with glass window, TCO, front and back contact.

Figure 11 shows the JV-characteristics of both used types of solar cells. As already mentioned above the use of multijunction solar cells improves the photovoltage in contrast to the single junction. While the open circuit voltage of the a-Si:H | a-Si:H | µc-Si:H solar cell reaches 2.27 V, the µc-Si:H solar cell only reaches 0.53 V. However, the current density is much larger in case of the µc-Si:H solar cell (22.5 mA/cm^2) compared to the 7.8 mA/cm^2 for the a-Si:H | a-Si:H | µc-Si:H solar cell. These JV-characteristics will be important when evaluating the photoelectrochemical performance of the solar cells, which is part of chapter 5 and 6.

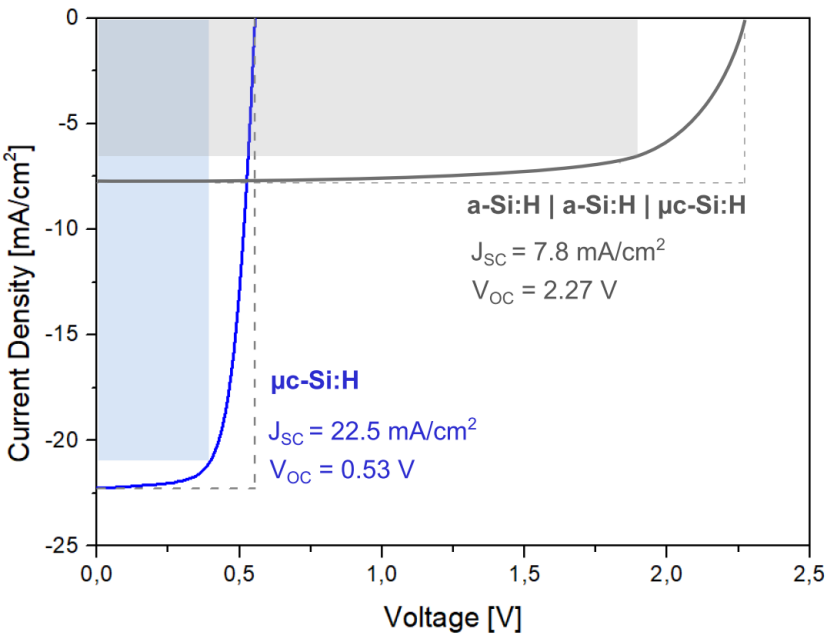

Figure 11: JV-characteristics of a µc-Si:H and an a-Si:H | a-Si:H | µc-Si:H solar cell. This information originates from the A-LEAF project partner Forschungszentrum Jülich GmbH.

2.4 Photoelectrochemical Cells

A photoelectrochemical cell is used to perform photoelectrochemical measurements under different illumination conditions. On one side, it consists of a photoabsorber as the cathode (in the used setup), which provides enough photocurrent and photovoltage to drive the electrochemical reaction. A catalytically active layer, which is in direct contact to the photoabsorber as well as the electrolyte enhances the reaction rate. On the other side is the counter electrode consisting of a metal plate or mesh, which is also covered by a catalytically active layer to enhance the anodic half-reaction. The reaction which takes place at the cathode is called reduction reaction while the reaction at the anode is called oxidation reaction. The used electrolyte should provide a high ionic conductivity as the charge transfer in liquid materials is transported by ions, contrary to metals where the charge transfer is conducted by electrons. In solar cells the current is determined by the majority charge carriers. In general, the ion mobility in an electrolyte is five to six orders of magnitude smaller than the mobility of electrons and holes in a crystalline semiconductor. Therefore, it is very important to take into account that low ion concentrations can limit the efficiency of the photoelectrochemical cell due to high resistive losses. Therefore, an appropriate electrolyte should be chosen.[30][24]

The photoelectrochemical measurement of one half-cell reaction can be realized by a three electrode setup: working electrode (WE), reference electrode (RE) and counter electrode (CE). Here, the working electrode refers to the half-cell where the oxidation or reduction takes place which means that this electrode is connected to the sample. The reference electrode which has a defined potential in the used electrolyte is used to measure the potential of the sample (WE). The current between working electrode and counter electrode (platinum (Pt) wire) is adjusted and therefore the potential of the sample (WE) can be measured.

Reduction and oxidation reactions (redox reactions) are described by electron transfer between the involved species. The work, which is needed to add a charged particle to a redox system, is described by the so-called electrochemical potential. This description is analogous to the Fermi level within semiconductors. Usually the electrochemical potential is given in units of joule per mole (J/mol) while the Fermi energy is given in units of electron volts (eV).[24]

When the half-cell reaction at the working electrode take place at the same rate for the involved reduction and oxidation reaction the redox potential is at its thermodynamic equilibrium. However, the redox potential may change when deviating from standard conditions. This can happen for example if both components have different concentrations. The Nernst equation can be used to calculate changes of the redox potential:

$$E_{redox} = E^0_{redox} + \frac{RT}{nF} ln\left(\frac{c_{ox}}{c_{red}}\right), \quad (2)$$

where E^0_{redox} is the redox potential under standard conditions, R the gas constant, T the temperature, c_{ox} the concentration of the oxidized species and c_{red} the concentration of the reduced species.[31] Analogous to the electron energy in vacuum, which is used as reference for semiconductors, the redox potential under standard conditions E^0_{redox} is usually referred to the standard hydrogen electrode (SHE). The potential of the SHE lies at -4.5 eV with respect to the vacuum level.[32][33] Therefore, the standard electrochemical potential can be related to the Fermi level in the electrolyte by using the vacuum level as a reference. Although, the behavior of particles in a solution differs from electrons in a semiconductor, a quantitative description of photoelectrochemical concepts is possible by adjusting the energy scale of both systems.

Usually, an electrochemical cell is not under equilibrium as this state can be easily be disturbed by applying an overpotential or by adding reactants which will result in an increased reaction rate of the cathodic or the anodic reaction. As a consequence a net current flow appears. The applied overpotential should be high enough to drive the charge transfer which is defined as difference between the electrochemical potential and the electrode potential in case of equilibrium.[34][24]

The Butler-Volmer equation (3) expresses the overall current voltage dependence of an electrochemical reaction which contains the cathodic as well as the anodic reaction kinetics.

$$j = j_0 \left[e^{\left(\frac{\alpha nF}{RT}\eta_{ct}\right)} - e^{\left(-\frac{(1-\alpha)nF}{RT}\eta_{ct}\right)} \right] \quad (3)$$

Here, j_0 is the exchange current density, which describes the velocity of the charge transfer under equilibrium conditions, which is also correlated to the catalytic activity of the electrode. The overpotential is expressed by η_{ct}, while α is the transfer coefficient, n the number of charges and F the Faraday constant.[35]

Figure 12 a) shows the schematic setup of a photoelectrochemical cell which used a µc-Si:H solar cell in pin-configuration as photocathode. This is only an exemplary setup as different cathode materials can be used such as pn^+-Si single junctions or a-Si:H | a-Si:H | µc-Si:H and µc-Si:H solar cells. Nevertheless, the main parts as well as the working principle are the same. One important part of the photoelectrochemical cell is the interface between the metallic back contact and the electrolyte. When a metal is brought into contact with an electrolyte charges flow from one phase to the other in order to equilibrate the electrochemical potential. This mechanism can be compared to the energy band alignment of pn-junctions of semiconductors. The charge flow between the metal and the electrolyte leads to a potential difference across the interface causing an electrical field. As a consequence, the ions in the electrolyte as well as the water molecules near the interface will redistribute resulting in a Helmholtz double layer and a diffusion layer. The catalytic active metal layer does not only play an

important role in terms of charge flow across the metal electrolyte interface, but it is also important to bury the semiconductor structure in order to protect it from the electrolyte. From Figure 12 a) it can be seen that under illumination charge carriers are generated in the µc-Si:H solar cell which are then injected from the back contact into the electrolyte. Here, the electrons take part in the reduction reaction. On the other side holes are transferred from the TCO layer and front contact to the anode and take part in the oxidation reaction.

It can be concluded that the photoelectrochemical cell is a series connection of a photovoltaic cell and an electrolysis cell. The electrolysis is biased by the photovoltage, which is generated by the used absorber material when being illuminated.

Figure 12 b) shows the schematic energy band alignment of a p-i-n Si solar cell with a metal contact (Cu/ Ag) in the dark and c) under illumination. In the dark the applied potential at the Si junction is equal to the potential at the metal contact. In contrast, under illumination the potential at the metal contact is shifted (into negative direction), which is an effect of the formation of Quasi-fermi levels due to the induced photovoltage.

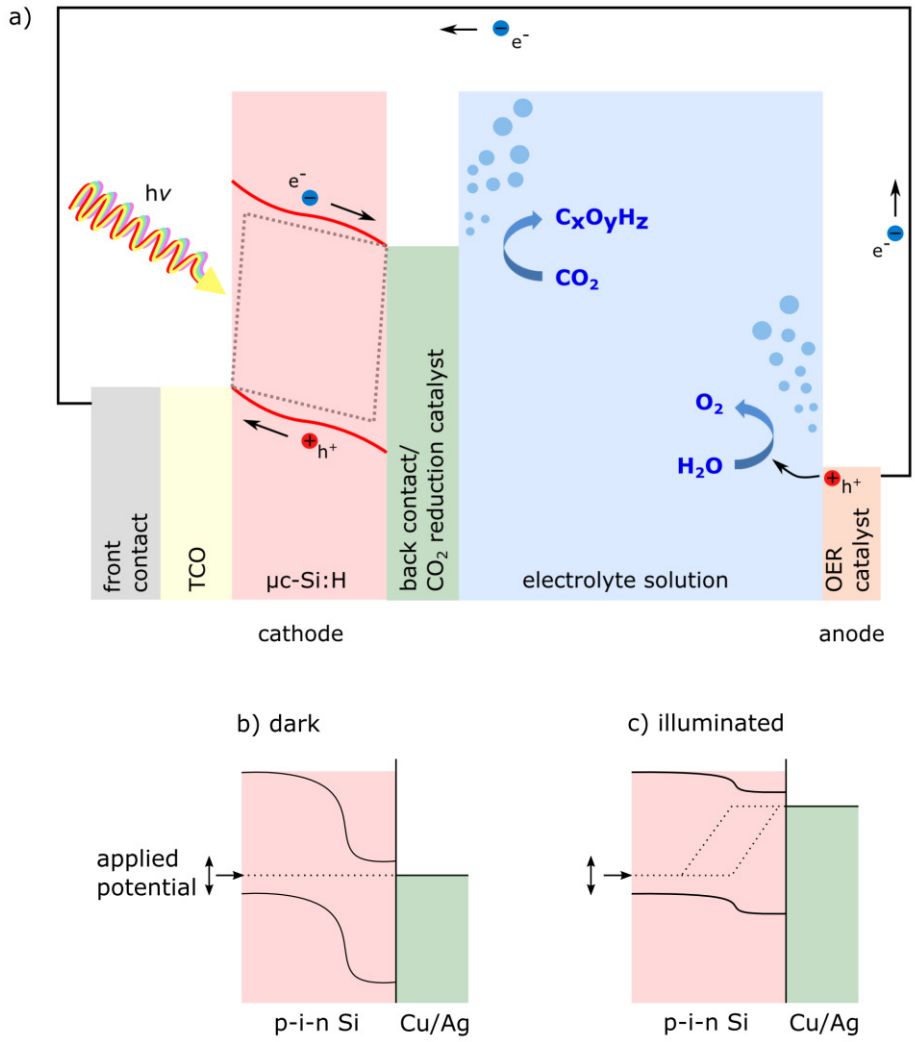

Figure 12: a) Schematic setup of a photoelectrochemical cell consisting of a front contact, a transparent conductive oxide (TCO), a μc-Si:H solar cell in pin-configuration with back contact which acts as CO_2 reduction catalyst (photocathode), the electrolyte solution and a catalyst for the oxygen evolution reaction which acts as anode. b) Schematic energy band diagram in the dark and c) under illumination.

2.5 CO_2 Reduction Reaction

Carbon dioxide (CO_2) is a well-known and abundant chemical compound, which acts as a greenhouse gas. Since its worldwide concentration has drastically increased within the last centuries, it is becoming of more and more importance to develop a technique to utilize these carbon sources and hence reduce the CO_2 concentration in our atmosphere. Analogous to the well-established technique of water splitting, the electrochemical reduction of CO_2 to useful products is possible. However, the energy conversion efficiency of the CO_2 reduction is comparably low, which results in a challenging task in science.[36][37]

One problem concerning the CO_2 reduction is the low chemical reactivity of CO_2. But compared to the hydrogen evolution reaction (HER) the equilibrium potentials of the CO_2 reduction are similar. While the standard electrode potential of HER at neutral pH value is -0.414 V with respect to the standard hydrogen electrode (SHE) at 25°C, the standard electrode potential for the electrochemical reduction of CO_2 to formate ($HCOO^-$) is very similar as shown below. For sake of comparison the values are additionally calculated related to RHE by $E_{RHE} = E_{SHE} + 0.059 \cdot pH$ with $pH_{0.3\ M\ KHCO3} = 8.27$.

$$CO_2 + H_2O + 2e^- \rightarrow HCOO^- + OH^- \ (-0.43\ V\ vs.SHE\ at\ pH\ 7.0, 0.058\ V\ vs.RHE) \quad (4)$$

However, the real electrolysis potentials for the CO_2 reduction are much more negative under operation conditions than in the equilibrium case, which explains why CO_2 reduction does not take place easily. The reason for that is the initial formation of the intermediate species $CO_2^{\bullet -}$, which results from an electron transfer to a CO_2 molecule. In the following possible CO_2 reduction reactions are presented, where all values were calculated from thermodynamic data for pH 7. Furthermore, the values are also presented in V vs. RHE as described above. [24][38]

$$CO_2 + H_2O + 2e^- \rightarrow CO + 2OH^- \ (-0.52\ V\ vs.SHE, -0.032\ V\ vs.RHE) \quad (5)$$

$$CO_2 + 6H_2O + 8e^- \rightarrow CH_4 + 8OH^- \ (-0.25\ V\ vs.SHE, 0.238\ V\ vs.RHE) \quad (6)$$

$$2CO_2 + 8H_2O + 12e^- \rightarrow C_2H_4 + 12OH^- \ (-0.34\ V\ vs.SHE, 0.148\ V\ vs.RHE) \quad (7)$$

$$2CO_2 + 9H_2O + 12e^- \rightarrow C_2H_5OH + 12OH^- \ (-0.33\ V\ vs.SHE, 0.158\ V\ vs.RHE) \quad (8)$$

$$3CO_2 + 13H_2O + 18e^- \rightarrow C_3H_7OH + 18OH^- \ (-0.32\ V\ vs.SHE, 0.168\ V\ vs.RHE) \quad (9)$$

Which products result from the CO_2 reduction mainly depends on the electrode material as well as the used electrolyte solution. While the electrode provides the reaction sites and the product selectivity, the electrolyte is also involved in the concentration and stability of the reactants and the intermediate species.

By cathodic polarization HER takes place easily and is usually in competition with CO_2 reduction. The rate of HER is proportional to the proton activity in aqueous solution. This is valid for a variety of metal electrodes.[39] Therefore, CO_2 reduction prevails over HER if the reaction does not take place in acidic solutions. In alkaline solutions CO_2 molecules do not exist which justifies studies with neutral electrolyte solutions. [39]–[41]

Several electrode materials have been studied and it has been found that the selectivity of the CO_2 reduction is mainly affected by the purity of the electrode materials as well as the electrolyte solution. [41]–[46] Depending on the product selectivity electrode materials can be divided into four groups. Electrode materials which mainly form $HCOO^-$ as reaction product belong to the first group. Examples for first group electrode materials are Cd [42], [43], [47]–[49] Sn [42], [43], [47]–[51], In [42], [43], [46]–[48], [50], [52], Hg [40], [42], [47]–[49], [52]–[56]and Pb [42], [43], [59], [47]–[52], [57], [58]. Electrode materials which mainly give CO as major reaction product are categorized as second group electrode material. Examples for materials of the second group are Au [43], [46], [47], [49], [60]–[63], Ag [42], [43], [46], [47], [49], [64]–[66], Zn [42], [46]–[48], [52], [67], Pd [68]–[71] as well as Ni-Cd alloy [72]. Cu electrodes are the only material in the third group as Cu has the outstanding ability to produce CH_4, C_2H_4 and alcohols in reproducible amounts.[43], [47], [81]–[84], [73]–[80] Furthermore Cu alloys such as Cu-Ni and Cu-Fe [85], Cu-Sn, Cu-Pb, Cu-Zn and Cu-Cd [86], Cu-Ag [86][87] can be used for the CO_2 reduction.[73]

As in this work Cu has been mainly used as CO_2 reduction catalyst, the reaction mechanism needs to be introduced. It has been shown in previous studies that CO and $HCOO^-$ are formed first and then act as precursors to the further reduction to hydrocarbons and alcohols.[73], [88]–[90] One characteristic feature about Cu electrodes is the medium heat adsorption which results in a CO adsorption which is neither too strong nor too weak. This leads to more effective formation of hydrocarbons.

After the initial formation of CO, further reduction to CH_4 or C_2H_4 can take place. It has been proven that the formation of CH_4 starts at more negative potentials compared to C_2H_4 which leads to the assumption that the reaction pathways are different for both reduction reactions. Figure 13 gives an overview of the molecular reaction pathway suggested for the chemical reduction of CO_2 starting from the intermediate species CO.[73]

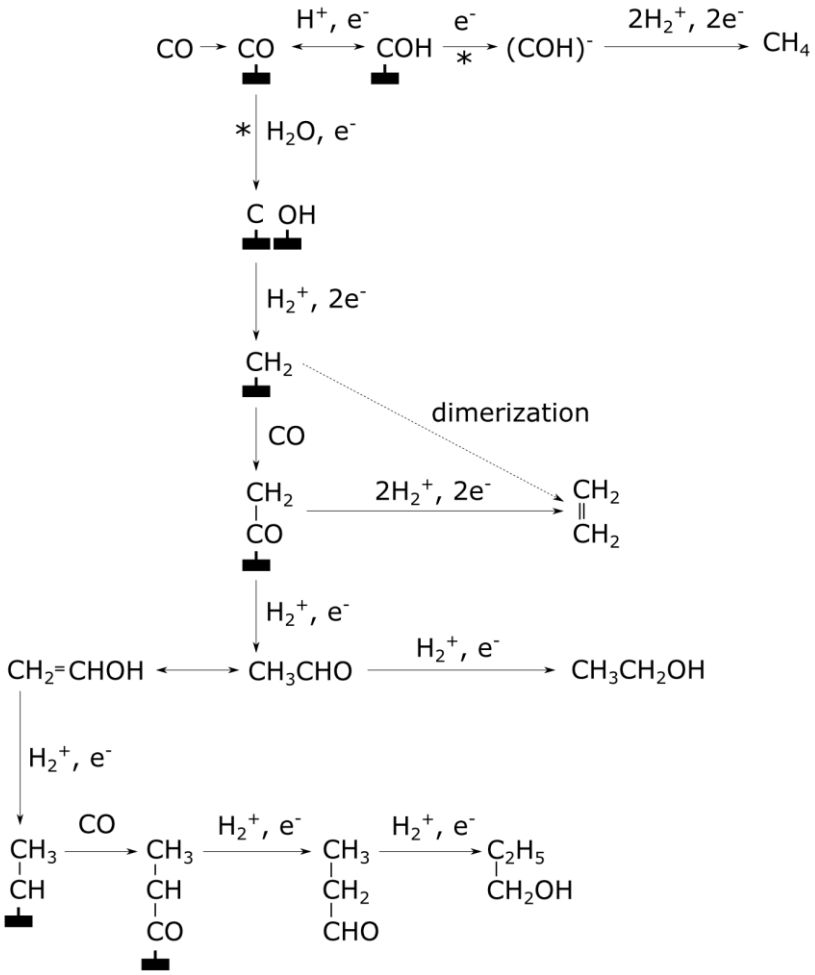

*Figure 13: Schematic drawing of the molecular reaction pathway of the chemical reduction of CO, which is suggested for the reaction mechanism on metallic Cu electrodes. With * denoted reaction pathways are rate determining steps.*

3 Experimental Methods

In this chapter the experimental methods are introduced, which were used to obtain the results of this work. The subjects will be electron beam deposition and photoelectron spectroscopy, which includes the physical fundamentals as well as the principles of an interface experiment. Moreover, photoelectrochemical measurements and scanning electron microscopy are introduced.

3.1 Electron Beam Deposition

Electron beam deposition (e-beam deposition) is a physical vapor deposition technique where the evaporant is either evaporated from a rod, a bar or from a crucible within a vacuum chamber. The target anode is bombarded by an electron beam, which is emitted from a charged tungsten filament. The bombarding electrons induce a temperature rise of the evaporant, which causes atoms from the target to be transferred into the gaseous phase. The evaporated material then precipitates onto the sample. The schematic drawing in Figure 14 shows the deposition principle. Here, the evaporation from a crucible is shown. The choice of the evaporation technique depends on the desired deposition material. While rod evaporation leads to element distribution in all directions, crucible evaporation is more directional and therefore more effective. Furthermore, the evaporant volume in a crucible is much larger compared to a rod. However, there is one advantage of the rod evaporation. As there is no crucible involved, the evaporated material usually shows a higher cleanliness than thin films which were evaporated from a crucible. Some typical material examples for rod evaporation are titanium (Ti), molybdenum (Mo), carbon (C) and aluminum oxide (Al_2O_3). Examples for crucible evaporation are copper (Cu), silver (Ag), lead (Pb) and nickel (Ni). Here, commonly the crucibles are made out of tungsten (W), Mo or C. The vapor pressure of the material to be deposited, which is required for the evaporation, is in the range of 10^{-4} to 10^{-8} mbar. The thickness of the deposited film was controlled by the intensity ratio of the substrate and the film measured by photoelectron spectroscopy, which is described in detail in chapter 4.5.

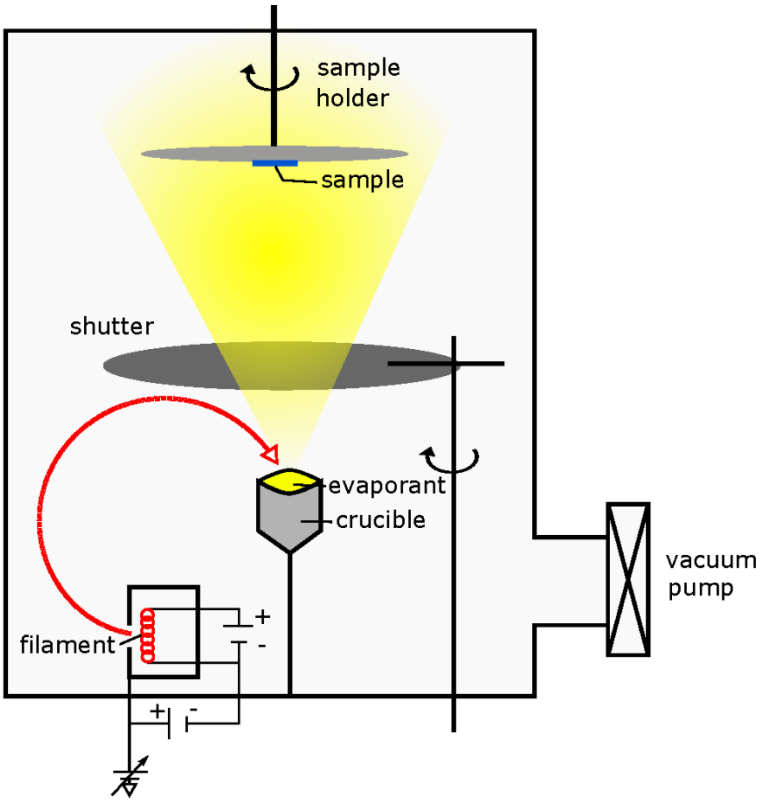

Figure 14: Schematic set-up of an electron beam deposition process using crucible evaporation instead of rod or bar evaporation, which is suitable for a variety of materials such as Cu and Ag.

3.2 Photoelectron Spectroscopy

3.2.1 Physical Basics

Photoelectron Spectroscopy (PES) or Electron Spectroscopy for Chemical Analysis (ESCA) is an advanced method for qualitative and quantitative elemental analysis. This method is usually used to investigate the chemical composition of surfaces. The physics of PES is based on the external photoelectric effect. Here, a sample is illuminated with electromagnetic radiation, which results in the emission of electrons from the sample surface.[91][92] Commonly, X-rays are used to irradiate the sample which is known as X-ray Photoelectron Spectroscopy (XPS). Typically, monochromatic Al Kα (1486.64 eV) or Mg Kα (1253.6 eV) photons are used for excitation. If a very high resolution and sensitivity is desired, synchrotron irradiation has to be used as X-ray source.[93] XPS is a surface sensitive method delivering information of the first 1-10 nm of the sample. The reason for this sensitivity is the limited inelastic mean free path of primary electrons in the sample material. Consequently, only electronic states near the surface can be analyzed.[92][94]

In Figure 15 the inelastic mean free path of electrons in solids is plotted versus the kinetic energy of the electrons. It can be concluded that the most surface sensitive information can be obtained with an

electron energy of approximately 50 eV, which possess a mean free path of 5Å. Another option of PES is the so called Ultraviolet (UV) Photoelectron Spectroscopy (UPS) where UV radiation is used instead of X-rays. Here, a gas discharge lamp which is operated with Helium (He) gas is utilized as radiation source. It can be differentiated between He-I (21.2 eV) and He-II (40.6 eV). Which radiation is used depends on the gas pressure. Whether XPS or UPS is used depends on the desired information. While XPS analyses core level states corresponding to specific chemical elements, UPS gives the opportunity to access valence electron states which gives mostly information about the electronic structure.[92]

In order to point out the measurement principle of the kinetic energy of the photoelectrons, the general measurement set-up is explained in Figure 16. A monochromator is used to select the radiation of desired energy on the sample, which leads to the emission of photoelectrons. First, these electrons pass through the electrostatic optics of the system before reaching the hemispheric energy analyzer. The intensity of the photoelectrons is measured by an electron multiplier after leaving the analyzer.[93]

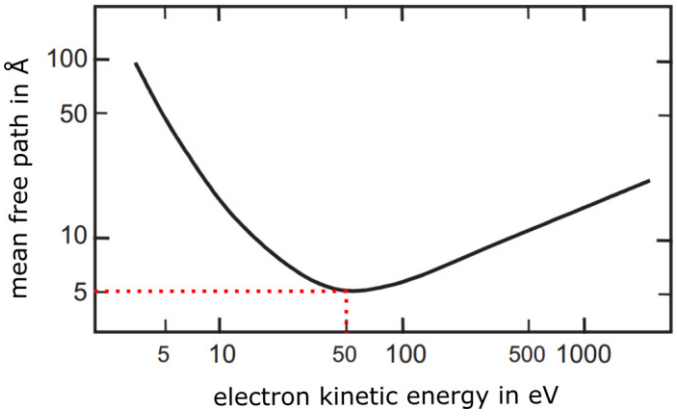

Figure 15: The inelastic mean free path of electrons in solid state materials vs. the kinetic energy according to.[92]

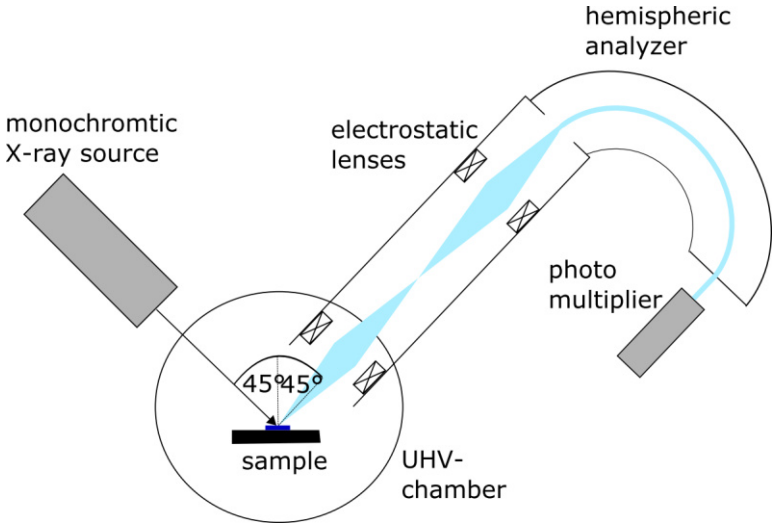

Figure 16: Schematic set-up of a photoelectron spectrometer, which shows its main parts: the monochromatic X-ray source, the hemispheric analyzer, the photo multiplier and the electrostatic lens system.

An important feature of PES is the independence of the kinetic energy (E_{kin}) of the photoelectrons of the work function of the sample. With the help of Figure 17 this relationship can be understood by showing the energy transition of a photoelectron during the measurement process. The kinetic energy can be derived as following:

$$hv = E_B + \phi_s + E'_{kin} \tag{10}$$

$$E_{kin} = E'_{kin} - \phi_a + \phi_s \tag{11}$$

$$E_{kin} = hv - E_B - \phi_a \tag{12}$$

where hv is the photon energy, E_B the binding energy of the sample holder, ϕ_s the work function of the sample and ϕ_a the work function of the analyzer. It can be concluded that the work function of the sample does not influence the measured kinetic energy of the photoelectrons. The influence of the work function of the analyzer on the kinetic energy of the measurement photoelectrons is eliminated by calibrating the PES. For calibration the electronic core level lines of silver, copper or gold are determined.

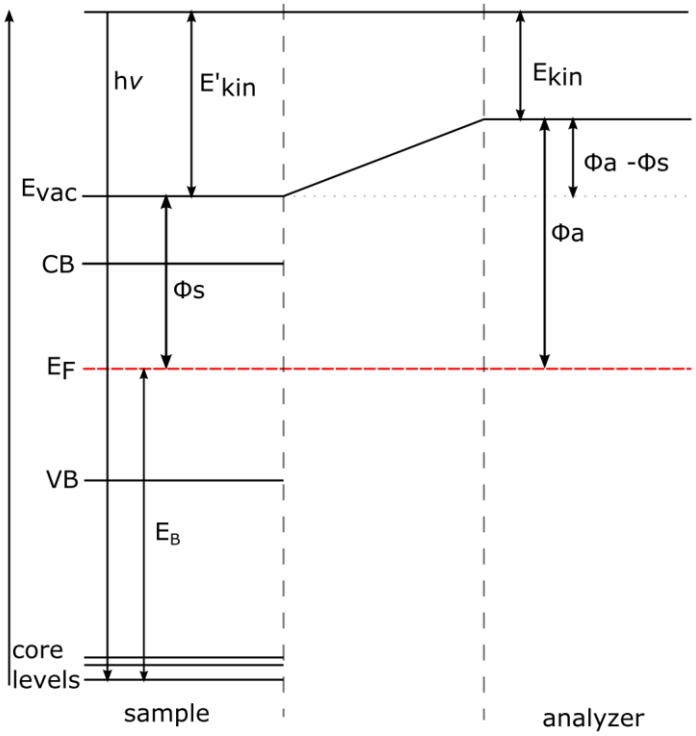

Figure 17: Band diagram, which schematically shows the energetically relationship between the measured kinetic energy and the binding energy of the electron in the sample during the photoelectron spectroscopy.

The work function of a sample as well as the ionization potential I_P can be determined from PES. For the determination of the work function ϕ_U with UPS the measured binding energy of the secondary

electron edge (SEE) is subtracted from the He-I energy according to equation (13). Then the ionization potential in given by adding this result to the value of the valence band maximum VBM_U measured by UPS (eq. 14). When subtracting the value of the valence band maximum VBM_X from the ionization potential I_P (measured by XPS) it gives the work function ϕ_X, according to equation (15).

$$\phi_U = 21.22\ eV - SEE \tag{13}$$

$$I_P = \phi_U + VBM_U \tag{14}$$

$$\phi_X = I_P - VBM_X \tag{15}$$

In addition to that, the work function can also be determined by XPS. According to equation (16) the SEE is subtracted from the 1486.64 excitation energy. From the resulting value the applied negative bias of -3 V needs to be subtracted as well which then gives the work function ϕ_X.

$$\phi_X = 1486.64 - SEE - 3\,V \tag{16}$$

The elemental composition of a sample can be deduced from the measured spectra by evaluating the positions of the emission lines. For a quantitative analysis the measured emission lines have to be integrated in order to gain the area. For the integration a suitable background correction needs to be considered. The atomic fraction of any element in the sample can subsequently be calculated by equation (17) where C is the fraction of the atoms x and i, S is the atomic sensitivity factor which is tabulated in literature [94] and I is the integrated intensity after background correction. According to Tougaard and Shirley different background corrections are possible. [95][96] The Shirley method gives a root mean square deviation from theory a deviation of approximately 35% while the Tougaard method gives a deviation from theory of around 3%.[95]

$$C = \frac{I_X/S_X}{\sum I_i/S_i} \tag{17}$$

3.2.2 Interface Experiments

As the deposition chamber, where the electron beam deposition takes place, and the PES are connected in-line within an ultra-high vacuum (UHV) system, interface studies are possible, which allow the analysis of the position and mobility of the Fermi level in the band gap of a semiconductor. The terminus "interface experiment" refers to the stepwise deposition of a material B on a substrate A. First, the core level lines of the clean substrate A are measured by XPS as a reference. Afterwards, a very thin layer of material B is deposited without leaving the UHV system. Subsequently, the sample is measured by XPS again. The signal of the substrate will still be predominant in comparison to the deposited contact material B. These steps are repeated until the substrate A cannot be observed by XPS anymore. Instead,

the bulk properties of material B are measured. This experimental procedure is reasonable as the substrate A needs to adjust its Fermi level when coming in contact to material B. Furthermore, an occurring band bending can be observed.

3.3 Photoelectrochemical Measurements

Photoelectrochemical measurements are used to investigate the catalytic properties of the prepared samples. These measurements can be performed either in a two- or a three-electrode setup. The two-electrode setup can be used to measure the reference electrode (e.g. Ag/AgCl) against a reversible hydrogen electrode (RHE). The three-electrode configuration is used to measure the current between the sample at the working electrode (WE) and the counter electrode (CE) which is realized by a Pt wire. This configuration enables the investigation of the half-cell reaction, which takes place at the WE without considering the electrochemical reactions at the CE. As the potential of the reference electrode is constant for each electrolyte, it can be used to measure the changes of the cell potential. Figure 18 shows the three-electrode configuration for photoelectrochemical measurements. Depending on the shape of the back plate where the working electrode is connected, the sample can be illuminated either from the front or the back. The option where the sample is illuminated from the back is usually used for solar cells, which are illuminated by a solar simulator through the glass substrate of the solar cell. Here the WE is connected to the sample by a clamp. The setup for the illumination with an LED can be used for any sample, which can be contacted at the back. Furthermore, the catalytic active layer must be transparent enough to allow the LED light to pass.

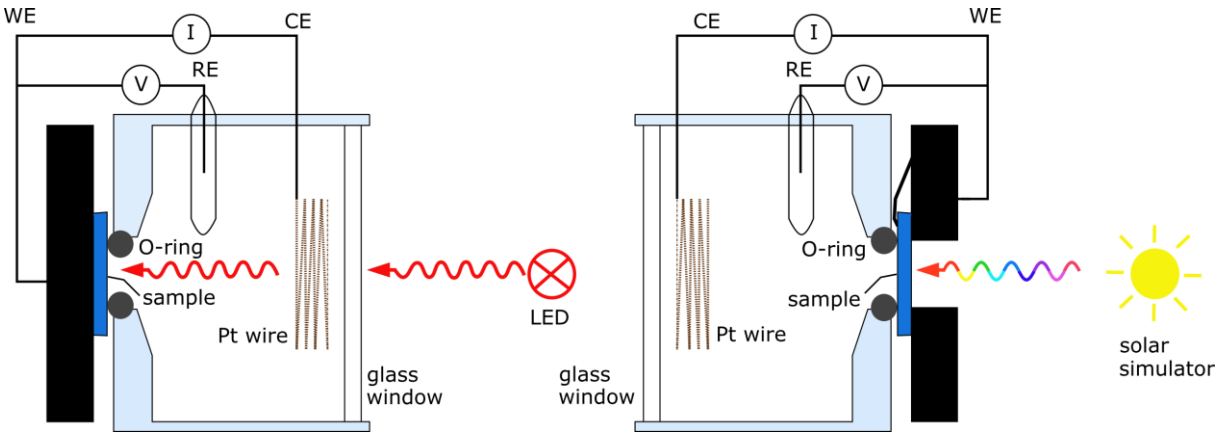

Figure 18: Three electrode configuration for photoelectrochemical measurements. Left: illumination with LED, right: illumination with solar simulator (special configuration for photoelectrochemical measurements of solar cells).

3.4 Scanning Electron Microscopy

The scanning electron microscopy (SEM) is an imaging technique to analyze the morphology of solid samples. The imaging process takes place in vacuum by focusing an electron beam onto the sample which is done with the help of an electromagnetic lens system. A schematic drawing of the SEM setup and the electron beam pathway is shown in Figure 19. The used energy of the electron beam is typically in a range of 0.2 to 40 keV. The beam is scanned across the sample in a fixed pattern, which leads to backscattered, or secondary electrons resulting in an image of the sample surface. For this purpose the sample needs to be electrically conductive. If that is not the case the sample needs to be partially covered with a conductive material. When incident electrons (primary electrons) hit the sample different elastic and inelastic interactions can take place. Depending on the sample depth Auger electrons (1 nm), secondary electrons (1-10 nm), backscattered electrons (0.1-1 µm), and characteristic X-rays (0.2-2 µm) can be detected. While. Furthermore, the chemical composition of the sample can be determined by analyzing the secondary electrons give information about the topography of the sample, backscattered electrons enable the mapping of surfaces characteristic X-rays using energy dispersive X-ray spectroscopy (EDX).[97]

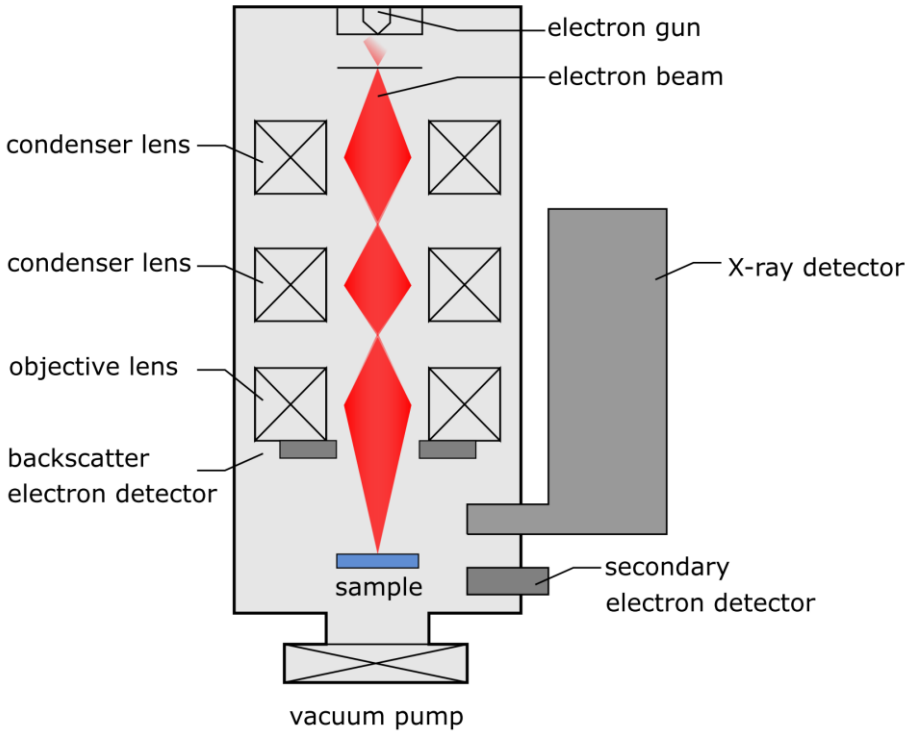

Figure 19: Schematic drawing of a SEM setup with the corresponding electron beam pathway.

4 Experimental Procedure

All samples have been prepared in the integrated vacuum system of the Technical University of Darmstadt DAISY-FUN (Darmstadt Integrated System for Fundamental research). A schematical drawing of the system is shown in Figure 20. It consists of several preparation and analysis chambers. For the preparation the MBE chamber can be used which contains two magnetron sputter sources, two electron beam evaporators as well as a sample heating stage. Furthermore, the organic chamber is equipped with two more electron beam evaporators. Thin films can also be prepared by atomic layer deposition (ALD) in the ALD chamber. High resolution electron energy loss spectroscopy (HREELS) is possible in the HREELS chamber which has a Delta 0.5 with LaB6 filament from SPECS available with an electron energy of 4 eV and 60° mirror geometry. The key part of the system is the PES unit, which contains a XPS with a SPECS Phoibos 150 set-up (Focus 500 with XR50M) using $Al_{K\alpha}$ irradiation at 1486.64 eV, an UPS (Focus HIS 13), a low energy electron diffraction (LEED) (BDL 800 IR-LMX from OCI vacuum microengineering), an argon (Ar) sputter gun and a heating system for temperatures up to 1000°C. Moreover, there is a buffer chamber available, which is mainly used for heating up to 1200°C or as an adapter station for the transportable system called DAISY-Move, which allows the sample transportation in vacuum for example to other vacuum systems. Within the DAISY-FUN system electrochemical measurements can be done in the EC chamber, which provides the connection to a glass cross.[98] One advantage of such an integrated vacuum system is the opportunity of measuring electronic properties in-line directly after thin film deposition or for instance after additional heat or plasma treatment. As in this case the sample is free of any adsorbates, it exhibits excellent film quality which is crucial when addressing surface science experiments.

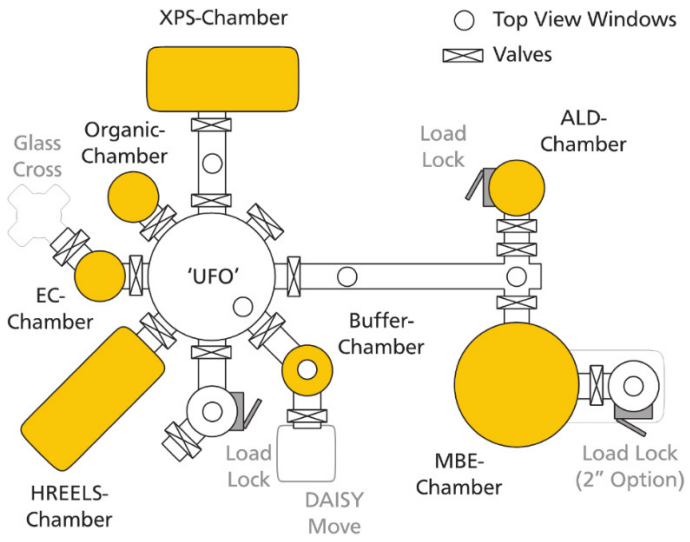

Figure 20: Schematic set-up of the integrated vacuum system of the Technical University of Darmstadt DAISY-FUN (Darmstadt Integrated System for Fundamental research). The system contains different chambers for sample preparation as well as analysis units.

4.1 Sample Preparation

For all experiments different Si substrates with different surface terminations were used. First experiments were performed on 1 cm x 1 cm pieces of 100 mm diameter (100) boron doped p-type Si wafers (p=10^{16} cm^{-3}). These samples were cleaned in an ultrasonic bath for 10 min in acetone, isopropanol and MilliQ water. For the Si surface termination with native oxide no further preparation steps were necessary. For the hydrogen terminated Si surface the sample was first etched in piranha solution (H_2SO_4:H_2O=2:1) at 80°C for 10 min and afterwards in 5% HF also for 10 min. After another etching step in freshly prepared piranha for again 10 min at 80°C, the sample was finally etched for 10 min in 40% NH_4F at room temperature.[99] In between each step the sample was thoroughly rinsed with MilliQ water.

The same procedure was applied for samples of 100 mm diameter (100) boron doped p-type Si wafers (p = 10^{16} cm^{-3}) with a 50 nm thick arsenic doped n^+-type silicon layer on top (n = 10^{19} cm^{-3}) from Fraunhofer IISB, Erlangen. Additionally, p-Si | µcn-Si junctions, µc-Si:H solar cells (p-i-n structure) as well as a-Si:H | a-Si:H | µc-Si:H solar cells (triple p-i-n structure) from Forschungszentrum Jülich GmbH were used for the experiments. All samples from Forschungszentrum Jülich GmbH were prepared by a plasma enhanced chemical vapor deposition (PECVD) technique using a silane (SiH_4)/ hydrogen gas mixture. Depending on the desired doping, trimethylborane (TMB) or phosphine (PH_3) was added to deposit a p-doped or an n-doped Si layer.[100] After the samples from Forschungszentrum Jülich GmbH arrived to TU Darmstadt, they were prepared to start the interface investigations. However, as the solar cells are not stable in 5% HF, etching was not possible. Therefore, the solar cells were only cleaned by acetone, isopropanol and MilliQ water as described before.

Afterwards, the samples were introduced into UHV at the DAISY-FUN. In order to obtain thermally grown oxide the samples with H terminated surface were introduced to a deposition chamber of the DAISY-FUN where they were held in a mixed oxygen argon atmosphere (50 sccm O_2, 50 sccm Ar, 0.1 mbar) for 45 min at 800°C.

4.2 Electron Beam Deposition

For the deposition different substrates have been used which were 1 x 1 cm pieces of p-Si wafers, pn^+-Si wafers, p-Si | µcn-Si wafers as well as µc-Si:H and a-Si:H | a-Si:H | µc-Si:H solar cells. Before inserting the samples into the vacuum system they have been cleaned as described in section 4.1. For the deposition Cu or Ag from Kurt J. Lesker were used with a purity of 99.999%. Both materials were deposited from a Mo crucible by an EFM 3 from FOCUS GmbH. Here, voltages up to 1000 V can be applied to the e-beam, which results in a crucible temperature of 300 - 2000°C. The beam spot diameter at the sample is 4 - 15 mm. For the Cu deposition a large Mo crucible with a volume of 600 mm^{-3} was

used. The melting temperature of Cu is 1083°C. In order to evaporate Cu the filament current (I_f) was set to 2.60 A while a voltage (U) of 1000 V was applied. The pressure in the deposition chamber of the DAISY-FUN was 5 x 10^{-7} mbar or better. For depositing Ag a medium size Mo crucible with a volume of 250 mm^{-3} was used. Ag has a melting temperature of 962°C. For the deposition a filament current of 2.55 A with a voltage of 800 V was used. During the depositions the substrate was held at room temperature. In order to reach a homogenously deposited film, the sample was rotated during deposition. Depending on the used substrate different masks for the deposition were used. The two options are shown in Figure 21. In one case only a round area in the center of the sample is deposited with Cu or Ag. This mask was used for all p-Si, pn^+-Si and p-Si | µcn-Si samples. The deposited area does not only present the catalytic active layer but also the metallic back contact for subsequent electrochemical measurements. In the other case the same round area in the center of the sample was deposited with Cu or Ag and additionally one edge of the sample. This edge was scratched with a diamond cutter during sample preparation. Reason for this, is the deposition of an additional front contact, instead of only a back contact. This mask was used for all µc-Si:H and a-Si:H | a-Si:H | µc-Si:H solar cells.

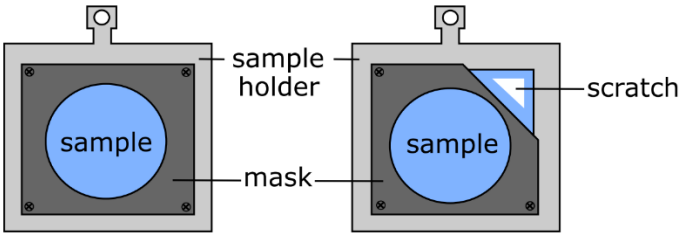

Figure 21: Omicron sample holder with different masks for Cu and Ag deposition.

Figure 22 a) shows a cross section of the Cu or Ag deposition on top of an a-Si:H | a-Si:H | µc-Si:H solar cell when using a mask. Figure 22 b) illustrates the deposited front and back contact of an a-Si:H | a-Si:H | µc-Si:H solar cell. From the cross section it seems likely that the deposited front contact causes a short circuit within the solar cell. Nevertheless, this short circuit is only very local and is necessary to contact the solar cell for subsequent electrochemical measurements.

It can be concluded that the creation of the front contact results in minor damages in the solar cell structure. However, these damages are only local and do not influence the whole structure. Due to the low electric conductivity along the individual layers of the solar cells, the caused damaged are locally isolated.[101]

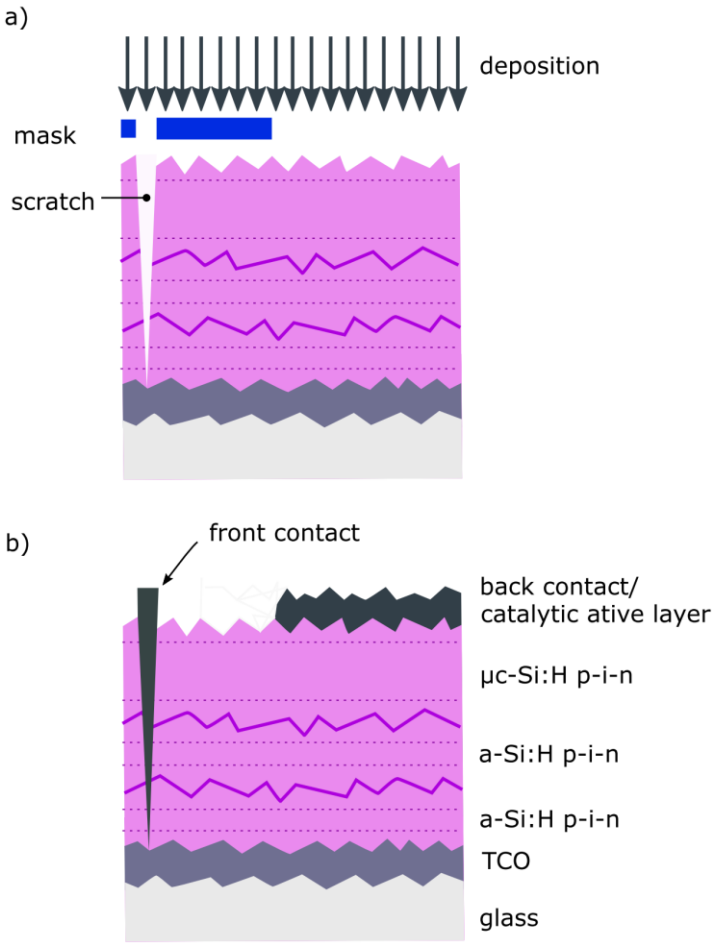

Figure 22: a) Deposition of front and back contact (Cu or Ag) by using a mask, b) created front and back contact of an a-Si:H | a-Si:H | µc-Si:H solar cell. The back contact also serves as catalytic active layer. The same deposition technique can be used for µc-Si:H solar cells.

The deposition time depends on the desired film thickness. For depositing approximately 10 nm of Cu or Ag a deposition time of 1 h is required. Most of the depositions were done within an interface experiment where the deposited film thickness increased from about 0.5 nm to 10 nm. The determination of the film thickness will be explained in detail in chapter 4.5.

An overview of the differently prepared samples including deposition parameters is given in table 1.

Table 1: Overview of deposited substrates with different surface terminations.

substrate	surface termination	film	I_f [A]	U [V]
p-Si	native SiO_2	Cu /Ag	2.60 /2.55	1000 /800
	thermal SiO_2	Cu /Ag	2.60 /2.55	1000 /800
	H-terminated	Cu /Ag	2.60 /2.55	1000 /800
pn^+-Si	native SiO_2	Cu /Ag	2.60 /2.55	1000 /800
	thermal SiO_2	Cu /Ag	2.60 /2.55	1000 /800
	H-terminated	Cu /Ag	2.60 /2.55	1000 /800
p-Si | µcn-Si	native SiO_2	Cu /Ag	2.60 /2.55	1000 /800
	thermal SiO_2	Cu /Ag	2.60 /2.55	1000 /800
	H-terminated	Cu /Ag	2.60 /2.55	1000 /800
µc-Si:H solar cell	native SiO_2	Cu /Ag	2.60 /2.55	1000 /800
a-Si:H | a-Si:H | µc-Si:H solar cell	native SiO_2	Cu /Ag	2.60 /2.55	1000 /800

4.3 XPS Measurements

The XPS measurements were all performed at a pressure of 5 x 10^{-10} mbar or better using a SPECS Phoibos 150 set-up (Focus 500 with XR50M) which is part of the DAISY-FUN. For all measurements the monochromatized $Al_{K\alpha}$ line of 1486.64 eV was used as X-ray excitation. Survey measurements were obtained with a pass energy of 20 eV while all detail spectra were measured with a pass energy of 10 eV. For valence band measurements a negative bias of -3 V has been applied. As Si 2p is the most intense peak of the used substrates, it has been used in order to align the sample in z-direction (perpendicular to the spectrometer entrance). First, survey spectra were measured to examine whether the sample contains undesired elements. Second, detail spectra of relevant core levels were measured. Before the experiments the spectrometer was calibrated against Cu 2p, Ag 3d and Au 4f core levels as well as the valence band edges.

For all samples a survey spectrum has been acquired by XPS in order to gain an overview of the sample composition. Furthermore, XP detail spectra were measured of the relevant core level lines: Si 2p, O 1s, C 1s, Cu 2p and Cu LMM or Ag 3d. As evaluation software Igor Pro was used.

4.4 Interface Experiments

Before depositing the first layer of the catalyst material on the differently prepared Si samples, the bare substrates were analyzed by XPS in order to check if the surface is free of any contaminations. Afterwards the samples were transferred into a deposition chamber where a thin layer of the catalyst material (Cu or Ag) was deposited by electron beam deposition at pressures below 10^{-7} mbar. Subsequently, the samples were analyzed again by XPS followed by another deposition and so on, until the Cu 2p or Ag 3d emission lines became dominant and the signals from the Si substrate were barely visible anymore. The XPS measurements were all performed at a pressure of 5 x 10^{-10} mbar or better using a Specs Phoibos 150 setup (Focus 500 with XR50M). For all measurements the monochromatized Al K_α line of 1486.64 eV was used as X-ray excitation. Survey measurements were obtained with a pass energy of 20 eV while all detail spectra were measured with a pass energy of 10 eV. The spectrometer was calibrated against the Cu 2p, Ag 3d and Au 4f core levels as well as the valence band edges. As evaluation software Igor Pro was used.

To calculate the band bending before and after contact formation the Si $2p_{3/2}$ emission line needs to be analyzed. For the initial band alignment, the position of the corresponding Si $2p_{3/2}$ emission line is determined. Accordingly, the distance between the valence band maximum to the Fermi level can be determined by subtracting the known value of E_B(VB)-E_B(Si $2p_{3/2}$) of 98.74 eV from the measured value of the Si $2p_{3/2}$ emission line (E_B'(Si $2p_{3/2}$)).[11] Additionally, the distance between conduction band and Fermi level is defined by the effective density of states as well as the doping concentration. This correlation is given by

$$E_{CB} - E_F = kT\, In\left(\frac{N_{CB}}{n}\right), \qquad (18)$$

where N_{CB} is the effective density of states (DOS) in the conduction band and n the doping concentration. Finally, both derived values are subtracted from the known value of the Si band gap (E_g=1.12 eV) which results in the band bending E_b

$$E_b = 1.12\ eV - \left(98.74\ eV - E_B'\left(Si\ 2p_{\frac{3}{2}}\right)\right) - (E_{CB} - E_F). \quad (19)$$

Analogous to this approach the band alignment after contact formation can be determined when evaluating the measured XP spectra after the last Cu deposition step.[102]

4.5 Film Thickness

The film thickness of the native or thermally grown SiO_2 as well as of the deposited Cu or Ag film was calculated from experimentally gained results. The respective XP detail spectra where used to determine the film thicknesses by solving the following numerical equation

$$\frac{I_{Cu/Ag}}{I_{Si}} = \frac{N_{Cu/Ag}}{N_{Si}} \frac{1 - \exp\left(\frac{-d_{Cu/Ag}}{\lambda_{Cu/Ag}(E_{kin,Si})cos\partial}\right)}{\exp\left(\frac{-d_{Cu/Ag}}{\lambda_{Cu/Ag}(E_{kin,Si})cos\partial}\right)} \quad (20)$$

which can be used either for the Cu thin film or the Ag thin film (Cu/Ag) on the bulk Si substrate.[103][104] Here, $I_{Cu/Ag}$ and I_{Si} are the integrated core level line intensities which are corrected with a Shirley background for Si and Ag and with a Tougaard background for Cu.[96][95] $\lambda_{Cu/Ag}$ and λ_{Si} are the inelastic mean free paths (IMFP) for the kinetic energy of the electrons in the thin surface layer. $N_{Cu/Ag}$ as well as N_{Si} are the materials atomic densities. The electron emission angle is defined as ∂. In order to determine the layer thickness of the oxide, the initial Si 2p peak intensity needs to be considered. In order to remove the background of the spectrum a Shirley background correction has been applied. Additionally to the Si 2p peak the SiO_2 peak can be seen at 103.5 eV (literature: 103.2 eV).[105] For calculating the layer thickness d of the SiO_2 the relation of the integrated core level lines I_{Si2p} and I_{SiO2} needs to be taken into account. Furthermore, the materials atomic densities N_{Si} and N_{SiO2}, the inelastic mean free path λ of SiO_2 and the electron emission angle ∂ are defining the layer thickness as shown in the following equation

$$d_{SiO2} = \lambda_{SiO2} \cos\partial\ ln\left(1 + \frac{I_{SiO2}}{I_{Si}} \frac{N_{Si}}{N_{SiO2}}\right). \quad (21)$$

4.6 Photoelectrochemical Measurements

After the interface experiments were completed, the samples were extracted from UHV in order to perform photoelectrochemical (PEC) measurements. Therefore, the samples were inserted into an EC cell from Zahner (PECC-2). For electrically contacting the samples two different methods were used. In

case of pn^+-Si and p-Si | µcn-Si substrates gallium indium (GaIn) (Alfa Aesar, 99.99% pure) was scratched into the back of the samples in order to form an ohmic back contact. As front contact the deposited active material (Cu or Ag) was used. In case of µc-Si:H and a-Si:H | a-Si:H | µc-Si:H solar cells the back contact was deposited by e^--beam deposition. Therefore, one edge of the samples was scratched manually with a diamond cutter. Afterwards, this area was deposited by Cu or Ag as described in chapter 4.2. Due to the previous scratching the deposited material reaches the TCO of the solar cell structure and hence forms an electrical contact. Before setting up the Zahner cell and filling it with the electrolyte (0.3 M $KHCO_3$), the Ag/AgCl reference electrode was calibrated. For this purpose the open circuit potential (OCP) of the Ag/AgCl reference versus the reversible hydrogen electrode (RHE) was measured for 10 min in a standard two-electrode set-up controlled by the potentiostat (Zennium, PP221 Zahner-Elektrik).

Subsequently, the electrolyte was filled into the Zahner cell and the OCP of the sample versus the before calibrated Ag/AgCl reference electrode was measured for 10 min in a standard three-electrode set-up. Furthermore, cyclic voltammetry (CV) measurements were performed in the dark and under illumination or with chopped light with illumination time intervals of four seconds. The CV scans were performed with a scan rate of 10 mV/s and edge potentials of 1 V vs. RHE to -2.5 V vs. RHE. The measurements were performed with and without nitrogen gas bubbling through the electrolyte. For the illumination of the samples two different options were utilized. For the pn^+-Si and p-Si | µcn-Si samples a LED with a wave length of 625 nm was used as light source, which was operated with a power of 180 W/m^2. For µc-Si:H and a-Si:H | a-Si:H | µc-Si:H solar cells a solar simulation system was used in order to imitate real life conditions. The two different illumination modes and when they are used, are described in chapter 3.3. As the solar simulator cannot be operated under chopped light conditions, only OCP and CV were measured for these samples. The measurement parameters are equal to the ones of the pn^+-Si and p-Si | µcn-Si samples, however these results were measured using another potentiostat (GAMRY Interface 1000E). Moreover, the set-up of the Zahner cell was slightly different for Si wafers and Si solar cells. While the back plate of the Zahner cell was a solid round plate for the wafer set-up, the back plate for the solar cells had a hole in the center of the plate. The reason for that is the different illumination direction during the measurement as explained in chapter 2.3.

5 Characterization of the Si | Cu Interface

In this chapter different Si | Cu interfaces will be systematically analyzed with respect to the electronic band structure and the corresponding photoelectrochemical performance. Furthermore, it will be discussed how the photoelectrochemical measurement affects the deposited Cu thin films. The aim is to find a correlation between the electronic band structure at the Si | Cu interface and the photoelectrochemical performance. In order to systematically understand Si | Cu interfaces, different model systems have been developed. The first model system is presented by a very basic p-Si | Cu junction with thermal SiO_2 as passivating interlayer. However, advanced Si | Cu model systems containing buried junctions are expected to be essential as integrated photoelectrochemical device. Therefore, more advanced model systems such as pn^+-Si | Cu, p-Si | µcn-Si | Cu, µc-Si:H | Cu and a-Si:H | a-Si:H | µc-Si:H | Cu are also characterized.

5.1 p-Si | Cu Interface

The first approach of the systematic characterization of Si | Cu interfaces is the investigation of a p-Si | therm. SiO_2 | Cu reference system. This is an important step in order to understand a basic model system before going to more complex Si | Cu systems.

5.1.1 Energy Band Alignment

The electronic band structure of p-Si | thermal SiO_2 | Cu was investigated by an XPS interface experiment. The corresponding XP survey spectrum is shown in Figure 23 and the XP detail spectra of the Si 2p, O 1s and Cu 2p emission lines are displayed in Figure 24. Furthermore, the development of the Cu LMM Auger line is shown in the appendix A 1. In the survey spectra in Figure 23 the development of the emission lines during the Cu deposition is displayed. Here, the bottom spectrum shows the survey spectrum of the bare substrate while the top spectrum represents the measurement after the last Cu deposition step. In between the different deposition steps are shown. From the survey spectrum of the substrate it can be seen that the sample is free of contaminations such as carbon (C) at a binding energy of approximately 285 eV. Due to the intense cleaning steps which were described in chapter 4.1 contaminations were not expected. The only emission lines which appear are Si 2p at a binding energy of 99.26 eV, Si 2s at 151.89 eV, O 1s at 532.48 eV as well as the O KLL Auger line at 979.10 eV which is barely visible. As it is expected no Cu emission line is visible at that state of the interface experiment. After the first deposition step a small emission line corresponding to the Cu 2p emission appears at around 933 eV. At this state the Cu 2s and the Cu LMM lines are still very weak.

With ongoing interface experiment the Cu 2s, Cu 2p and Cu LMM lines become more intense while the intensities of the Si 2p, Si 2s, O 1s and O KLL line continuously decrease until they vanish completely. Furthermore, the Cu 3s, Cu 3p and Cu 3d emission lines arise at 140 eV, 90 eV and 10 eV. However, these emission lines are not relevant for the experiment.

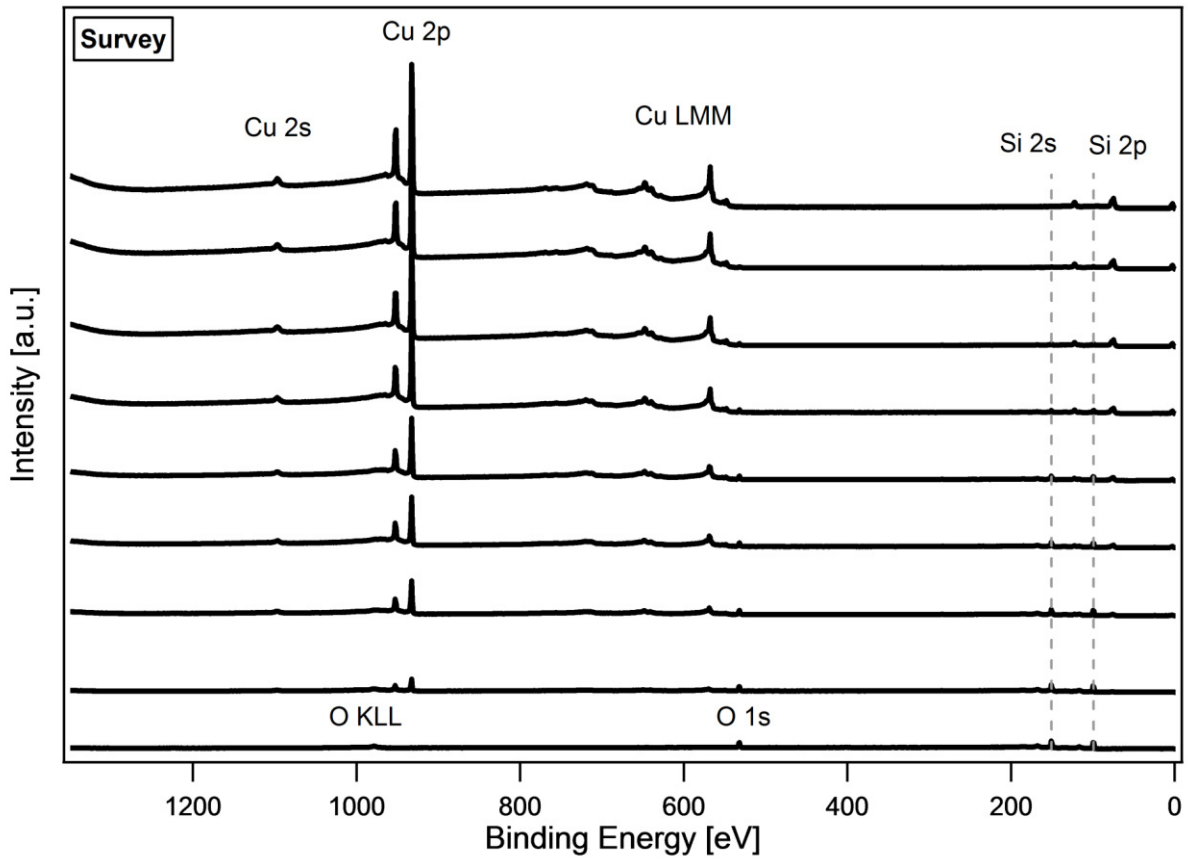

Figure 23: Development of the XP survey spectra of the p-Si | therm. SiO_2 | Cu contact during the interface experiment. The measurement of the bare p-Si | therm. SiO_2 substrate is displayed at the bottom of the diagram while the last deposition step at the top shows the final measurement of a relatively thick Cu layer.

The relevant XP detail spectra are displayed in Figure 24. Again, the spectrum at the bottom presents the first measurement of the interface experiment showing the surface of the bare substrate. The Si 2p emission line is split into two signals Si $2p_{3/2}$ and Si $2p_{1/2}$. The more intense Si $2p_{3/2}$ emission line appears at a binding energy of 99.26 eV and the Si $2p_{1/2}$ emission line is has its maximum at 99.90 eV. At a binding energy of 103.20 eV a peak appears, which corresponds to the contribution of the thermally grown thin SiO_2 layer. The presence of SiO_2 can also be observed from the O 1s emission line, which has its maximum at 532.48 eV at this point of the experiment. As expected no Cu 2p emission is detected within the first measurement.

After the first deposition step the XP detail spectra change. The intensities of the Si 2p and the O1s emission lines are slightly reduced although this effect is still very weak. The Cu 2p emission lines becomes visible but the intensity is not very strong. As explained in chapter 4.5 the film thickness of the Cu layer can be determined from the peak areas. From this the Cu film has a thickness of approximately 5 Å after the first deposition step.

With ongoing interface experiment the intensity of the Si 2p emission line is reduced. When determining the maximum of the Si $2p_{3/2}$ emission line after each deposition step a small shift can be observed. As mentioned the position of the Si $2p_{3/2}$ emission line was detected at 99.26 eV before the Cu deposition. After the last deposition step the Si $2p_{3/2}$ emission line shows a total shift of +0.1 eV resulting in a binding energy of 99.36 eV before vanishing completely.

As the Cu film reaches a layer thickness of 100 Å the disappearance of the Si 2p emission line is reasonable as the limit of the information depth of the XPS analyses is reached. From the O 1s emission line it can be concluded that the emission line at 532.48 eV is continuously reduced. However, an emission at 529.75 eV arises with ongoing deposition steps. This line indicates the formation of small amounts of Cu_2O. Due to the deposition conditions it is very unlikely that the Cu oxidizes during the deposition process. It is more probable that the Cu is oxidized after the adhesion to the SiO_2 layer. The shape of the Cu LMM Auger line, which is displayed in the appendix A 1, shows that after the first deposition step Cu_2O has formed instead of metallic Cu. Nevertheless, the position as well as the shape of the Cu 2p emission line indicates the deposition of metallic Cu. The measured binding energy of 932.60 eV is a typical value for metallic Cu. Furthermore, the spectrum remains flat within the Cu 2p splitting, which is also an indication of metallic Cu.[106]–[109] Moreover, the shape of the Cu LMM Auger line can be taken into account when evaluating the stoichiometry. The corresponding development of the Cu LMM Auger line during the interface experiment is shown in the appendix A 1. The shape of the Auger spectrum at the end of the interface experiment proves the deposition of metallic Cu.

The aim of the performed XPS measurements is the investigation of the interfaces and thus of the energy band alignments before and after contact formation of the p-Si | therm. SiO_2 with Cu. Therefore, the band bending before and after the interface experiment was calculated as described in chapter 4.4. The resulting energy band diagrams are schematiclaly sketched in Figure 25. Here, Figure 25 a) shows the initial situation before contact formation. There is a large downward band bending of 0.4 eV, which is not expected after extensive preparation steps such as etching to form H terminated surfaces or subsequent oxidation to form a thermal oxide. A preferable flat band situation is not achieved in this experiment, which is due to midgap defects at the p-Si surface and Fermi level pinning as a consequence. In Figure 25 b) it can be seen that for the p-Si | thermal SiO_2 sample the band bending is slightly reduced from 0.4 eV to 0.3 eV after being in contact with Cu. Presumably the band alignment after contact formation is not determined by the Cu contact but by the initial Fermi level pinning. In such cases, which

are expected to be the dominating case for most experiments using p-Si as substrate, the contact properties to a metal as e.g. a Cu thin film deposited onto a p-Si | thermal SiO_2 sample will be dominated by Fermi level pinning.[11], [102], [110]–[112]

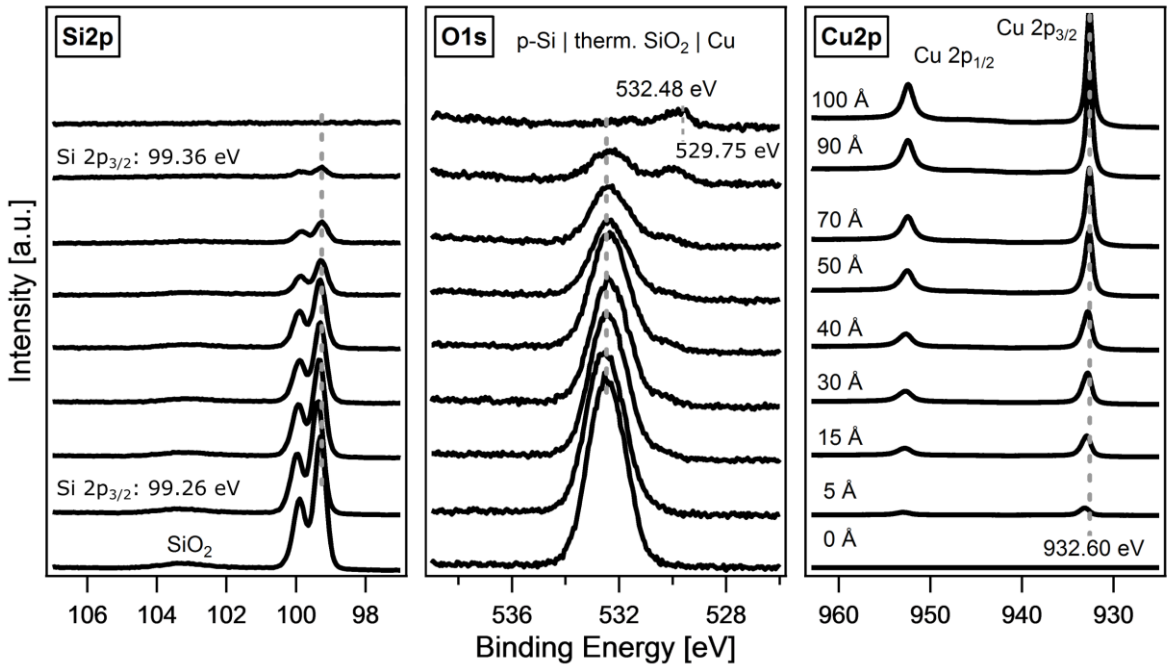

Figure 24: Development of the Si 2p, O 1s and Cu 2p detail spectra of the p-Si | therm. SiO_2 | Cu contact during the interface experiment. The measurement of the bare p-Si | therm. SiO_2 substrate is displayed at the bottom of the diagram while the last deposition step at the top shows the final measurement of a relatively thick Cu layer.

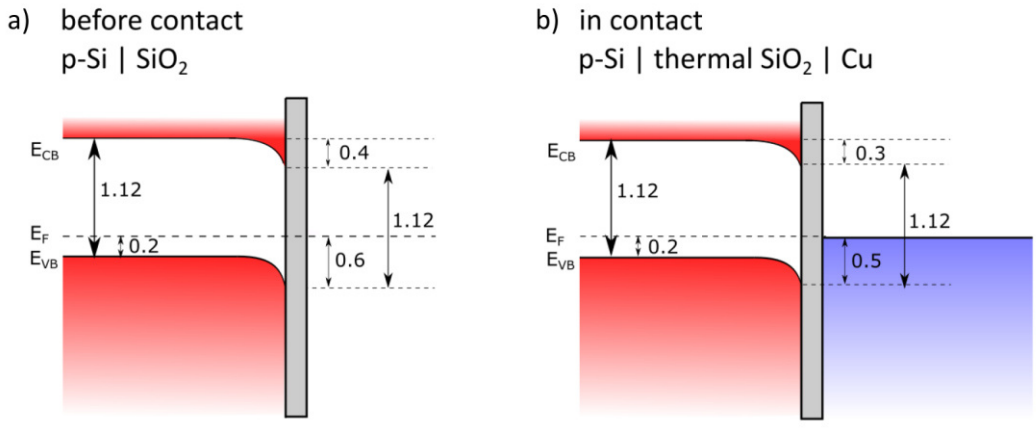

Figure 25: Energy band diagrams before and after contact formation. a) p-Si | therm. SiO_2 before contact formation with pinned Fermi level and initial downward band bending of 0.4 eV and b) p-Si | therm. SiO_2 | Cu with a slightly reduced band bending of 0.3 eV.

5.1.2 Electrochemistry

The photoelectrochemical performance of the p-Si | therm. SiO_2 sample with a 100 Å thick Cu layer on top is shown in Figure 26. The displayed cyclic voltammetry (CV) measurement under chopped light shows the difference between the CV measurement in the dark and under illumination. For the illumination a red LED with a wavelength of 625 nm and an intensity of 180 W/m^2 was used. It is obvious that the sample does not show a classical chopped light behavior as the dark current density reaches values below -1 mA/cm^2 for potentials smaller than -0.9 V vs. RHE. This behavior differs from expectations for an ideal Schottky barrier.[102], [103], [113] The reason for this behavior is the occurrence of Fermi level pinning at midgap position which is already evident from the p-Si | therm. SiO_2 surface before contacted to Cu as it is described in section 5.1.1. The remaining midgap defects in the Si | SiO_2 phase boundary lead to effective tunneling across the junction without forming the desired diode behavior across the interface. The p-Si | therm. SiO_2 | Cu junction represents a basic model system, which is not expected to supply enough voltage nor current to drive the CO_2 reduction reaction.

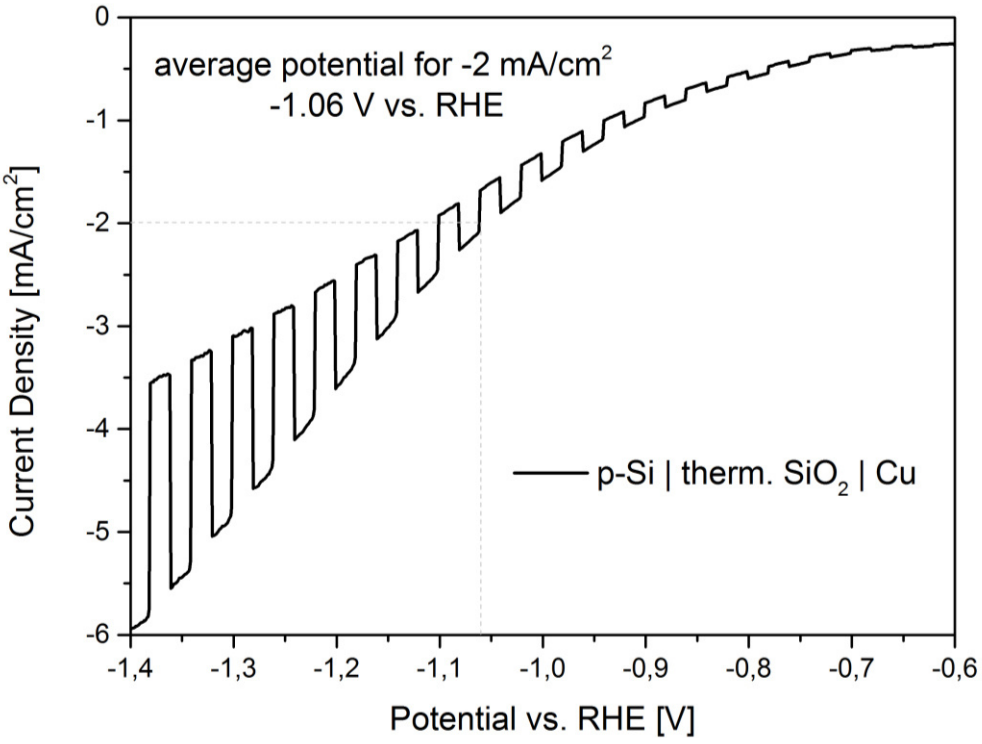

Figure 26: Cyclic voltammetry measurement of the p-Si | therm. SiO_2 | Cu model system in 0.3 M $KHCO_3$ under chopped light conditions: 4 sec interval for the illumination of 180 W/m^2 with λ = 625 nm.

5.1.3 XPS after Electrochemistry

To characterize possible modifications of the Cu thin film, XPS after EC was performed. In Figure 27 the corresponding XP detail spectra of the Cu 2p, O 1s, C 1s and Si 2p emission lines are displayed. From the Cu 2p emission line it is obvious that the stoichiometry of the Cu has changed in comparison to the last deposition step of the interface experiment as seen in Figure 24. Within the Cu 2p multiplet lines the spectrum does not remain flat as it was the case directly after depositing the Cu layers. Instead, an intense satellite has formed which clearly indicates the formation of copper oxide. As the satellite is quite strong the formation of CuO or $Cu(OH)_2$ is indicated.[94][114]

Moreover, it can be observed that the Cu $2p_{3/2}$ emission line has shifted from 932.60 eV after the last deposition step to 935.57 eV after EC. This increase in binding energy also proves the change from metallic Cu to a non-metallic Cu compound. From the position it can be assumed that the formed species is mostly $Cu(OH)_2$.[114] A conceivable reason for the transformed Cu surface is the used electrolyte during EC. As $KHCO_3$ contains oxygen, it can be expected that it reacts with the Cu atoms at the surface and hence forms Cu oxides. From the C 1s emission line it can be assumed that C-H and C-C (285.56 eV) compounds as well as small amounts of C-O (288.98 eV) compounds are present on the surface.[114][94] This assumption is reasonable when taking into account that $KHCO_3$ has been used as electrolyte. For further studies it could be experimentally examined whether the Cu film is contaminated only by being in contact to the electrolyte without performing photoelectrochemical measurements. However, these experiments were not performed here as the focus of this work was the investigation of the correlation between the Si | metal energy band alignment and the corresponding electrochemical performance.

The O 1s emission line appears in a symmetric shape with its maximum at 532.27 eV. Similar to the initial binding energy of 532.48 eV of the p-Si | therm. SiO_2 substrate this is a typical value for the presence of SiO_2. While the Si 2p emission was not visible anymore after the last step of the interface experiment, it is quite intense after EC. The reason for that might be a partial detachment of the Cu film during the electrochemical measurement procedure. The maximum of the Si $2p_{3/2}$ emission line at 99.32 eV did not significantly shift compared to the Si $2p_{3/2}$ emission line at 99.36 eV before the last deposition step. Also the SiO_2 peak at 103.09 eV does not show a remarkable shift. However, the amount of O is increased, which is quite obvious from the intensity of the SiO_2 peak, which is much stronger compared to the spectra before EC. This effect can be explained by the reduced Cu film thickness due to the partial dissolution of the top Cu layer. According to calculations as explained in chapter 4.5, the Cu film thickness was reduced from initial 100 Å to about 55 Å.

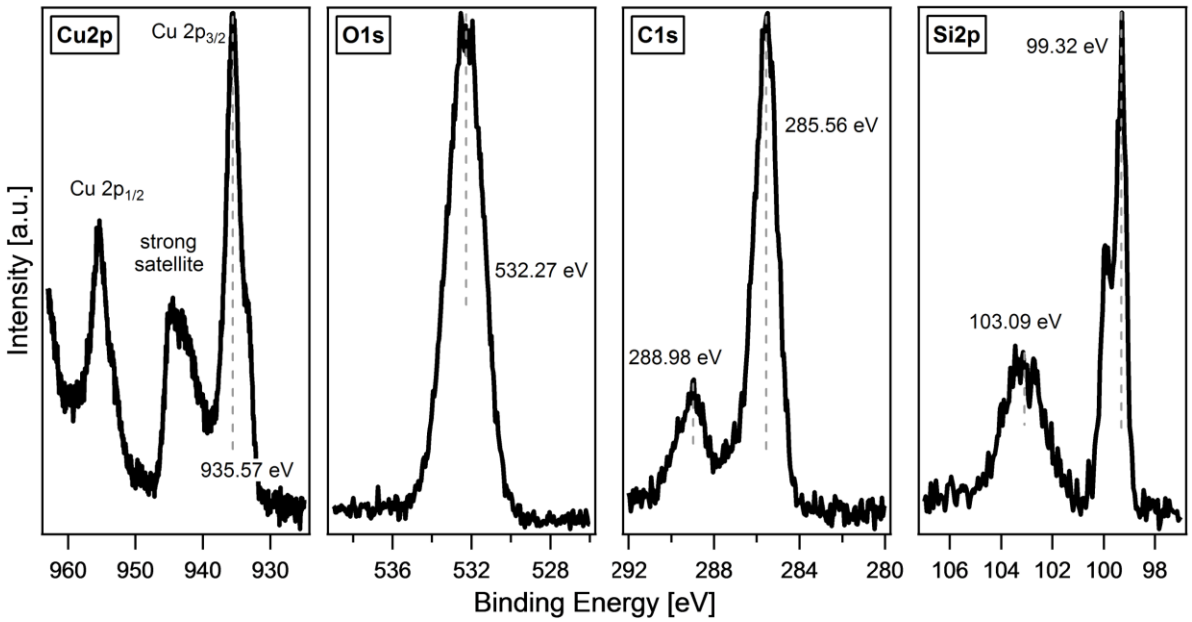

Figure 27: XP detail spectra of the p-Si | therm. SiO_2 | Cu sample showing the Cu 2p, O 1s, C 1s and Si 2p emission lines after performing cyclic voltammetry measurements.

5.2 pn^+-Si | Cu Interface

The next step in order to systematically investigate Si | Cu interfaces is the use of pn^+-Si substrates which already contain a buried junction contrary to the basic model system which only uses a bare p-Si substrate. Furthermore, the effect of different Si surface terminations is examined. Here, different preparation methods lead to pn^+-Si substrates with native SiO_2, H termination and thermal SiO_2 as described in chapter 4.1.

5.2.1 Energy Band Alignment

First, survey spectra were measured by XPS to analyze the initial electronic band structure of the three different Si surface terminations prior to Cu deposition and to verify whether the surfaces are free of contaminations. The resulting survey spectra are displayed in Figure 28. The two dominant emissions for the hydrogen terminated surface are Si 2s and Si 2p with binding energies of 151.05 eV and 99.98 eV, respectively, which are in agreement to literature[94], [102], [105], [115], [116] There is also a very small amount of oxygen present on the surface of the sample with the H terminated surface as can be deduced from the O 1s line and the O KLL Auger line at 531 eV and 979.15 eV, respectively. [102], [117], [118] The specific photoelectron lines of Si also dominate the spectra of the two samples with additional oxide layers. While the intensities of the Si 2s and Si 2p lines are similar, the O 1s and O KLL lines are more intense for the sample with the thermal SiO_2 as compared to the native SiO_2 layer. From the survey spectra in Figure 28 it can be concluded that the H terminated sample and the sample with the thermal SiO_2 are free of any severe contamination. The native SiO_2 sample shows a photoelectron

line at 285 eV, which is specific for the C 1s emission line. As this sample did not undergo a piranha etching procedure the C contamination from storage in ambient air was not removed. Therefore, the presence of C is reasonable for the native SiO_2 sample.

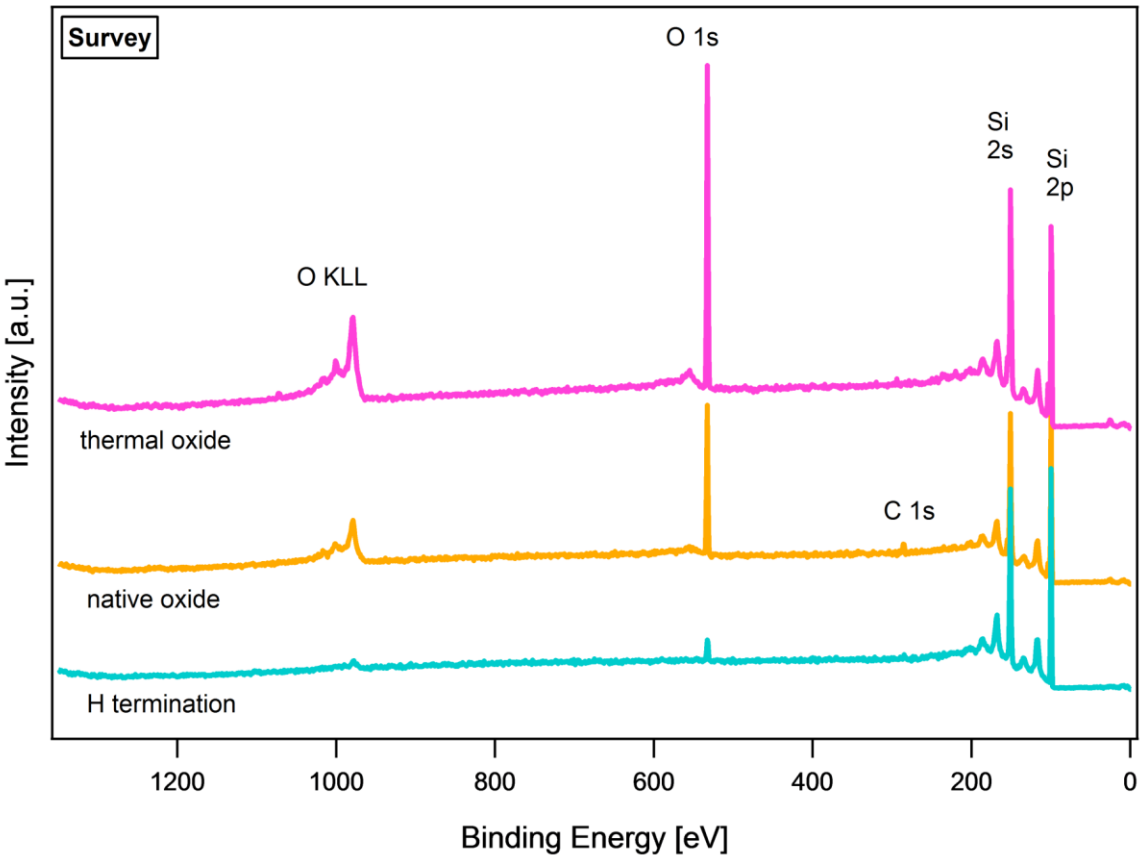

Figure 28: XP survey spectra of the pn⁺-Si substrates with different surface terminations: H-termination, native SiO_2 and thermal SiO_2.

pn⁺-Si | nat. SiO_2 | Cu

After this initial analysis, Cu was deposited stepwisely on all three Si surfaces with different termination, followed again by XPS analysis after each step. In Figure 29 the development of the survey spectra during the interface experiment of the pn⁺-Si | nat. SiO_2 | Cu sample is shown. While the spectrum at the bottom presents the measurement of the bare pn⁺-Si | nat. SiO_2 substrate directly after inserting the sample into the UHV system, the top spectrum displays the survey spectrum of the pn⁺-Si | nat. SiO_2 | Cu contact after finishing all deposition steps. As expected the substrate signals Si 2p, Si 2s, O1s and O KLL decrease within ongoing interface experiment while the Cu 2s, Cu 2p and Cu LMM lines corresponding to the deposited overlayer increase. Moreover, the Cu 3s, Cu 3p and Cu 3d emission lines arise at 140 eV, 90 eV and 10 eV, which are not further used for the analysis.

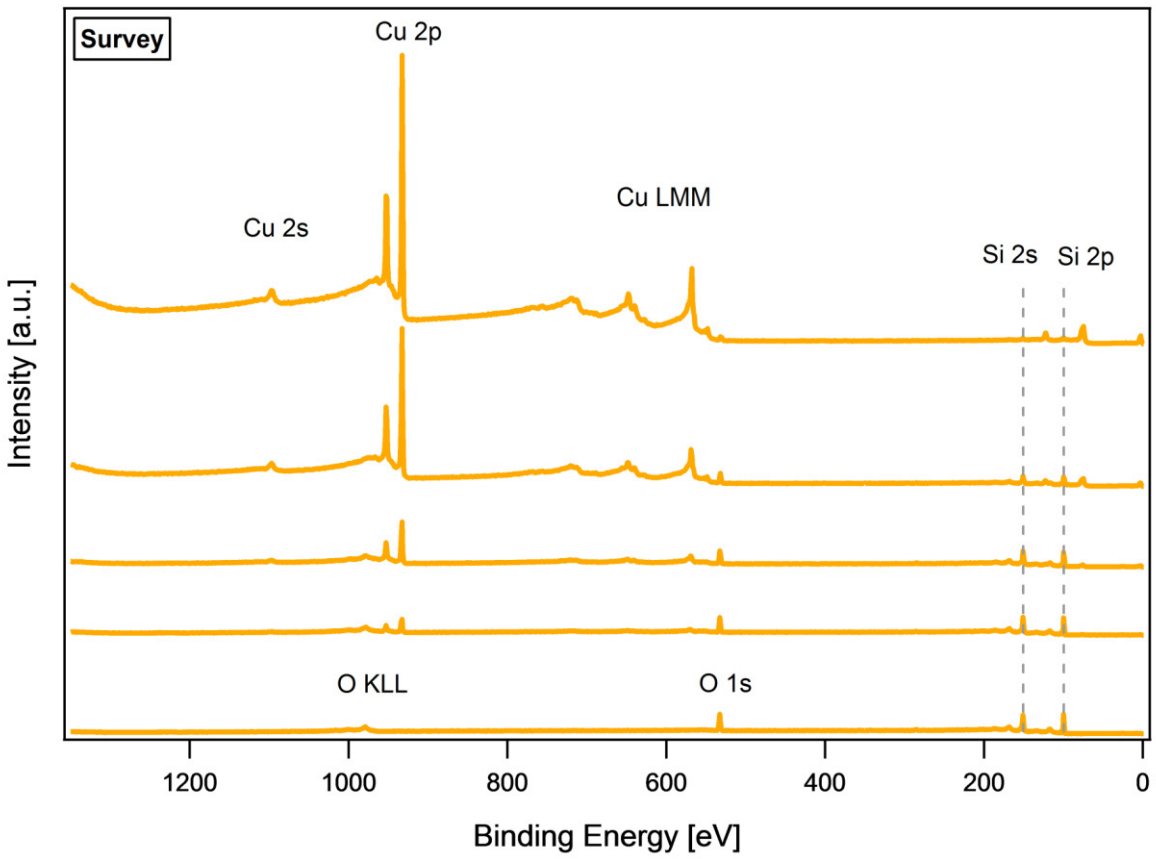

Figure 29: Development of the XP survey spectra of the pn⁺-Si | nat. SiO_2 | Cu contact during the interface experiment. The measurement of the bare pn⁺-Si | nat. SiO_2 substrate is displayed at the bottom of the diagram while the last deposition step at the top shows the final measurement of a relatively thick Cu layer.

The evolution of the corresponding XP detail spectra of the pn⁺-Si | nat. SiO_2 | Cu sample during the interface experiment are shown in Figure 30. Analogous to the previously discussed survey spectra, the Cu 2p emission line in Figure 30 shows zero intensity for the measurement of the bare pn⁺-Si | nat. SiO_2 substrate. Consequently, the substrate signals of the Si 2p and O 1s emission lines are very intense. The Si $2p_{3/2}$ emission line has its maximum at a binding energy of 99.77 eV. Also the maximum of the Si $2p_{1/2}$ is clearly visibly at 100.03 eV. The distinct separation of the Si $2p_{3/2}$ and Si $2p_{1/2}$ emission line is a high-resolution feature and indicates an initial electronic flat band situation. The SiO_2 peak appears at 103.5 eV, which can be expected for the pn⁺-Si | nat. SiO_2 substrate as well as the O 1s emission line with a position of 533.05 eV.

After the first Cu deposition step the film reaches a thickness of about 5 Å. In the corresponding O 1s and Si 2p emission lines a shift to lower binding energies can be observed. When analyzing the valley between the Si $2p_{3/2}$ and Si $2p_{1/2}$ emission lines it can be seen that the previously observed splitting effect decreases. This is already an indication of band bending at the interface when the pn⁺-Si | nat. SiO_2 | Cu

contact forms. At that point the maximum of the Si $2p_{3/2}$ emission line has shifted to 99.64 eV, which also proves the effect of the band bending at the interface.

With the next deposition step the Cu $2p_{3/2}$ emission line of the Cu layer is detected at 933.25 eV. The Si 2p emission line splitting becomes more indistinct and the maximum is shifted to 99.50 eV. At the same time the O 1s emission line is also further shifted to lower binding energies. When the Cu film reaches a thickness of 45 Å the Si $2p_{3/2}$ maximum is detected at 99.48 eV. Within the Cu 2p splitting the spectrum remains flat, which proves the presence of mostly metallic Cu. From the O 1s emission line not only a shift can be observed but also the formation of an additional emission line corresponding to the formation of a copper oxide compound.

After the last deposition step the Cu film reaches a thickness of 91 Å, showing the maximum of the Cu $2p_{3/2}$ emission line at 932.68 eV. The Si 2p emission line is still slightly visible but the position of the Si $2p_{3/2}$ emission line has not changed compared to the previous step of the interface experiment. Therefore, the interface experiment can be assumed to be completed. While the emission at 529.80 eV within the O 1s region indicates the presence of Cu_2O, the Cu LMM Auger line, which is displayed in the appendix A 2 proves the formation of mostly metallic Cu. However, the presence of Cu_2O can be proven by the shape of the Cu LMM Auger line after the first deposition step. Similar effects were already observed for the p-Si | therm. SiO_2 | Cu contact as described in section 5.1.1.

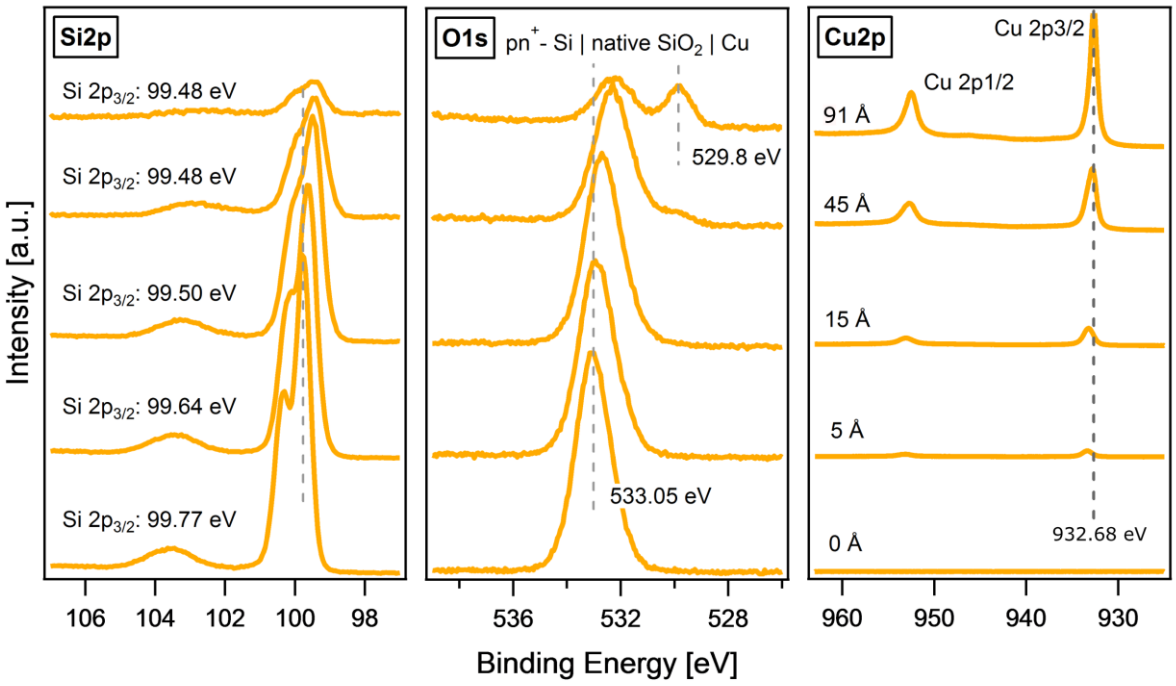

Figure 30: Development of the Si 2p, O 1s and Cu 2p detail spectra of the pn^+-Si | nat. SiO_2 | Cu contact during the interface experiment. The measurement of the bare pn^+-Si | nat. SiO_2 substrate is displayed at the bottom of the diagram while the last deposition step at the top shows the final measurement of a relatively thick Cu layer.

pn$^+$-Si:H | Cu

Analogous to the pn$^+$-Si | nat. SiO_2 | Cu sample the pn$^+$-Si:H | Cu contact was investigated. The resulting survey spectra of each step of the interface experiment are shown in Figure 31. Contrary to the pn$^+$-Si | nat. SiO_2 substrate the H-terminated pn$^+$-Si substrate contains only a very small amount of oxygen, which is proven by a barely detectable O 1s emission line and the missing O KLL Auger line. Furthermore, it can be noted that the sample surface is completely free of contaminations, which can be expected due to the very intense etching steps the sample had to undergo during the preparation. With continuous deposition steps the Cu 2s, Cu 2p and Cu LMM lines emerge while the O 1s, Si 2s and Si 2p emission lines become less intense. Furthermore, the Cu 3s, Cu 3p and Cu 3d emission lines arise at 140 eV, 90 eV and 10 eV. However, these emission lines are not further used.

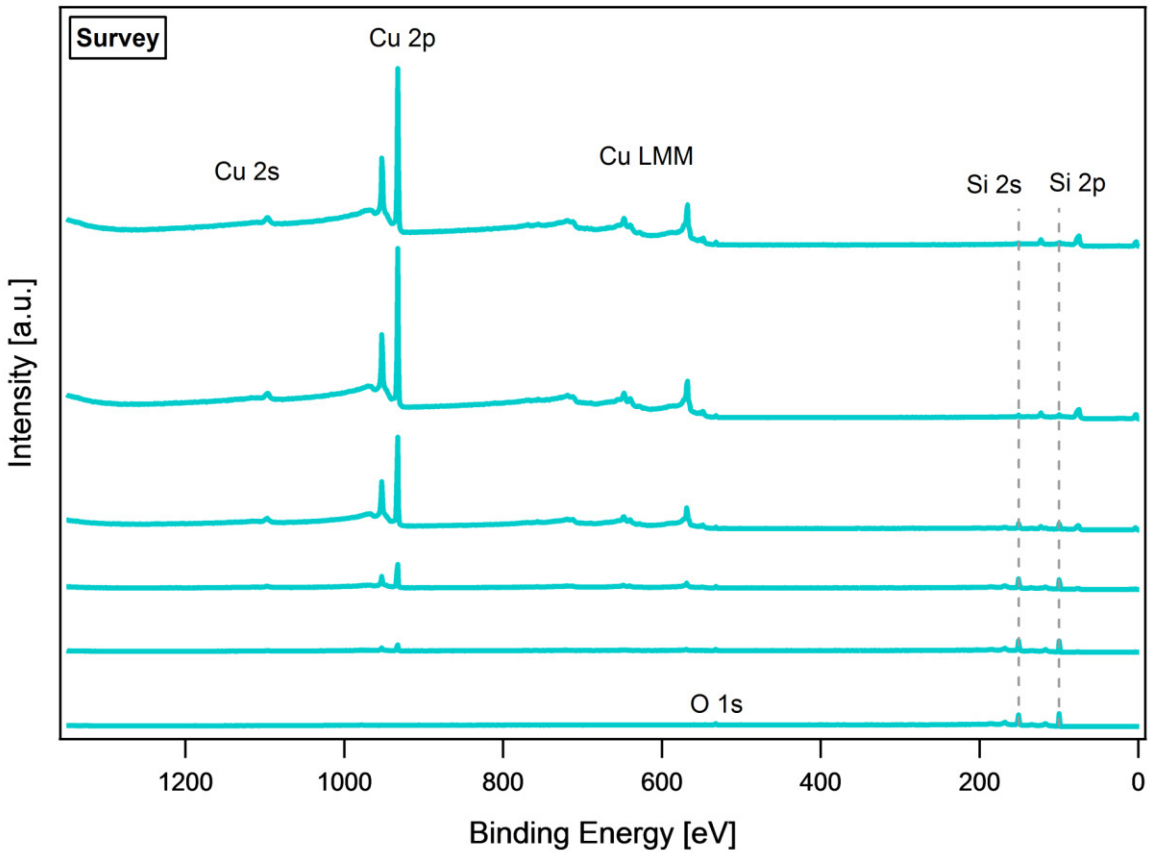

Figure 31: Development of the XP survey spectra of the pn$^+$-Si:H | Cu contact during the interface experiment. The measurement of the bare pn$^+$-Si:H substrate is displayed at the bottom of the diagram while the last deposition step at the top shows the final measurement of a relatively thick Cu layer.

From the development of the Si 2p XP detail spectra in Figure 32 it can be observed that the initial Si 2p emission line shows a minimum at 100.02 eV indicating a flat band situation. Contrary to the surface of the pn$^+$-Si | nat. SiO_2 substrate the Si 2p emission line of the H-terminated sample does not exhibit a SiO_2 peak at around 103 eV. However, a weak signal of the O 1s emission line could be detected, which

is reasonable as even with HF etching a small amount of O can be expected to remain on the surface. The first deposition step induces a quite large shift of the Si 2p emission line from 99.82 eV to 99.65 eV. A shift can also be observed in the O 1s emission line, however it is less significant. Besides the shift of the binding energy, the shape of the Si 2p emission line indicates a band bending at the interface. The previous clearly visible minimum within the Si 2p emission line has vanished.

With each deposition step the Cu 2p emission line becomes more intense and the corresponding film thickness increases. The Si 2p emission line becomes weaker and continuously shifts to lower binding energies. Contrary to that, a reduced intensity of the O 1s emission line cannot be observed. The intensity stays similar with each deposition step and slightly increases after the Cu film has reached its final thickness of 95 Å. Furthermore, it can be noticed that in contrast to the p-Si | therm. SiO_2 | Cu and the pn^+-Si | nat. SiO_2 | Cu contact no oxygen reaction takes place as the O 1s emission line remains symmetric and does not exhibit a signal, which indicates the formation of a copper oxide compound. As it is assumed that the Cu is oxidized when the interface to the SiO_2 layer is formed, it is reasonable that no oxidation can be observed in case of the hydrogen terminated Si surface. From the flat progression of the spectrum between the Cu $2p_{3/2}$ and Cu $2p_{1/2}$ emission line as well as the corresponding Cu LMM Auger line, which is shown in the appendix A 3, it can be concluded that the deposited Cu film is mainly metallic.[106]–[108], [119] A weak satellite would denote the formation of Cu_2O and a strong satellite indicates the formation of CuO.[120] In contrast to the sample with a native SiO_2 interlayer, the film exhibits metallic character directly after the first deposition step, which can be concluded from the shape of the Cu LMM Auger line in the appendix A3. This is due to the hydrogen surface termination, which does not oxidize the deposited Cu film.

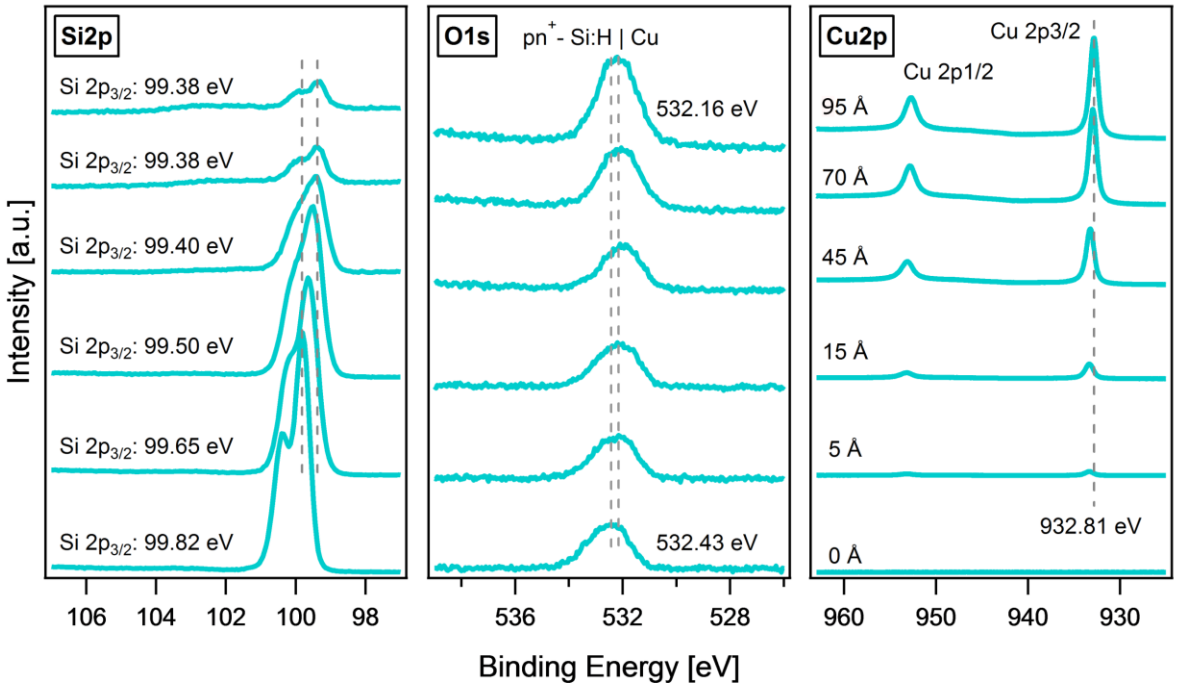

Figure 32: Development of the Si 2p, O 1s and Cu 2p detail spectra of the pn$^+$-Si:H | Cu contact during the interface experiment. The measurement of the bare pn$^+$-Si:H | substrate is displayed at the bottom of the diagram while the last deposition step at the top shows the final measurement of a relatively thick Cu layer.

pn$^+$-Si | therm. SiO_2 | Cu

Figure 33 shows the development of the XP survey spectra of the pn$^+$-Si | therm. SiO_2 | Cu contact. Beside the Si 2p, Si 2s and O 1s emission line, the O KLL Auger line is also detected as the amount of O is large enough. This was not the case for the pn$^+$-Si:H | Cu sample. During the interface experiment the substrate signals become weaker while the signals of the deposited Cu layer become dominant.

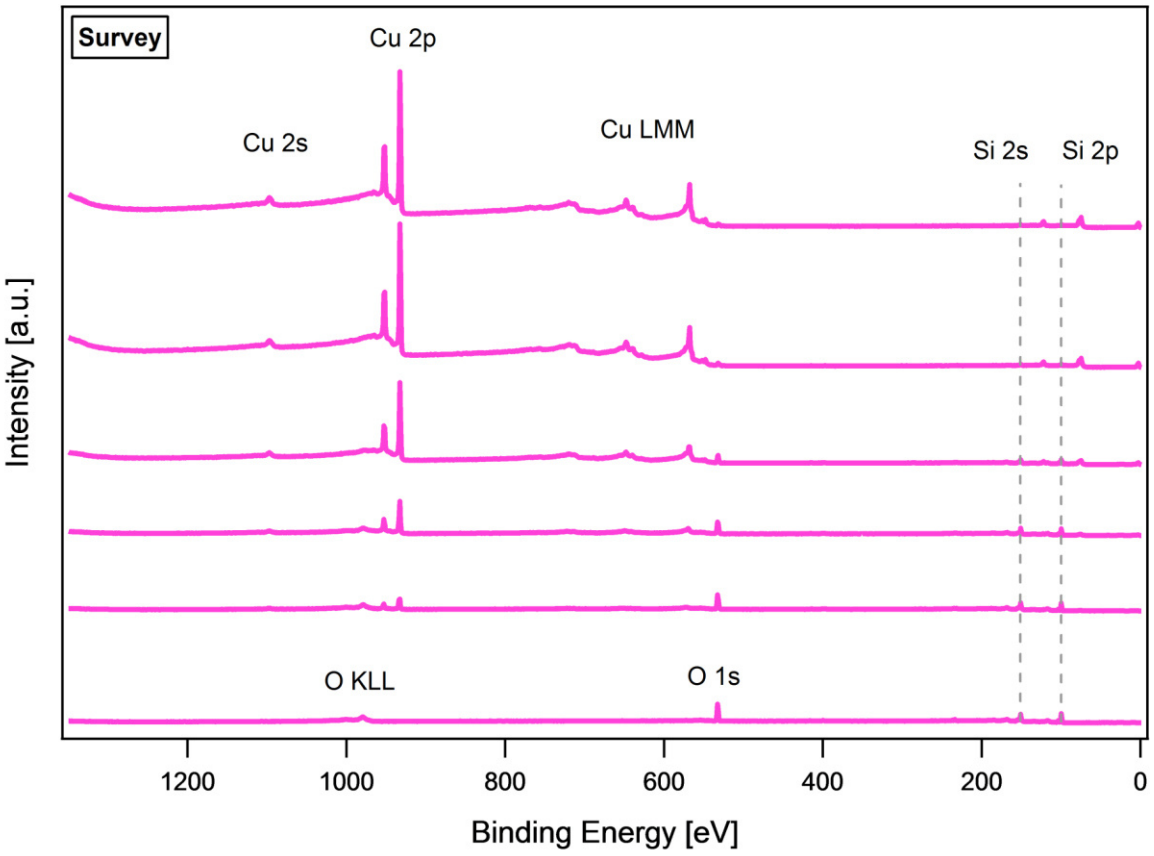

Figure 33: Development of the XP survey spectra of the pn$^+$-Si | therm. SiO_2 | Cu contact during the interface experiment. The measurement of the bare pn$^+$-Si | therm. SiO_2 substrate is displayed at the bottom of the diagram while the last deposition step at the top shows the final measurement of a relatively thick Cu layer.

From the XP detail spectra of the pn$^+$-Si | therm. SiO_2 | Cu sample in Figure 34 it can be seen that the Si 2p emission line of the bare pn$^+$-Si | therm. SiO_2 substrate has its maximum at a binding energy of 99.77 eV and exhibits a more intense SiO_2 signal compared to the pn$^+$-Si | nat. SiO_2 substrate. This is an indication that the thermally grown SiO_2 layer is thicker than the native SiO_2 layer on the Si substrate. The exact layer thickness can be calculated and will be discussed afterwards. When the Cu film reaches a thickness of 15 Å the O 1s emission line already shows an asymmetry with a very small additional line forming, which indicates the presence of a copper oxide compound, most likely Cu_2O. At that point the Si $2p_{3/2}$ emission line has shifted to 99.65 eV.

With the following two deposition steps the Si 2p emission line is further shifted and loses its dominance. Same is valid for the O 1s emission line. Moreover, the O 1s low binding energy signal becomes more intense. In contrast to the pn^+-Si:H | Cu contact a surface reaction takes place. Finally, the Cu film reaches a thickness of around 92 Å at the end of the interface experiment. With the last step the position of the Si 2p emission line has not changed anymore. The O 1s emission line has almost vanished while the satellite is clearly visible. The shape of the Cu 2p emission line exhibits metallic features, which is also proven by the Cu LMM Auger line in the appendix A 4. However, analogous to the sample with native SiO_2, after the first deposition step the formation of Cu_2O can be concluded from the shape of the Cu LMM Auger line.

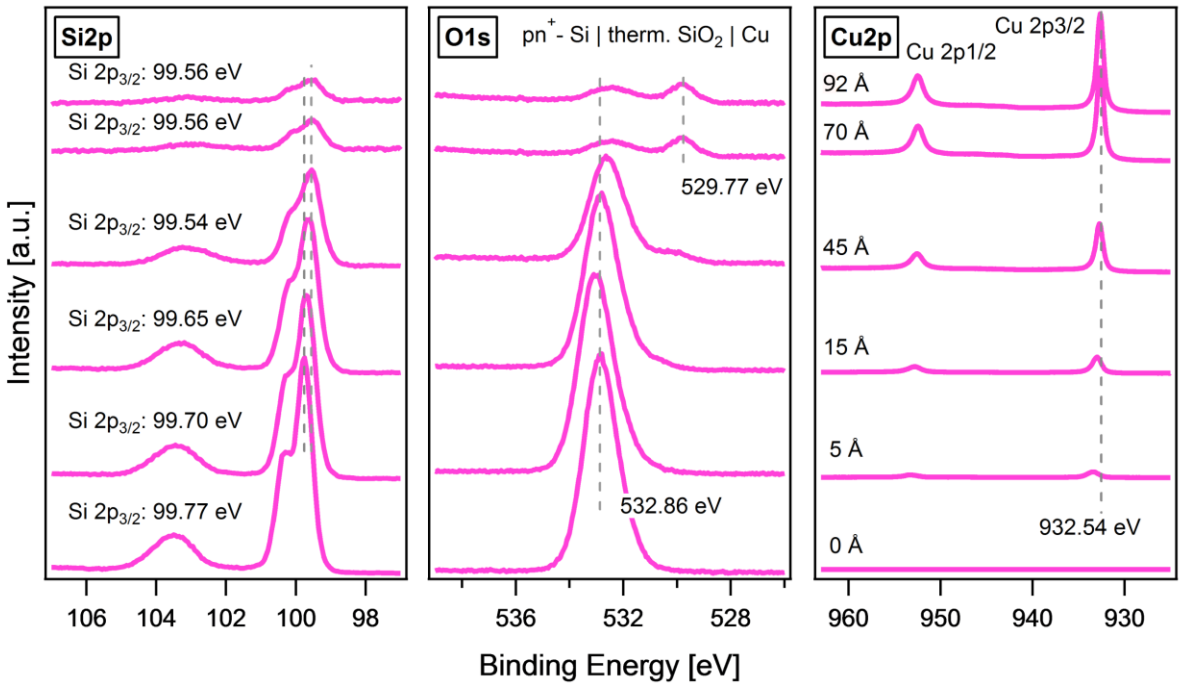

Figure 34: Development of the Si 2p, O 1s and Cu 2p detail spectra of the pn^+-Si | therm. SiO_2 | Cu contact during the interface experiment. The measurement of the bare pn^+-Si | therm. SiO_2 substrate is displayed at the bottom of the diagram while the last deposition step at the top shows the final measurement of a relatively thick Cu layer.

The aim of all performed XPS measurements is the investigation of the interfaces and thus of the energy band alignments of the differently prepared pn^+-Si surfaces. Therefore, especially the values of the binding energy of the Si $2p_{3/2}$ emission line before and after contact formation are relevant. Therefore, these values are summarized in table 2.

Table 2: Overview of the position of the Si $2p_{3/2}$ emission line before and after contact formation for the pn^+-Si model systems with different surface terminations.

Model system	**Position of Si $2p_{3/2}$ emission line**		
	before contact	after contact	resulting shift
pn^+-Si | nat. SiO_2 | Cu	99.77 eV	99.48 eV	0.29 eV
pn^+-Si:H | Cu	99.82 eV	99.38 eV	0.44 eV
pn^+-Si | therm. SiO_2 | Cu	99.77 eV	99.56 eV	0.21 eV

The investigated band diagrams for pn^+-Si with and without SiO_2 layer before and after being in contact with Cu are displayed in Figure 35. Here, Figure 35 a) shows the initial energetic situation of the pn^+-Si | SiO_2 before the Cu deposition. The band gap of 1.12 eV for Si is sketched as well as the distance of the Fermi level to the valence band, which is 0.2 eV.[11] This value was determined by the solution of equation (22).

$$E_F - E_{VB} = kT\ ln\left(\frac{N_{VB}}{p}\right). \qquad (22)$$

Here, N_{VB} is the effective density of states (DOS) in the valence band ($N_{VB} = 2.8 \cdot 10^{19}$ cm^{-3}) and p is the doping concentration ($p = 10^{-16}$ cm^{-3}). In the n^+-Si layer the doping concentration n is much higher ($n = 10^{19}$ cm^{-3}), which results in a very small distance of the Fermi level to the conduction band of 0.03 eV. The effective density of states as well as the doping concentration are sample specific values, which were provided by Forschungszentrum Jülich and Fraunhofer IISB Erlangen, who delivered the samples. With a slight upward band bending of 0.06 eV a flat band like situation for the n^+-Si top layer and a space charge layer between the pn^+-Si layers can be assumed as initial electronic structure. For this starting situation a Si $2p_{3/2}$ core level binding energy at 99.77 eV has been measured for the native SiO_2 terminated pn^+-Si surface. With the known value of $E_B(VB) - E_B(Si\ 2p_{3/2})$ of 98.74 eV this corresponds to a value of $E_F - E_{VB}$ of 1.03 eV in agreement to the presented energy diagram. Figure 35 b) shows the electronic band structure of pn^+-Si | nat. SiO_2 | Cu contact. A band bending upwards of 0.35 eV induced in the n^+ surface layer can be observed. In case of the thermal SiO_2 this surface band bending is smaller having a value of 0.27 eV, as can be seen in Figure 35 c). The reason for the more ideal band alignment in case of the thermal SiO_2 interlayer might be the better surface passivation due to the higher layer thickness. From the different intensities of the initial SiO_2 peaks in the Si 2p emission lines of the pn^+-Si | nat. SiO_2 and pn^+-Si | therm. SiO_2 substrates a different layer thickness was already assumed (see Figure 30 and Figure 34). The SiO_2 layer thickness d_{SiO2} can be determined by solving equation (23).

$$d_{SiO2} = \lambda\ cos\delta\ ln\left(1 + \frac{I_{SiO2} N_{Si}}{I_{Si} N_{SiO2}}\right) \qquad (23)$$

Here, λ is the inelastic mean free path of SiO_2, δ is the electron emission angle, I_{SiO2} and I_{Si} describe the integrated core level lines while N_{SiO2} and N_{Si} are the materials atomic densities. For the native SiO_2 layer a thickness of 3 Å and for the thermal SiO_2 a thickness of 7 Å was calculated. Furthermore, different properties of the oxide layers may play an additional role. For the hydrogen terminated model system the initial electronic structure before the Cu deposition is illustrated in Figure 35 d). With an initial band bending of only 0.01 eV at the surface a flat band situation in the n^+ layer is given. When being in contact with Cu an upward band bending of 0.45 eV develops as illustrated in Figure 35 e). These band bending changes in the topmost Si n^+ layer can directly be deduced from the different shifts of the Si $2p_{3/2}$ binding energy values with each Cu deposition step which are listed in table 2. As the photoelectrons, which come from the conduction band of the pn^+-Si junction need to overcome the energetic barrier between n^+-Si and Cu layer, it is advantageous if the interface exhibits only a small upward band bending at this point. Thus, it can be concluded that the model system pn^+-Si | therm. SiO_2 | Cu with a barrier of only 0.27 eV provides the best electronic transport properties followed by the model system pn^+-Si | nat. SiO_2 | Cu with 0.35 eV and pn^+-Si:H | Cu with 0.45 eV barriers respectively.

It should be mentioned that the displayed energy band alignments do not consider the presence of a possible additional Cu_2O layer in case of the samples with native and thermal SiO_2 (Figure 35 b) and c)). However, small amounts of Cu_2O were detected in the O 1s region, it was proven by the Cu 2p line as well as the Cu LMM Auger line that the deposited film is mostly metallic.

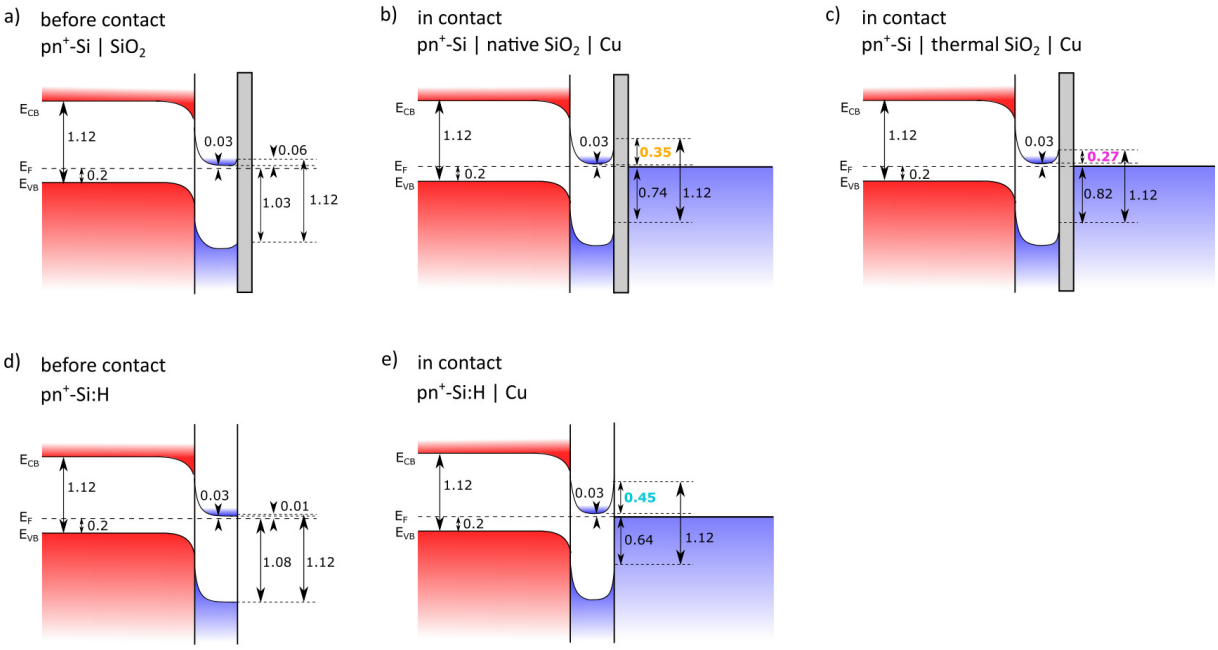

Figure 35: Energy band diagrams before and after contact formation. a) pn^+-Si | SiO_2 before contact formation with flat band situation, b) pn^+-Si | nat. SiO_2 | Cu with an upward band bending of 0.35 eV, c) pn^+-Si | therm. SiO_2 | Cu with an upward band bending of 0.27 eV, d) pn^+-Si:H before contact formation with flat band situation and e) pn^+-Si:H | Cu with an upward band bending of 0.45 eV.

5.2.2 Electrochemistry

The differences in the band energy diagrams as deduced from the XPS interface experiments described above were compared to additional CV measurements, to determine the influence of the energy level alignment on the photoelectrochemical performance. It is assumed that the samples with lower energetic barriers at the n^+-Si | Cu interface deliver a better performance compared to the samples with higher barriers. The catalytic performance was measured by CV for all three systems. The resulting CV curves are displayed in Figure 36. First, it can be concluded that under an illumination of 180 W/m^2 with λ = 625 nm all samples reach a similar saturation current density of -5.7 to -6 mA/cm^2. However, for obtaining a current density of -2 mA/cm^2 a potential of averaged -0.7 V (vs. RHE) was necessary for the pn^+-Si:H | Cu sample. For the pn^+-Si | native SiO_2 | Cu sample a potential of -0.6 V was sufficient while the pn^+-Si | thermal SiO_2 | Cu sample was able to reach a current density of -2 mA/cm^2 at an applied potential of only -0.4 V. These results are in excellent agreement with the expectations from the investigated electronic band structure of the samples since the photoelectrochemical performance is improved for low energy barriers at the interface after contact formation. Additionally, the layer thickness of the intermediate SiO_2 can be discussed. While the native SiO_2 has only a thickness of 3 Å, the thermal SiO_2 layer is 7 Å thick. As a thicker thermal SiO_2 layer probably results in a better surface passivation compared to a thinner native SiO_2 the photoelectrochemical performance can be assumed to be improved. In addition, all the samples show a strongly improved behavior compared to the p-Si | Cu sample which was introduced in section 5.1. There are well defined photo current voltage curves and low dark current curves (-0.7 mA/cm^2 to -1.1 mA/cm^2) as expected for a diode in the reverse saturation potential regime. Table 3 gives an overview of the necessary potential to obtain -2 mA/cm^2, the saturation current density under illumination ($J_{sat,\ illum}$) and in the dark ($J_{sat,\ dark}$) as well as the corresponding energy barrier at the interface ($eV_{b,n}$) for the three different pn^+-Si | Cu model systems.

Table 3: Overview of the necessary potential to obtain -2 mA/cm^2, the saturation current density under illumination ($J_{sat,\ illum}$) and in the dark ($J_{sat,\ dark}$) as well as the corresponding energy barrier at the interface ($eV_{b,n}$) for different pn^+-Si | Cu model systems.

Model System	potential to reach -2 mA/cm^2 [V vs. RHE]	$J_{sat,illum}$ [mA/cm^2]	$J_{sat.dark}$ [mA/cm^2]	$eV_{b,n}$ [eV]
pn^+-Si | nat. SiO_2 | Cu	-0.6	-6.0	-1.1	+0.35
pn^+-Si:H | Cu	-0.7	-6.0	-0.7	+0.45
pn^+-Si | therm. SiO_2 | Cu	-0.4	-5.7	-0.7	+0.27

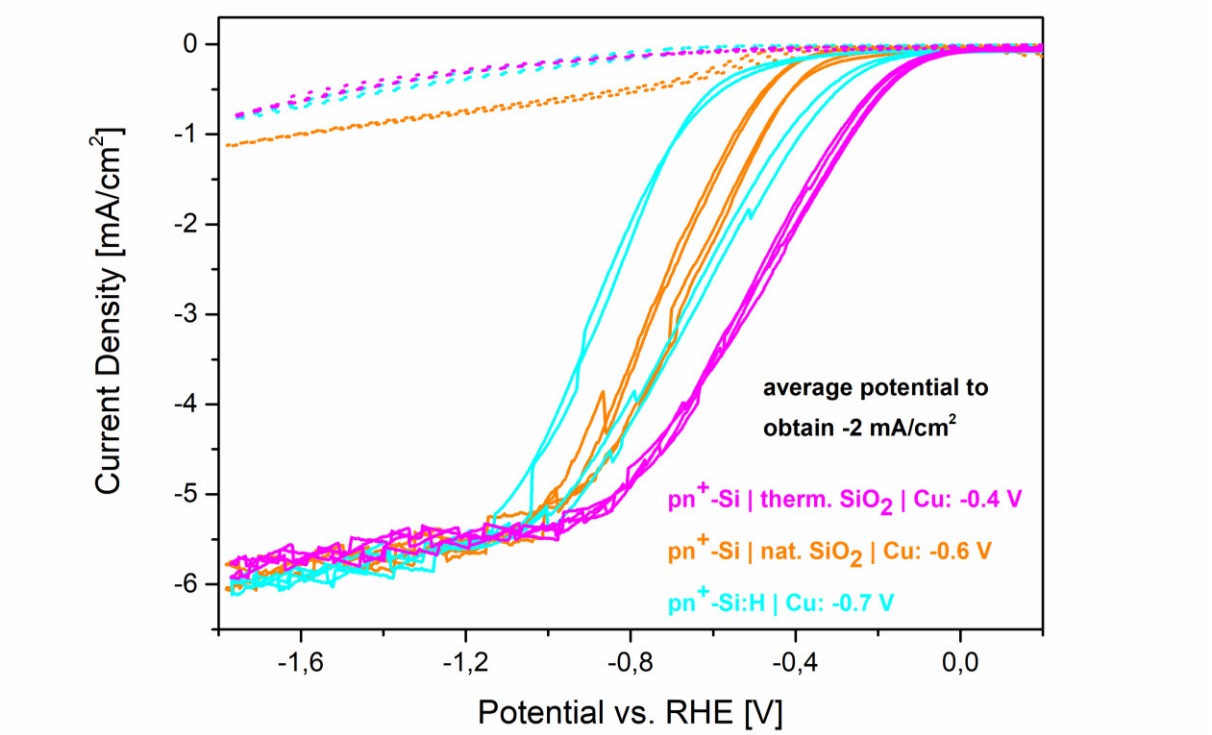

Figure 36: Comparison of the cyclic voltammetry behavior of the three different model systems: pn^+-Si | nat. SiO_2 | Cu (pink), pn^+-Si:H | Cu (cyan) and pn^+-Si | therm. SiO_2 | Cu (orange) in the dark and under an illumination of 180 W/m² with λ = 625 nm in 0.3 M $KHCO_3$. Solid lines: EC behavior under illumination. Dashed lines: EC behavior in the dark. As predicted from the interface investigations the samples show different behaviors depending on the surface barrier height.

5.2.3 Characterization after Electrochemistry

XPS measurements were performed after the photoelectrochemical measurements in order to analyze the quality of the Cu film after being in contact to the electrolyte (0.3 M $KHCO_3$) as well as further changes of the sample surfaces due to the electrochemical CO_2 reduction reaction. Figure 37 shows the relevant XP detail spectra of the pn^+-Si | Cu samples with different surface terminations (orange: native SiO_2, blue: H-termination and pink: thermal SiO_2). First, it is obvious that in general all spectra seem to be shifted, which might come from charging effects.

As already observed in case of the p-Si | therm. SiO_2 | Cu sample the initial metallic Cu film has changed to $Cu(OH)_2$ for all three samples, which can be concluded from the presence of the strong satellite within the Cu 2p splitting. Furthermore, it can be noted that the position of the Cu $2p_{3/2}$ emission line has shifted to higher binding energies for all samples. While the initial positions of the Cu $2p_{3/2}$ emission line were at 932.68 eV, 932.81 eV and 932.54 eV for the sample with native SiO_2, H-termination and thermal SiO_2, the maxima have been shifted to 936.50 eV, 937.05 eV and 935.64 eV. This large shift cannot only be explained by the formation of $Cu(OH)_2$ [121]–[123], but also charging effects of the samples.

Second, the O 1s emission lines are quite intense for all samples although the corresponding signals were very week or barely visible before performing EC. One the one hand, it is possible that the Cu films became thinner during EC so that the oxygen from the substrates is detected by XPS. On the other hand, it is very probable that due to the used electrolyte solution as well as the CO_2 reduction reaction at the surface, hydroxides and carbon oxides are formed.[124][125] However, this assumptions cannot be proven only by having a look at the maximum positions of the O1s emission lines, which were detected at 533.10 eV, 533.65 eV and 534.08 eV for the sample with native SiO_2, H-termination and thermal SiO_2. Further experiments such as gas chromatography are necessary in order to analyze reaction products.

Effects of the used electrolyte or the chemical CO_2 reduction can also be observed in the C 1s spectra. The C 1s emission lines of all samples have a maximum at 286 – 287 eV, which could be assigned to the formation of C-H or C-C bonds. In case of the sample with native oxide as well as H-termination an additional signal can be detected at around 290 eV, which could be referred to the formation of carbonates.[126]

When analyzing the Si 2p emission line it can be noticed, that the Si $2p_{3/2}$ emission line only appears in case of the pn^+-Si | nat. SiO_2 | Cu at around 99.5 eV. This indicates that the Cu layer on top of the pn^+-Si | nat. SiO_2 is thinner after the EC measurement compared to the pn^+-Si:H | Cu and the pn^+-Si | therm. SiO_2 | Cu sample. This assumption is also confirmed by the reduced intensity of the Cu 2p emission line of the pn^+-Si | nat. SiO_2 | Cu sample. At binding energies of 104.10 eV, 104.72 eV and 104.72 eV SiO_2 can be detected for all three samples, which is slightly shifted to higher binding energies, but still in agreement with literature.[127][128] As the initial pn^+-Si:H | Cu sample did not contain a SiO_2 layer between the Si and the Cu film, it may be assumed that oxygen has diffused through the Cu layer during EC and hence oxidized the underlying Si substrate. This phenomenon could also explain the quite intense SiO_2 signals for the other two samples.

It can be concluded that after the performance of photoelectrochemical measurements in 0.3 M $KHCO_3$ the initial metallic Cu catalyst became thinner and is at least partially transformed to $Cu(OH)_2$. To evaluate the exact film thickness of the Cu is more inaccurate compared to the calculation directly after deposition as the spectra after EC show more background noise. However, from the Cu 2p and Si 2p intensity ratio a Cu film thickness of 40 – 45 Å was determined after the electrochemical measurements, in contrast to 90 – 95 Å directly after deposition. Moreover, the Si substrates were oxidized. C-C and C-H bonds could be detected at the surface of all three samples and additionally C-O was detected in case of the sample with native SiO_2 and hydrogen termination.

In order to prevent the modification of the metallic Cu catalyst and to improve the CO_2 reduction reaction, deaeration of the electrolyte is reasonable, as described in the following section.

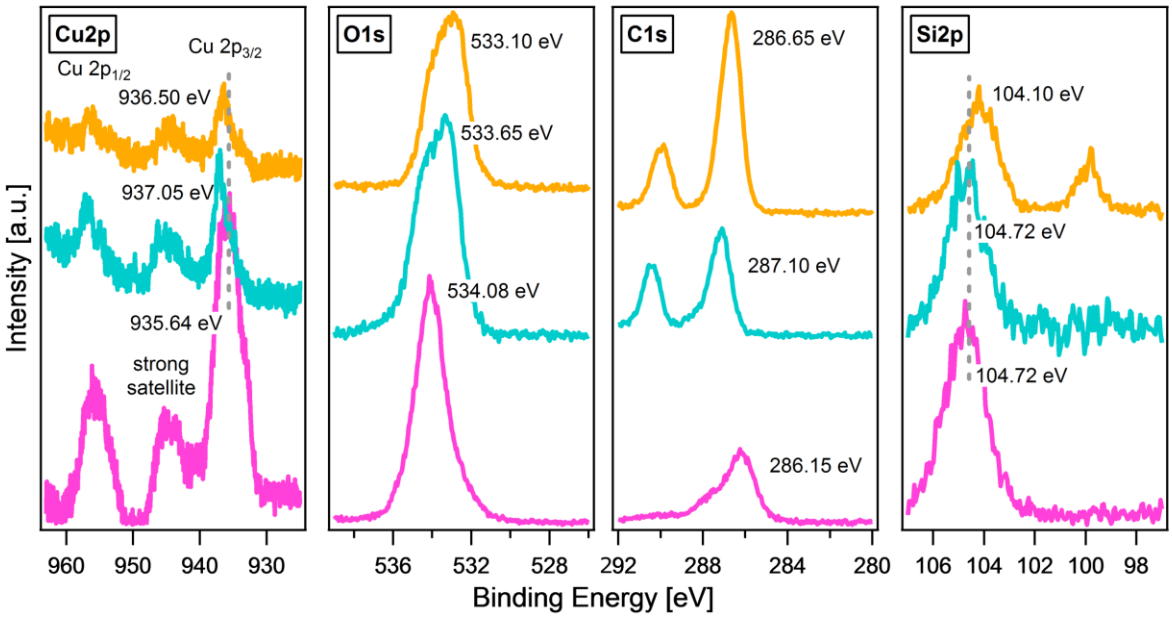

Figure 37: XP detail spectra of the pn$^+$-Si | Cu samples with different surface terminations showing the Cu 2p, O 1s, C 1s and Si 2p emission lines after performing cyclic voltammetry measurements (orange: native SiO_2, blue: H-termination and pink: thermal SiO_2).

As it is essential that the Cu catalyst does not change during photoelectrochemical measurements, a further EC measurement was performed where nitrogen gas was additionally bubbled through the photoelectrochemical cell. The idea was to prevent oxygen adsorption on the Cu film, which might lead to the formation of $Cu(OH)_2$. This experiment was only done once for the pn$^+$-Si | nat. SiO_2 | Cu sample. Figure 38 shows the XP detail spectra of the pn$^+$-Si | nat. SiO_2 | Cu sample after EC with and without nitrogen gas bubbling. From the Cu 2p emission line it can be seen that contrary to the measurement without nitrogen gas bubbling, the metallic character of the Cu film remains after EC if N_2 was bubbled through the electrolyte. This can be assumed due to the absence of the satellite within the Cu 2p splitting. Furthermore, the maximum position of the Cu 2p emission line can be detected at 933.50 eV, which is a characteristic value for metallic Cu.[129] Nevertheless, the shape as well as the Cu $2p_{3/2}$ position could also be assigned to Cu_2O. While the Cu LMM Auger line, which was measured during the interface experiment, was used to distinguish between both Cu phases, this is not possible after the electrochemical measurements as the spectra of the samples show more background noise. Therefore, the Cu LMM region cannot be evaluated.

Nevertheless, the O 1s emission line can also be used to make a statement concerning the present Cu phase. The position of the O 1s emission line does almost not change in both performed experiments. However, the shape is much more distinct, symmetric and not broadened, which leads to the assumption that pure SiO_2 is present instead of a mixture of SiO_2 and a variety of Cu-O species in case of nitrogen gas bubbling. The formation of Cu_2O would lead to a shift of the O 1s emission line to about 530.51 eV,

which cannot be observed in this experiment. Therefore, it can be assumed that the initial metallic character of the deposited Cu film remains after the electrochemical measurement.

With additional bubbling with nitrogen gas, the maximum of the C 1s emission line is detected at 285.20 eV instead of 286.70 eV. A binding energy of around 285 eV indicates the formation of C-H and C-C bonds.[94] It can also be noted that the C 1s emission line shows an asymmetry with contributions at binding energies >286 eV. A variety of carbon species may have formed due to the used electrolyte or the CO_2 reduction reaction. However, it is not possible to evaluate reaction products with XPS analysis only.

When investigating the Si 2p emission line, it is obvious that the substrate signal is much better detectable in case of the sample, which has been exposed to nitrogen gas. The maximum of the Si $2p_{3/2}$ emission line can be clearly measured at 99.74 eV which is characteristic for Si. Furthermore, the SiO_2 peak is present at a typical value of 103.58 eV. As the substrate is clearly visible in case of additional bubbling, it leads to the assumption that the Cu film is slightly dissolved by the N_2 bubbles. This effect leads to a reduced Cu film thickness and therefore, to an increased substrate signal when performing XPS. The Cu 2p to Si 2p intensity ratio has shown that the initial Cu film thickness (91 Å) is reduced to about 15 Å during the electrochemical measurement with additional nitrogen gas bubbling.

However, it can be concluded that additional bubbling with nitrogen gas during the photoelectrochemical measurement improves the quality of the remaining Cu film as possible adsorbates are dispatched from the catalyst surface.

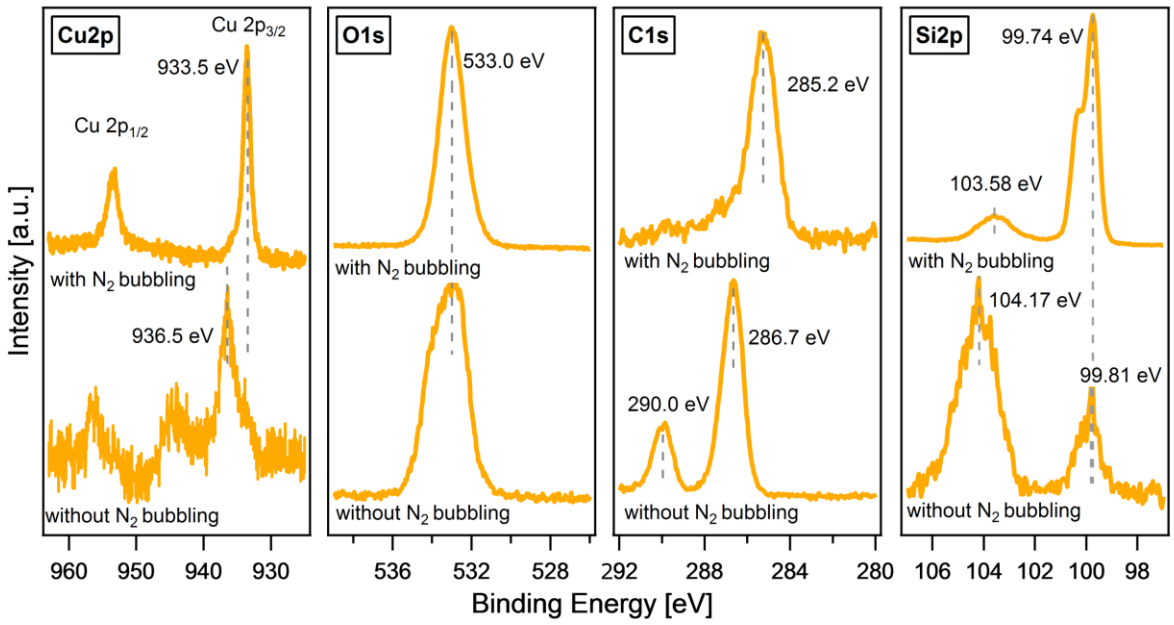

Figure 38: XP detail spectra of the pn^+-Si | nat. SiO_2 | Cu sample showing the effect of N_2 gas bubbling during performing cyclic voltammetry measurements.

Another quality feature of the Cu film is the overall adhesion and the intactness. As XPS only analyses a specific point on the sample surface, additionally the sample surface was imaged by SEM. The corresponding SEM images with a magnification of 1000 shown in Figure 39 give an overview of the pn^+-Si | nat. SiO_2 | Cu surface a) before and b) after performing photoelectrochemical measurements. However, the surface termination does not play a role as it cannot be visualized by SEM. Before EC the Cu film is very flat and homogeneous, which can be expected when depositing Cu on a Si wafer by electron beam deposition. No structure and no defects can be visualized by the SEM technique. In Figure 39 b) it can be seen that the surface structure of the Cu film is damaged within a large area. For a more detailed impression of the sample surface the cross section of the samples were scanned with a magnification of 25000, which can be seen in Figure 40 a) and b). Again Figure 40 a) presents the very flat and clean surface before EC measurement while the situation after EC is shown in Figure 40 b). The overall damage of the Cu film after EC becomes very clear. It seems as if the Cu film has partially detached from the Si surface and formed bubbles between the Si | Cu interface. However, holes or cracks cannot be found on the surface which leads to the assumption that the Cu film is still intact. Merely, the adhesion of the deposited film has suffered from the photoelectrochemical procedure.

Combining the results of the XPS and SEM investigations it can be concluded that the Cu film is mostly intact after the photoelectrochemical performance. Although the film thickness is reduced, no cracks or holes are build, but the film is partially detached from the substrate. However, the stoichiometry of the film may change depending on whether EC is performed with or without nitrogen gas bubbling. This effect is not surprising as the electrolyte is not deaerated without nitrogen gas bubbling. Nevertheless, experiments were mainly performed without bubbling because the focus of this work was the investigation of the correlation between the energy band alignment and the electrochemical performance and not the electrochemical CO_2 reduction.

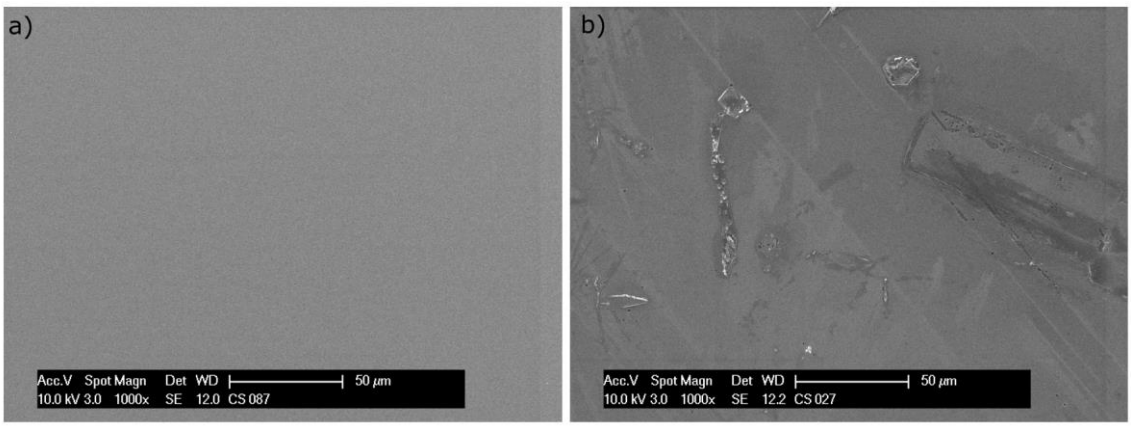

Figure 39: SEM images of pn^+-Si | nat. SiO_2 | Cu samples with a magnification of 1000, a) before photoelectrochemistry and b) after photoelectrochemistry.

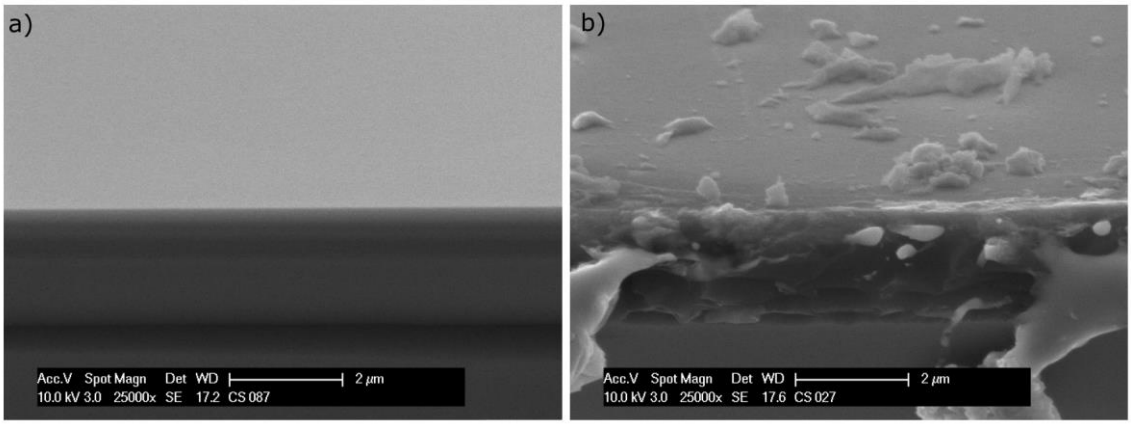

Figure 40: SEM images of the cross section of the pn$^+$-Si | nat. SiO_2 | Cu samples with a magnification of 25000, a) before photoelectrochemistry and b) after photoelectrochemistry.

5.3 p-Si | µcn-Si | Cu

The next step towards a systematic understanding of Si | Cu interfaces is the investigation of p-Si | µcn-Si substrates, which contain a buried junction such as the previously analyzed pn$^+$-Si substrate. However, the top n-layer is microcrystalline in contrast to the single crystalline n-layer of the pn$^+$-Si substrate. To examine the µcn-Si | Cu interface is important, as it is the aim to use a µc-Si:H multi junction solar cell to realize the idea of an artificial leaf. Analogous to the investigations of the pn$^+$-Si | Cu interface the three different Si surface terminations (native SiO_2, H termination and thermal SiO_2) were examined.

5.3.1 Energy Band Alignment

Before the electronic band structure can be determined, survey spectra were measured to prove whether the samples are contaminated and to demonstrate the differences of the three differently prepared samples. The resulting XP spectra in Figure 41 give an overview of the elements which are present on the sample surfaces. The bottom green spectrum presents the H-terminated p-Si | µcn-Si surface, the middle red spectrum shows the surface of the p-Si | µcn-Si substrate with an additional native SiO_2 layer on top and the purple spectrum displays the etched p-Si | µcn-Si substrate on which a SiO_2 layer was thermally grown as described in chapter 4.1 The most noticeable feature of the three different spectra is the different amount of oxygen as it can be deduced from the O 1s emission line at around 533 eV. Even after HF and NH_4F etching a small amount of O remains on the p-Si | µcn-Si:H surface, which was already observed for the pn$^+$-Si:H sample. Analogous to the appearance and intensity of the O 1s emission line, the O KLL Auger line at about 979 eV can be detected for all three surfaces. Furthermore, the Si 2s and Si 2p emission lines are clearly visible for all the samples and also a small amount of C can be found on all three samples.

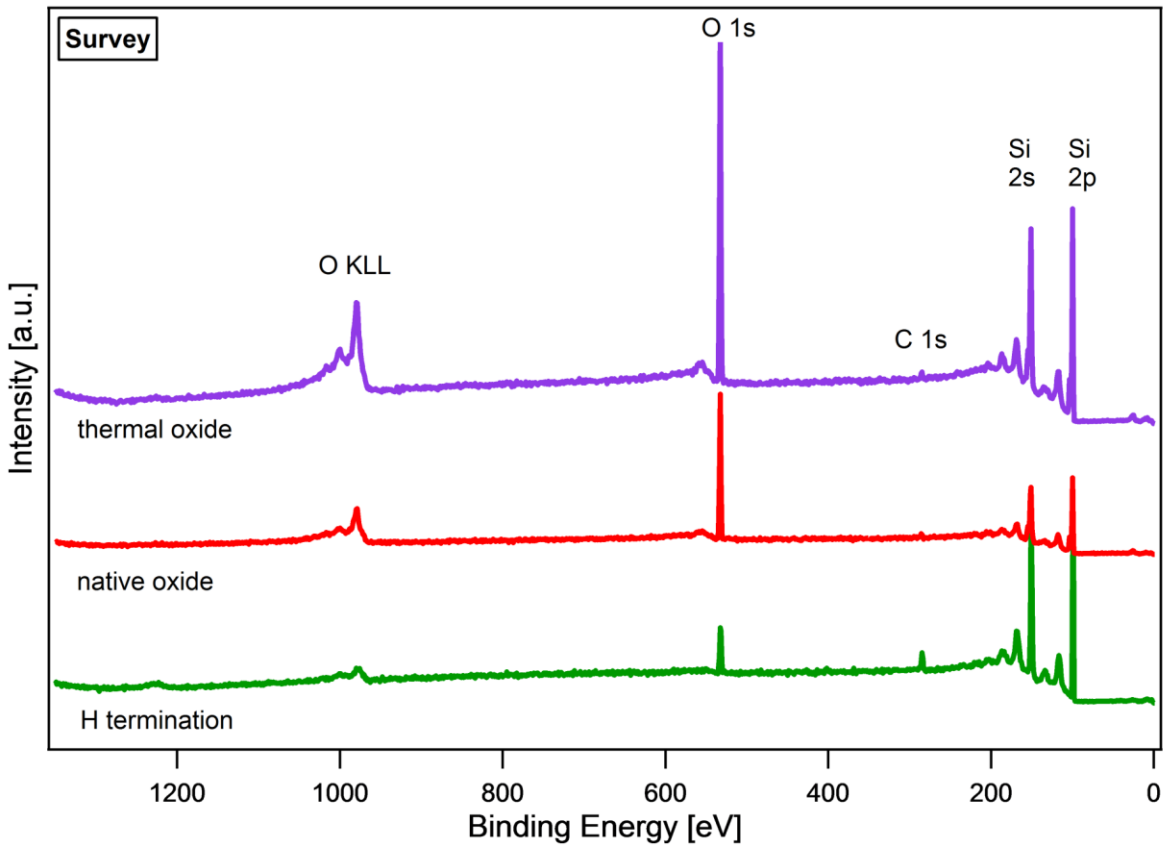

Figure 41: XP survey spectra of the p-Si | µcn-Si substrates with different surface terminations: H-termination, native SiO_2 and thermal SiO_2.

p-Si | µcn-Si | nat. SiO_2 | Cu

For investigating the energy band alignment of the three different samples, interface experiments were performed for all p-Si | µcn-Si | Cu model systems. First, the development of the survey spectra of the p-Si | µcn-Si | nat. SiO_2 | Cu contact during the experiment is displayed in Figure 42. The spectra from bottom to top represent the measurements from the bare p-Si | µcn-Si | nat. SiO_2 substrate to the p-Si | µcn-Si | nat. SiO_2 | Cu contact. With ongoing deposition steps the substrate contributions Si 2p, Si 2s, O 1s and O KLL become weaker while the Cu 2s, Cu 2p and Cu LMM lines become dominant.

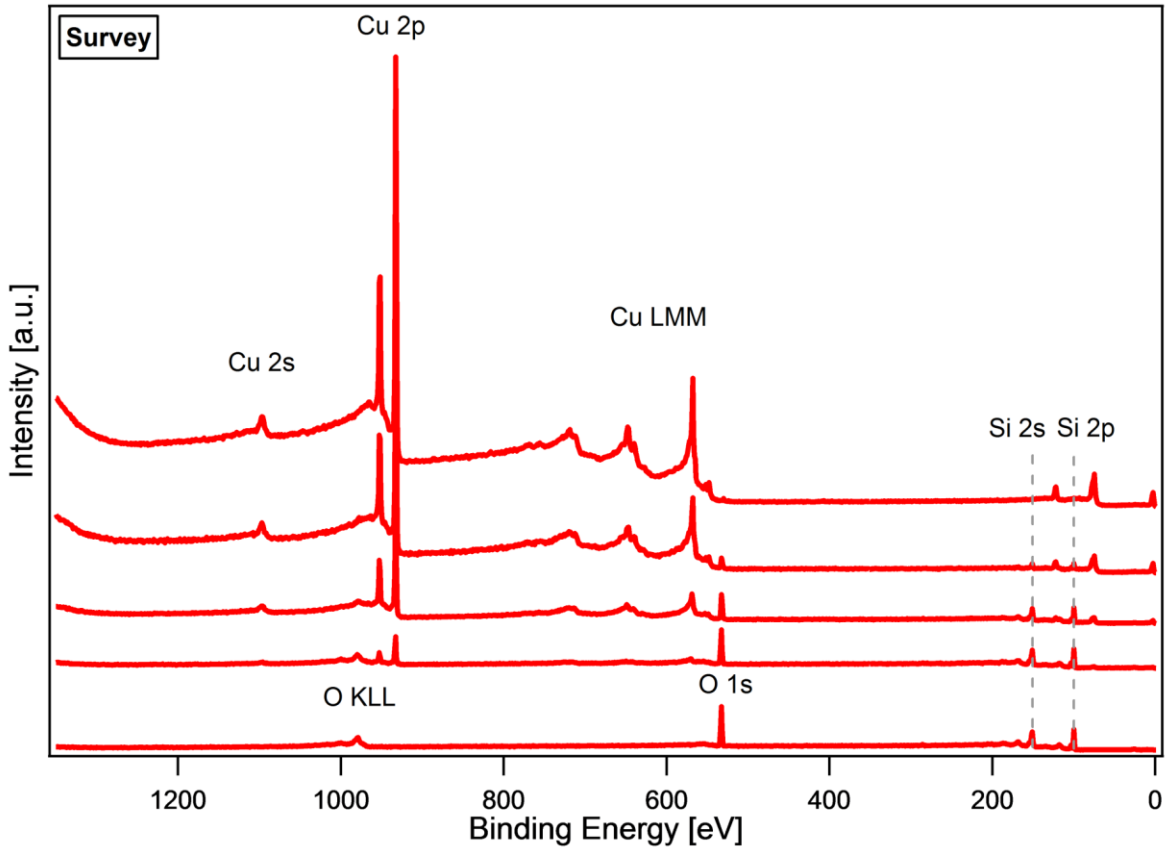

Figure 42: Development of the XP survey spectra of the p-Si | µcn-Si | nat. SiO_2 | Cu contact during the interface experiment. The measurement of the bare p-Si | µcn-Si | nat. SiO_2 substrate is displayed at the bottom of the diagram while the last deposition step at the top shows the final measurement of a relatively thick Cu layer.

The relevant XP detail spectra showing the development of the Si 2p, O 1s and Cu 2p emission lines are presented in Figure 43. As for the survey spectra in Figure 42 the bottom spectra display the measurement of the bare p-Si | µcn-Si | nat. SiO_2 substrate while the spectra at the top present the measurements of the final p-Si | µcn-Si | nat. SiO_2 | Cu contact. The Si 2p emission line is split into Si $2p_{3/2}$ and Si $2p_{1/2}$. While the more intense Si $2p_{3/2}$ emission line arises at a binding energy of 99.84 eV, the Si $2p_{1/2}$ emission line can be detected at 100.35 eV. From the intensities of the Si $2p_{3/2}$ and Si $2p_{1/2}$

emission lines it can be determined that the thickness of the SiO_2 layer is 10 Å. The contribution of the SiO_2 layer is clearly visible at 103.58 eV. Because of the native SiO_2 layer on the p-Si | µcn-Si surface, the O 1s emission line at a binding energy of 533.10 eV is quite intense.

After the first deposition step the position of the Si $2p_{3/2}$ emission line has not changed, in contrast to the O 1s emission line, which is slightly shifted to lower binding energies. As this effect is surprising, it is important to have a look at the SiO_2 emission line, which is marked in grey in Figure 43. Although the maximum of the Si $2p_{3/2}$ emission line does not change, the SiO_2 peak shifts and also becomes asymmetric. This leads to the assumption that the Cu deposition is responsible for a change of the stoichiometry of the oxygen in the silicon. In order to prove this assumption the Cu LMM Auger line can be taken into account, which is shown in the appendix A 5. With a Cu film thickness of only 5 Å, the Cu LMM line is still quite noisy. However, the maximum can be detected at around 570 eV, which corresponds to Cu_2O (Cu^0: 568 eV, CuO: 569 eV). Furthermore the shape of the Auger liner confirms the Cu_2O phase instead of metallic Cu or CuO.[130]

After the second deposition step the Cu film reaches a thickness of approximately 15 Å, which results in further changes in the XP detail spectra. It is obvious and reasonable that the intensities of the Si 2p and O 1s emission lines decrease and the Cu 2p emission line becomes more intense. While the position of the Si $2p_{3/2}$ emission line stays constant, the position of the O 1s emission line is now further shifted to lower binding energies and also the shape of the O 1s line becomes slightly asymmetric. Within the Si 2p region it can be noticed that the minimum between the Si $2p_{2/3}$ and Si $2p_{1/2}$ emission line becomes less distinct. The SiO_2 signal is slightly shifted and broadened, which may still be an indication of a changed stoichiometry of the Si substrate. Although, the shape of the Cu LMM Auger line becomes more significant, still it does not allow a clear statement whether metallic Cu has formed.

With the third deposition step additional 35 Å of Cu are deposited. The Si 2p and O 1s signals are further decreasing but still visible. While the maximum of the Si $2p_{3/2}$ emission line can still be detected at 99.84 eV, the shape has drastically changed compared to the initial Si 2p emission line. The O 1s emission line is further shifted to lower binding energies and the shape is different compared to the previous measured O 1s emission lines. The O 1s line becomes more asymmetric and a small satellite at a binding energy of about 523.30 eV forms. This feature can be explained with the formation of Cu_2O.[106][130] The Cu 2p emission line becomes more intense and the maximum of the Cu $2p_{3/2}$ emission line can be detected at 932.62 eV, which is a typical value for metallic Cu.

With the final deposition step the Cu film reaches a thickness of 100 Å. Compared to the previous deposition step the position of the Cu $2p_{3/2}$ emission line has not changed, however, the intensity is increased. The spectrum is characteristic for metallic Cu. As it remains flat within the Cu 2p splitting, a Cu oxide cannot be identified. Contrary to that, a weak O 1s signal at around 530 eV may indicate the formation of a small amount of Cu_2O. As Cu_2O only exhibits a weak satellite between the Cu $2p_{3/2}$ and

Cu $2p_{1/2}$ emission line, it is not easy to distinguish between metallic Cu and Cu_2O. However, the shape of the Cu LMM Auger line supports the assumption that mostly metallic Cu has formed during deposition. After the last step of the interface experiment no signal of the substrate remains for the original Si 2p and O 1s emission line. With a Cu film thickness of 100 Å the limits of the information depth of XPS analyses is reached. Therefore, the initial O 1s emission line at 533.10 eV has vanished. Nevertheless, the deposited Cu film exhibits mainly metallic character as proven by the Cu LMM Auger line.

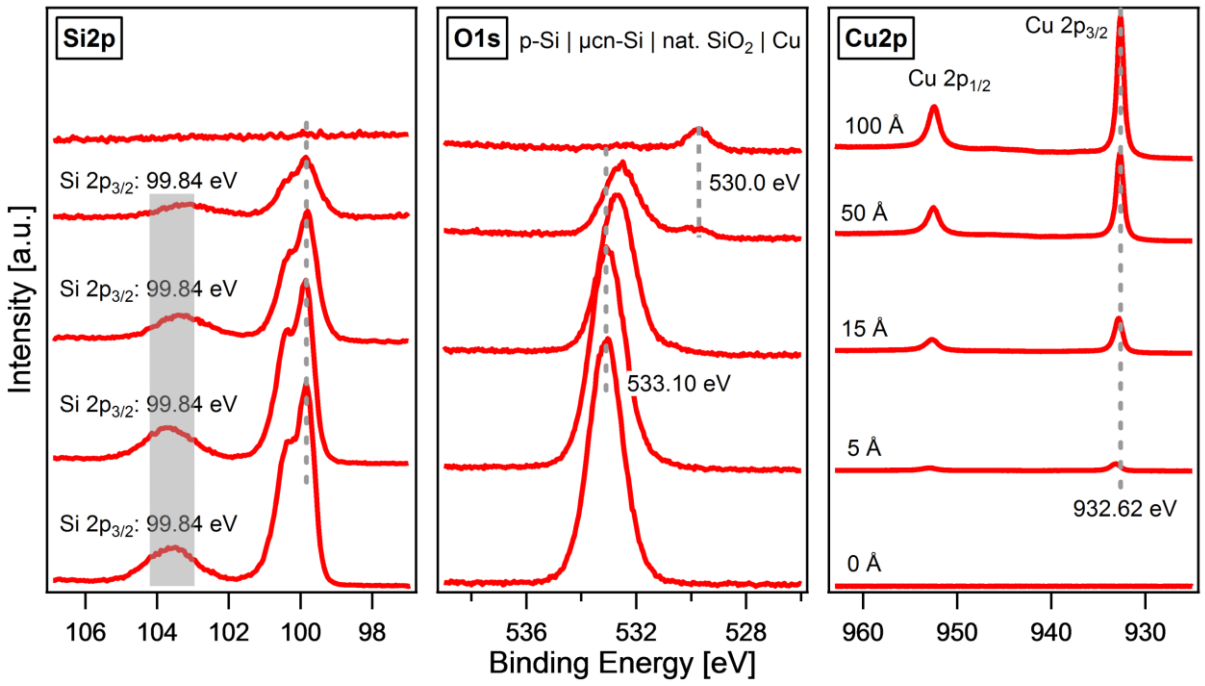

Figure 43: Development of the Si 2p, O 1s and Cu 2p detail spectra of the p-Si | µcn-Si | nat. SiO_2 | Cu contact during the interface experiment. The measurement of the bare p-Si | µcn-Si | nat. SiO_2 substrate is displayed at the bottom of the diagram while the last deposition step at the top shows the final measurement of a relatively thick Cu layer.

p-Si | µcn-Si:H | Cu

Before evaluating the corresponding energy band diagrams before and after contact formation, the XP spectra of the p-Si | µcn-Si:H | Cu and the p-Si | µcn-Si | therm. SiO_2 | Cu contact are discussed. Figure 44 displays the development of the survey spectra of the p-Si | µcn-Si:H | Cu contact. The spectra from bottom to top present the measurement of the bare p-Si | µcn-Si:H substrate to the final p-Si | µcn-Si:H | Cu contact. The decreasing substrate signals as well as the increasing film signals are noticeable with each deposition step. Figure 45 shows the corresponding XP detail spectra.

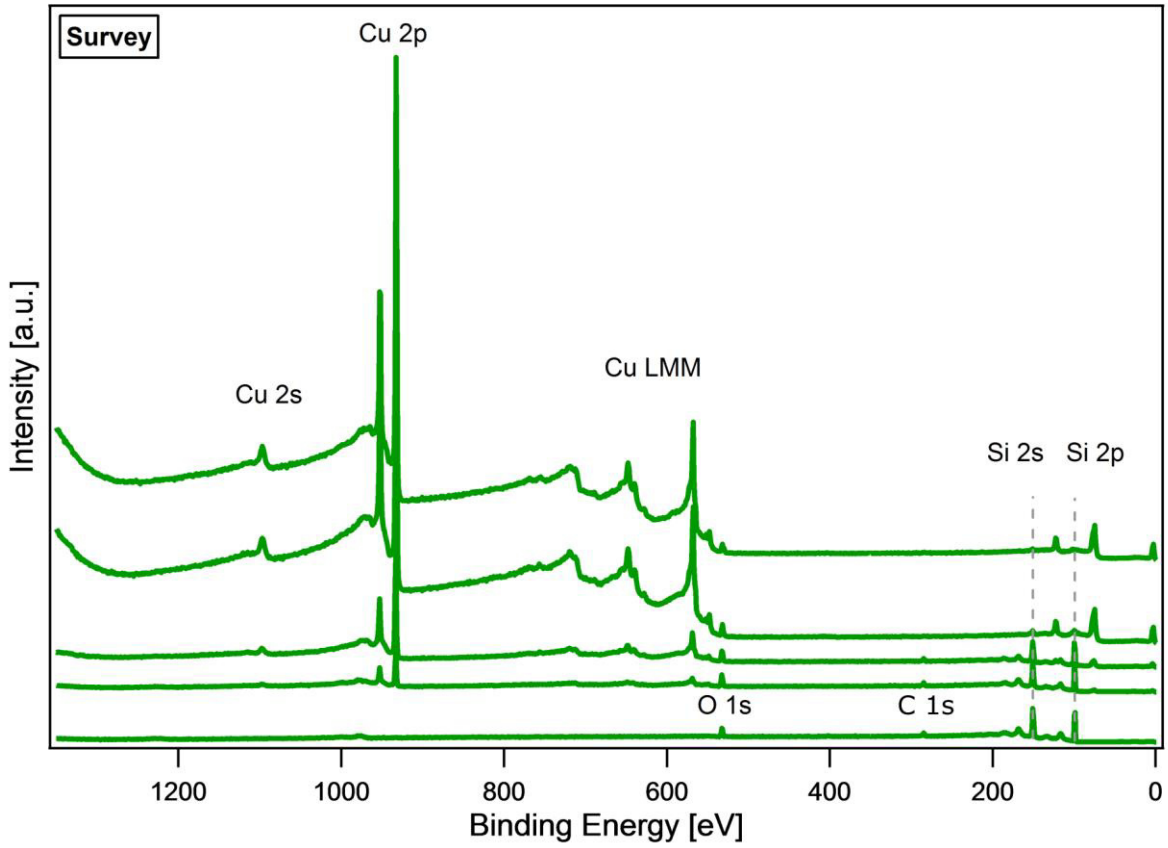

Figure 44: Development of the XP survey spectra of the p-Si | µcn-Si:H | Cu contact during the interface experiment. The measurement of the bare p-Si | µcn-Si:H substrate is displayed at the bottom of the diagram while the last deposition step at the top shows the final measurement of a relatively thick Cu layer.

The Si 2p emission line of the bare p-Si | µcn-Si:H substrate does not exhibit a peak corresponding to the emission of SiO_2, which is expected as the natural SiO_2 layer has been removed by various preparation steps. The maximum of the Si $2p_{3/2}$ emission line can be detected at a binding energy of 99.82 eV. The Si $2p_{3/2}$ and Si $2p_{1/2}$ emission lines are clearly separated by a distinct minimum, which is

an indication of an initial flat band situation. The O 1s emission line has its maximum at 532.47 eV and is not very intense as the amount of O is comparable small due to the etching steps.

After the first deposition step when the Cu film reaches a thickness of 5 Å the Si 2p emission line shows changes in shape as well as position. The well-defined shape with the minimum between the Si $2p_{3/2}$ and Si $2p_{3/2}$ emission line becomes less specific and the position of the Si $2p_{3/2}$ emission line is shifted to 99.65 eV. There are no crucial changes in the O 1s emission line, which need to be considered at that point. The Cu 2p emission line as well as the Cu LMM Auger line, which is shown in the appendix A 6 arise. In contrast to the p-Si | µcn-Si | nat. SiO_2 | Cu sample Cu LMM Auger line already shows typical features of metallic Cu.

With the second deposition step the Cu film possesses a thickness of 15 Å. While the Cu 2p and Cu LMM lines become more intense, the intensity of the Si 2p emission line is reduced compared to the initial spectrum. Moreover, the position of the Si 2p emission line is further shifted to 99.50 eV. At that point it is not possible anymore to distinguish between the Si $2p_{3/2}$ and Si $2p_{1/2}$ emission line as the initial separating minimum has vanished. The shape and intensity of the O 1s emission line has not noticeably changed. However, the maximum is slightly shifted to lower binding energies, which is induced by the formation of small amounts of Cu_2O or CuO. As there is no strong satellite detectable within the Cu 2p region, the formation of CuO is unlikely.

With the next deposition step the Si 2p emission line changes drastically. The intensity is radically decreased, however, the shape is still distinct enough to evaluate the maximum at 99.28 eV, which means a further shift of 0.22 eV. Furthermore, the shape of the O 1s emission line has changed as it is more asymmetric and a satellite corresponding to copper oxide compounds has formed. At that point the Cu film has reached a thickness of 45 Å.

With the deposition of additional 45 Å of Cu, the interface experiment is completed. The Si 2p emission line is barely visible anymore but still the position can be defined at a binding energy at 99.28 eV, which means no further shift compared to the previous measurement. The initial O 1s emission line is still available and the additional satellite is increased compared to the previous deposition step. In contrast to the pn^+-Si:H | Cu interface where no oxygen reaction at the surface was observed, in case of the p-Si | µcn-Si:H | Cu contact a surface reaction can be verified by the presence of the O 1s satellite. From the results of the pn^+-Si | Cu samples it was assumed that the Cu oxidation to Cu_2O takes place only for Si | Cu interfaces with additional SiO_2 interlayer. However, Figure 45 shows the Cu_2O formation also for the p-Si | µcn-Si:H | Cu interface. Although, the deposition conditions were precisely controlled, it could be that residual oxygen gas from other experiments in the deposition chamber has affected the Cu stoichiometry.

Comparing the two hydrogenated samples it can be noted that the initial amount of O is larger in case of the p-Si | µcn-Si:H substrate, which can then lead to the formation of a small quantity of Cu oxide,

most likely Cu_2O. How much of the native SiO_2 layer remains after the etching steps depends on the initial layer thickness, which in turn is dependent on the storage time of the sample between production and preparation. As the etching procedure is equal for all samples, it cannot be ensured that the SiO_2 layer will be completely removed. After the last deposition step the Cu $2p_{3/2}$ emission line has its maximum at 932.64 eV, which is in good agreement with literature values for metallic Cu. As there is no satellite appearing within the Cu 2p splitting the formation of metallic Cu can be assumed. This assumption is confirmed by the typical shape of the Cu LMM Auger line (A 6). Accordingly, the presence of a mainly metallic Cu film is proven.

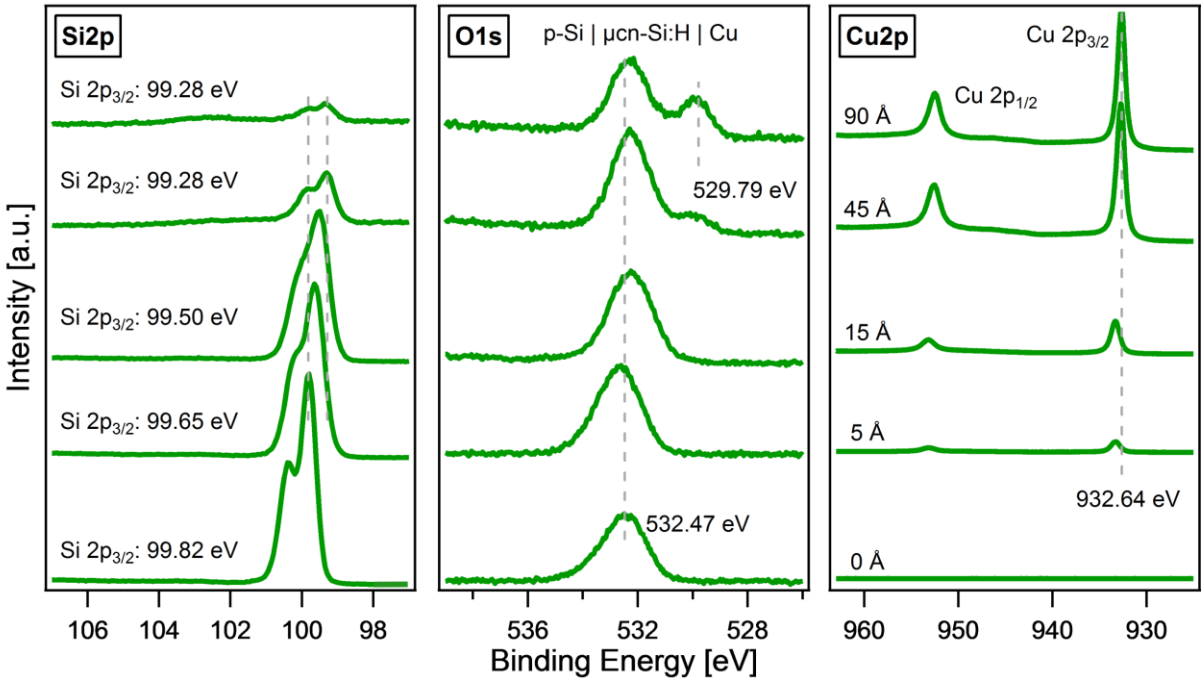

Figure 45: Development of the Si 2p, O 1s and Cu 2p detail spectra of the p-Si | µcn-Si:H | Cu contact during the interface experiment. The measurement of the bare p-Si | µcn-Si:H substrate is at the bottom of the diagram while the last deposition step at the top shows the final measurement of a relatively thick Cu layer.

p-Si | µcn-Si | therm. SiO_2 | Cu

In order to examine whether there is a difference between native SiO_2 and thermally grown SiO_2 as passivating interlayer, a thin SiO_2 layer was grown on a p-Si | µcn-Si:H substrate as described in chapter 4.1. Figure 46 shows the development of the XP survey spectra of the p-Si | µcn-Si | therm. SiO_2 | Cu contact. It is obvious that this interface experiment contains more deposition steps compared to the previously presented experiments. Due to the necessary installation of a new filament for the electron beam deposition, it is reasonable to perform the interface experiment with smaller steps as the use of a different filament may slightly change the deposition rate. However, besides the number of deposition steps the procedure of the interface experiment is equal to all previous XPS measurements. From the survey spectra in Figure 46 the decrease of all substrate signals (Si 2p, Si 2s, O 1s and O KLL) as well as the increase of the Cu signals (Cu 2p, Cu 2s and Cu LMM) can be clearly recognized.

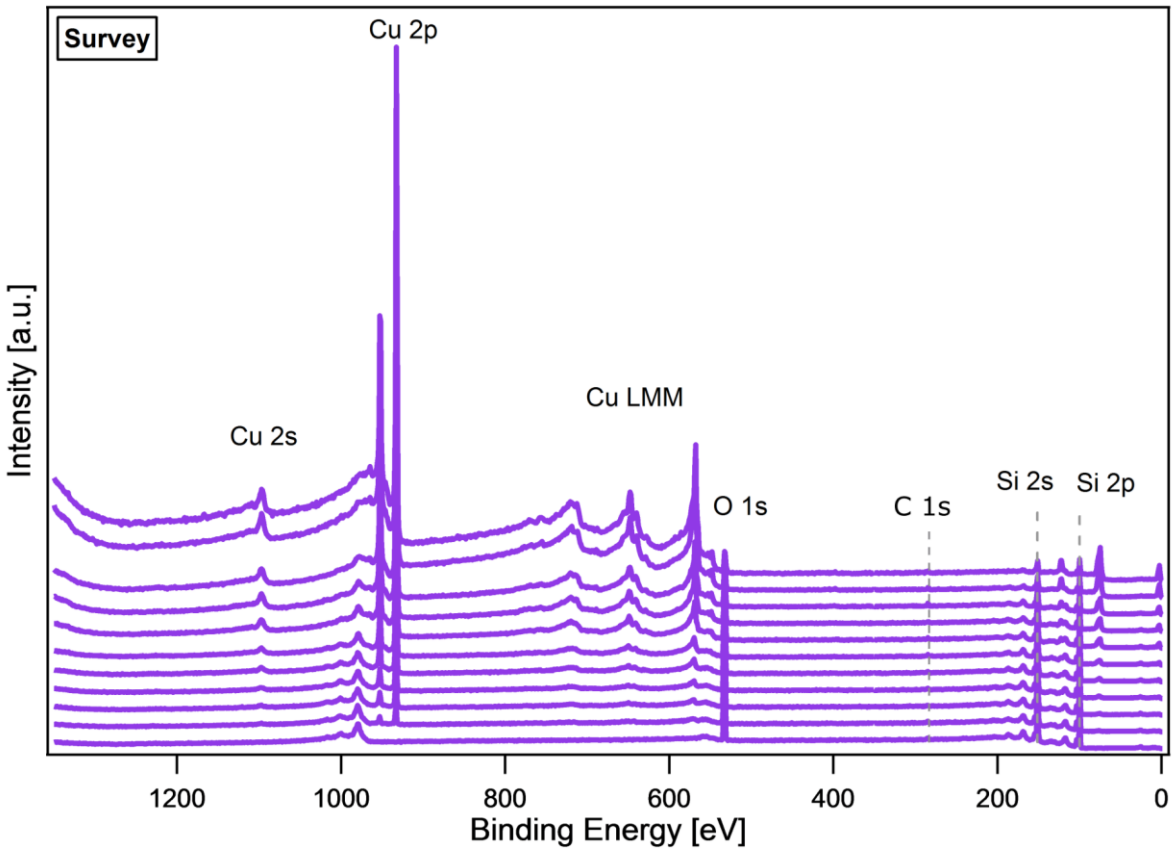

Figure 46: Development of the XP survey spectra of the p-Si | µcn-Si | therm. SiO_2 | Cu contact during the interface experiment. The measurement of the bare p-Si | µcn-Si | therm. SiO_2 substrate is displayed at the bottom of the diagram while the last deposition step at the top shows the final measurement of a relatively thick Cu layer.

The corresponding XP detail spectra showing the development of the Si 2p, O 1s and Cu 2p emission lines are displayed in Figure 47. The maximum of the Si $2p_{3/2}$ emission line of the bare p-Si | µcn-Si | therm. SiO_2 substrate can be evaluated at a binding energy of 99.84 eV, which is the same value as

measured for the bare p-Si | µcn-Si | nat. SiO_2 substrate. As expected, the SiO_2 contribution in form of a peak in the Si 2p emission line is available. The position of this peak at 103.58 eV does not differ from the position of the SiO_2 peak for the p-Si | µcn-Si | nat. SiO_2 substrate. The calculated initial thickness of the thermally grown SiO_2 layer is 9 Å, which is negligibly thinner compared to the native SiO_2 (10 Å). Also the initial maximum of the O 1s emission line at 533.10 eV is equal to the determined value in case of the native SiO_2 sample. This correspondence already indicates that the initial energy band structure before contact formation with Cu will be equal independent on the preparation of the SiO_2 layer. After depositing 2 Å Cu, the initial Si 2p and O 1s spectra do not remarkably change. However, a very weak intensity of the Cu 2p emission line can be detected. When depositing another 2 Å Cu the position of the Si $2p_{3/2}$ emission line shifts from 99.84 eV to 99.83 eV. However, this difference is too small to be informative as it lies within the inaccuracy of the measurement equipment. The shape is still very similar to the initial Si 2p spectrum. The same can be concluded for the O 1s emission line. While the third Cu deposition (7 Å) does not cause any changes in the Si 2p and O 1s emission line, the position of the Si $2p_{3/2}$ maximum is minimally shifted to 99.82 eV with the fourth deposition step when the Cu film reaches a film thickness of 10 Å. Again this small shift could also be an inaccuracy of the XPS. At that point also the O 1s emission line slowly starts to shift to lower binding energies.

With the following deposition step the measured detail spectra remain the same as before, but when the Cu reaches a film thickness of 15 Å, the Si $2p_{3/2}$ emission line is detected at 99.81 eV, which means a total shift of 0.03 eV. Similar to the p-Si | µcn-Si sample with native SiO_2 where no shift could be observed, the shift of the position of the Si $2p_{3/2}$ emission line in this system is negligible.

As for the p-Si | µcn-Si sample with native SiO_2 a shift can be observed in the maximum position of the O 1s emission line, which is larger than the shift in the Si 2p line. This effect was assigned to a stoichiometry change of the oxygen in the silicon substrate during the first deposition steps. Nevertheless, the Cu LMM Auger line corresponding to a Cu film thickness of 7 Å, which is shown in the appendix A 7 already contains features, which prove the metallic character of the Cu film. However the, maximum position can still be detected at a binding energy of 570 eV, which may also corresponds to Cu_2O (Cu^0: 568 eV), a shoulder already arises, which is characteristic for metallic Cu.[130]

At that point of the experiment the Cu 2p emission line can be clearly identified and the signal becomes more intense. The following three deposition steps, which correspond to a Cu film thickness of 25 Å, 45 Å and 80 Å, do not further change the position of the Si $2p_{3/2}$ emission line at 99.81 eV as well as the position of the O 1s emission line at 532.58 eV. However, each deposition step reduces the intensity of the Si 2p and O 1s emission lines while the Cu 2p line becomes more intense. Here, the maximum of the Cu $2p_{3/2}$ emission line can be detected at a binding energy of 932.64 eV. When having a closer look at the O 1s emission line it can be noticed that the emission line becomes slightly asymmetric. However, a distinct appearance of a satellite cannot be assured.

With the final deposition step the Cu film reaches a thickness of 100 Å. With that the Si 2p emission line has completely vanished. The O 1s emission line can still be detected at 532.58 eV with reduced intensity. A very small additional line emerges at around 529 eV leading to the assumption that a surface reaction has taken place as already observed for the p-Si | µcn-Si | nat. SiO_2 | Cu sample. However, less oxygen is involved in a chemical reaction to form Cu oxide. The Cu $2p_{3/2}$ emission line still has its maximum at 932.64 eV. Because of the shape of the Cu 2p emission line as well as the Cu LMM Auger line, which is shown in the appendix A 7 the formation of mainly metallic Cu can be concluded.

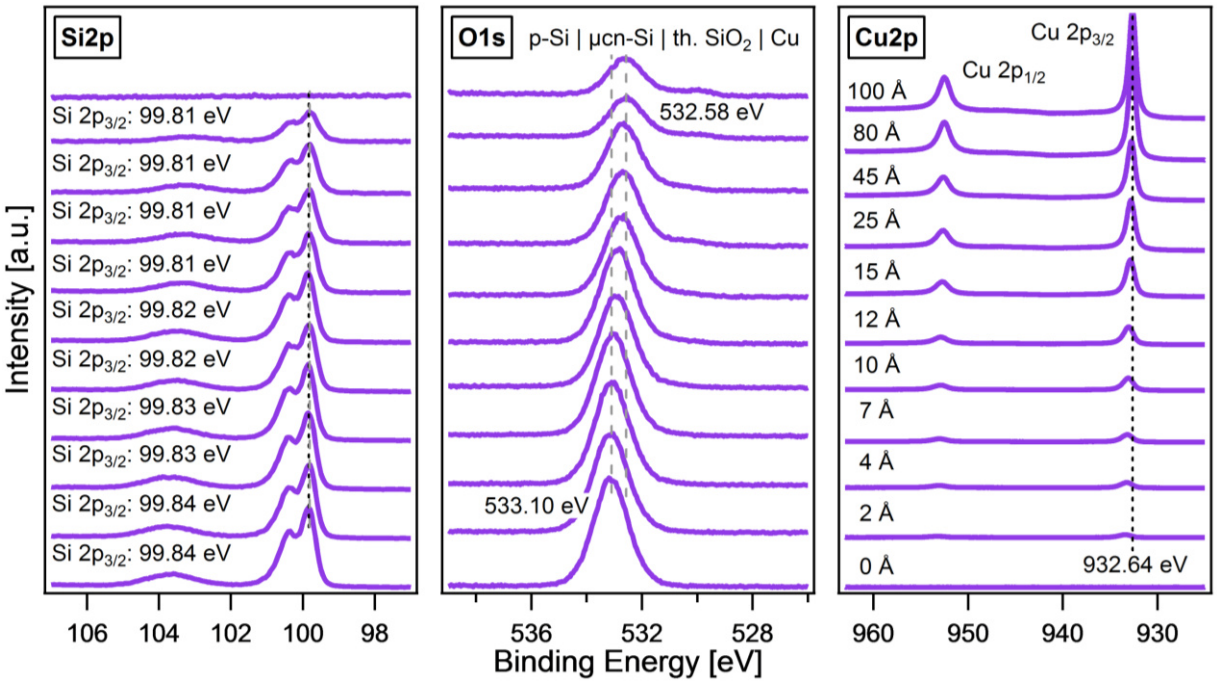

Figure 47: Development of the Si 2p, O 1s and Cu 2p detail spectra of the p-Si | µcn-Si | therm. SiO_2 | Cu contact during the interface experiment. The measurement of the bare p-Si | µcn-Si | therm. SiO_2 substrate is displayed at the bottom of the diagram while the last deposition step at the top shows the final measurement of a relatively thick Cu layer.

To sketch the energy band diagrams of the different p-Si | µcn-Si | Cu contacts, the above analyzed positions of the Si $2p_{3/2}$ emission lines of the corresponding spectra need to be evaluated. Table 4 is an extension of table 2 and lists all values of the position of the Si $2p_{3/2}$ emission line before and after contact formation with Cu as well as the resulting shifts for all pn^+-Si | Cu and p-Si | µcn-Si | Cu model systems. It can be noted that the Cu contact formation less impacts the electronic structure at the p-Si | µcn-Si | SiO_2 | Cu interface. Here, it seems to be negligible whether the SiO_2 layer has native character or is thermally grown. Furthermore, it is obvious that the H-terminated surfaces are strongly affected by the Cu deposition resulting in an undesired band lineup.

The schematical drawings of the derived energy band diagrams are displayed in Figure 48. Here, Figure 48 a) shows the situation before contact formation for the p-Si | µcn-Si | SiO_2, which is equal for the

native and the thermal SiO_2 passivation layer. The energy band gap of 1.12 eV, the distance from the valance band maximum to the Fermi level in the p-layer (0.2 eV) as well as the distance of the conduction band minimum to the Fermi level in the n-layer (0.03 eV) are equal to the pn^+-Si junction as the doping concentrations in the p and the n layer are the same in the p-Si | µcn-Si junction ($p = 10^{16}$ cm^{-3}, $n = 10^{19}$ cm^{-3}). At the surface the bands are slightly bended downwards (0.01 eV), resulting in a distance from the conduction band minimum to the Fermi level of 0.02 eV, which lies within the measurement inaccuracy of the XPS. Therefore, this electronic structure can be assumed as flat band situation. In case of the p-Si | µcn-Si sample with the native SiO_2, this electronic structure does not change when being in contact with Cu as it can be seen in Figure 48 b). For the p-Si | µcn-Si | Cu sample with the thermally grown SiO_2 interlayer, an upward band bending of 0.02 eV at the interface can be observed, which is illustrated in Figure 48 c). However, the energy band diagrams of both samples can be assumed to be identical as the barrier heights are negligible. Therefore, it can be concluded that both systems with passivating interlayers (native and thermal SiO_2) seem to be beneficial in terms of electron transport across the interface.

As shown in Figure 48 d) the H-terminated p-Si | µcn-Si surface exhibits an negligible upward band bending of 0.01 eV before contact, which can be considered as flat band situation. After contact formation this initial flat band situation changes and results in an energy barrier of 0.55 eV as shown in Figure 48 e). Compared to the energy band diagrams of the samples with additional SiO_2 layer, it can be assumed that the huge energetic barrier at the interface may impact the electrochemical properties of the sample due to unfavorable electron transport across the interface.

It should be mentioned that Figure 48 does not consider additional intermediate Cu_2O layer. As for the pn^+-Si | nat./ therm. SiO_2 | Cu samples, the deposited metallic Cu partially reacts with SiO_2 to Cu_2O. However, due to the mainly metallic character of the film, this effect is not further investigated.

Table 4: Overview of the position of the Si $2p_{3/2}$ emission line before and after contact formation for the pn^+-Si and the p-Si | µcn-Si model systems with different surface terminations.

Model system	**Position of Si $2p_{3/2}$ emission line**		
	before contact	after contact	resulting shift
pn^+-Si | nat. SiO_2 | Cu	99.77 eV	99.48 eV	0.29 eV
pn^+-Si:H | Cu	99.82 eV	99.38 eV	0.44 eV
pn^+-Si | therm. SiO_2 | Cu	99.77 eV	99.56 eV	0.21 eV
p-Si | µcn-Si | nat. SiO_2 | Cu	99.84 eV	99.84 eV	0.00 eV

p-Si | µcn-Si:H | Cu	99.82 eV	99.28 eV	0.54 eV
p-Si | µcn-Si | therm. SiO_2 | Cu	99.84 eV	99.81 eV	0.03 eV

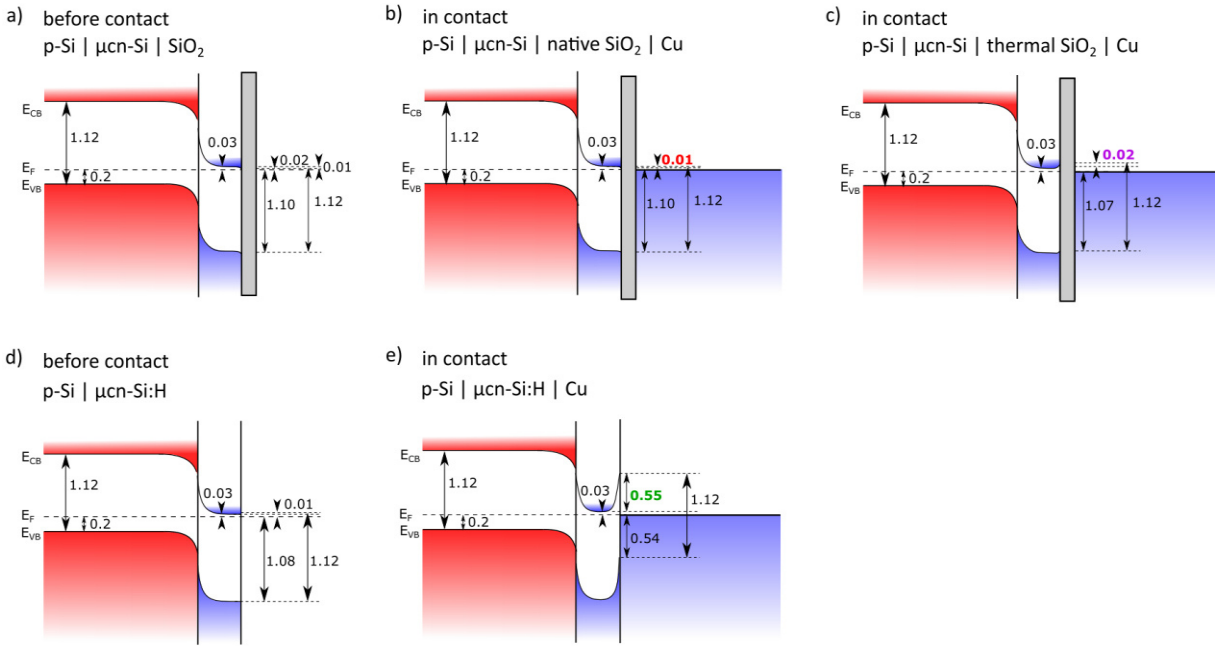

Figure 48: Energy band diagrams before and after contact formation. a) p-Si | µcn-Si | SiO_2 before contact formation with almost flat band situation, b) p-Si | µcn-Si | nat. SiO_2 | Cu with a slight downward band bending of 0.01 eV, c) p-Si | µcn-Si | therm. SiO_2 | Cu with an upward band bending of 0.02 eV, d) p-Si | µcn-Si:H before contact formation with almost flat band situation and e) p-Si | µcn-Si:H | Cu with a high upward band bending of 0.55 eV.

5.3.2 Electrochemistry

In order to analyze the impact of the energy band alignment at the interface on the photoelectrochemical performance, CV measurements were performed. These experiments were first performed without nitrogen gas bubbling. From the height of the energy barriers at the interfaces of the different p-Si | µcn-Si | Cu systems it can be assumed that the photoelectrochemical performance will be beneficial for the p-Si | µcn-Si | nat. SiO_2 | Cu and the p-Si | µcn-Si | therm. SiO_2 | Cu sample as in both cases the energy barrier is very small (p-Si | µcn-Si | nat. SiO_2 | Cu: 0.01 eV, p-Si | µcn-Si | therm. SiO_2 | Cu: 0.02 eV). In contrast, the p-Si | µcn-Si:H | Cu contact exhibits a band bending at the interface of 0.55 eV, which leads to the assumption that the photoelectrochemical performance will be reduced compared to the samples with additional SiO_2 passivation layers. However, Figure 49 proves that the assumption is not completely true.

Figure 49 shows the CV measurements of the three p-Si | µcn-Si | Cu samples with different surface terminations. The measurements have been performed in the dark and under an illumination of 180 W/m^2 with $\lambda = 625$ nm. Contrary to the pn$^+$-Si | Cu samples the total saturation current density under

illumination differs from sample to sample. While the p-Si | µcn-Si | nat. SiO_2 | Cu sample reaches a maximum current density of around -6.2 V mA/cm^2, the current density of the H-terminated sample saturates at -5.5 mA/cm^2 and contrary to expectations the p-Si | µcn-Si | therm. SiO_2 | Cu sample only reaches a current density of -4.5 mA/cm^2. Furthermore, the onset potential is shifted to more negative values. To obtain -2 mA/cm^2 an applied potential of -0.4 V (vs. RHE) is necessary in case of the p-Si | µcn-Si | nat. SiO_2 | Cu and the p-Si | µcn-Si:H | Cu sample, while -0.8 V need to be applied for the p-Si | µcn-Si | therm. SiO_2 | Cu sample. That the hydrogen terminated sample reaches comparable good photoelectrochemical results is surprising as the electronic band banding at the interface is much larger compared to the samples with additional SiO_2 as passivating interlayer. A possible explanation could be that the electrons are able to tunnel through the very thin barrier at the interface so that the electron transport is improved, which in turn improves the photoelectrochemical activity.

In case of the p-Si | µcn-Si | therm. SiO_2 | Cu sample the photoelectrochemical activity is comparably low. Therefore, it is important to discuss the possible reason for this behavior. When reconsidering all different process steps the sample had to undergo during the performed experiments, it is conspicuous that the sample was held in an Ar/O gas mixture at 800°C to grow the thermal SiO_2 layer. In contrast, the temperature to fabricate a p-Si | µcn-Si wafer is only 220°C during the PECVD process. The enormous heat, which is necessary to grow the thermal SiO_2 damages the microcrystalline pn-junction and therefore, drastically reduces its performance.

Although, the p-Si | µcn-Si | nat. SiO_2 | Cu sample shows no barrier at the interface (0.01 eV) compared to the p-Si | µcn-Si:H | Cu sample with an upward band bending of 0.55 eV, the necessary potential to obtain -2 mA/cm^2 is -0.4 V for both samples. Nevertheless, the p-Si | µcn-Si | nat. SiO_2 | Cu sample reaches a saturation current density of -6.2 mA/cm^2, while the saturation current density of the p-Si | µcn-Si:H | Cu sample is only -5.5 mA/cm^2, which proves losses in the photoelectrochemical performance if the energy barrier at the surface is increased.

The dark currents are even lower (-0.1 mA/cm^2 to -0.6 mA/cm^2) compared to the pn$^+$-Si | Cu samples (-0.7 mA/cm^2 to -1.1 mA/cm^2), which confirms the expected behavior for such pn-Si junctions. Table 5 gives an overview of the necessary potentials to obtain -2 mA/cm^2, the saturation current density under illumination ($J_{sat,\ illum}$) and in the dark ($J_{sat,\ dark}$) as well as the corresponding energy barrier at the interface($eV_{b,n}$) for different p-Si | µcn-Si | Cu model systems in comparison with the pn$^+$-Si | Cu and p-Si | µcn-Si | Cu samples.

Table 5: Overview of the necessary potential to obtain -2 mA/cm², the saturation current density under illumination ($J_{sat,\ illum}$) and in the dark ($J_{sat,\ dark}$) as well as the corresponding energy barrier at the interface ($eV_{b,n}$) for different pn⁺-Si | Cu and p-Si | µcn-Si | Cu model systems.

Model System	potential to reach -2 mA/cm² [V vs. RHE]	$J_{sat,illum}$ [mA/cm²]	$J_{sat.dark}$ [mA/cm²]	$eV_{b,n}$ [eV]
pn⁺-Si | nat. SiO_2 | Cu	-0.6	-6.0	-1.1	+0.35
pn⁺-Si:H | Cu	-0.7	-6.0	-0.7	+0.45
pn⁺-Si | therm. SiO_2 | Cu	-0.4	-5.7	-0.7	+0.27
p-Si | µcn-Si | nat. SiO_2 | Cu	-0.4	-6.2	-0.6	+0.01
p-Si | µcn-Si:H | Cu	-0.4	-5.5	-0.1	+0.55
p-Si | µcn-Si | therm. SiO_2 | Cu	-0.8	-4.5	-0.1	+0.02

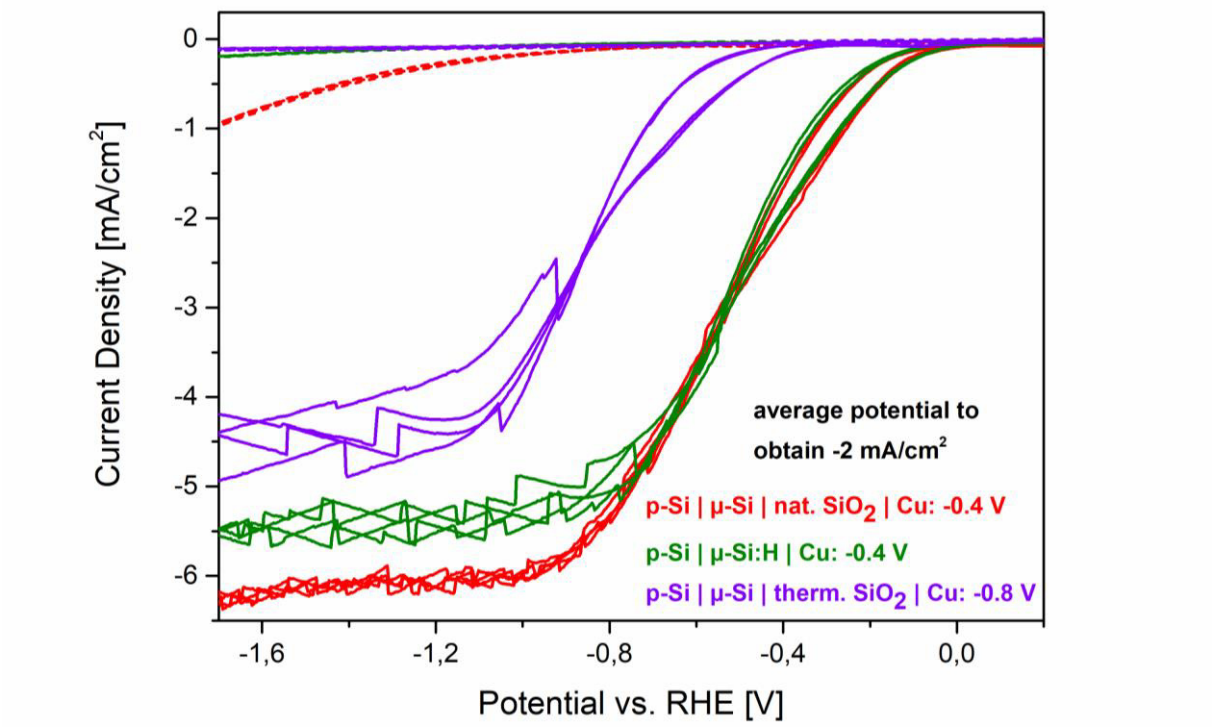

Figure 49: Comparison of the cyclic voltammetry behavior of the three different model systems: p-Si | µcn-Si | nat. SiO_2 | Cu (red), p-Si | µcn-Si:H | Cu (green) and p-Si | µcn-Si | therm. SiO_2 | Cu (purple) in the dark and under an illumination of 180 W/m² with λ = 625 nm in 0.3 M $KHCO_3$. Solid lines: EC behavior under illumination. Dashed lines: EC behavior in the dark. The measurements were performed without nitrogen gas bubbling.

5.3.3 Characterization after Electrochemistry

To characterize the composition of the Cu thin films after performing the photoelectrochemical measurements (without nitrogen gas bubbling) XPS and SEM analyses were done. Figure 50 shows the relevant XP detail spectra of the p-Si | µcn-Si | Cu samples with different surface terminations (red: native SiO_2, green: H-termination and purple: thermal SiO_2). From the Cu 2p spectra it can be noted that the shape differs from the measurement directly after deposition as the spectra do not remain flat within the Cu 2p multiplet splitting. Instead, a quite intense satellite can be detected at around 945 eV for all three samples, which indicates the formation of $Cu(OH)_2$. The same was already observed for the pn^+-Si | Cu samples.

It is also noticeable that, the intensity of the Cu 2p emission line of p-Si | µcn-Si | therm. SiO_2 | Cu sample is reduced compared to the p-Si | µcn-Si | nat. SiO_2 | Cu and the p-Si | µcn-Si:H | Cu sample. This indicated that the Cu film thickness is reduced during performing the electrochemical measurements in case of the sample with thermal SiO_2. The modified thickness was calculated by using the XPS substrate: film intensity ratio as explained in chapter 4.5. While the Cu film of the samples with native SiO_2 and hydrogen termination are still comparably large (p-Si | µcn-Si | nat. SiO_2 | Cu: 65 Å, p-Si | µcn-Si:H | Cu: 50 Å), the Cu film of the sample with thermally grown SiO_2 is reduced to about 10 Å. This phenomenon is unexpected as the initial Cu film thicknesses were comparable (90 – 100 Å) for all three samples and the experimental procedure was the same for each sample. A reduced adhesion of the Cu film on thermally grown SiO_2 cannot be assumed and was also not observed in case of the pn^+-Si | therm. SiO_2 | Cu sample.

In general the whole spectra seem to be shifted to slightly higher binding energies. A similar phenomenon was already observed in case of the pn^+-Si | Cu samples. A possible explanation is charging of the samples. Here, the position of the Cu $2p_{3/2}$ emission line is shifted to much higher binding energies compared to the initial Cu film deposition (native SiO_2: 932.62 eV → 937.20 eV, H-termination: 932.64 eV → 936.95 eV and thermal SiO_2: 932.64 eV → 936.33 eV). A shift to slightly higher binding energies can be explained by the formation of $Cu(OH)_2$.[121][122][123] However, the measured shifts must contain charging effects as the binding energy values are too high. But still it can be conducted from the strong satellite in the Cu 2p region that $Cu(OH)_2$ has formed on all sample surfaces as it was also the case for the pn^+-Si | C samples.

In addition to the measurements of the pn^+-Si | Cu samples SiO_2 seems to be the dominant contribution of the O 1s emission. Nevertheless, these spectra are also shifted, which makes a clear statement more difficult. Moreover, the O 1s emission lines show an asymmetry, which could also be an indication of the formation of C-O species.[124][125] The position of the C 1s emission lines are also shifted to higher binding energies for all three p-Si | µcn-Si | Cu samples, which can be correlated to charging effects, the used electrolyte or the formation of CO_2 reduction products. Most likely the measured C emissions are

due to C-H and C-C.[94][126] Above 289 eV a week signal can also be detected for all three samples, which can correspond to carbonates.[126] Again it cannot be stated whether these bonds were formed due to the CO_2 reduction or because of the presence of $KHCO_3$.

As for the pn^+-Si | Cu samples the SiO_2 contribution is clearly detectable in the Si 2p region for all three p-Si | µcn-Si | Cu samples. In case of the p-Si | µcn-Si | therm. SiO_2 | Cu sample the Cu film is definitively thinner compared to the p-Si | µcn-Si:H | Cu and p-Si | µcn-Si | nat. SiO_2 | Cu sample as here the Si $2p_{3/2}$ emission line at 99.60 eV can still be observed. In addition, the corresponding intensity of the Cu 2p emission line is strongly reduced in case of the p-Si | µcn-Si | therm. SiO_2 | Cu sample as already mentioned above. The same phenomenon has been observed for the pn^+-Si | nat. SiO_2 | Cu sample.

It can be concluded that after photoelectrochemical measurements in 0.3 M $KHCO_3$ the initial metallic Cu catalyst became thinner and most likely the surface has transformed to $Cu(OH)_2$. Moreover, the underlying Si substrates were oxidized for all three samples. C-C and C-H bonds could be detected at all surfaces. Furthermore, it can be assumed that small amounts of C-O were formed in all cases.

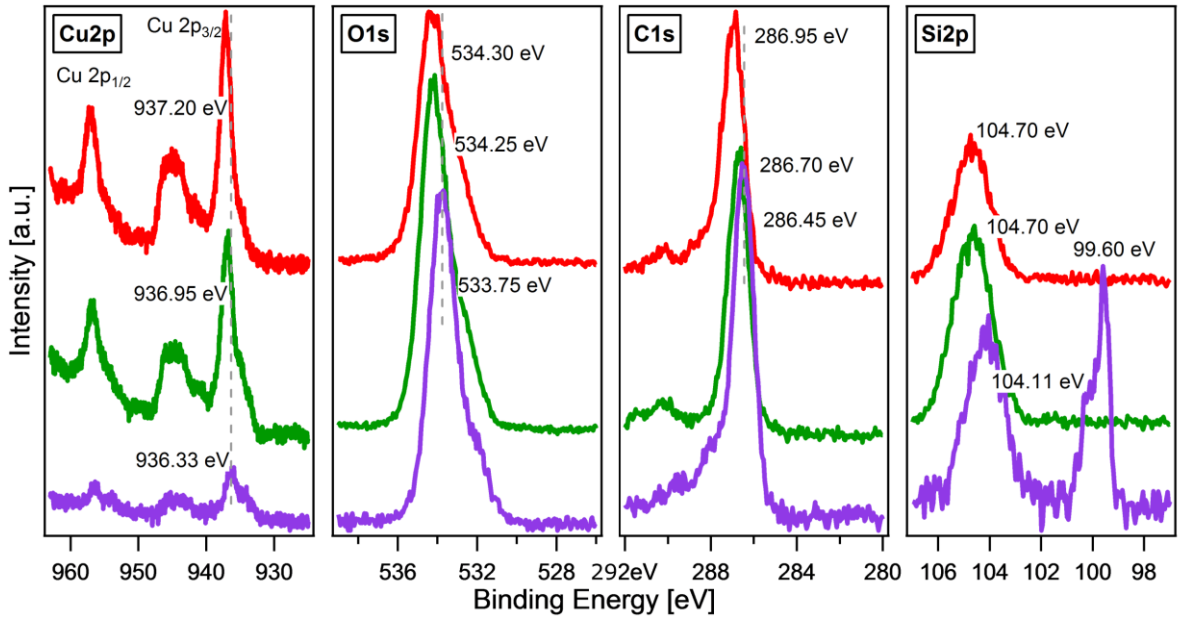

Figure 50: XP detail spectra of the p-Si | µcn-Si | Cu samples with different surface terminations showing the Cu 2p, O 1s, C 1s and Si 2p emission lines after performing cyclic voltammetry measurements (red: native SiO_2, green: H-termination and purple: thermal SiO_2).

The positive effect of bubbling with nitrogen gas during EC was already investigated when analyzing the XP spectra after EC of the pn^+-Si | nat. SiO_2 | Cu sample. Therefore, this measurement was exemplary repeated for the p-Si | µcn-Si | nat. SiO_2 | Cu sample. The resulting Cu 2p, O 1s, C 1s and Si 2p emission lines are shown in Figure 51. From the Cu 2p emission line it becomes very clear that the bubbling of nitrogen prevents the transformation of metallic Cu to $Cu(OH)_2$, which can be assumed due to the missing satellite within the Cu 2p splitting. Nevertheless, the position of the Cu $2p_{3/2}$ emission line at

933.60 eV could also indicate the presence of CuO. But CuO also exhibits a strong satellite in the Cu 2p region. As this in not the case in the measured spectrum with nitrogen gas bubbling, the formation of $Cu(OH)_2$ as well as CuO can be excluded. Therefore, the Cu 2p emission line indicates that the Cu film is mainly metallic.

Furthermore, the whole spectrum is strongly shifted to higher binding energies when no nitrogen gas was bubbled during EC. This was already discussed before and assigned to charging effects. The sample, which was measured after performing electrochemical measurements while nitrogen gas bubbling does not seem to be charged as the peak positions can be detected at expected binding energies. While the position of the O 1s emission line is shifted to high binding energies when no nitrogen gas was bubbled during EC, the position of the O 1s emission line in case of nitrogen gas bubbling can be clearly identified as SiO_2.

The formation of C-H and C-C bonds can be assumed from the maximum position of the C 1s emission line at 285.70 eV. Moreover, it can be noted that at binding energies between 286 - 290 eV the emission line contains more components, which can be assigned to a variety of carbon species, such as phenols, carbonyl groups, carboxyl groups and alcohols.[94][131] The presence of these signals could be interpreted as CO_2 reduction products. However, the species could also be assigned to the used electrolyte, which is even more likely.

The Si 2p emission line is different for the differently treated samples. It might be surprising that the sample without nitrogen gas bubbling does not show any pure Si signal but only SiO_2 contribution at 104.70 eV. Nevertheless, this effects is reasonable as the Cu film thickness is further reduced in case of nitrogen gas bubbling, because of an increased movement of the electrolyte solution, which results in an ablation of the film until the film thickness of the Cu is reduced to approximately 10 Å. Without nitrogen gas bubbling the remaining Cu film thickness was about 65 Å.

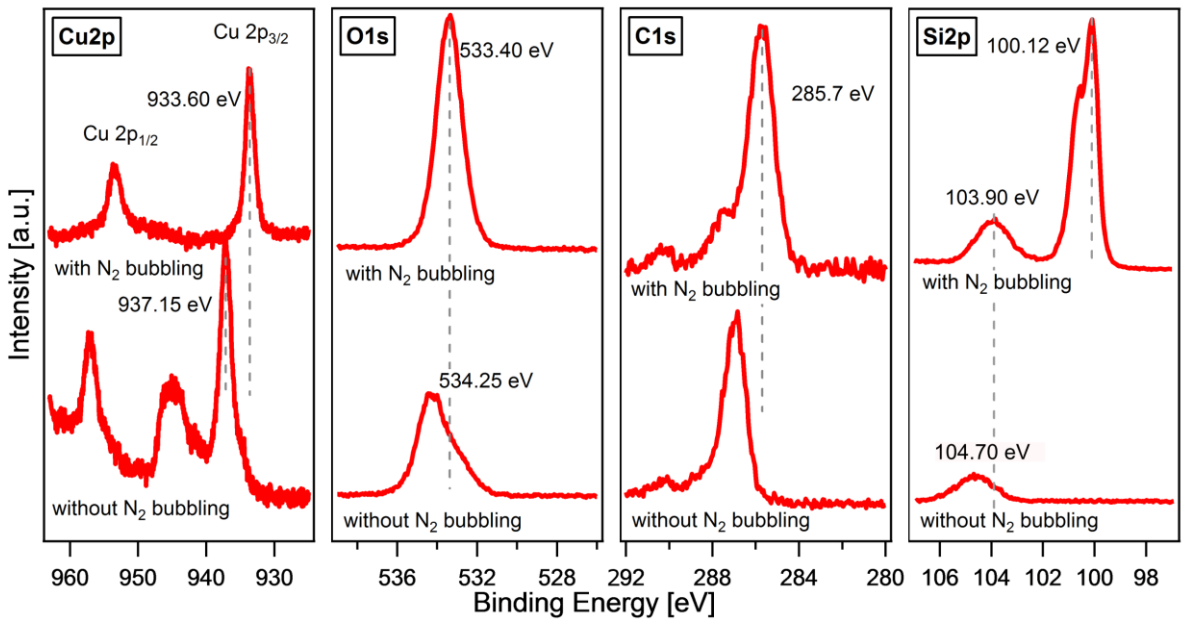

Figure 51: XP detail spectra of the p-Si | µcn-Si | nat. SiO_2 | Cu sample showing the effect of N_2 gas bubbling during performing cyclic voltammetry measurements.

The SEM images in Figure 52 and Figure 53 show the surfaces of a p-Si | µcn-Si | Cu sample before and after EC with a magnification of 1000 and 10000, respectively. The deposited Cu film is very flat and homogeneous, which is evident from Figure 52 a). After photoelectrochemistry the Cu film is damaged as shown in Figure 53 b). The same effect was observed for the pn^+-Si | Cu sample. Again, the surface termination also does not play a role. The more detailed images in Figure 53 show the cross section of the sample. Similar to the pn^+-Si | Cu sample it can be seen that the Cu film is slightly detached from the Si surface and bubbles have formed beneath the Cu film. Nevertheless, the Cu film seems to be mostly intact without any holes or cracks. However, the film is not as smooth as before photoelectrochemistry.

From the XPS and SEM investigations it can be concluded that the Cu film is mostly stable during the photoelectrochemical performance. But, the stoichiometry of the film may change depending on whether EC is performed with or without bubbling of nitrogen gas. Furthermore, it could be shown that bubbling with nitrogen gas can result in a reduced Cu film thickness due to the ablation caused by the movement of the bubbles in the electrolyte. Similar observations were made for the pn^+-Si | Cu samples with different surface terminations.

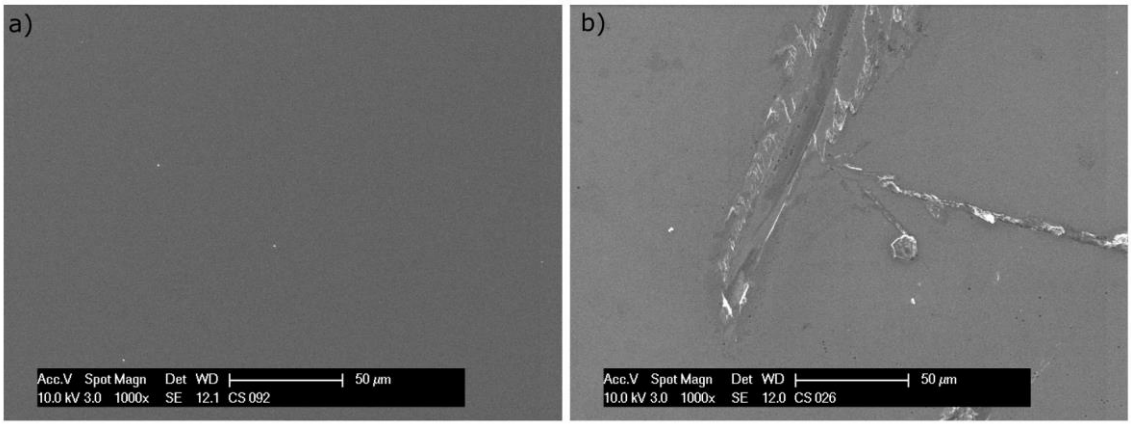

Figure 52: SEM images of p-Si | µcn-Si | Cu samples with a magnification of 1000, a) before photoelectrochemistry and b) after photoelectrochemistry.

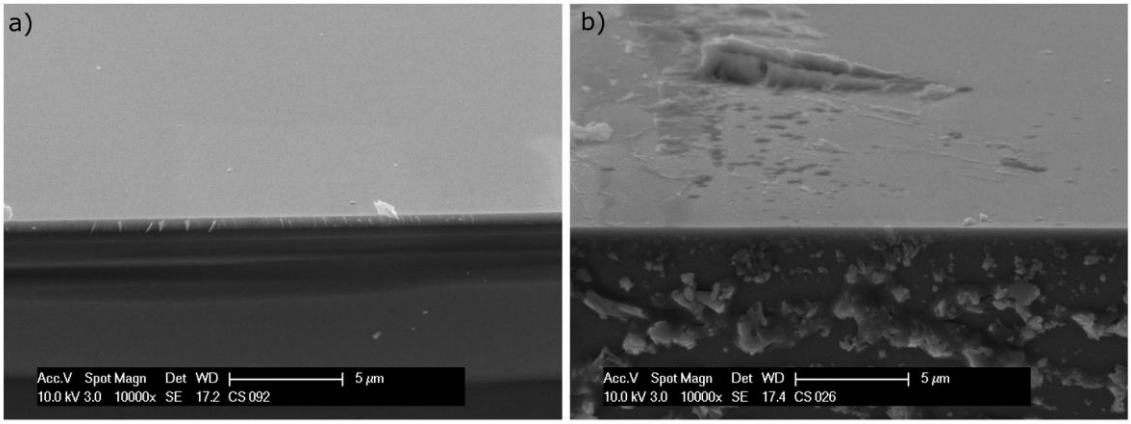

Figure 53: SEM images of the cross section of the p-Si | µcn-Si | Cu samples with a magnification of 10000, a) before photoelectrochemistry and b) after photoelectrochemistry.

5.4 pin-Si | Cu Interface

The next step of a systematical understanding of Si | Cu interfaces is the investigation of µc-Si:H solar cells with p-i-n structure (pin-Si) in contact to the Cu catalyst. As previous investigations of pn^+-Si | Cu and p-Si | µcn-Si | Cu systems have shown that the samples with native SiO_2 as Si surface termination lead to reasonable results concerning energy band alignment as well as photoelectrochemical performance, native SiO_2 has also been chosen as surface termination for the pin-Si | Cu interface studies. Furthermore, it was shown that the high temperatures, which are necessary to thermally grow SiO_2 lead to damage within the Si structure, native SiO_2 is used instead.

5.4.1 Energy Band Alignment

Analogous to the previously examined Si | Cu model systems, XP survey spectra were measured first in order to prove whether the sample is free of contaminations. Figure 54 shows the corresponding development of the XP survey spectra of the pin-Si | nat. SiO_2 | Cu contact during the interface experiment. At 285 eV a very small amount of carbon can be detected, which vanishes with each deposition step. Apart from that the sample is not contaminated with other foreign species. The initial signals of the Si 2p, Si 2s, O 1s emission lines and O KLL Auger line decrease with ongoing interface experiment, while the Cu 2s, Cu 2p and Cu LMM signals corresponding to the deposited film increase until they are predominant. The Cu 3s, Cu 3p and Cu 3d emission lines at 140 eV, 90 eV and 10 eV are not considered for the experimental results.

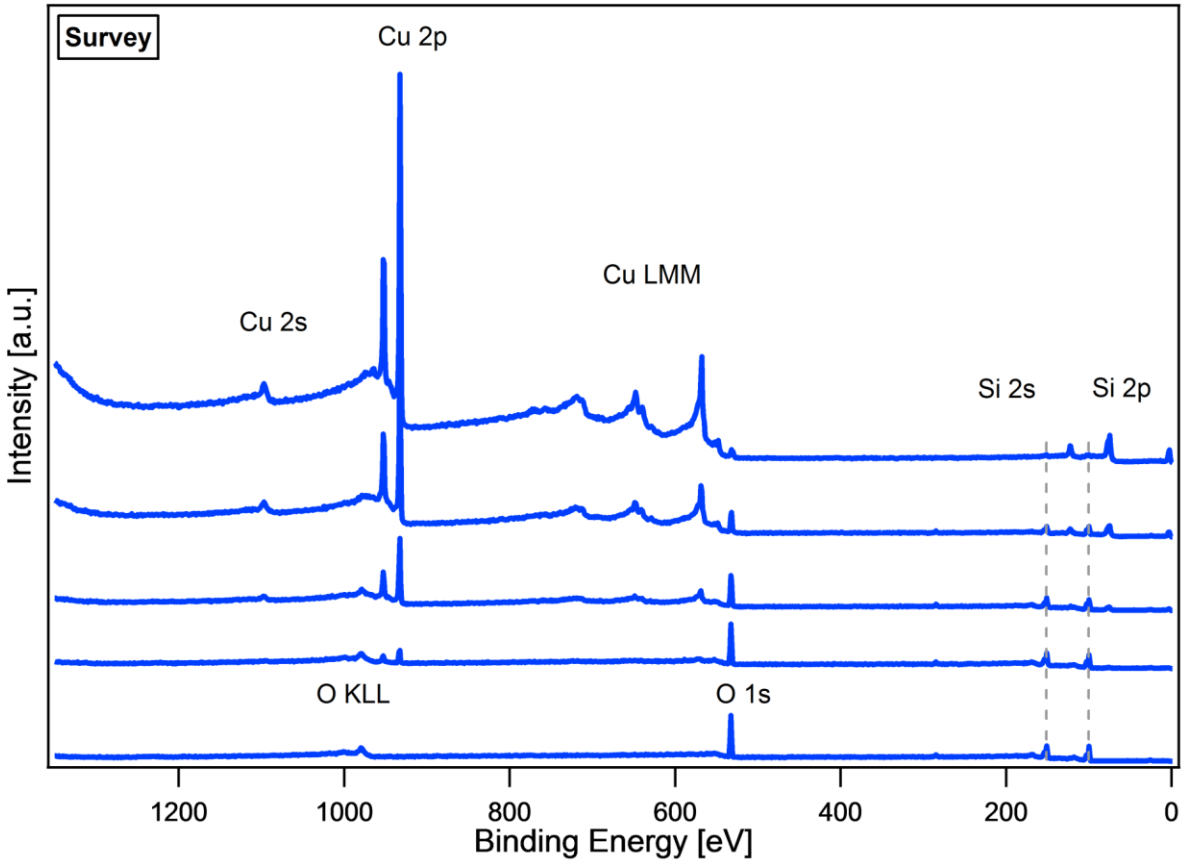

Figure 54: Development of the XP survey spectra of the pin-Si | nat. SiO_2 | Cu contact during the interface experiment. The measurement of the bare pin-Si | nat. SiO_2 substrate is displayed at the bottom of the diagram while the last deposition step at the top shows the final measurement of a relatively thick Cu layer.

For a more detailed analysis XP detail spectra were measured for the regions of the Si 2p, O 1s and Cu 2p emission lines, which is shown in Figure 55. Here, the bottom spectra present the measurement of the bare substrate, while the top spectra were measured after the last Cu deposition. The initial maximum of the Si $2p_{3/2}$ emission line can be detected at 99.82 eV, which agrees with the previously

investigated pn^+-Si and p-Si | µcn-Si substrates. The SiO_2 emission is present at around 103 eV. The presence of SiO_2 is also proven by the position of the O 1s emission line at 532.90 eV.[94]

After the first deposition step the Cu film reaches a layer thickness of around 5 Å. The contact formation with Cu leads to a small shift of the Si $2p_{3/2}$ as well as the O 1s position. This shift increases further as soon as the Cu film reaches thicknesses of 15 Å and 45 Å after the second and third deposition step, respectively. From the shape of the corresponding Cu LMM Auger line, which is shown in the appendix A 8 it can already be assumed that the deposited Cu layer exhibits mainly metallic character. However, a signal at 529.87 eV can be detected within the region of the O 1s emission, which indicates the formation of a copper oxide compound, which can be assigned to Cu_2O. This could already be observed in case of pn^+-Si | Cu and p-Si | µcn-Si | Cu model systems. After the last deposition step a 90 Å thick Cu layer covers the pin-Si solar cell. The signal within the Cu $2p_{3/2}$ and Cu $2p_{1/2}$ emission lines remains flat, confirming the formation of metallic Cu. At that state the Si 2p signal is drastically decreased and the maximum position of 99.70 eV has not changed anymore compared to the previous deposition step. Small amounts of Cu oxide can be proven by the O 1s emission at 529.87 eV. Nevertheless, the shape of the Cu LMM Auger line of the last deposition step clearly indicates the formation of mainly metallic Cu.

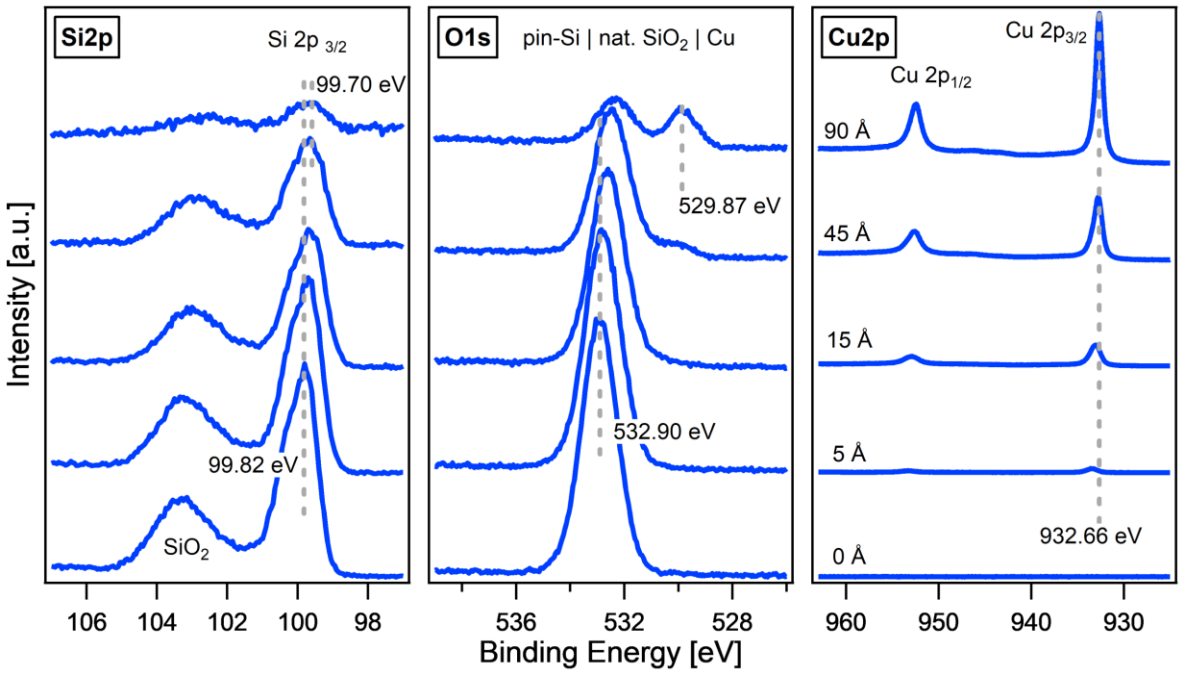

Figure 55: Development of the Si 2p, O 1s and Cu 2p detail spectra of the pin-Si | nat. SiO_2 | Cu contact during the interface experiment. The measurement of the bare pin-Si | nat. SiO_2 substrate is displayed at the bottom of the diagram while the last deposition step at the top shows the final measurement of a relatively thick Cu layer.

With the results from the interface experiment the energy band diagram of the pin-Si | nat. SiO_2 | Cu contact can be calculated, which is sketched in Figure 56. Figure 56 a) shows the situation at the surface before contact formation with Cu. Compared to the previously investigated band alignments of the p-Si | Cu, pn^+-Si | Cu and p-Si | µcn-Si | Cu contacts, it can be noticed that the dimensions of the p- and n-layer are different, which comes from different layer thicknesses as explained in chapter 2.3.

Before contact formation a flat band situation is given at the surface. After the deposition of Cu a band bending of 0.13 eV occurs. Table 6 gives an overview of the positions of the Si $2p_{3/2}$ emission lines before and after contact formation for the pn^+-Si, p-Si | µcn-Si model systems with different surface terminations as well the pin-Si | nat. SiO_2 | Cu contact.

Table 6: Overview of the position of the Si $2p_{3/2}$ emission line before and after contact formation for the pn^+-Si, p-Si | µcn-Si model systems with different surface terminations as well the pin-Si | nat. SiO_2 | Cu contact.

Model system	**Position of Si $2p_{3/2}$ emission line**		
	before contact	after contact	resulting shift
pn^+-Si | nat. SiO_2 | Cu	99.77 eV	99.48 eV	0.29 eV
pn^+-Si:H | Cu	99.82 eV	99.38 eV	0.44 eV
pn^+-Si | therm. SiO_2 | Cu	99.77 eV	99.56 eV	0.21 eV
p-Si | µcn-Si | nat. SiO_2 | Cu	99.84 eV	99.84 eV	0.00 eV
p-Si | µcn-Si:H | Cu	99.82 eV	99.28 eV	0.54 eV
p-Si | µcn-Si | therm. SiO_2 | Cu	99.84 eV	99.81 eV	0.03 eV
pin-Si | nat. SiO_2 | Cu	99.82 eV	99.70 eV	0.12 eV

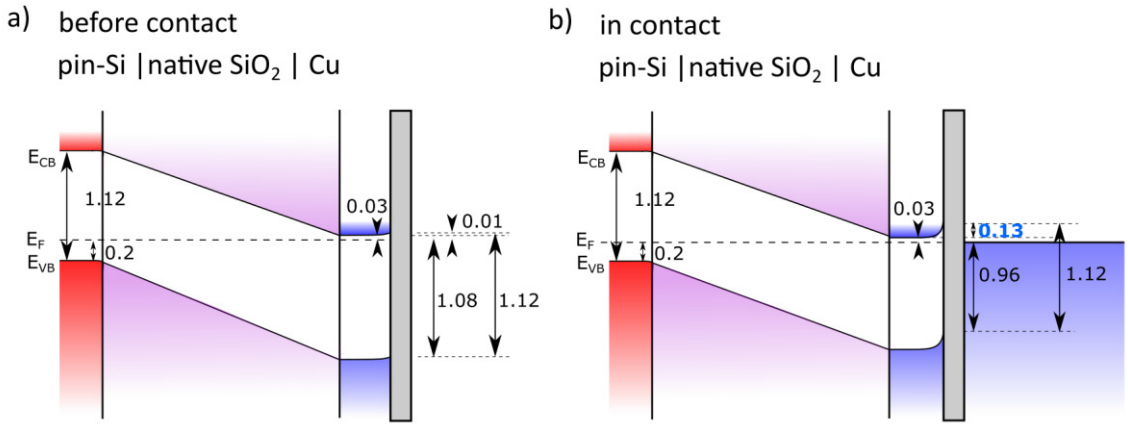

Figure 56: Energy band diagrams before and after contact formation. a) pin-Si | nat. SiO_2 before contact formation with flat band situation and b) pin-Si | nat. SiO_2 | Cu with an upward band bending of 0.13 eV.

5.4.2 Electrochemistry

As a solar cell is able to absorb not only one specific wave length but also those, which are larger than the bandgap, the photoelectrochemical measurements were performed under nearly real conditions by using a solar simulator with AM 1.5 G. However, in order to compare the photoelectrochemical performance of the pin-Si | Cu system to the previously analyzed pn^+-Si | Cu and p-Si | µcn-Si | Cu model systems, first an EC measurement was performed under the same conditions.

Figure 57 shows the cyclic voltammetry behavior of the pin-Si | nat. SiO_2 | Cu sample in the dark and under an illumination of 180 W/m^2 with $\lambda = 625$ nm in 0.3 M $KHCO_3$. The measurement was performed while bubbling with N_2 gas, which does not influence the photoelectrochemical performance. The EC curve under illumination is similar to the curves of the pn^+-Si | Cu and p-Si | µcn-Si | Cu samples. The maximum saturation current density is reached at -5.5 mA/cm^2, which is similar to the previous investigated samples as listed in table 7.

However, the average potential, which is necessary to reach a current density of -2 mA/cm^2 is lower compared to all other samples. This improvement is due to the increased photovoltage, which is generated within the pin-Si-junction when light enters the solar cell. If the photovoltage, which is delivered by the solar cell, is higher, the reaction will take place earlier (at less negative potentials).

Additionally, it can be observed that one of the CV curves exhibits a wave when scanning to a positive potential of +0.2 V. This wave indicates the oxidation of Cu^0 to Cu^{2+}.

When characterizing the EC behavior in the dark, it is evident that the absolute value of the current density continuously increases when the applied potential becomes more negative than -0.8 V vs. RHE. The maximum measured dark current density reaches -3.5 mA/cm^2, which is unexpectedly high. It is clear that the solar cell is not able to deliver such a high current density without illumination as in that

case no charge carriers are generated in the dark, which can result in a photocurrent. As none of the previously measured samples showed such a behavior, an explanation for this phenomenon must be found in the different structure or different electrical contact of the pin-Si solar cell compared to the pn^+-Si and p-Si | µcn-Si junctions.

It was shown in Figure 22 that the deposition of the necessary front contact results in a localized short circuit, which does not affect the whole solar cell. It is to be expected that the measured current density in the dark does not represent the charge carrier transport, but the lateral current ensuring from the local short circuit. Such observations are in agreement with literature. [101][132]

Another possible explanation could be the penetration of Cu atoms and diffusion along the grain boundaries of the solar cell structure resulting in an internal leakage current. However, this assumption may be proven for example by transmission electron microscopy (TEM), energy dispersive X-ray spectroscopy (EDX) or secondary ion mass spectroscopy (SIMS). Nevertheless, proving the assumed Cu penetration will be difficult as the intense sample preparation for the suggested methods can easily damage the sample and change or remove the thin Cu layer. Furthermore, the detection of small amounts of foreign atoms in a sample is always challenging.

Table 7: Overview of the necessary potential to obtain -2 mA/cm², the saturation current density under illumination ($J_{sat,\ illum}$) and in the dark ($J_{sat,\ dark}$) as well as the corresponding energy barrier at the interface ($eV_{b,n}$) for different pn^+-Si | Cu, p-Si | µcn-Si | Cu and pin-Si | Cu model systems.

Model System	potential to reach -2 mA/cm² [V vs. RHE]	$J_{sat,illum}$ [mA/cm²]	$J_{sat.dark}$ [mA/cm²]	$eV_{b,n}$ [eV]
pn^+-Si | nat. SiO_2 | Cu	-0.6	-6.0	-1.1	+0.35
pn^+-Si:H | Cu	-0.7	-6.0	-0.7	+0.45
pn^+-Si | therm. SiO_2 | Cu	-0.4	-5.7	-0.7	+0.27
p-Si | µcn-Si | nat. SiO_2 | Cu	-0.4	-6.2	-0.6	+0.01
p-Si | µcn-Si:H | Cu	-0.4	-5.5	-0.1	+0.55
p-Si | µcn-Si | therm. SiO_2 | Cu	-0.8	-4.5	-0.1	+0.02
pin-Si | nat. SiO_2 | Cu	-0.2	-5.5	-3.5	+0.13

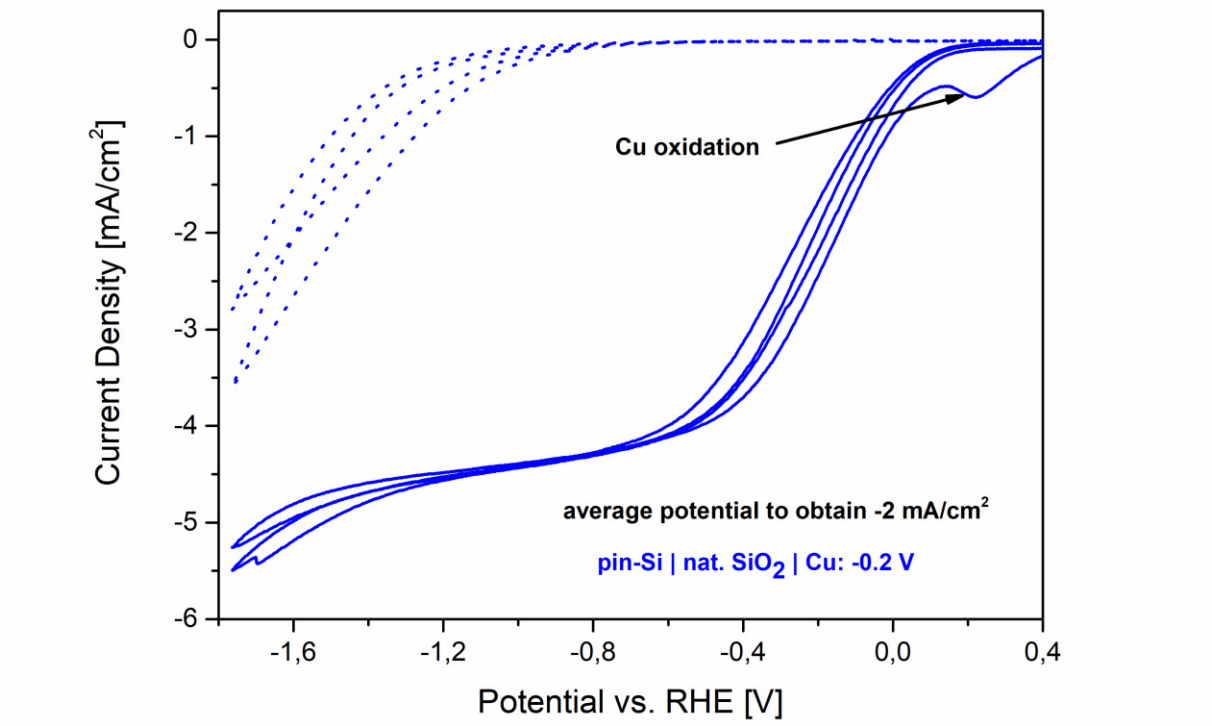

Figure 57: Cyclic voltammetry behavior of the pin-Si | nat. SiO_2 | Cu sample in the dark and under an illumination of 180 W/m² with λ = 625 nm in 0.3 M $KHCO_3$. Solid line: EC behavior under illumination. Dashed line: EC behavior in the dark.

The same EC measurement was repeated with the use of a solar simulation with AM 1.5 G in order to analyze the EC performance under more real conditions. For this measurement a freshly prepared sample was used, which is identical to the just analyzed pin-Si | nat. SiO_2 | Cu sample. Figure 58 shows the cyclic voltammetry measurements of an equally produced pin-Si | nat. SiO_2 | Cu sample in the dark and under an illumination of AM 1.5 G in 0.3 M $KHCO_3$. It can be noted that the value of the maximum reached current density of -16 mA/cm² is much larger compared to all previous measurements. This can be ascribed to the increased amount of charge carriers, which are generated in the solar cell due to the absorption of different wavelengths instead of one single wavelength (625 nm) in case of all previously performed measurements. Furthermore, the intensity of the solar simulator (1000 W/m²) is much higher compared to the red LED. The potential, which is required to reach a current density of -2 mA/cm² is -0.2 V vs. RHE, which is equal to the measurement where the LED was used. The electrochemical behavior in the dark resembles the previously discussed measurement. Therefore, the occurrence of a lateral current due to a localized short circuit or Cu penetration is also assumed in that case, which is reasonable as the two samples are identical.

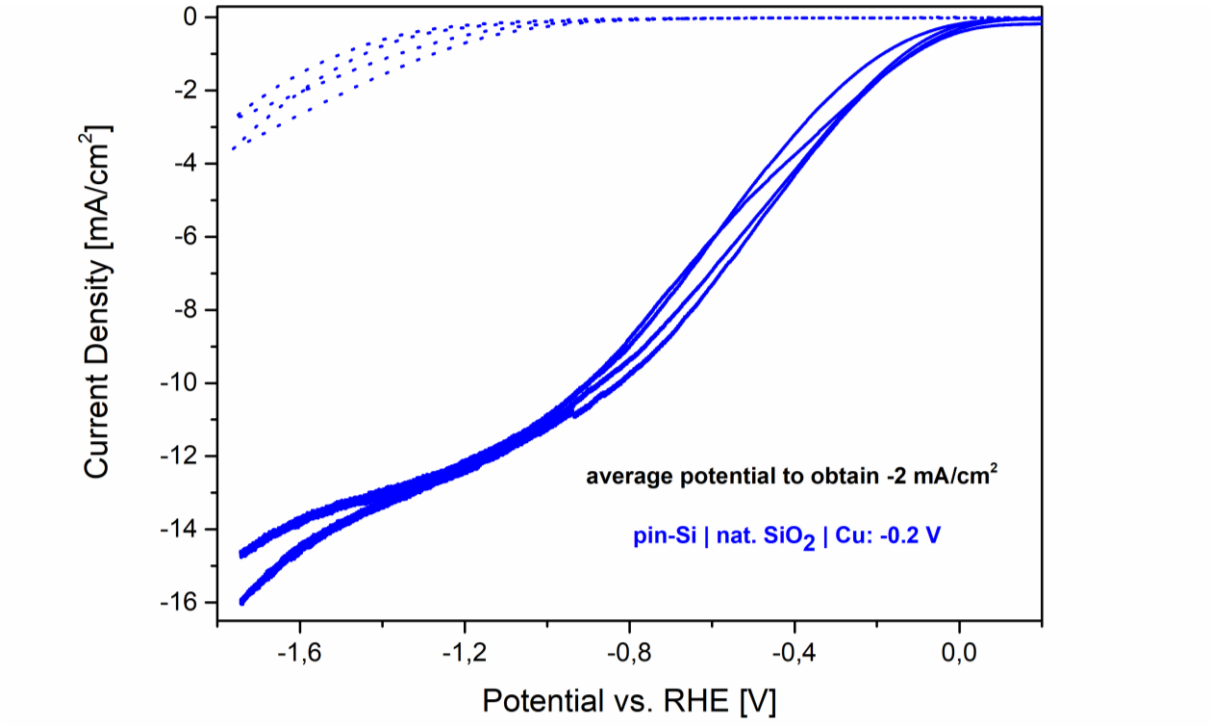

Figure 58: Cyclic voltammetry behavior of the pin-Si | nat. SiO_2 | Cu sample in the dark and under an illumination of AM 1.5 G (1000 W/m^2) in 0.3 M $KHCO_3$. Solid line: EC behavior under illumination. Dashed line: EC behavior in the dark.

5.4.3 Characterization after Electrochemistry

The XP detail spectra shown in Figure 59 were performed to prove whether the Cu film has changed after the photoelectrochemical measurement. As it was already proven for the pn^+-Si | Cu and p-Si | µcn-Si | Cu samples that the metallic character of the Cu film only remains if nitrogen gas is bubbled during EC, experiments without bubbling were not performed in case of the pin-Si | Cu system. From the Cu 2p spectrum in Figure 59 it can be noticed that the binding energy maximum can be detected at 933.30 eV, which indicates the presence of metallic Cu or the formation of CuO. Also a distinct satellite, which corresponds to the formation of CuO or $Cu(OH)_2$ cannot be identified in the Cu 2p region. Nevertheless, the spectrum does not remain completely flat between the Cu $2p_{3/2}$ and Cu $2p_{1/2}$ emission line, which leads to the assumption that the catalytic layer contains mostly metallic Cu but also small amounts of copper oxide species after the photoelectrochemical measurement.

From the O 1s emission line at 533.10 eV it becomes clear that CuO cannot be the predominantly formed phase as copper oxides exhibit an emission line at binding energies below 530 eV, whereas the maximum position of the O 1s emission line at 533.10 eV can be clearly assigned to SiO_2.[114] The SiO_2 emission is a substrate signal, which is also detectable within the Si 2p region. At 103.65 eV the Si 2p emission line shows a peak, which is even more intense than the main Si 2p emission line at 99.78 eV. It is supposed that during EC the Si substrate with a native SiO_2 layer on top is further oxidized. Such a strong oxidation was not observed for previously analyzed Si | Cu systems. Therefore, the quality of the Cu film must be different in case of the pin-Si | Cu sample to allow oxygen to penetrate through the deposited layer. It is possible that the thin film solar cells exhibit a more porous structure compared to the Si wafers, which may also influence the quality of the deposited Cu film. From the Si:Cu intensity ration the Cu film thickness was determined, which is approximately 15 Å.

Subsequent SEM images will show whether the morphology of the Cu film is different, which can justify the assumption of oxygen penetration. But first, the C 1s emission line in Figure 59 needs to be discussed. The maximum at 285.8 eV can be assigned to C-H and C-C bonds, which could already be observed for the previously analyzed Si | Cu systems. However, at binding energies above 288 eV carbonates and further possible CO_2 reduction products can be detected.[126][94]

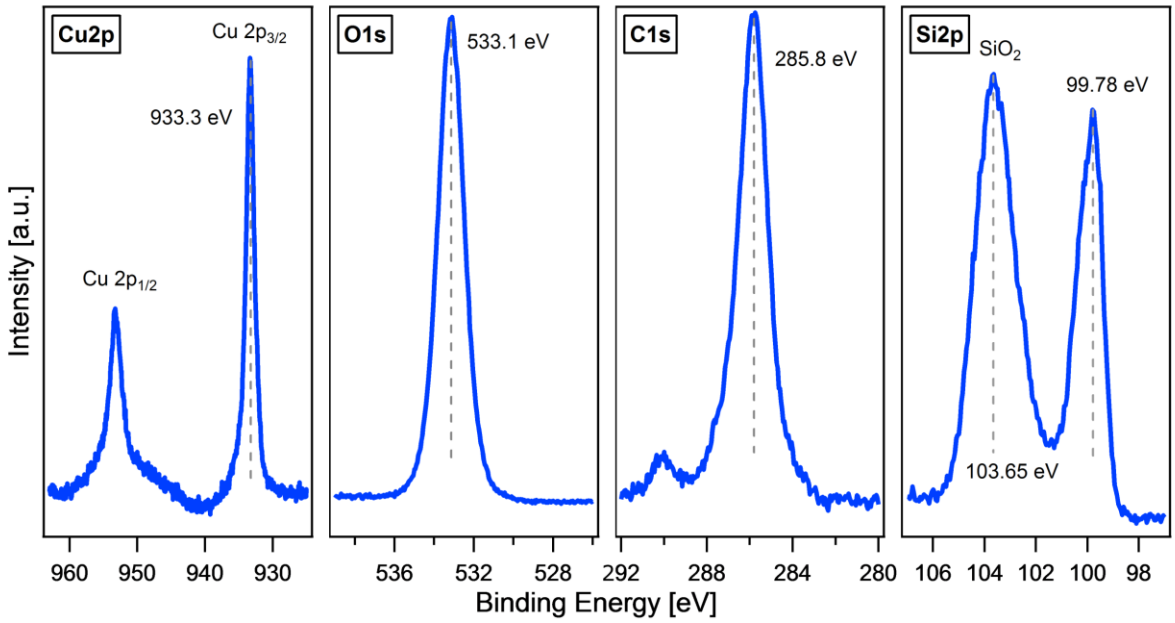

Figure 59: XP detail spectra of the pin-Si | nat. SiO_2 | Cu sample showing the Cu 2p, O 1s, C 1s and Si 2p emission lines after performing cyclic voltammetry measurements. The photoelectrochemical measurement was performed while bubbling with N_2 gas.

The SEM images in Figure 60 show the pin-Si | nat. SiO_2 | Cu sample surface a) before and b) after photoelectrochemical measurements with a magnification of 1000. Contrary to the pn^+-Si | Cu and the p-Si | µcn-Si | Cu sample surfaces the depicted SEM images show a rough structure. It is unlikely that the deposited Cu film itself has a rough structure. In fact, the morphology of underlying solar cell becomes visible as the ultra-thin Cu film emulates the structure. The difference between before and after EC is not as dominant as for the pn^+-Si | Cu and the p-Si | µcn-Si | Cu sample surfaces. Nevertheless, it can be seen in Figure 60 b) that some additional particles are deposited to the surface. The rough surface can be seen even more clearly in Figure 61 which images the surfaces with a magnification of 10000. It is assumed that due to the roughness of the film oxygen atoms can easily penetrate through the film and hence further oxidize the underlying SiO_2 interface.

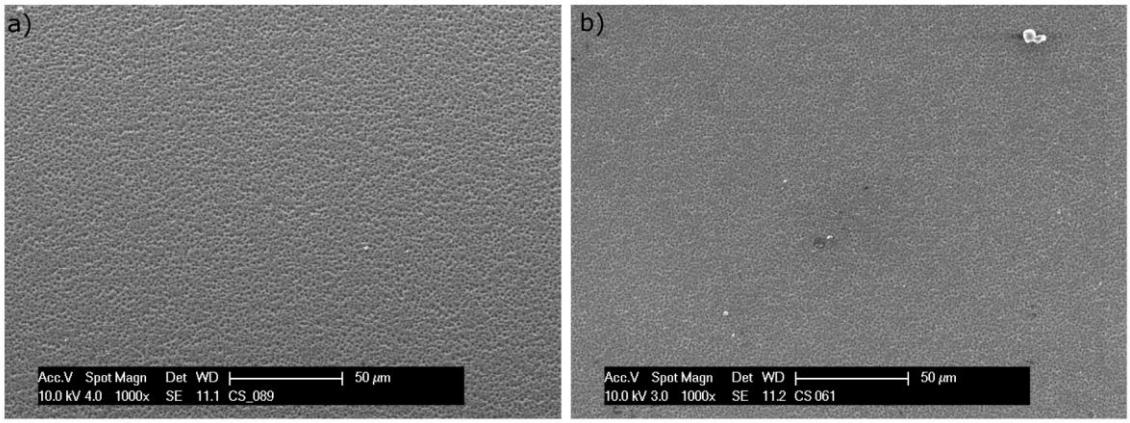

Figure 60: SEM images of pin-Si | nat. SiO_2 | Cu samples with a magnification of 1000, a) before photoelectrochemistry and b) after photoelectrochemistry.

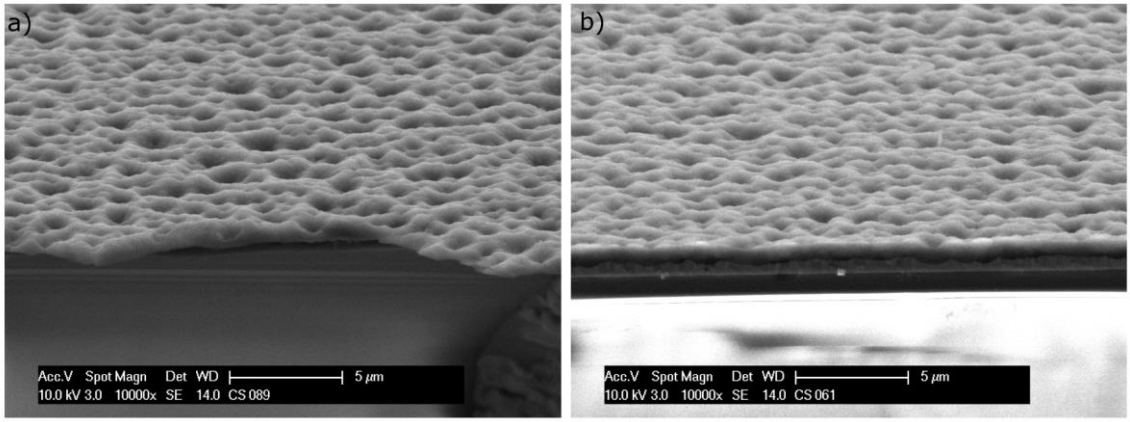

Figure 61: SEM images of the cross section of the pin-Si | nat. SiO_2 | Cu samples with a magnification of 10000, a) before photoelectrochemistry and b) after photoelectrochemistry.

5.5 a-Si:H | a-Si:H | µc-Si:H | Cu Interface

After the investigations of pn^+-Si | Cu, p-Si | µcn-Si | Cu as well as pin-Si (µc-Si:H) | Cu systems, a triple junction solar cell is used to improve the photoelectrochemical performance due to advantageous solar light absorption. The used solar cell has an a-Si:H | a-Si:H | µc-Si:H configuration with p-i-n structure. Thus, the top µc-Si:H solar cell with p-i-n structure is identical to the previously analyzed pin-Si solar cell. Therefore, the energy band alignment at the a-Si:H | a-Si:H | µc-Si:H | Cu contact will be identical and does not need to be investigated. Also XPS studies after EC as well as SEM measurements are not necessary as the interface is equal. Nevertheless, differences concerning the photoelectrochemical performance are expected. As well as the pin-Si solar cell, the a-Si:H | a-Si:H | µc-Si:H solar cell contains a thin layer of native SiO_2 on top. The photoelectrochemical measurements were performed in 0.3 M $KHCO_3$ in the dark and under a solar simulation with AM 1.5 G global spectra. The resulting CV curves are shown in grey in Figure 62 in comparison to the already discussed pin-Si | nat. SiO_2 | Cu sample in blue. It is evident that in case of illumination, the saturation current density of the a-Si:H | a-Si:H | µc-Si:H | nat. SiO_2 | Cu sample is much lower (-6.7 V vs. RHE) compared to the pin-Si | nat. SiO_2 | Cu sample (-16 V vs. RHE), whereas the onset potential is remarkably higher. This can be explained by different JV-characteristics of the two different solar cells, which was shown in Figure 11. While the single junction solar cell reaches more negative current densities, the triple cell suffers from poor current density, but improved photovoltage. However, to measure the onset potential the scanning range needs to be adjusted, which means an applied anodic potential of up to +1.6 V. Within this region Cu corrosion can be assumed. Nevertheless, no redox waves are visible in this potential regime, which indicate Cu oxidation. But still it needs to be taken into account that the Cu layer might have been partially dissolved due to the applied potential range of the CV measurement.

To reach a current density of -2 mA/cm^2 a potential of +1.1 V vs. RHE is required. This positive effect is attributed to the wide energy band gap of amorphous Si and the absence of light-trapping structure.[133] Furthermore, a tripe junction solar cell delivers more photovoltage due to an optimum use of the solar light spectrum. It needs to be taken into account that according to Figure 12 c) the applied potential at the Cu contact is not as large as at the Si junction. Due to the increased photovoltage of the triple Si solar cell the potential at the Cu contact is shifted into the negative regime. Hence, Cu oxidation is not expected whereas Cu oxidation was observed for the pin-Si single junction solar cell, which delivers less photovoltage (see Figure 57). The a-Si:H | a-Si:H | µc-Si:H | nat. SiO_2 | Cu sample also shows an unexpected high dark current density, which is assumed to be caused by a lateral current or a leakage current. The same phenomenon was already observed in case of the single pin-Si | nat. SiO_2 | Cu sample. However, the effect is even higher for the triple junction solar cell.

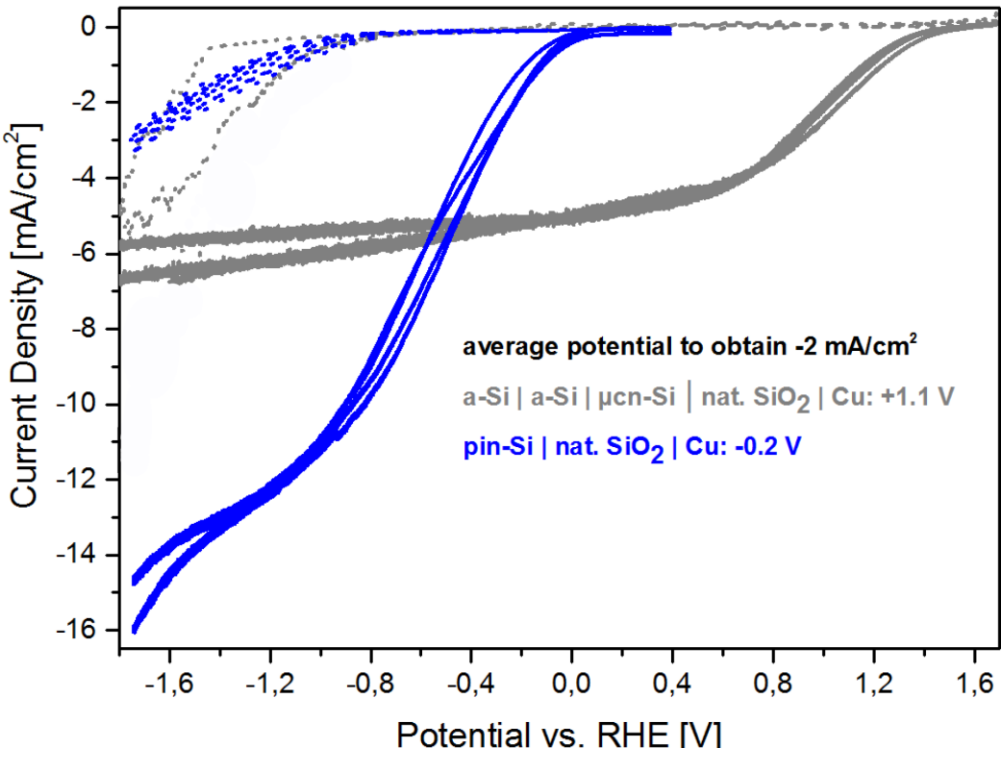

Figure 62: Cyclic voltammetry behavior of the a-Si:H | a-Si:H | µc-Si:H | nat. SiO_2 | Cu sample (grey) in the dark and under an illumination of AM 1.5 G (1000 W/m²) in 0.3 M $KHCO_3$ in comparison to the pin-Si | nat. SiO_2 | Cu sample (blue). Solid lines: EC behavior under illumination. Dashed lines: EC behavior in the dark.

5.6 Comparison of all Si | Cu Interfaces

Table 8 gives an overview of all obtained results from XPS as well as photoelectrochemical measurements. It can be concluded that a passivating interlayer such as SiO_2 between the Si | Cu interface improves the energy band alignment, which is advantageous for the electron transport properties across the interface. As a result less negative onset potentials are required in case of lower energy barriers at the Si | Cu interface. This trend was especially observed for the pn^+-Si | Cu model system.

When investigating the p-Si | µcn-Si | Cu interfaces, the hydrogen terminated sample did not show a reduced electrochemical performance although the barrier height at the interface was comparably high (+0.55 eV). It was assumed that the tunneling effects play a role in this case.

Moreover, it was observed that Cu_2O interface phases are formed during deposition when the Si structure contains a SiO_2 layer on top. How this additional Cu_2O layer influences the interface formation could not be examined. However, the presence of Cu_2O after the first deposition steps was proven by the Cu LMM Auger line. It was assumed that the deposition conditions were ideal for metallic Cu deposition and hence, it was expected that Cu oxidation happens by reacting with the SiO_2 layer.

It could also be concluded that thermally grown SiO_2 is not an option for µc-Si substrates as the required preparation temperature of 800°C damages the structure and therefore, limits the photoelectrochemical performance. The same is valid for the hydrogen termination in case of the Si solar cells as they are not stable under the required etching conditions.

Furthermore, it could also be observed that the initial Cu film thickness is reduced from about 100 Å to averaged 40 Å when performing photoelectrochemical measurements. This film thickness is even further reduced to approximately 15 Å when additionally bubbling with nitrogen gas during the photoelectrochemical measurements. Nevertheless, nitrogen gas bubbling is considered to be reasonable as the metallic character of the Cu film remains during EC, instead of the formation of a copper oxide compound. Reason for this behavior is the used electrolyte ($KHCO_3$) which contains oxygen and hence, leads to Cu oxidation when the electrolyte solution is not bubbled with nitrogen. In terms of CO_2 reduction further experiments with CO_2 bubbling during EC should be performed. Bubbling with CO_2 would also saturate the electrolyte solution and therefore prevent Cu oxidation. Moreover, the selectivity of the CO_2 reaction is expected to be improved when introducing CO_2 gas into the electrolyte. However, these experiments were not performed here, as the main focus of this work was the investigation of the correlation of the electronic band structure and the corresponding electrochemical behavior.

CV measurements have shown that under illumination the Cu film oxidizes when deposited on pin-Si single junction whereas no oxidation takes place in case of Cu deposited on pin-Si triple junction. Reason for this is different photovoltage and hence different positions of the Fermi level. During EC measurements under illumination the applied potential at the Si solar cell is not equal to the potential at the Cu contact. The higher the induced photovoltage, the more negative the actual potential at the Cu contact. Therefore, no Cu oxidation could be observed in case of the a-Si | a-Si | µcn-Si | Cu sample, which provides more photovoltage compared to the pin-Si single junction.

SEM images before and after EC as well as XPS analyses after EC have proven that the Cu films are still intact after EC, even though the films are partially damaged. Besides the Cu films, which were deposited on solar cells, all films exhibit a very smooth surface structure. The Cu films deposited on solar cells form a more rough structure on the solar cell surface.

Further experiments should be done to analyze the resulting products of the CO_2 reduction reaction. Here, gas chromatography would be a suitable method. Moreover, the electrochemical behavior of the pin-Si | Cu and a-Si | a-Si | µcn-Si | Cu samples in the dark should be analyzed more in detail. TEM images or EDX could be helpful to see whether Cu atoms penetrate into the Si structure. A subsequent diffusion along the grain boundaries of the microcrystalline structure of the solar cell structure might cause a leakage current. However, lateral current flow could also be an explanation for high dark currents.

*Table 8: Overview of the results from XPS as well as photoelectrochemical measurements of all pn⁺-Si | Cu, p-Si | µcn-Si | Cu, pin-Si | Cu and a-Si | a-Si | µcn-Si | Cu samples. The electrochemical parameters refer to an illumination with λ = 625 nm, unless otherwise stated. Theoretical values are marked with *.*

Model system	**Position of Si $2p_{3/2}$ emission line**		
	before contact	after contact	resulting shift
pn⁺-Si | nat. SiO_2 | Cu	99.77 eV	99.48 eV	0.29 eV
pn⁺-Si:H | Cu	99.82 eV	99.38 eV	0.44 eV
pn⁺-Si | therm. SiO_2 | Cu	99.77 eV	99.56 eV	0.21 eV
p-Si | µcn-Si | nat. SiO_2 | Cu	99.84 eV	99.84 eV	0.00 eV
p-Si | µcn-Si:H | Cu	99.82 eV	99.28 eV	0.54 eV
p-Si | µcn-Si | therm. SiO_2 | Cu	99.84 eV	99.81 eV	0.03 eV
pin-Si | nat. SiO_2 | Cu	99.82 eV	99.70 eV	0.12 eV
a-Si:H | a-Si:H | µc-Si:H | nat. SiO_2 | Cu	99.82 eV*	99.70 eV*	0.12 eV*

Model System	potential to reach -2 mA/cm² [V vs. RHE]	$J_{sat,illum}$ [mA/cm²]	$J_{sat.dark}$ [mA/cm²]	$eV_{b,n}$ [eV]
pn⁺-Si | nat. SiO_2 | Cu	-0.6	-6.0	-1.1	+0.35
pn⁺-Si:H | Cu	-0.7	-6.0	-0.7	+0.45
pn⁺-Si | therm. SiO_2 | Cu	-0.4	-5.7	-0.7	+0.27
p-Si | µcn-Si | nat. SiO_2 | Cu	-0.4	-6.2	-0.6	+0.01
p-Si | µcn-Si:H | Cu	-0.4	-5.5	-0.1	+0.55
p-Si | µcn-Si | therm. SiO_2 | Cu	-0.8	-4.5	-0.1	+0.02
pin-Si | nat. SiO_2 | Cu	-0.2	-5.5	-3.5	+0.13
pin-Si | nat. SiO_2 | Cu (AM 1.5 G)	-0.2	-16.0	-3.5	+0.13
a-Si:H | a-Si:H | µc-Si:H | nat. SiO_2 | Cu (AM 1.5 G)	+1.1	-6.7	-4.7	+0.13*

6 Characterization of the Si | Ag Interface

As Ag is also known to be an appropriate catalyst for the CO_2 reduction, the Si | Ag interface was investigated. [42], [43], [46], [47], [49], [64]–[66] However, these investigations were only done for the pn^+-Si | nat. SiO_2 | Ag, the p-Si | µcn-Si | nat. SiO_2 | Ag and the a-Si:H | a-Si:H | µc-Si:H | nat. SiO_2 | Ag contacts. Native SiO_2 has been chosen as surface termination because it has been proven in case of the Si | Cu interface investigations that compared to hydrogen terminated Si surfaces, SiO_2 as surface passivation lead to a better electronic band alignment as well as photoelectrochemical performance. Moreover, it was shown that the heat treatment, which is necessary to thermally grow SiO_2 can damage the Si structure.

6.1 pn^+-Si | Ag Interface

6.1.1 Energy Band Alignment

Analogous to the pn^+-Si | nat. SiO_2 | Cu interface experiment, the pn^+-Si | nat. SiO_2 | Ag contact was investigated. Figure 63 shows the development of the survey spectra during the interface experiment. While the substrate signals of the O KLL Auger line, the O 1s, Si 2s and Si 2p emission lines become weaker with each deposition step, the corresponding film signals arise at 368.13 eV (Ag 3d), 573.01 eV (Ag $3p_{3/2}$), 604.03 eV (Ag $3p_{1/2}$), 720.00 eV (Ag 3s) and 1135 eV (Ag MNV). Furthermore, the Ag 4s, Ag 4p and Ag 4d emission lines arise at 110 eV, 69 eV and 11 eV. As these emission lines are not relevant for the evaluation of the experiment, they are not assigned within the XP survey spectrum.

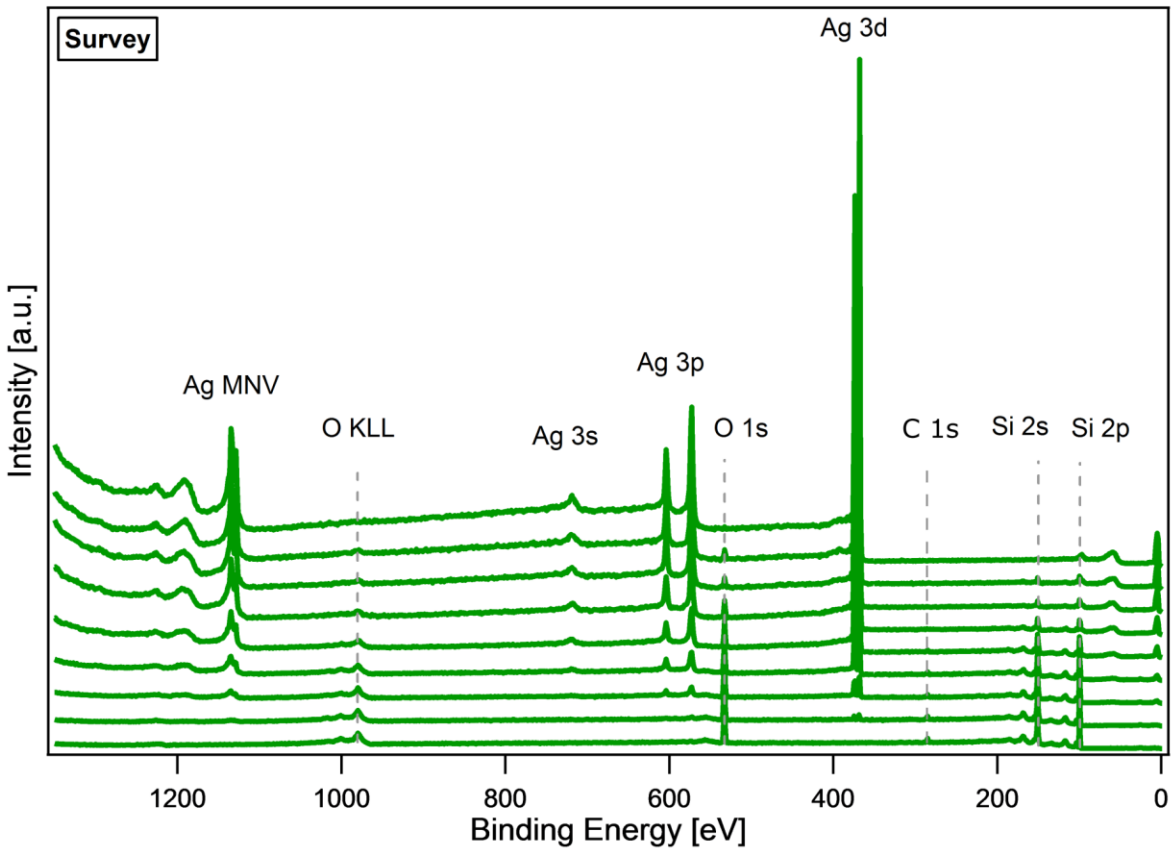

Figure 63: Development of the XP survey spectra of the pn^+-Si | nat. SiO_2 | Ag contact during the interface experiment. The measurement of the bare pn^+-Si | nat. SiO_2 substrate is displayed at the bottom of the diagram while the last deposition step at the top shows the final measurement of a relatively thick Ag layer.

Besides the survey spectra, XP detail spectra were measured, which are shown in Figure 64. Before Ag deposition the Si $2p_{3/2}$ emission line is detected at 99.70 eV. At a binding energy of 103.60 eV the SiO_2 peak arises. The corresponding O 1s emission line shows its maximum at 533.18 eV. These binding energies do not change after the deposition of the first 3 Å of Ag. With the following deposition steps the Ag 3d emission line becomes more intense and the Si 2p as well as O 1s substrate signal slightly shift to lower binding energies. When the Ag film reaches a thickness of 38 Å, the Si $2p_{3/2}$ and Si $2p_{1/2}$ emission lines cannot be clearly distinguished anymore. At that point the position of the Si 2p emission line is shifted to 99.50 eV, while the O 1s emission line has its maximum at 532.92 eV.

With the next two deposition steps the shape of the Si 2p emission line becomes less distinct and the maximum reaches its final position at a binding energy of 99.49 eV. The O 1s emission line can be evaluated at 532.83 eV. After the last deposition step the Ag film reaches a thickness of 100 Å and the Ag $3d_{5/2}$ line has its maximum at 368.13 eV, which is a typical value for metallic Ag. Furthermore, the distance between the Ag $3d_{5/2}$ and the Ag $3d_{3/2}$ emission lines can be evaluated, which results in 6.01 eV, which also proves the metallic character of the deposited film. At approximately 372 eV and 378 eV

plasmon loss features are detectable corresponding to metallic Ag as well.[94][134] At that state of the interface experiment the Si 2p and O 1s emission lines have almost vanished.

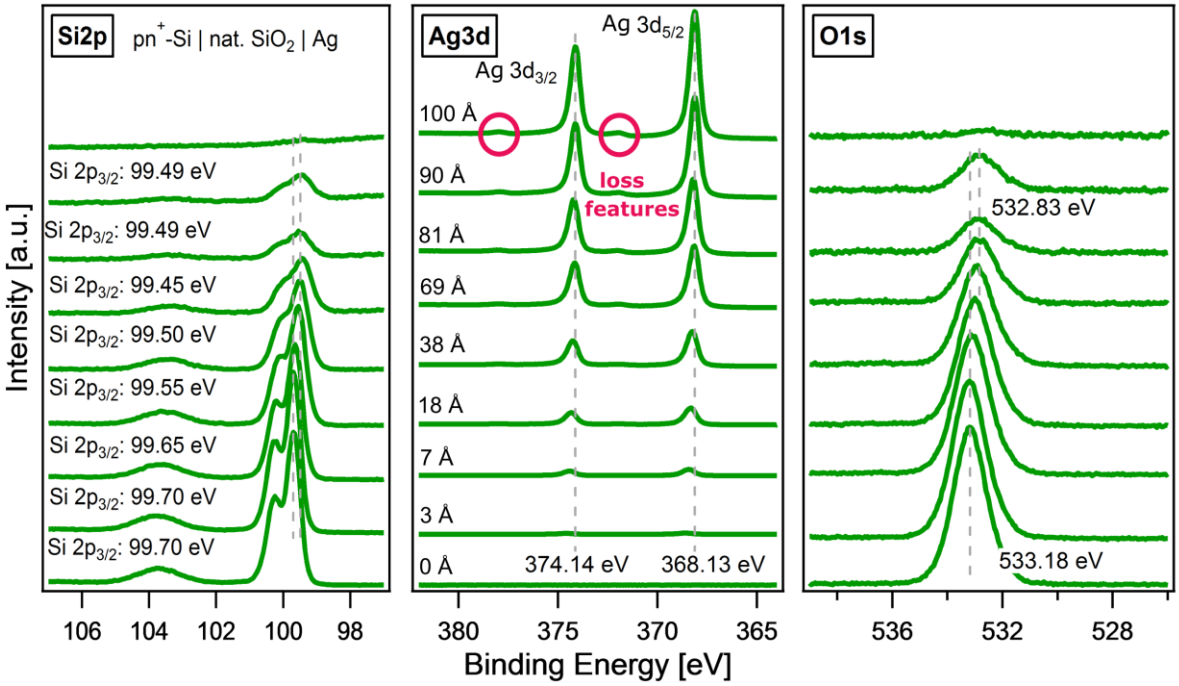

Figure 64: Development of the Si 2p, Ag 3d and O 1s detail spectra of the pn$^+$-Si | nat. SiO$_2$ | Ag contact during the interface experiment. The measurement of the bare pn$^+$-Si | nat. SiO$_2$ substrate is displayed at the bottom of the diagram while the last deposition step at the top shows the final measurement of a relatively thick Ag layer. The marked areas within the Ag 3d emission line show the loss features.

From the initial position and the final shift of the Si 2p$_{3/2}$ emission line the energy band alignment before and after contact formation with Ag can be calculated. Figure 65 a) shows the situation before contact formation. At the surface an upward band bending of 0.13 eV can be observed, which is comparably high with respect to the corresponding pn$^+$-Si | nat. SiO$_2$ interface for the Cu deposition experiments discussed in chapter 5.2.1, where an initial upward band bending of only 0.06 eV was calculated. The different initial energetic band alignment can be ascribed to the aging of the pn$^+$-substrate. The evaluation of the thickness of the SiO$_2$ interlayer yield a 7 Å thick layer in case of the pn$^+$-Si | nat. SiO$_2$ | Ag sample in contrast to the pn$^+$-Si | nat. SiO$_2$ | Cu sample, where the SiO$_2$ interlayer only had a thickness of 3 Å. Thus, it is assumed that the upward band bending before contact formation in case of the pn$^+$-Si | nat. SiO$_2$ | Ag sample is not an effect of Fermi level pinning. This is also proven as the bands further bend upwards when being in contact to Ag, which is illustrated in Figure 65 b). The resulting band bending of 0.34 eV is very similar to the band bending of the pn$^+$-Si | nat. SiO$_2$ | Cu interface (0.35 eV). The similar energetic situation at the Si | metal contact is reasonable as the work functions of Ag and Cu are not very different (φ_{Ag} = 4.33 eV, φ_{Cu} = 4.61 eV).[135] Table 9 compares the positions

of the Si $2p_{3/2}$ emission lines of the pn^+-Si | nat. SiO_2 | Cu and pn^+-Si | nat. SiO_2 | Ag model systems before and after contact formation as well as the resulting shift.

Table 9: Overview of the position of the Si $2p_{3/2}$ emission line before and after contact formation for the pn^+-Si | nat. SiO_2 | Cu and the pn^+-Si | nat. SiO_2 | Ag interfaces.

Model system	**Position of Si $2p_{3/2}$ emission line**		
	before contact	after contact	resulting shift
pn^+-Si | nat. SiO_2 | Cu	99.77 eV	99.48 eV	0.29 eV
pn^+-Si | nat. SiO_2 | Ag	99.70 eV	99.49 eV	0.21 eV

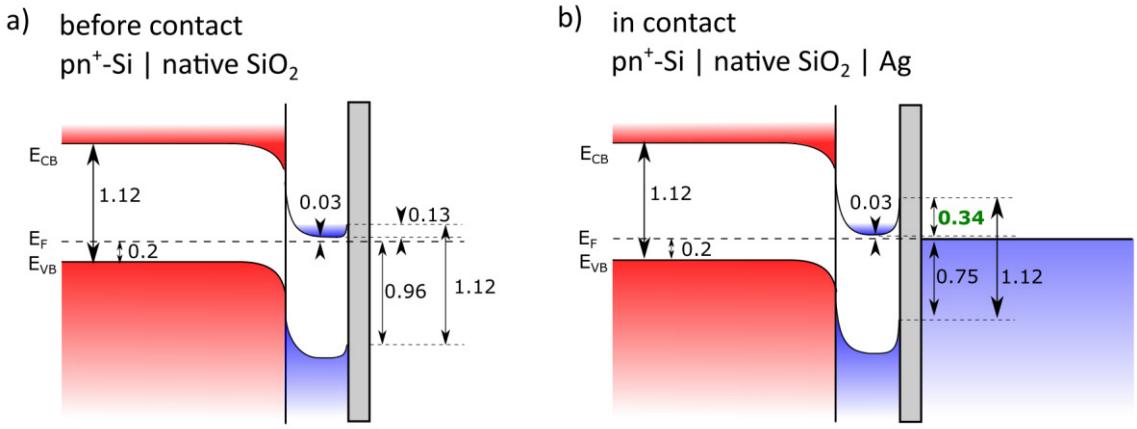

Figure 65: Energy band diagrams before and after contact formation. a) pn^+-Si | nat. SiO_2 before contact formation with an upward band bending of 0.13 eV and b) pn^+-Si | nat. SiO_2 | Ag with an upward band bending of 0.34 eV.

6.1.2 Electrochemistry

As the energy band alignments of the pn^+-Si | nat. SiO_2 | Ag and the pn^+-Si | nat. SiO_2 | Cu interface are almost identical, the electrochemical performance is expected to be similar as well. However, Figure 66 shows that the behavior is different. Figure 66 displays the EC behavior of the pn^+-Si | nat. SiO_2 | Ag sample in comparison to the pn^+-Si | nat. SiO_2 | Cu sample. The CV curves of the Ag sample were measured without nitrogen gas bubbling. XPS measurements after EC have shown that in case of Ag films N_2 gas bubbling is not necessary as the metallic character of the film remains during EC measurement procedure as demonstrated in chapter 6.1.3.

While the orange curve in Figure 66 presents the CV performance of the pn^+-Si | nat. SiO_2 | Cu sample in the dark (dashed line) and under illumination (solid line), the green curves correspond to the pn^+-Si | nat. SiO_2 | Ag sample. The dark current is very low and therefore, satisfies expectations. Under

illumination with the red LED (625 nm) the two measured cycles are very different. The first cycle proceeds as expected and follows the CV curve of the pn^+-Si | nat. SiO_2 | Cu sample. But, by cycling the second time, the EC performance is drastically reduced, which results in a more negative onset potential as well as reduced current density. While the potential, which is required to obtain -2 mA/cm^2, is -0.6 V (vs. RHE) for the first cycle, it shifts to -0.8 V when cycling the second time. The value of the current density is reduced from initial -6 mA/cm^2 to -3.6 mA/cm^2. This phenomenon leads to the assumption that the Ag film is destroyed or even removed during cycling. The first visual impression of the sample after demounting it from the electrochemical setup already proves this assumption as shown in the photograph in Figure 67. It can clearly be seen that the silver film is completely removed within the red marked area. Also the preserved parts of the Ag film seem to be damaged. Nevertheless, XPS and SEM measurements will prove the quality of the remaining Ag film.

Another aspect, which needs to be considered is the different optical absorption coefficient of Ag and Cu. As the measurement setup requires the illumination of the sample through the catalytically active layer, different optical absorption can influence the EC performance. For a wavelength λ of 625 nm, which corresponds to an energy of 1.98 eV due to equation (24), the optical absorption α is approximately $9.0 \cdot 10^5$ cm^{-1} for Ag and $6.7 \cdot 10^5$ cm^{-1} for Cu.[136]

$$E = \frac{hc}{\lambda} \qquad (24)$$

Here, h represents Planck's constant ($6.626 \cdot 10^{-34}$ Js) and c is the velocity of light (299792458 m/s). If the absorption coefficient α is high, the material is able to shield a large amount of the incoming light and vice versa. Hence, Cu allows more light to enter the underlying Si junction and therefore, more photons can contribute to the electron hole pair generation, which can result in a slightly better EC performance. However, the difference in optical absorption of Ag and Cu is not large, which is evident from the similar photocurrent in the saturation regime of the first scan, but should be noted at that point.

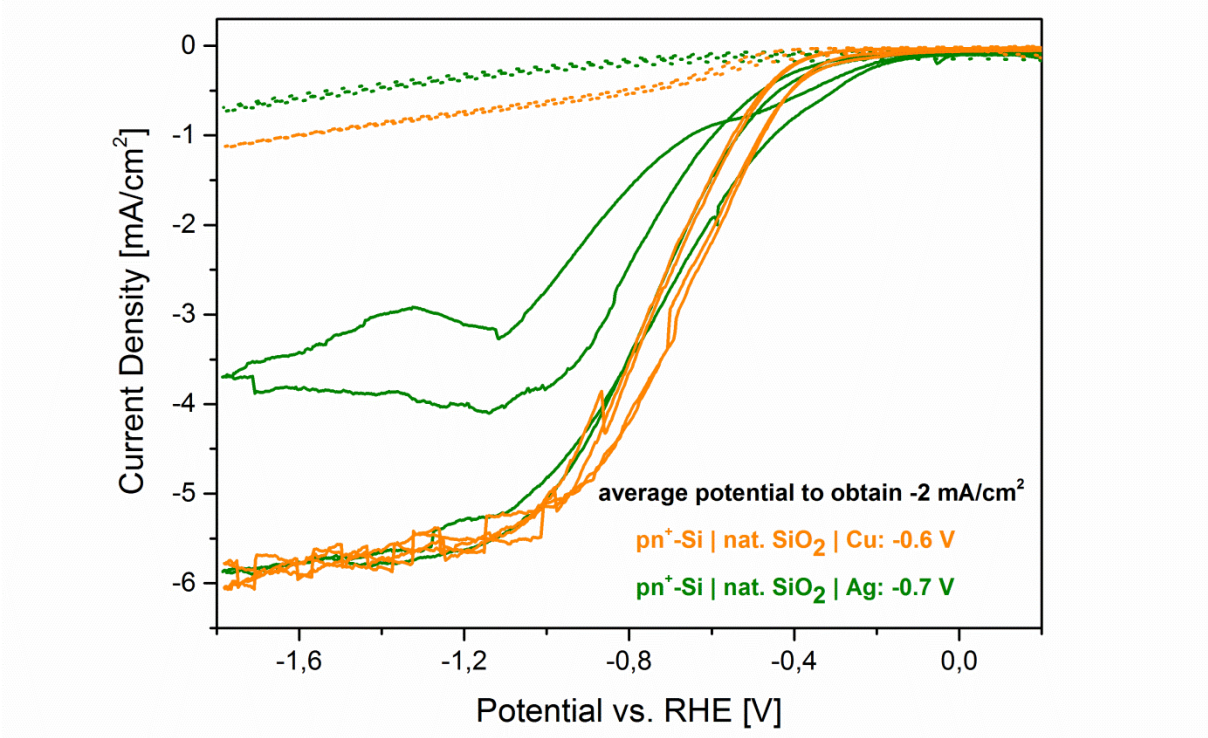

Figure 66: Comparison of the cyclic voltammetry behavior of the pn⁺-Si | nat. SiO_2 | Ag sample (green) and the, pn⁺-Si | nat. SiO_2 | Cu (orange) in the dark and under an illumination of 180 W/m² with λ = 625 nm in 0.3 M $KHCO_3$. Solid lines: EC behavior under illumination. Dashed lines: EC behavior in the dark.

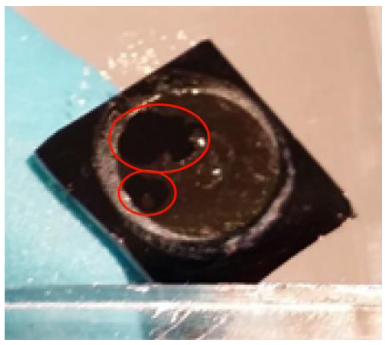

Figure 67: Photograph of the pn⁺-Si | nat. SiO_2 | Ag sample after performing photoelectrochemical measurements. The red marked areas show regions where the Ag film in partially removed. The whole Ag film seems to be damaged.

6.1.3 Characterization after Electrochemistry

Before evaluating the XPS data, which were measured after EC, it is important to consider that XPS is only measured on a specific spot on the sample surface. As it could already been seen with the bare eye that the Ag film was partially removed by the cyclic voltammetry measurement, it needs to be considered that the XP spectra do not represent the whole sample surface and may be different on different spots on the surface.

Figure 68 shows the corresponding XP detail spectra of the O 1s, Ag 3d, C 1s and Si 2p regions. The position of the O 1s emission line at 533.24 eV indicates the SiO_2 from the substrate, which was also detected in case of the pn^+-Si | nat. SiO_2 | Cu. The corresponding peak at 103.69 eV in the Si 2p region proves this assumption. Furthermore, the Si $2p_{3/2}$ emission line is detected at 99.82 eV, which can be clearly identified as substrate signal. Nevertheless, the Ag $3d_{5/2}$ emission line at 368.74 eV and the Ag $3d_{3/2}$ emission line at 374.72 eV are still visible. The maximum positions show a shift of +0.5 eV compared to ideal metallic Ag which may be a result of charging effects. However, Ag oxidation is not assumed as here the Ag $3d_{5/2}$ line is expected to be below 368 eV. Furthermore, the distance between the Ag $3d_{5/2}$ and Ag $3d_{3/2}$ emission line of 5.98 eV is a typical value for metallic Ag and do not indicate the formation of Ag oxides.[94] Additional Auger spectra, which can help to identify the present Ag phase could not be measured as the background noise does not allow an accurate measurement of the Auger line and hence, cannot be evaluated. Due to the noisy background the typical loss features in the Ag 3d emission line are not identifiable, which is a result of the small amount of Ag, which is left on the sample surface. In comparison to the 100 Å thick Ag film directly after deposition, the layer has been reduced to approximately 30 Å.

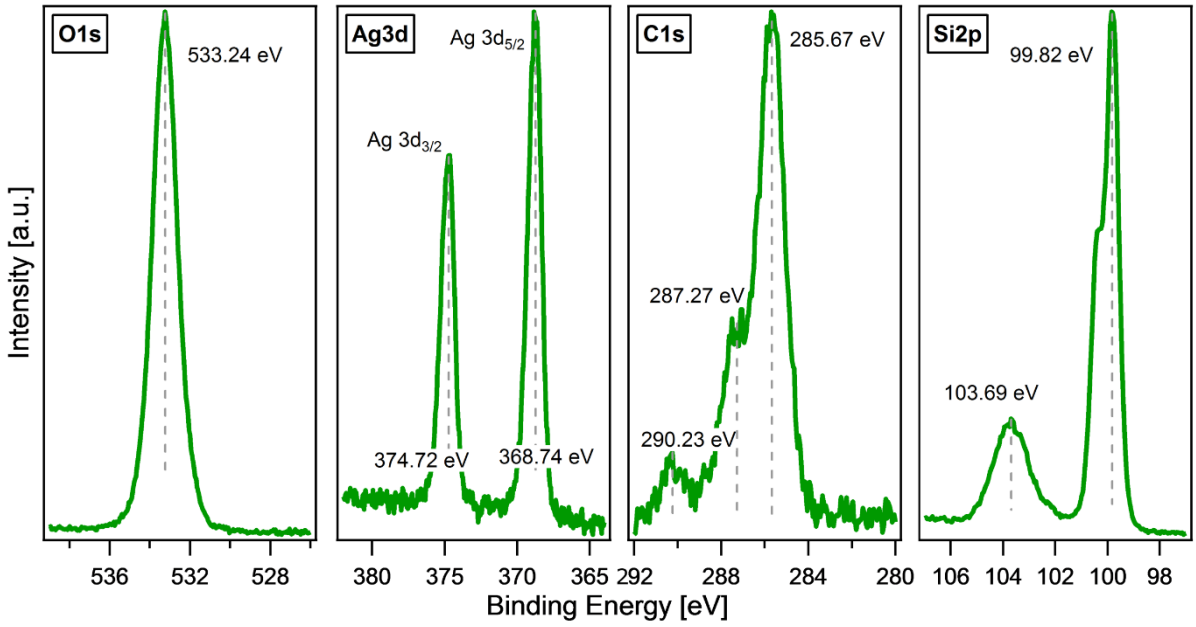

Figure 68: XP detail spectra of the pn^+-Si | nat. SiO_2 | Ag sample showing the O 1s, Ag 3d, C 1s and Si 2p emission lines after performing cyclic voltammetry measurements.

From the C 1s emission line CO_2 reduction products can be proven. The maximum position at 285.67 eV represents a typical value for C-H and C-C bonds, which could already be observed for the experiments performed with Si | Cu samples. Moreover, the C 1s emission line exhibits a maximum at 287.27 eV, and 290.23 eV, which indicate the formation of various carbon species, which may have formed due to the used electrolyte or the CO_2 reduction reaction.

Besides the first optical impression of the pn^+-Si | nat. SiO_2 | Ag sample as well as the XPS analysis after EC, SEM images were obtained to prove the quality of the Ag films. Figure 69 shows SEM images of the pn^+-Si | nat. SiO_2 | Ag sample after CV measurements were performed. In Figure 69 a) an overview with a magnification of 1000 is displayed, which demonstrates that the Ag layer is highly damaged. Some parts of the Ag film are completely detached from the Si surface and folded. Figure 69 b), which displays the sample with a magnification of 10000, clearly show that some parts of the sample are not covered with Ag anymore.

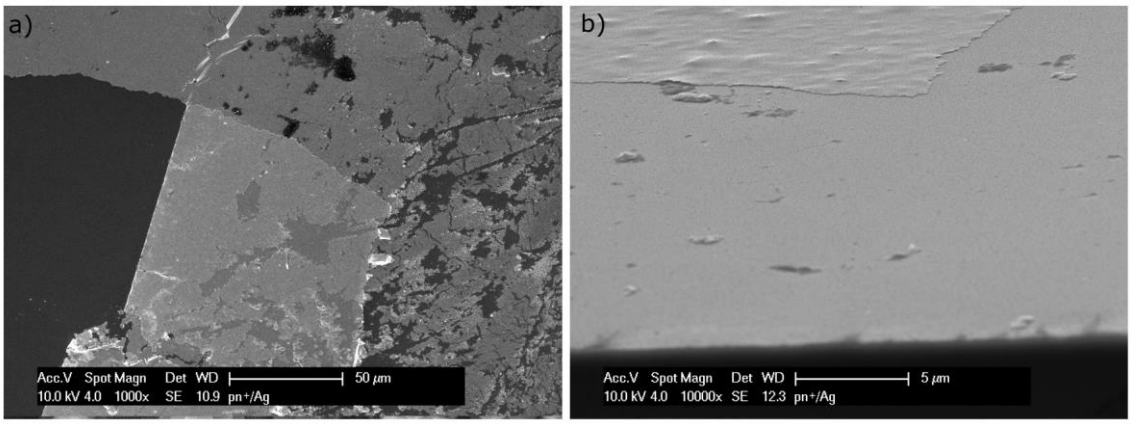

Figure 69: SEM images of the pn^+-Si | nat. SiO_2 | Ag sample after performing photoelectrochemical measurements with a magnification of a) 1000 and b) 10000.

6.2 p-Si | µcn-Si | Ag Interface

6.2.1 Energy Band Alignment

Analogous to the previous interface experiments, the p-Si | µcn-Si | nat. SiO_2 | Ag contact was investigated. Figure 70 shows the development of the XP survey spectra of the p-Si | µcn-Si | nat. SiO_2 | Ag interface. As expected the substrate signals O KLL, O 1s, Si 2s and Si 2p become weaker with each deposition step, while the corresponding film signals Ag MNV, AG 3s, Ag 3p and Ag 3d become more intense. It can be noticed that at around 285 eV the bare substrate contains a small amount of carbon, which vanishes with the ongoing interface experiment.

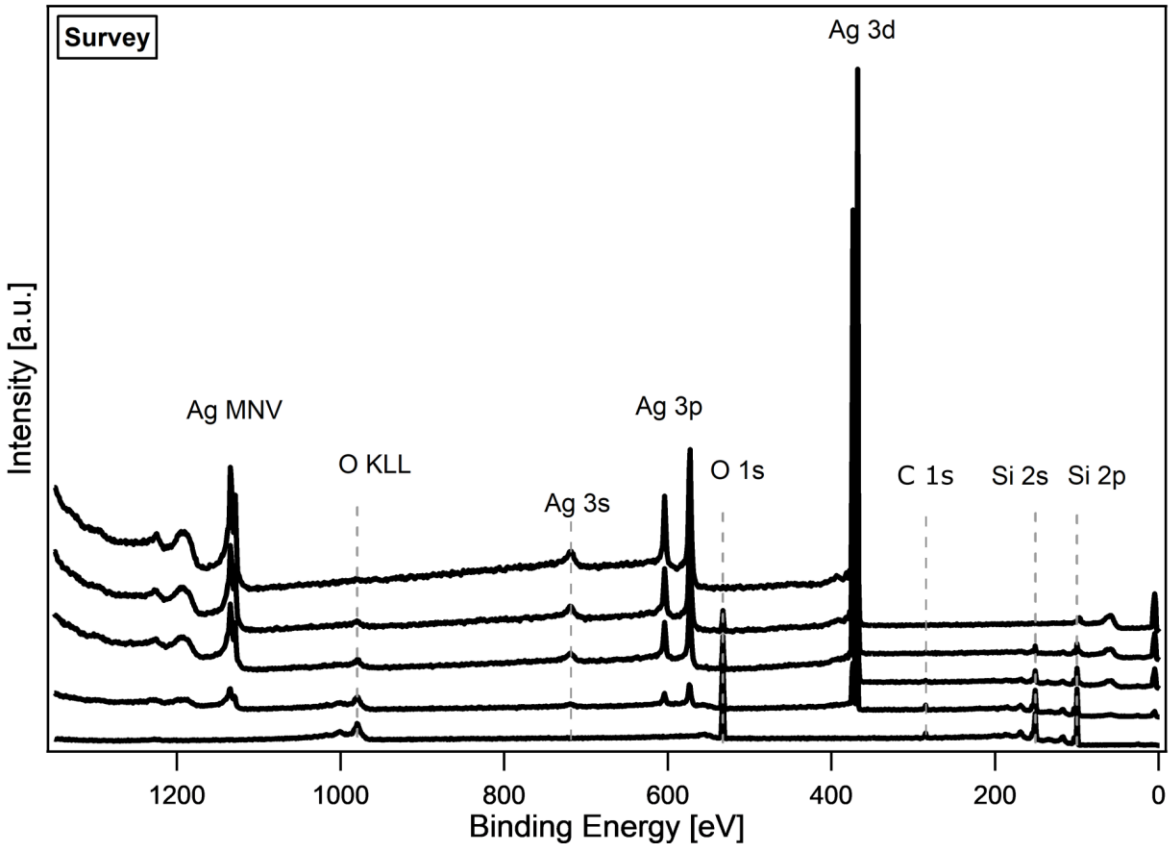

Figure 70: Development of the XP survey spectra of the p-Si | µcn-Si |nat. SiO_2 | Ag contact during the interface experiment. The measurement of the bare p-Si | µcn-Si | nat. SiO_2 substrate is displayed at the bottom of the diagram while the last deposition step at the top shows the final measurement of a relatively thick Ag layer.

The relevant XP detail spectra are shown in Figure 71. At the beginning of the interface experiment only the Si 2p (99.76 eV) and O 1s (533.09 eV) emission lines are present at typical binding energies proving the Si | nat. SiO_2 substrate. After the first deposition step the Ag overlayer reaches a thickness of 15 Å, which does not yet result in a shift of the Si 2p or O 1s emission line. With the following two deposition

steps the Si 2p emission line is shifted to 99.68 eV and the O 1s emission line is detected at 532.90 eV. The Ag 3d emission line reaches its final position at 368.18 eV, which is not further shifted with the last deposition step. The distance from the Ag $3d_{5/2}$ to the Ag $3d_{3/2}$ emission line is 6.01 eV, which indicates the presence of metallic Ag. Furthermore, the loss features within the Ag 3d emission prove the metallic character of the film.

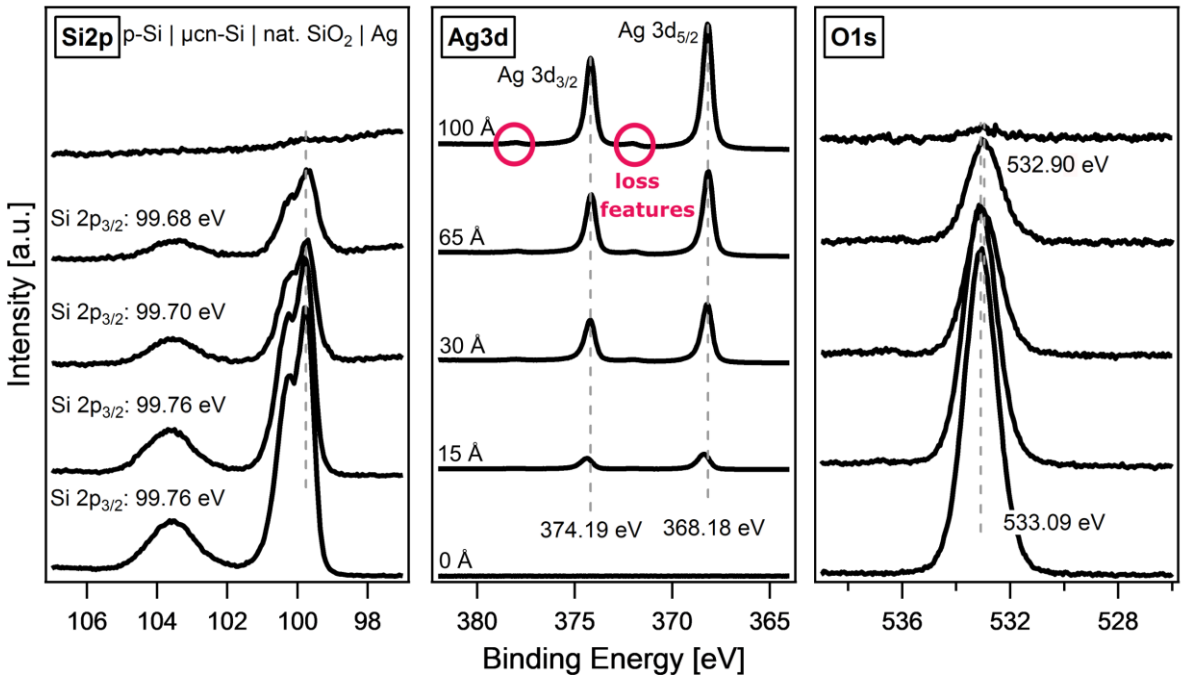

Figure 71: Development of the Si 2p, Ag 3d and O 1s detail spectra of the p-Si | µcn-Si | nat. SiO_2 | Ag contact during the interface experiment. The measurement of the bare p-Si | µcn-Si | nat. SiO_2 substrate is displayed at the bottom of the diagram while the last deposition step at the top shows the final measurement of a relatively thick Ag layer. The marked areas within the Ag 3d emission line show the loss features.

After evaluating the resulting shifts during the interface experiment, the corresponding energy band diagrams can be calculated, which are illustrated in Figure 72. The relevant values are listed in table 10. The band alignment of the bare p-Si | µcn-Si | nat. SiO_2 substrate shows a negligible small upward band bending of 0.05 eV, which can be assumed as flat band situation. When the same substrate was used for the p-Si | µcn-Si | nat. SiO_2 | Cu contact the bands were also assumed to be flat. Aging, which results in a thicker SiO_2 interlayer does not play a major role as the SiO_2 thicknesses are similar for both samples ($d_{SiO2,Cu}$ = 10 Å, $d_{SiO2,Ag}$ = 11 Å). Table 10 gives an overview of the position of the Si $2p_{2/3}$ emission line before and after EC as well as the resulting shift for the pn^+-Si | nat. SiO_2 | Cu/ Ag and the p-Si | µcn-Si | nat. SiO_2 | Cu/ Ag interface.

Table 10: Overview of the position of the Si $2p_{3/2}$ emission line before and after contact formation for the pn^+-Si | nat. SiO_2 | Cu, the pn^+-Si | nat. SiO_2 | Ag as well as the p-Si | µcn-Si | nat. SiO_2 | Cu and the p-Si | µcn-Si | nat. SiO_2 | Ag interfaces.

Model system	**Position of Si $2p_{3/2}$ emission line**		
	before contact	after contact	resulting shift
pn^+-Si | nat. SiO_2 | Cu	99.77 eV	99.48 eV	0.29 eV
pn^+-Si | nat. SiO_2 | Ag	99.70 eV	99.49 eV	0.21 eV
p-Si | µcn-Si | nat. SiO_2 | Cu	99.84 eV	99.84 eV	0.00 eV
p-Si | µcn-Si | nat. SiO_2 | Ag	99.76 eV	99.68 eV	0.08 eV

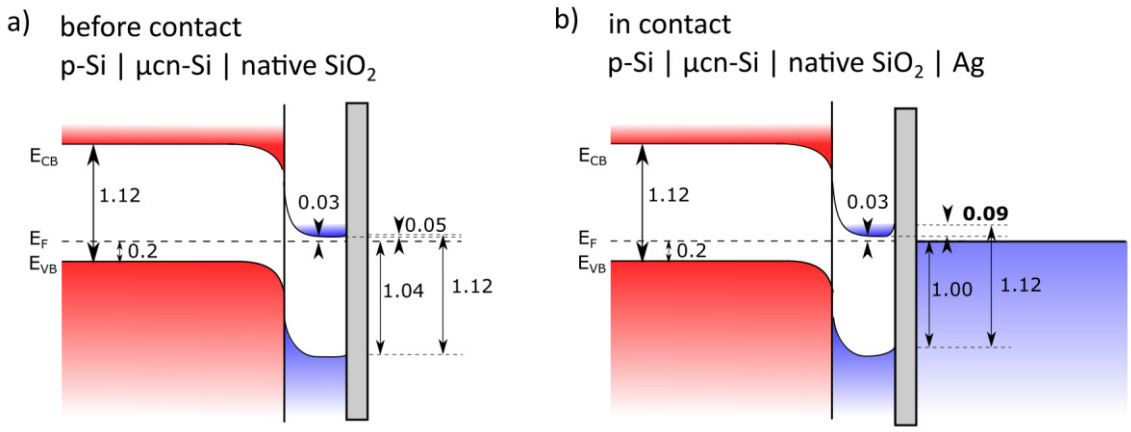

Figure 72: Energy band diagrams before and after contact formation. a) pn^+-Si | nat. SiO_2 before contact formation with an upward band bending of 0.05 eV and b) pn^+-Si | nat. SiO_2 | Ag with an upward band bending of 0.09 eV.

6.2.2 Electrochemistry

From the energy band alignments, it is expected that the p-Si | µcn-Si | nat. SiO_2 | Ag samples show a similar EC performance to the p-Si | µcn-Si | nat. SiO_2 | Cu contact as the energetic barrier at the interface is comparable. Figure 73 shows the comparison of the cyclic voltammetry behavior of the p-Si | µcn-Si | nat. SiO_2 | Ag sample (black) and the p-Si | µcn-Si | nat. SiO_2 | Cu (red) in the dark and under an illumination of 180 W/m^2 with λ = 625 nm in 0.3 M $KHCO_3$.

Obviously, the EC performance is degraded in case of the p-Si | µcn-Si | nat. SiO_2 | Ag sample. The average potential, which is required to obtain a current density of -2 mA/cm^2 under illumination, is -0.6 V (vs. RHE) compared to -0.4 V for the p-Si | µcn-Si | nat. SiO_2 | Cu sample. Furthermore, the

value of the saturation current density is drastically reduced from -6.2 mA/cm^2 for the p-Si | µcn-Si | nat. SiO_2 | Cu sample to -3.8 mA/cm^2 in the first cycle and -2.5 mA/cm^2 in the second cycle for the p-Si | µcn-Si | nat. SiO_2 | Ag sample. In contrast to this, the pn$^+$-Si | nat. SiO_2 | Ag sample showed a similar behavior compared to the corresponding Cu sample in the first cycle of the CV measurement under illumination. Hence, degradation starts earlier in case of the p-Si | µcn-Si | nat. SiO_2 | Ag sample. The dark current proceeds around zero for the overall potential range as it is expected.

The assumed early degradation of the Ag layer can already be proven by the bare eye. After the photoelectrochemical measurements the Ag film seems to be completely dissolved as it can be seen in Figure 74. Only the outer contour which has been protected by an O-ring seems to be remaining. Nevertheless, XPS needs to be performed in order to prove whether the Ag film is completely dissolved.

As already mentioned in case of the previously discussed pn$^+$-Si | nat. SiO_2 | Ag sample, optical absorption may also play a role. However, the effect of dissolving predominates.

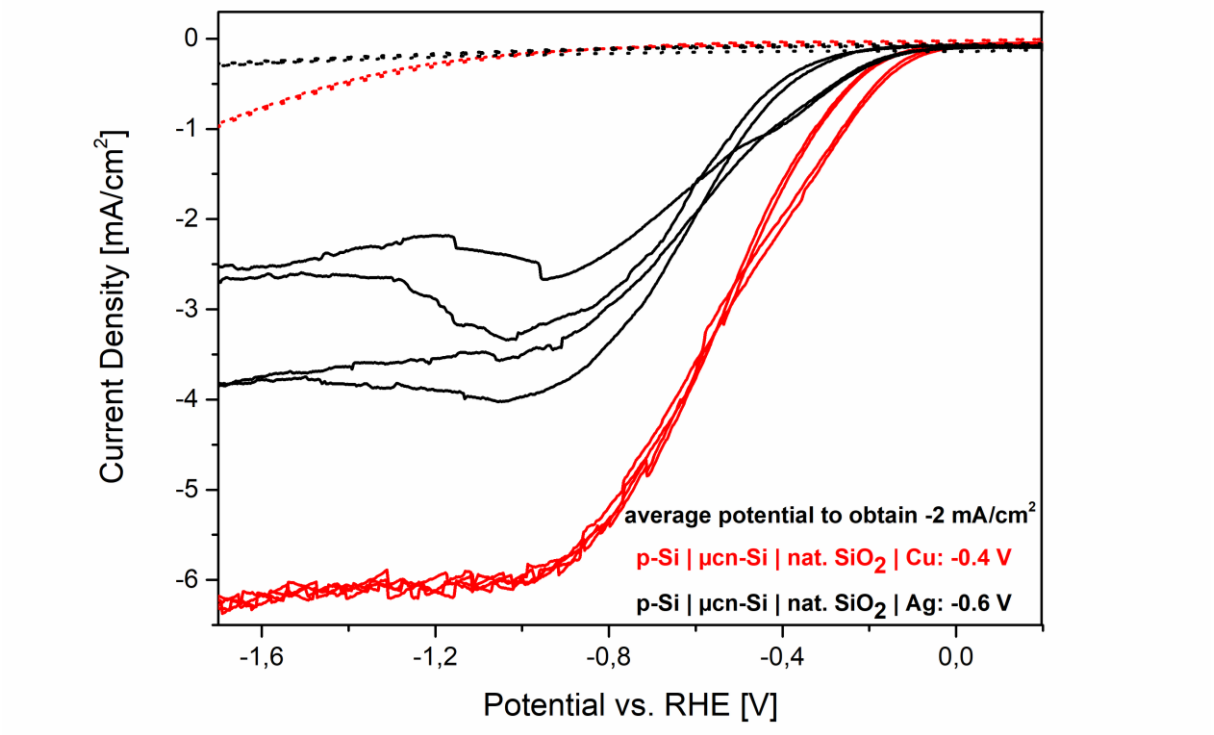

Figure 73: Comparison of the cyclic voltammetry behavior of the p-Si | µcn-Si | nat. SiO_2 | Ag sample (black) and the, p-Si | µcn-Si | nat. SiO_2 | Cu (red) in the dark and under an illumination of 180 W/m^2 with λ = 625 nm in 0.3 M $KHCO_3$. Solid lines: EC behavior under illumination. Dashed lines: EC behavior in the dark.

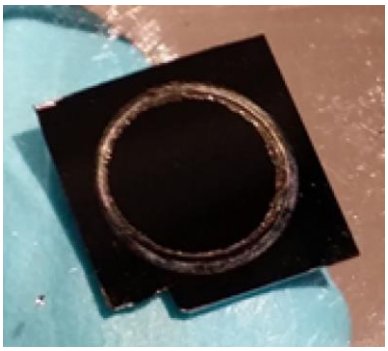

Figure 74: Photograph of the p-Si | µcn-Si | nat. SiO_2 | Ag sample after performing photoelectrochemical measurements. Only the outer edge of the Ag film seems to be preserved.

6.2.3 Characterization after Electrochemistry

As already mentioned in terms of the pn^+-Si | nat. SiO_2 | Ag sample, it needs to be taken into account that XPS probes only a small spot on the sample surface and may not represent the whole surface area. However, XPS analysis was performed in order to verify the presence of a remaining Ag layer. The corresponding detail spectra are shown in Figure 75.

The O 1s emission line at 533.35 eV as well as the peak at 103.83 eV are contributions of the native SiO_2 on the Si substrate, which was already detected on previously investigated Si | Cu and Si | Ag interfaces. Also the underlying Si substrate is detected with the Si 2p emission line at 100.10 eV. The Ag 3d signal proves that a thin layer of Ag (30 Å) is still remaining after performing EC. The Ag $3d_{5/2}$ emission line is detected at 368.96 eV, while the Ag $3d_{3/2}$ emission line lies at 374.95 eV. Both values show a shift of +0.7 eV in terms of ideal metallic Ag, which could be a charging effect. The position of the Ag emission line does not indicate the formation of Ag_2O (Ag $3d_{5/2}$: 367.64 eV).

However, the present background as well as the non-visible loss features are a result of strongly reduced Ag amounts on the sample surface. The C 1s emission line exhibits the same features as the C 1s emission line of the pn^+-Si | nat. SiO_2 | Ag sample after EC. Therefore, the main signal at 285.82 eV as well as the signals at 287.48 eV and 289.90 eV can be allocated to C-H, C-C bonds as well as carbonates, which were most likely formed at the surface because of the used electrolyte (KHCO3). It is also possible that the presence of various carbon species is an indication of the CO_2 reduction reaction.

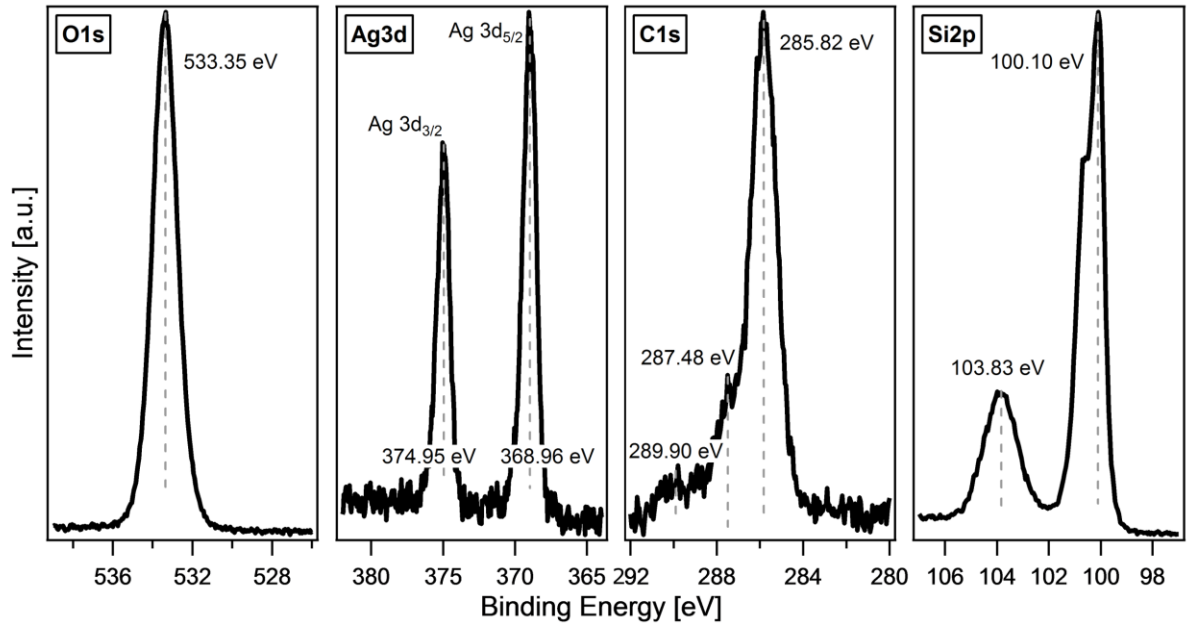

Figure 75: XP detail spectra of the p-Si | µcn-Si | nat. SiO_2 | Ag sample showing the O 1s, Ag 3d, C 1s and Si 2p emission lines after performing cyclic voltammetry measurements.

Additionally, SEM images were performed in order to prove the quality of the Ag film after the photoelectrochemical measurement procedure. Figure 76 presents images with a magnification of 1000 and 10000. Figure 76 a) gives an overview of the sample surface with a magnification of 1000 presenting a whole area, where the Ag film is completely removed. In Figure 76 b) a SEM image under the same conditions was recorded showing a small part of the sample surface, which is still covered by Ag. However, the film is destroyed as it can be seen from folded regions as well as large cracks within the layer. In Figure 76 c) the edge of the p-Si | µcn-Si | Ag sample demonstrates leftovers of the deposited Ag film with a magnification of 10000. It could be proven that the first optical impression of the disturbed Ag film was correct. But still, remaining parts of the Ag film are present on the surface.

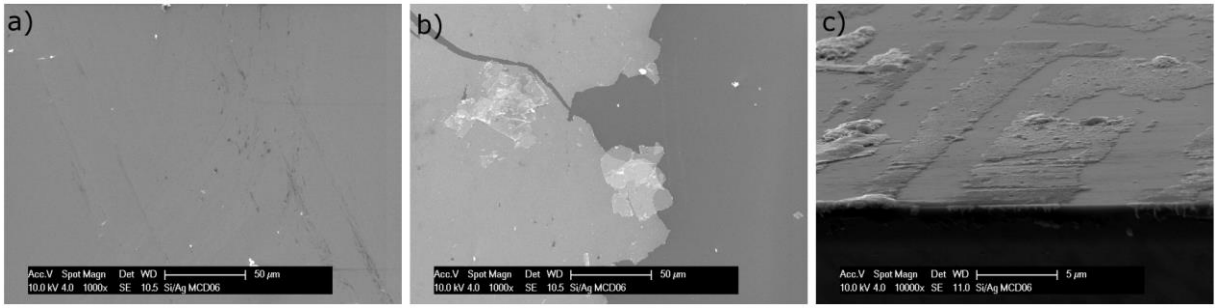

Figure 76: SEM images of a p-Si | µcn-Si | Ag sample after performing photoelectrochemical measurements with a magnification of a) 1000, showing an area where the Ag layer has been completely removed b) 1000, showing an area where the Ag layer is partially preserved and c) 10000, showing the edge of the sample.

6.3 a-Si:H | a-Si:H | µcn-Si:H | Ag Interface

The single µcn-Si:H (pin-Si) | Ag interface was not investigated, as it is equal to the top pin-Si solar cell | Ag contact of the triple a-Si:H | a-Si:H | µcn-Si:H | Ag interface. Hence, the present section will address the electronic band alignment of the a-Si:H | a-Si:H | µcn-Si:H | nat. SiO_2 | Ag contact, the photoelectrochemical performance as well as the catalyst film quality after performing cyclic voltammetry measurements.

6.3.1 Energy Band Alignment

The electronic band structure of a-Si:H | a-Si:H | µcn-Si:H | nat. SiO_2 | Ag was investigated by a XPS interface experiment. The development of the XP survey spectra is presented in Figure 77. As already observed for the previously investigated Si | Ag systems the substrate signals O KLL, O 1s, Si 2s and Si 2p vanish with ongoing interface experiment, while the film signals Ag MNV, Ag 3s, Ag 3p and Ag 3d become more intense with each deposition step. At the beginning of the experiment a small amount of carbon can be detected on the sample surface, which could not be removed by the cleaning steps during sample preparation. Moreover, the Ag 4s, Ag 4p and Ag 4d emission lines arise at 110 eV,

69 eV and 11 eV. As these emission lines are not relevant for the evaluation of the experiment, they are not assigned within the XP survey spectrum.

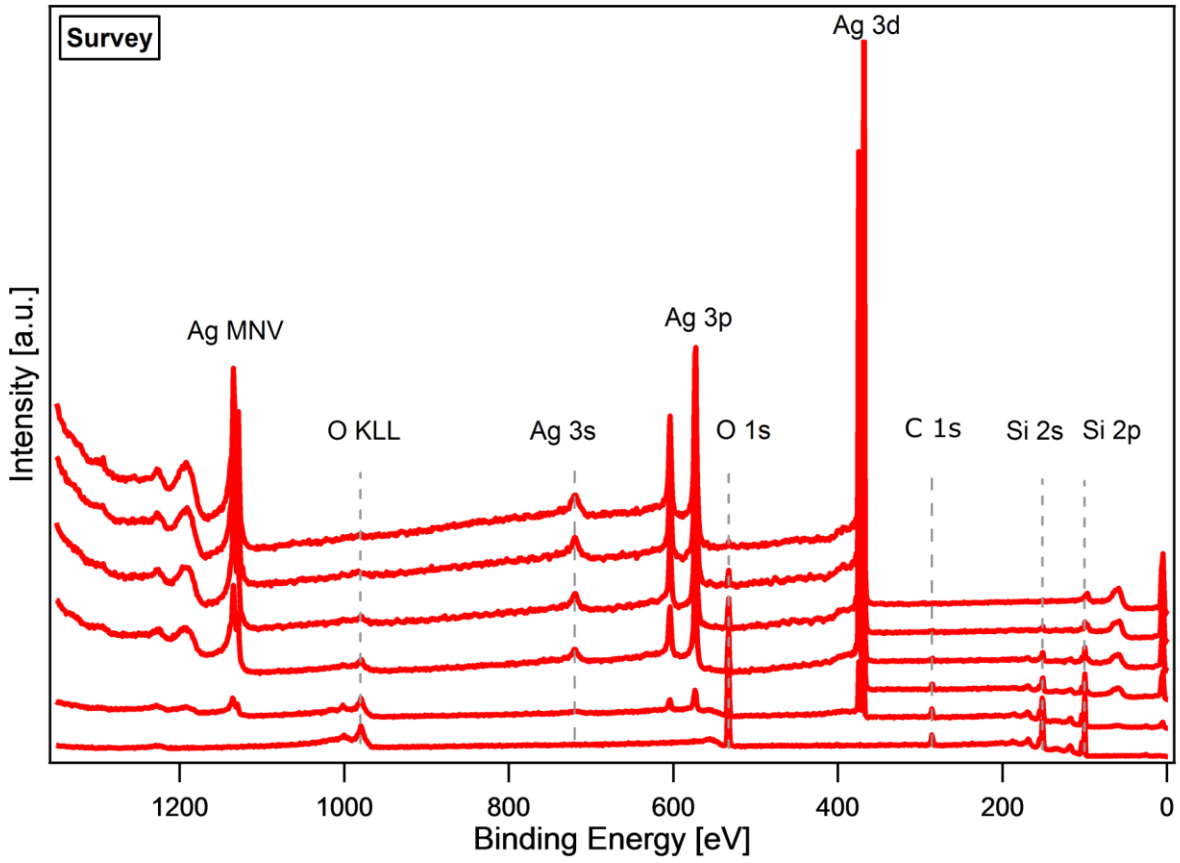

Figure 77: Development of the XP survey spectra of the a-Si:H | a-Si:H | µcn-Si:H | nat. SiO_2 | Ag contact during the interface experiment. The measurement of the bare a-Si:H | a-Si:H | µcn-Si:H | nat. SiO_2 substrate is displayed at the bottom of the diagram while the last deposition step at the top shows the final measurement of a relatively thick Ag layer.

The relevant XP detail spectra are displayed in Figure 78, showing the development of the Si 2p, Ag 3d and O 1s emission lines. At the beginning of the interface experiment when no Ag has been deposited on the a-Si:H | a-Si:H | µcn-Si:H | nat. SiO_2 substrate, the Si $2p_{3/2}$ emission line can be detected at a binding energy of 99.81 eV, which is comparable with the value of the µcn-Si:H (pin)-Si | nat. SiO_2 substrate from the pin-Si | nat. SiO_2 | Cu interface experiment (99.82 eV). Therefore, the initial electronic situation at the surface is more or less the same, which was expected as the top solar cell of the triple junction is identical to the single pin-Si solar cell structure.

With growing Ag film thickness the Si $2p_{3/2}$ emission line is shifted to lower binding energies until it reaches its final position at 99.71 eV. The Ag film, which has a thickness of about 103 Å at the end of the interface experiment, exhibits metallic character. This can be proven by the positions of the Ag $3d_{5/2}$

and Ag $3d_{3/2}$ emission lines at 368.46 eV and 374.45 eV, respectively. Moreover, the loss features within the Ag 3d emission indicate the deposition of metallic Ag. The O 1s emission shows only a very small shift in position and vanishes with each deposition step.

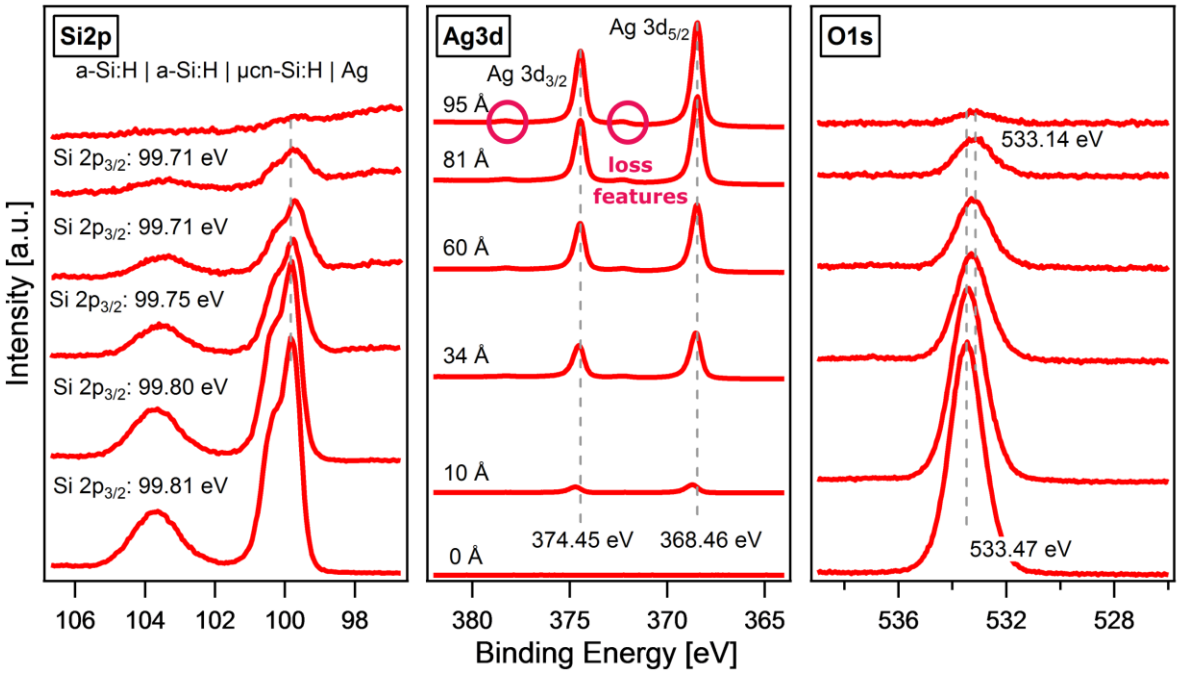

Figure 78: Development of the Si 2p, Ag 3d and O 1s detail spectra of the a-Si:H | a-Si:H | µcn-Si:H | nat. SiO_2 | Ag contact during the interface experiment. The measurement of the bare a-Si:H | a-Si:H | µcn-Si:H | nat. SiO_2 substrate is displayed at the bottom of the diagram while the last deposition step at the top shows the final measurement of a relatively thick Ag layer. The marked areas within the Ag 3d emission line show the loss features.

From the data of the XPS analysis the energy band diagram before and after contact formation can be calculated. The resulting band alignments are illustrated in Figure 79. Here, the contact formation of the underlying solar cells is schematically drawn as XPS gives only information about the surface. However, the band gap as well as the distance of the valence band to the Fermi level in the p-layer of the µcn-Si:H solar cell is known. The band gap of the underlying a-Si:H solar cells is slightly larger compared to the one of the µcn-Si:H solar cell, which was described in chapter 2.3. Before being in contact to Ag a flat band situation is given at the surface, which can be seen in Figure 79 a). The presence of a flat band situation was also given in case of the corresponding Cu sample (pin-Si | nat. SiO_2 | Cu). After the Ag contact has formed the energy bands slightly bend upwards resulting in an energy barrier of 0.12 eV, which is also comparable to the 0.13 eV for the pin-Si | nat. SiO_2 | Cu contact.

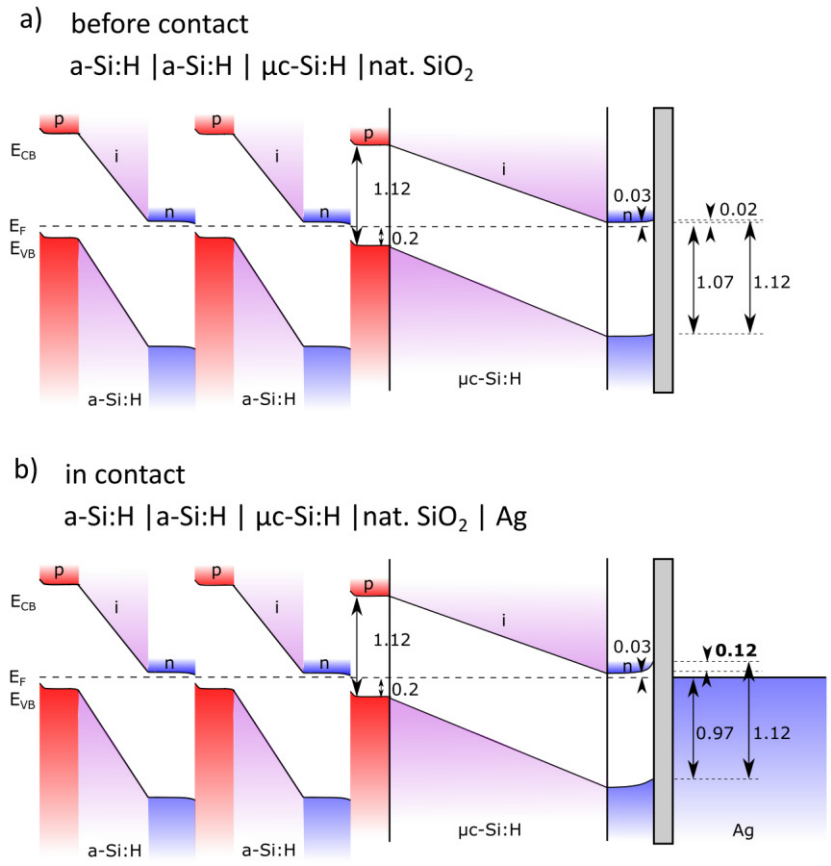

Figure 79: Energy band diagrams before and after contact formation. a) a-Si:H | a-Si:H | µcn-Si:H | nat. SiO_2 before contact formation with an upward band bending of 0.02 eV and b) a-Si:H | a-Si:H | µcn-Si:H | nat. SiO_2 | Ag with an upward band bending of 0.12 eV.

6.3.2 Electrochemistry

Figure 80 shows a comparison of the a-Si:H | a-Si:H | µcn-Si:H | nat. SiO_2 | Ag sample (red) and the a-Si:H | a-Si:H | µcn-Si:H | nat. SiO_2 | Cu sample (grey) in the dark and under solar simulation. It can be noted that the onset potential is earlier in case of the Cu sample. While 1.1 V (vs. RHE) are required to reach a current density of -2 mA/cm^2 for the Cu sample, the 0.8 V are necessary for the Ag sample. The shift of the onset potential to more cathodic potentials was already observed for the previously investigated Si | Ag systems in comparison to the corresponding Cu samples. As for the a-Si:H | a-Si:H | µcn-Si:H | nat. SiO_2 | Cu sample, the potential range up to +1.6 V is beyond the stability region of metallic Ag. However, no redox wave indicating Ag oxidation was measured. But still it cannot be excluded that the Ag film has been partially detached within the measurement procedure.

The maximum reached saturation current density of the Cu sample is -6.7 mA/cm^2, while the Ag sample reaches a value of -9.0 mA/cm^2. However, the CV curve under illumination of the Ag sample does not saturate, which might be a sign of a slowly dismantling solar cell. In contrast to the pn$^+$-Si | nat. SiO_2 | Ag sample and the p-Si | µcn-Si | nat. SiO_2 | Ag sample, the two cycles under illumination are not very

different from each other. While in previous measurements the Ag film detached during cycling which resulted in a reduced EC performance in the second cycle, this phenomenon cannot be observed in case of the present a-Si:H | a-Si:H | µcn-Si:H | nat. SiO_2 | Ag sample.

This leads to the assumption that the adhesion of the Ag film is improved on the a-Si:H | a-Si:H | µcn-Si:H substrate as it does not detach. This assumption can already be verified by inspecting the sample after demounting it from the measurement setup as shown in the photograph in Figure 81. Additionally, it needs to be mentioned that the difference in optical absorption between Ag and Cu is negligible in this case as the measurement setup in case of solar simulation allows an illumination directly through the solar cell without attenuation of the catalytic layer. The corresponding setup was described in chapter 3.3.

The CV characteristics in the dark is comparable to the Cu sample, which leads to the assumption that here also lateral current flow needs to be taken into account. As both contact materials (Ag and Cu) are excellent electrically conductive materials, good lateral current flow is reasonable.

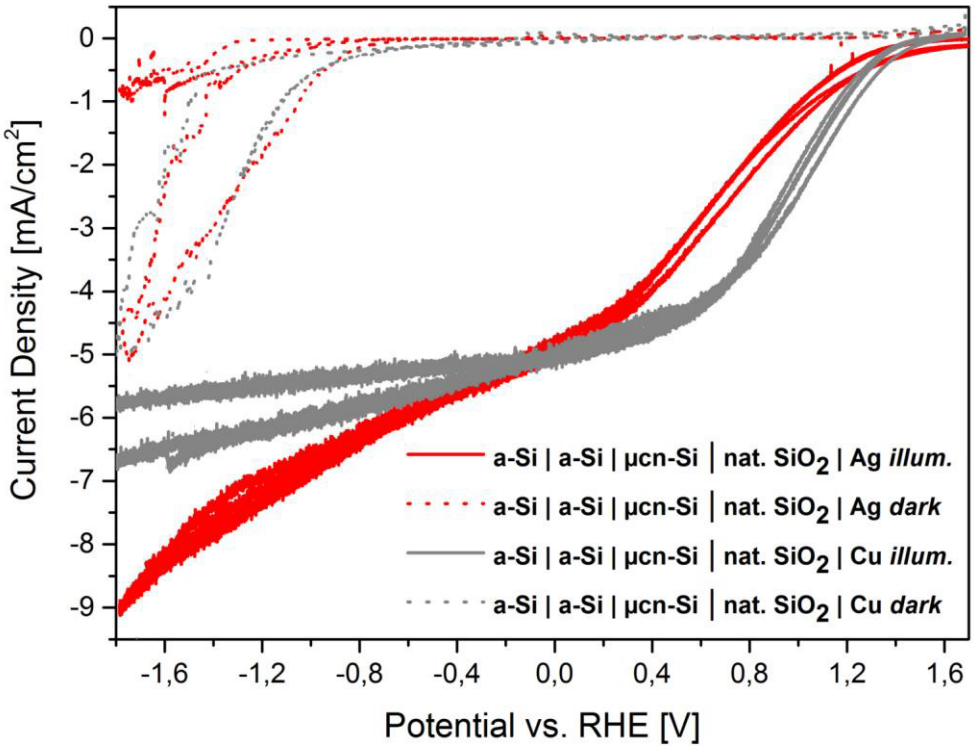

Figure 80: Comparison of the cyclic voltammetry behavior of the a-Si:H | a-Si:H | µcn-Si:H | nat. SiO_2 | Ag sample (red) and the, a-Si:H | a-Si:H | µcn-Si:H | nat. SiO_2 | Cu (grey) in the dark and under solar simulation of AM 1.5 G (1000 W/m²) in 0.3 M $KHCO_3$. Solid lines: EC behavior under illumination. Dashed lines: EC behavior in the dark.

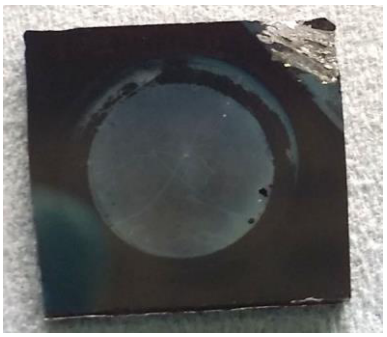

Figure 81: Photograph of the a-Si:H | a-Si:H | µcn-Si:H | nat. SiO_2 | Ag sample after performing photoelectrochemical measurements. From the first impression it seems that the Ag film is still intact.

6.3.3 Characterization after Electrochemistry

Contrary to the previously analyzed Ag samples, the Ag film in the a-Si:H | a-Si:H | µcn-Si:H | nat. SiO_2 | Ag sample has not been dissolved during EC. Therefore, it is expected that XP spectra after EC show a more distinct Ag 3d emission line with less background. But first, the O 1s emission line is shown in Figure 82. Its maximum position can be detected at a binding energy of 533.45 eV, which fits well to all earlier measurements of Ag samples. The position is correlated to the underlying native SiO_2 layer, which covers the a-Si:H | a-Si:H | µcn-Si:H substrate. The Si 2p emission line at 100.05 eV as well as the SiO_2 peak at 103.87 eV are as to be expected for non-reacted surfaces and clearly correspond to the a-Si:H | a-Si:H | µcn-Si:H substrate.

The Ag $3d_{5/2}$ emission line arises at 368.40 eV and the Ag $3d_{3/2}$ emission line has its maximum at 374.39 eV, which results in a typical distance of 5.99 eV for metallic Ag. As the Ag film was not dissolved after EC it is assumed to be thicker compared to the Ag films on the pn^+-Si and p-Si | µcn-Si substrates. This assumption can be confirmed by a lower background in the Ag 3d spectrum as well as the clearly visible loss features. On the other hand calculations according to chapter 4.5 have shown that the Ag film in the present experiment still has a thickness of 50 Å, in contrast to the 30 Å thick Ag films on the pn^+-Si and p-Si | µcn-Si substrates. The C 1s emission does not differ from the spectra of the previously analyzed Ag samples. The main contributions at 285.91 eV, 287.90 eV and 289.92 eV correspond to C-H, C-C and C-O bonds.

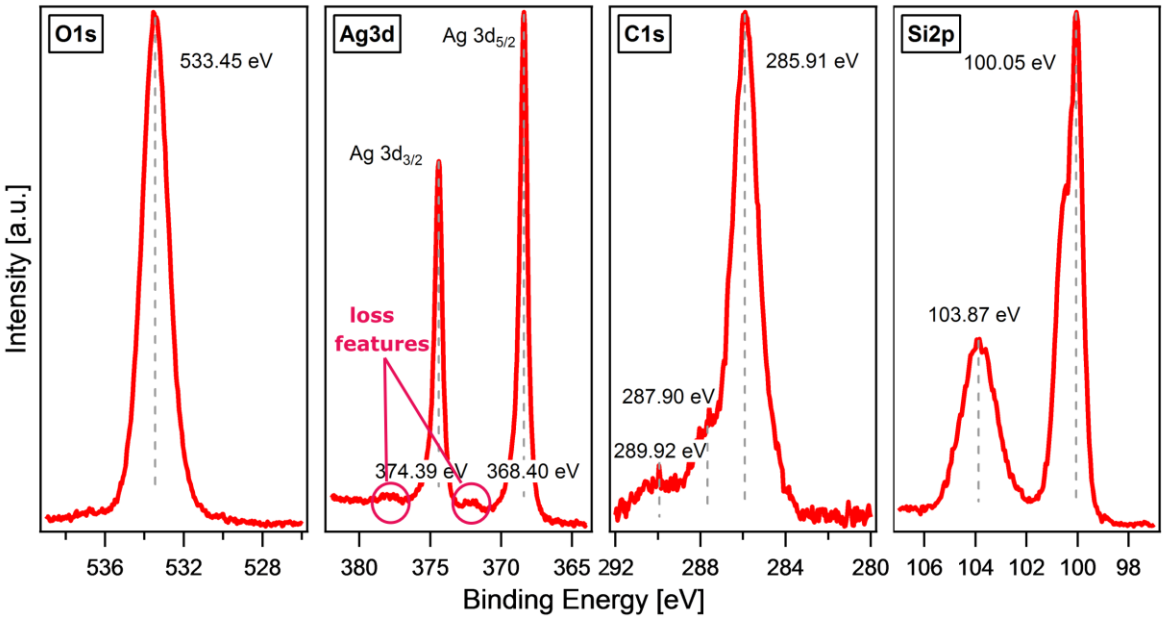

Figure 82: XP detail spectra of the a-Si:H | a-Si:H | µcn-Si:H | nat. SiO_2 | Ag sample showing the O 1s, Ag 3d, C 1s and Si 2p emission lines after performing cyclic voltammetry measurements. The marked areas within the Ag 3d emission line show the loss features.

From the optical impression of the a-Si:H | a-Si:H | µcn-Si:H | nat. SiO_2 | Ag sample as well as the corresponding Ag 3d XP detail spectrum it was expected that the Ag film is preserved after performing CV measurements, which is in contrast to the previously examined Ag samples. SEM images in Figure 83 prove that the Ag film is not as damaged as in case of the pn^+-Si | nat. SiO_2 | Ag or p-Si | µcn-Si | nat. SiO_2 | Ag sample. From the overview image in Figure 83 a) with a magnification of 1000, it can be seen that the Ag layer is slightly rough and exhibits small holes and cracks. However, in general the deposited layer seems to be preserved quite well. In Figure 83 b) the edge of the sample is shown, where it becomes visible that the Ag film is partially blown up from the Si surface but is still intact.

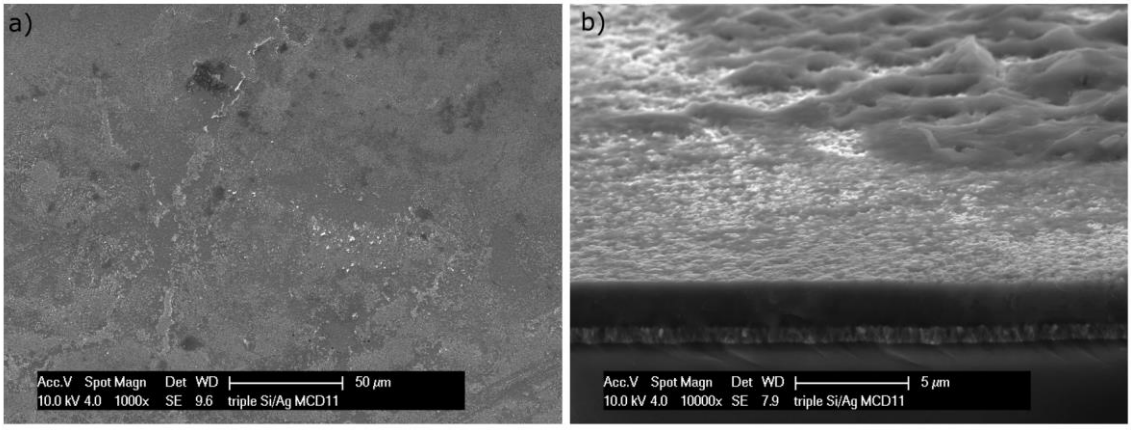

Figure 83: SEM images of an a-Si:H | a-Si:H | µcn-Si:H | Ag sample after performing photoelectrochemical measurements with a magnification of a) 1000 and b) 10000.

6.4 Comparison of all Si | Metal Interfaces

Table 11 gives an overview of all obtained results from XPS as well as electrochemical measurements. It can be concluded that compared to the corresponding Cu samples the electronic structure at the Si | Ag interface is very similar. Nevertheless, the resulting photoelectrochemical performance is reduced in terms of more negative onset potentials as well as instability for the Ag films. The latter becomes apparent by a decrease of the absolute value of the saturation current density under illumination while cycling. First assumptions of dissolving the Ag film from the pn^+-Si and p-Si | µcn-Si substrate during EC were proven by XPS as well as SEM images.

On the a-Si:H | a-Si:H | µcn-Si:H substrate the adhesion of the Ag film seems to be improved, which could be seen in stable CV curves under illumination as well as in XPS and SEM images. However, the illuminated CV curve characteristics of the a-Si:H | a-Si:H | µcn-Si:H | Ag sample differs from the a-Si:H | a-Si:H | µcn-Si:H | Cu sample as it does not saturate. Therefore, solar cell damage cannot be completely excluded. But still it could be shown that there is a correlation between the energy band alignment and the photoelectrochemical performance. If the energy barrier between the Si | Ag interface is low, electrochemical parameters such as onset potential as well as saturation current density are improved and vice versa. The same trend was observed in case of the Si | Cu interfaces.

The Ag film thickness was reduced in a similar way as the Cu film during the photoelectrochemical measurements. But, in contrast to the Cu samples the Ag films remained metallic during EC even without nitrogen gas bubbling.

It can also be concluded that in case of the a-Si:H | a-Si:H | µcn-Si:H | Ag sample a high dark current could be measured as it was already the case for the corresponding Cu sample. It can be noted that Ag as well as Cu are both excellent electrically conductive and hence a lateral current flow could explain the effect of high dark currents. A second possible explanation was diffusion along grain boundaries of the solar cell resulting in a leakage current. This assumption could be also valid for Ag atoms. However, further experiments are necessary to prove which theory is more reasonable.

Moreover, a detailed product analysis of the CO_2 reduction reaction should be done in order to compare the conversion efficiency of Cu and Ag as catalytic active material. Nevertheless, Cu seems to be the better catalyst as well as contact material due to low adhesion of Ag on the Si substrate during EC measurements.

Table 11: Overview of the results from the XPS as well as photoelectrochemical measurements of all pn⁺-Si | Ag, p-Si | µcn-Si | Ag and a-Si:H | a-Si:H | µcn-S:H | Ag samples in comparison to the corresponding Cu samples. The electrochemical parameters refer to an illumination with λ=625 nm, unless otherwise stated. [1)] first cycle of CV measurement, [2)] second cycle of CV measurement, [*] theoretical values,[#] does not correspond to saturation current density.

Model system	**Position of Si $2p_{3/2}$ emission line**		
	before contact	after contact	resulting shift
pn^+-Si | nat. SiO_2 | Ag	99.70 eV	99.49 eV	0.21 eV
pn^+-Si | nat. SiO_2 | Cu	99.77 eV	99.48 eV	0.29 eV
p-Si | µcn-Si | nat. SiO_2 | Ag	99.76 eV	99.68 eV	0.08 eV
p-Si | µcn-Si | nat. SiO_2 | Cu	99.84 eV	99.84 eV	0.00 eV
a-Si:H | a-Si:H | µc-Si:H | nat. SiO_2 | Ag	99.81 eV	99.71 eV	0.10 eV
a-Si:H | a-Si:H | µc-Si:H | nat. SiO_2 | Cu	99.82 eV[*]	99.70 eV[*]	0.12 eV[*]

	potential to reach -2 mA/cm² [V vs. RHE]	$J_{sat,illum}$ [mA/cm²]	$J_{sat.dark}$ [mA/cm²]	$eV_{b,n}$ [eV]
pn^+-Si | nat. SiO_2 | Ag	-0.6[1)], -0.8[2)]	-6.0[1)], -3.6[2)]	-0.7	+0.34
pn^+-Si | nat. SiO_2 | Cu	-0.6	-6.0	-1.1	+0.35
p-Si | µcn-Si | nat. SiO_2 | Ag	-0.6	-3.8[1)], -2.5[2)]	-0.3	+0.09
p-Si | µcn-Si | nat. SiO_2 | Cu	-0.4	-6.2	-0.6	+0.01
a-Si:H | a-Si:H | µc-Si:H | nat. SiO_2 | Ag (AM 1.5 G)	+0.8	-9.0[#]	-5.0	+0.12
a-Si:H | a-Si:H | µc-Si:H | nat. SiO_2 | Cu (AM 1.5 G)	+1.1	-6.7	-4.7	+0.13[*]

7 Summary and Outlook

An artificial leaf, which is able to convert CO_2 directly into fuels with the use of sunlight can be a solution of today's challenge of storing energy from renewable energy sources. One main component of such an artificial leaf is the photocathode, where the CO_2 reduction reaction should take place. For this application the interface between the photo absorber material and the catalyst material plays an important role. In this work Si based single- and multijunctions were investigated as absorber material, while Cu and Ag were chosen as catalyst. The aim was to systematically understand the Si | Cu and Si | Ag interface in terms of electronic band alignment as well as in the corresponding photoelectrochemical behavior.

Starting from a very basic model system, which uses a p-Si wafer as photocathode, the model system became more and more advanced. In the next steps, pn^+-Si and p-Si | µcn-Si junctions were used as well as µcn-Si:H and a-Si:H | a-Si:H | µcn-Si:H solar cells with p-i-n configuration. In order to modify the surface of the used Si substrates, different preparation methods were used to achieve a well-defined surface termination. Here, a treatment with acetone, isopropanol and MilliQ water was used to prepare Si | nat. SiO_2 surfaces. Also hydrogen terminated surfaces were investigated, which were realized by an etching procedure with HF, NH_4F and Piranha solution. Furthermore, thermal SiO_2 layers were grown on different Si:H surfaces by a heat treatment in plasma under a specific pressure. However, heat treatment was not an option for all samples as the microcrystalline Si structure is destroyed by high temperatures. Also the hydrogen termination was not possible for all Si substrates as the used solar cells are not stable under to necessary etching procedure.

All different Si surfaces were covered stepwise by metallic Cu or Ag within an XPS interface experiment. Here, the used deposition method was electron-beam deposition. The XPS data after each deposition step allowed the calculation of the electronic band alignment of the initial Si substrate before contact formation as well as the resulting Si | Cu or Si | Ag contact.

After the investigation of the electronic band structure of the different model systems, the photoelectrochemical performance was analyzed. A special focus was given on the relation of the electronic band alignment and the resulting electrochemical efficiencies. The electrochemical results were obtained by cyclic voltammetry measurements in a three electrode setup. The measurements were performed in dark and under illumination. Depending on which absorber material was used, a red LED with a wavelength of 625 nm or a solar simulator with AM 1.5 G was used. 0.3 M $KHCO_3$ was chosen as appropriate electrolyte for the electrochemical experiments. Furthermore, the effects of nitrogen gas bubbling during the cyclic voltammetry measurements was investigated with respect to possible modifications of the metallic catalyst.

In order to prove how the electrochemical measurement influences the catalyst material, XPS was performed afterwards. Furthermore, SEM images served as characterization method of the catalytic film quality before and after cyclic voltammetry.

From all performed experiments it can be concluded that the electronic band alignment of the p-Si | therm. SiO_2 | Cu contact is limited due to midgap defects and Fermi level pinning as a consequence. Therefore, further experiments, which uses a p-Si wafer as substrate were considered not to be reasonable. For the pn^+-Si | Cu model system, the energy band alignment is dependent on the surface termination. The pn^+-Si | Cu contact with a well-defined thermally grown SiO_2 interlayer results in a low energetic barrier of 0.27 eV at the interface, whereas a native SiO_2 interlayer leads to an increased barrier of 0.35 eV and the hydrogen terminated pn^+-Si surface forms an upward band bending of 0.45 eV in contact with Cu. It was found that during the deposition procedure a Cu_2O interface phase is formed on those Si surfaces which were covered by a SiO_2 layer. It was assumed that the Cu reacts with the SiO_2 and forms Cu_2O and SiO_{2-x}. The additional Cu_2O layer may influence the energetic band alignment, which was not considered in this work.

From the investigated energy band diagrams it was assumed that the photoelectrochemical performance is improved for those samples with lower energetic barrier at the interface, as the electronic transport across the interface is easier. The performed cyclic voltammetry measurements under an illumination with a red LED (625 nm) have confirmed this assumption. While all three samples with different surface terminations reach a saturation current density around -6 mA/cm^2, the onset potential is different. To obtain a current density of -2 mA/cm^2 the applied potential needs to be -0.4 V vs. RHE for the pn^+-Si | therm. SiO_2 | Cu sample, -0.6 V vs. RHE for the pn^+-Si | nat. SiO_2 | Cu sample and -0.7 V vs. RHE for the pn^+-Si:H | Cu sample. It can be concluded that low energy barriers at the Si | Cu interface result in earlier onset potentials when measuring cyclic voltammetry under illumination. In the dark the current density for all three model systems is around zero as it can be expected. Additionally, it should be mentioned that the position of the conduction band may be different for the experiments in the dark and under illumination, which may result in a different charge transfer.

The Cu films are still mostly intact after performing the photoelectrochemical measurements. However, it was shown by XPS that additional bubbling with nitrogen gas during cyclic voltammetry is necessary in order to retain the metallic character of the film. Otherwise, oxygen which is available in the electrolyte reacts with the Cu surface forming $Cu(OH)_2$. Furthermore, the C 1s emission line yields information about a possibly occurring chemical reaction. It is assumed that the CO_2 reduction reaction has taken place, although this assumption was not proven experimentally. However, a detailed analysis of chemical reaction products is necessary for example by gas chromatography. In order to perform such experiments, a gas chromatography setup needs to be built up or a cooperation with another research group is necessary. Besides XPS, SEM was used to qualitatively characterize the Cu films. It was

demonstrated that the Cu films were perfectly smooth directly after deposition, while after performing photoelectrochemical measurements, the films are damaged, but still preserved.

The same interface investigating experiments were performed for the p-Si | µcn-Si | Cu contact. It was found that the energy band alignment is advantageous for those samples containing a passivating SiO_2 interlayer. In terms of band alignment it does not play a role whether the SiO_2 layer is native or thermally grown. A flat band situation is given for native and thermal SiO_2, respectively. The hydrogen terminated p-Si | µcn-Si surface exhibits a strong upward band bending of 0.55 eV when being in contact with Cu. As the microcrystalline Si structure is not stable under high temperatures, which drastically decreases the photoelectrochemical performance, the p-Si | µcn-Si | therm. SiO_2 | Cu model system should not be further taken into account. The p-Si | µcn-Si | nat. SiO_2 | Cu and the p-Si | µcn-Si:H | Cu samples exhibit similar cyclic voltammetry behavior. While the sample with the native SiO_2 interlayer reaches a more negative saturation current density of -6.2 mA/cm^2, the current density of the hydrogen terminated surface saturates already at -5.5 mA/cm^2. Nevertheless, the onset potential is equal. Both samples need an applied potential of -0.4 V vs. RHE to reach a current density of -2 mA/cm^2 under illumination. That the sample with hydrogen termination shows a similar photoelectrochemical behavior although the energetic barrier is comparable high, could be explained by the ability of electrons to tunnel through the thin barrier. In the dark the cyclic voltammetry curves proceed flat around zero, as expected.

As for the pn$^+$-Si | Cu samples the Cu film of the p-Si | µcn-Si | Cu samples are mostly intact after photoelectrochemical measurements. The films still show metallic character as long as nitrogen gas is bubbled during the cyclic voltammetry test. Also SEM images prove the intactness of the Cu films after performing photoelectrochemical measurements, although the films were smoother directly after deposition. The different surface terminations do not influence the stability of the Cu films.

For the more advanced µc-Si:H (pin-Si single junction) | Cu model system only samples with a native SiO_2 interlayer were investigated. Reason for that is the instability of the microcrystalline Si structure under high temperatures as well as possible solar cell damages due to etching procedure, which is necessary for hydrogen termination. Furthermore, it was already shown that Si | Cu samples with native SiO_2 exhibit advantageous energy band alignments as well as sufficient photoelectrochemical performance. The upward band banding, which forms at the pin-Si | nat. SiO_2 | Cu interface is quite low with an energy of 0.13 eV. The cyclic voltammetry measurements were performed in the dark and under an illumination of a red LED (625 nm) as well as under solar simulation (AM 1.5 G). In both experiments a potential of -0.2 V vs. RHE was sufficient to reach a current density of -2 mA/cm^2. However, the maximum amount of current density is up to -16.0 mA/cm^2 in case of solar simulation and -5.5 mA/cm^2 if illuminated with the red LED. The different current densities are due to different light intensities as well as different amount of generated electron hole pairs. Furthermore, it was found that the dark current reaches a value of -3.5 mA/cm^2, which is beyond expectations. It is assumed that the dark cyclic voltammetry curve represents the occurrence of a lateral current. However, this assumption should be

proven by future experiments. Contrary to the previously introduced Si | Cu model systems, the more porous solar cells structure may allow Cu atoms to diffuse along grain boundaries.

After performing the photoelectrochemical measurements, XPS has proven that the Cu film is still present and exhibits metallic character as long as the electrolyte was bubbled with nitrogen gas. SEM images show that the Cu film is reasonable stable during the experimental procedure.

Finally, an a-Si:H | a-Si:H | µc-Si:H solar cell with p-i-n configuration was used as advanced Si | Cu system. For the same reasons as for the pin-Si solar cell only native SiO_2 was used as surface termination. As the top cell of the triple junction a-Si:H | a-Si:H | µc-Si:H solar cell is identical with the pin-Si solar cell, the energy band alignment does not need to be determined. It can be assumed that the energetic situation at the Cu contact is equal, which means an upward band bending of 0.13 eV. The corresponding electrochemical measurements were performed under solar simulation and in the dark. Under illumination the onset potential is strongly shifted to less cathodic potentials. A potential of +1.1 V is sufficient to reach a current density of -2 mA/cm^2. The overall reached current density saturated at -6.7 mA/cm^2. The different electrochemical performance can be assigned to the wide band gap of amorphous Si. In the dark a high lateral current flow can be measured, which reaches a current density of -4.7 mA/cm^2. This behavior was already observed for the pin-Si | Cu model system.

After the systematical investigation of the Si | Cu interface, the Si | Ag interface was characterized in a similar way. The used Si substrates were pn$^+$-Si, p-Si | µcn-Si, pin-Si and a-Si:H | a-Si:H | µc-Si:H. Native SiO_2 was chosen as surface termination for all model systems. It was shown that the energy bands at the Si | Ag interface align very similar to the corresponding Si | Cu interfaces, which is due to very similar work functions. However, the photoelectrochemical performance is different when Ag is used as catalyst material. The onset potential is always at a more cathodic potential compared to the analogous Cu sample. Also the saturation current densities are less in case of the Ag samples. Reason for the reduced photoelectrochemical performance is the instability of the Ag films. It was shown by XPS as well as by SEM that the Ag layers easily detach during cyclic voltammetry measurements.

Conclusively, it can be outlined that the Si | Cu and the Si | Ag interface was systematically investigated by XPS, CV and SEM measurements. Different Si surface terminations result in different electronic band alignments, which in turn are related to the photoelectrochemical performance. This knowledge should be exploited to control electrochemical parameters with interface engineering.

The most important next steps are the analysis of the chemical reaction products and to perform measurements of solar cells after Cu/ Ag deposition as solid state devices. A more detailed knowledge concerning the lateral current flow in a solar cell would also be helpful in order to understand the CV behavior in the dark. Furthermore, the analyses of the chemical reaction products is necessary as this is the most significant issue in terms of the application of an artificial leaf. Here, gas chromatography is an appropriate method to be used. Moreover, the photoelectrochemical measurement procedure can be

improved by introducing CO_2 gas during cyclic voltammetry. The mentioned problem of possible Cu and Ag diffusion could be proven by energy dispersive X-ray spectroscopy (EDX) or secondary ion mass spectroscopy (SIMS). However, the sample preparation is challenging for fragile and thin samples. In case of confirmed Cu and Ag diffusion an additional buffer layer between the Si solar cell and the catalyst material could prevent the diffusion problem and hence, avoid the occurrence of a leakage current.

Appendix

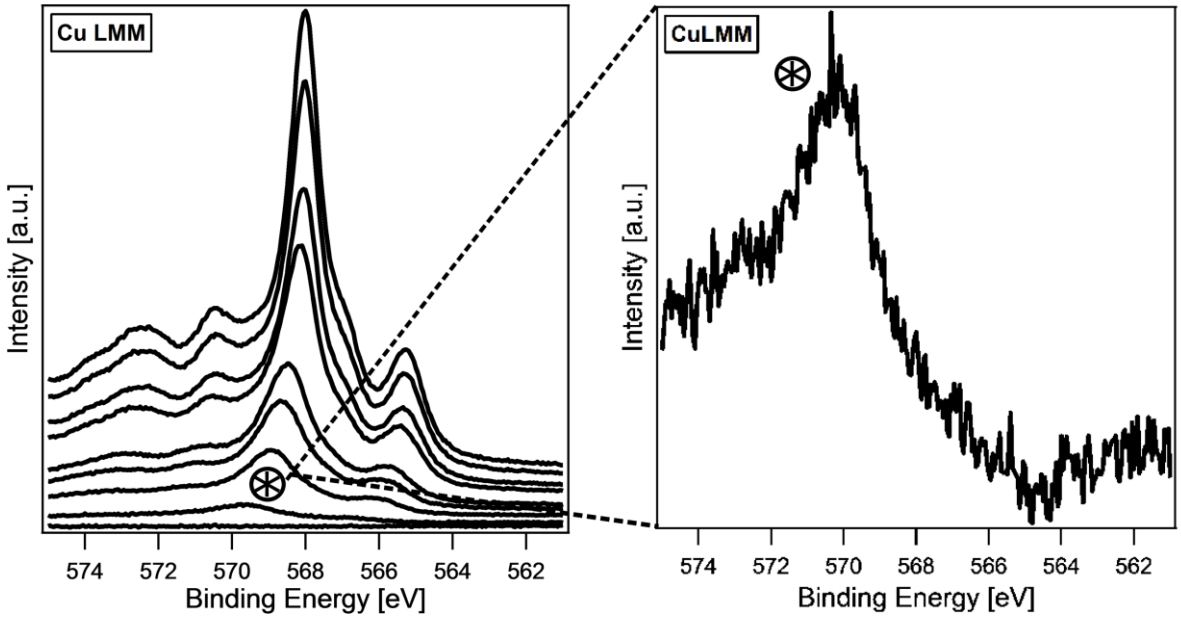

A 1: Development of the Cu LMM Auger emission line during the p-Si | therm. SiO_2 | Cu interface experiment. The measurement of the bare p-Si | therm. SiO_2 substrate is displayed at the bottom of the diagram while the last deposition step at the top shows the final measurement of a relatively thick Cu layer (0 Å, 5 Å, 15 Å, 30 Å, 40 Å, 50 Å, 70 Å, 90 Å, 100 Å). From the developing shape of the Cu LMM line it can be concluded that mostly metallic Cu has formed at the end of the interface experiment. However, after the first deposition step the Cu LMM auger line indicates the formation of Cu_2O.

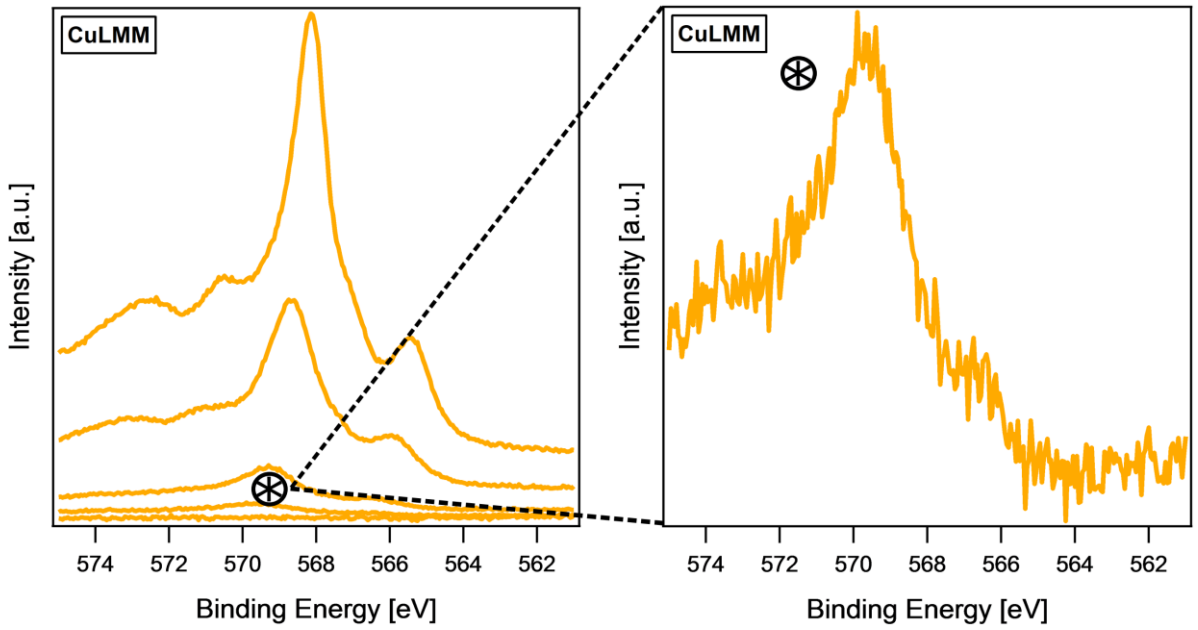

A 2: Development of the Cu LMM Auger emission line during the pn^+-Si | nat. SiO_2 | Cu interface experiment. The measurement of the bare pn^+-Si | nat. SiO_2 substrate is displayed at the bottom of the diagram while the last deposition step at the top shows the final measurement of a relatively thick Cu layer (0 Å, 5 Å, 15 Å, 45 Å, 91 Å). From the developing shape of the Cu LMM line it can be concluded that mostly metallic Cu has formed at the end of the interface experiment. However, after the first deposition step the Cu LMM auger line indicates the formation of Cu_2O.

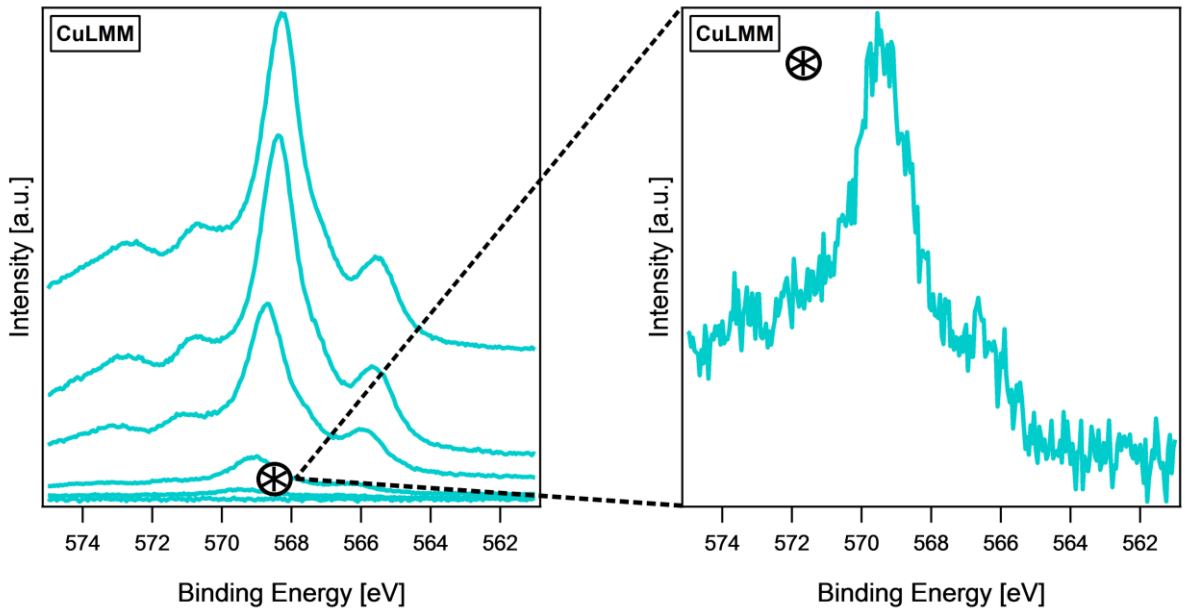

A 3: Development of the Cu LMM Auger emission line during the pn^+-Si:H | Cu interface experiment. The measurement of the bare pn^+-Si:H substrate is displayed at the bottom of the diagram while the last deposition step at the top shows the final measurement of a relatively thick Cu layer (0 Å, 5 Å, 15 Å, 45 Å, 70 Å, 95 Å). From the developing shape of the Cu LMM line it can be concluded that mostly metallic Cu has formed instead of a Cu_2O, which can already be observed after the first deposition step.

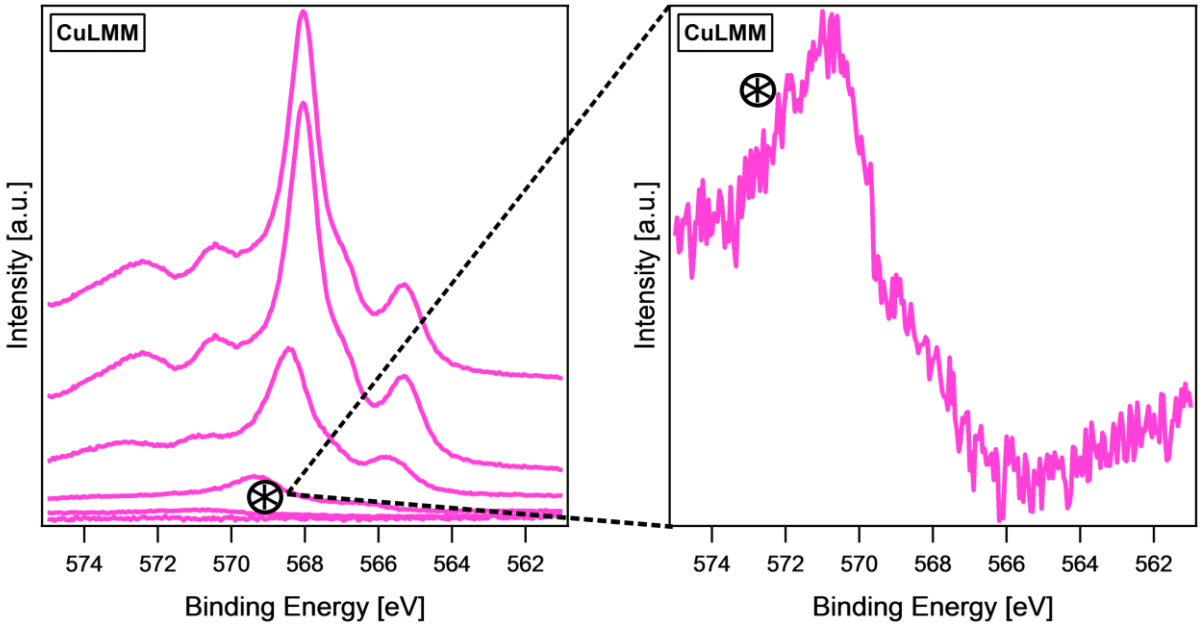

A 4: Development of the Cu LMM Auger emission line during the pn$^+$-Si | therm. SiO_2 | Cu interface experiment. The measurement of the bare pn$^+$-Si | therm. SiO_2 substrate is displayed at the bottom of the diagram while the last deposition step at the top shows the final measurement of a relatively thick Cu layer (0 Å, 5 Å, 15 Å, 45 Å, 70 Å, 92 Å). From the developing shape of the Cu LMM line it can be concluded that mostly metallic Cu has formed at the end of the interface experiment. However, after the first deposition step the Cu LMM auger line indicates the formation of Cu_2O.

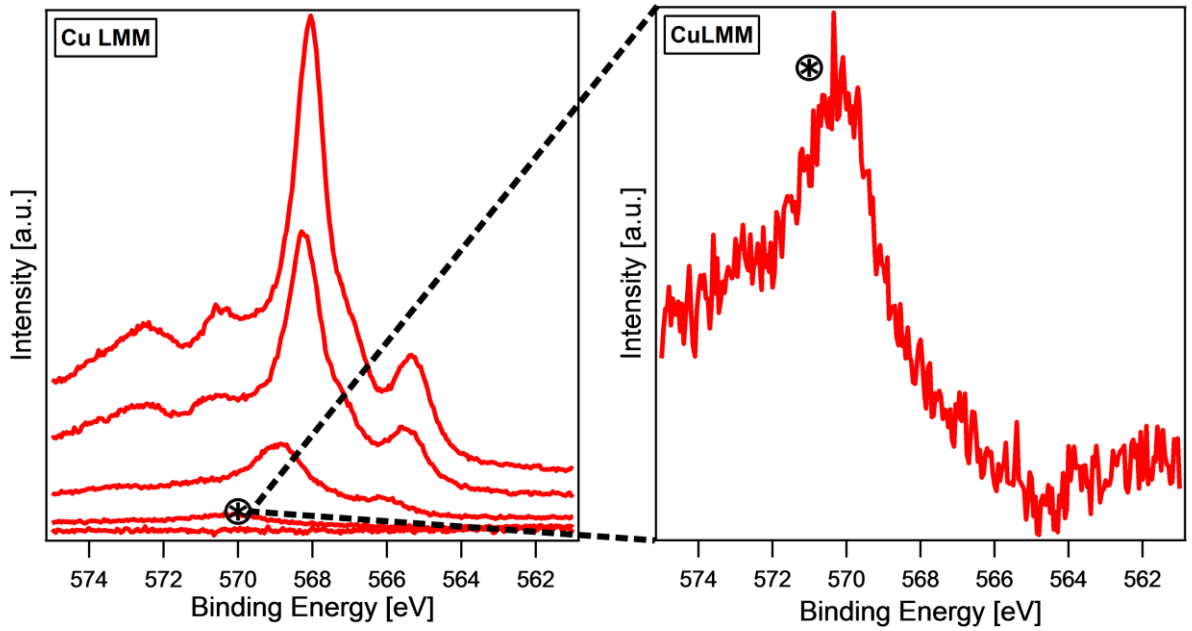

A 5: Development of the Cu LMM Auger emission line during the p-Si | µcn-Si | nat. SiO_2 | Cu interface experiment. The measurement of the bare p-Si | µcn-Si | nat. SiO_2 substrate is displayed at the bottom of the diagram while the last deposition step at the top shows the final measurement of a relatively thick Cu layer (0 Å, 5 Å, 15 Å, 50 Å, 100 Å). From the developing shape of the Cu LMM line it can be concluded that mostly metallic Cu has formed at the end of the interface experiment. However, after the first deposition step the Cu LMM auger line indicates the formation of Cu_2O.

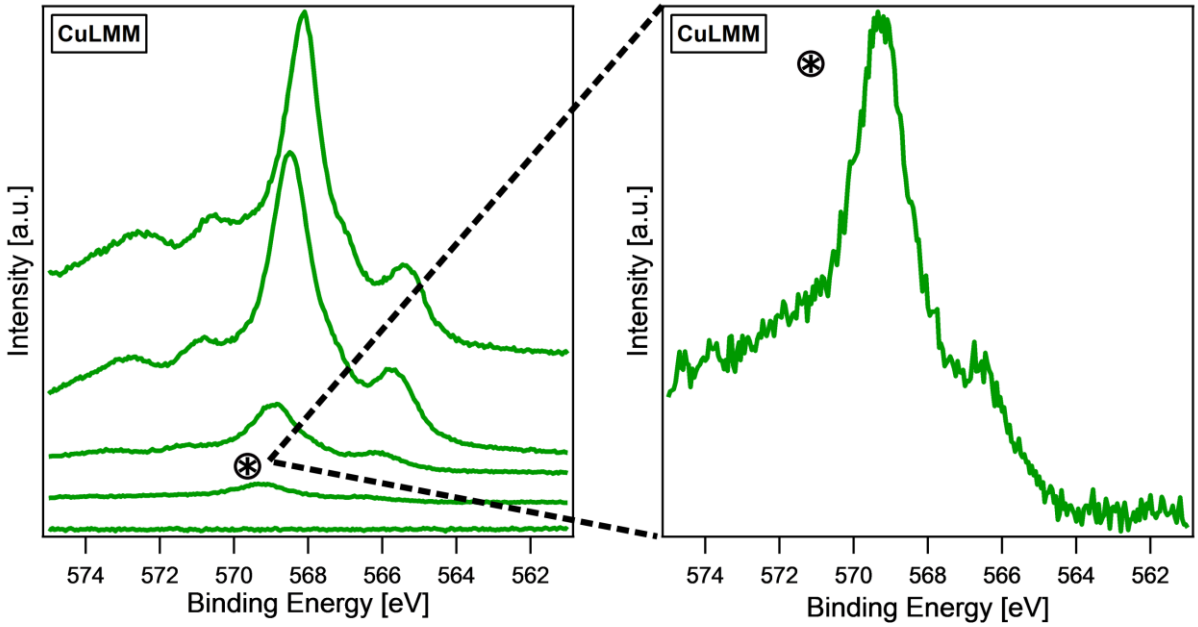

A 6: Development of the Cu LMM Auger emission line during the p-Si | µcn-Si:H | Cu interface experiment. The measurement of the bare p-Si | µcn-Si:H substrate is displayed at the bottom of the diagram while the last deposition step at the top shows the final measurement of a relatively thick Cu layer (0 Å, 5 Å, 15 Å, 45 Å, 90 Å). From the developing shape of the Cu LMM line it can be concluded that mostly metallic Cu has formed instead of a Cu oxide compound. The metallic character can already be assumed after the first deposition step.

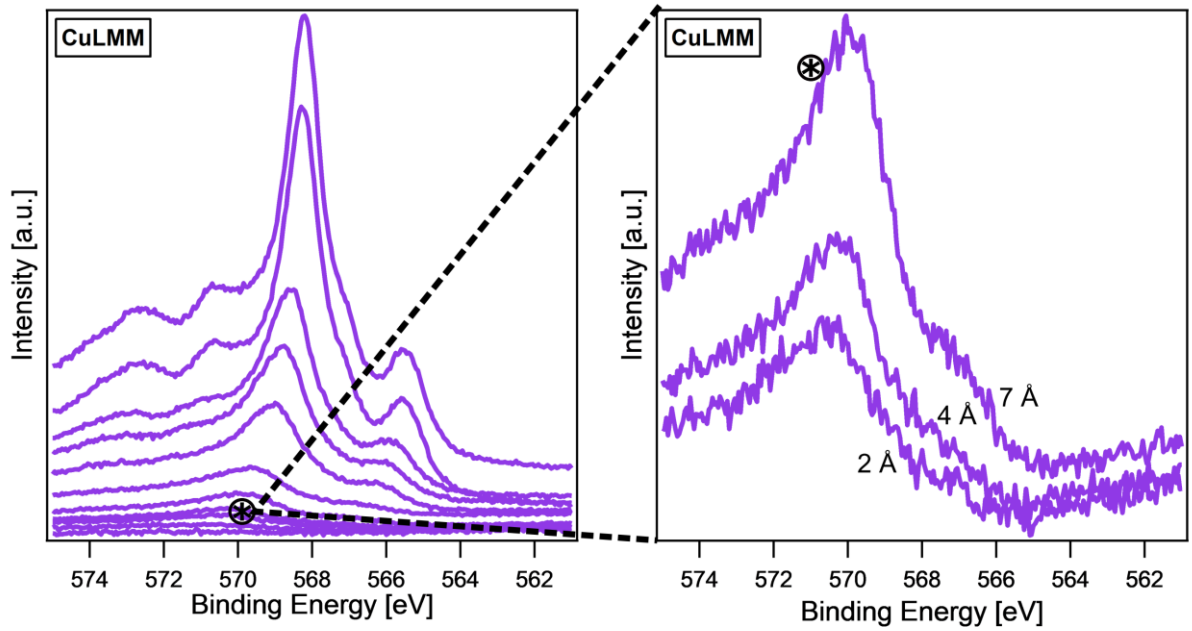

A 7: Development of the Cu LMM Auger emission line during the p-Si | µcn-Si | therm. SiO_2 | Cu interface experiment. The measurement of the bare p-Si | µcn-Si | therm. SiO_2 substrate is at the bottom of the diagram while the last deposition step at the top shows the final measurement of a relatively thick Cu layer (0 Å, 2 Å, 4 Å, 7 Å, 10 Å, 12 Å, 15 Å, 25 Å, 45 Å, 80 Å, 100 Å). From the developing shape of the Cu LMM line it can be concluded that mostly metallic Cu has formed at the end of the interface experiment. However, after the first deposition step the Cu LMM auger line indicates the formation of Cu_2O.

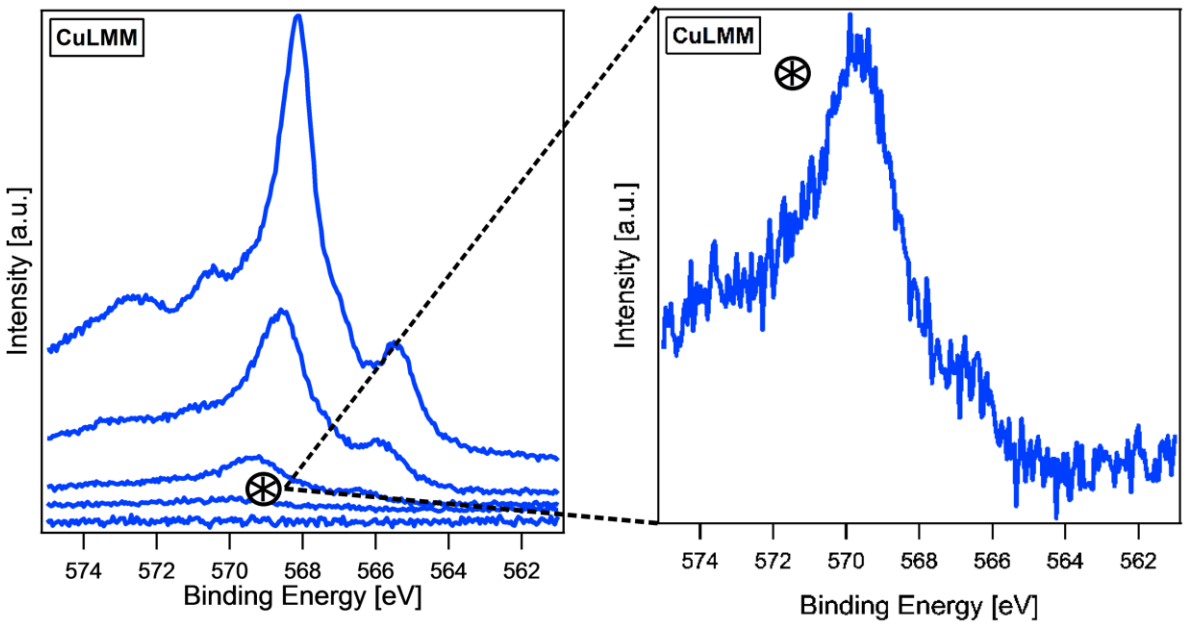

A 8: Development of the Cu LMM Auger emission line during the pin-Si | nat. SiO_2 | Cu interface experiment. The measurement of the bare pin-Si | nat. SiO_2 substrate is at the bottom of the diagram while the last deposition step at the top shows the final measurement of a relatively thick Cu layer (0 Å, 5 Å 15 Å, 45 Å, 90 Å). From the developing shape of the Cu LMM line it can be concluded that mostly metallic Cu has formed at the end of the interface experiment. However, after the first deposition step the Cu LMM auger line indicates the formation of Cu_2O.

Important Symbols and Abbreviations

φ	Work function
E_V	Vacuum level
E_G	Energy band gap
VB	Valence band
CB	Conduction band
I_P	Ionization potential
E_A	Electron affinity
Si	Silicon
E_F	Fermi level
μ_n, μ_p	Charge carrier mobility
σ	Electric conductivity
e	Electrical charge
Cu	Copper
Ag	Silver
U_{OC}	Open circuit potential
η	efficiency
MPP	Maximum power point
UV	Ultraviolet
IR	infrared
TCO	Transparent conductive oxide
WE	Working electrode
RE	Reference electrode

CE	Counter electrode
J_0	Exchange current density
η_{ct}	Overpotential
F	Faraday constant
HER	Hydrogen evolution reaction
SHE	Standard hydrogen electrode
RHE	Reversible hydrogen electrode
XPS	X-ray photoelectron spectroscopy
SEM	Scanning electron microscopy
PECVD	Plasma enhanced chemical vapor deposition
N_{CB}, N_{VB}	Effective density of states
I	Integrated core level line intensity
d	Film thickness
IMEP	Inelastic mean free path
PEC	Photoelectrochemical cell
EC	Electrochemistry
OCP	Open circuit potential
CV	Cyclic voltammetry
LED	Light emitting diode
UHV	Ultra high vacuum

List of Figures

Figure 1: Schematic illustration and comparison of the natural and artificial photosynthesis from macroscopic to nanoscale. 4

Figure 2: Scheme of an artificial leaf photoelectrochemical cell architecture including a Si based multijunction as photoabsorber, a CO_2 reduction catalyst as well as an oxygen evolution catalyst and an ion exchange membrane. 5

Figure 3: Energy band diagrams for a metal, a semiconductor and an insulator at a temperature of 0 K. The material class depends on the energy band gap E_G. The Fermi level E_F indicates the position below which all electronic states are fully occupied (dark blue bands are occupied, light blue bands are empty). 8

Figure 4: Possible energy band situations at an n-type semiconductor: a) accumulation, b) depletion and c) inversion. 9

Figure 5: Band diagram of a a) p-n-semiconductor contact with differently doped regions but equal energy band gap which results in a band bending of eV_b in both regions; b) semiconductor contact with differently doped regions and different energy band gaps which causes an offset in valence and conduction band. 10

Figure 6: Schottky contact with an n-semiconductor and a metal which causes a band bending of eV_b in the energy bands of the semiconductor. 11

Figure 7: Solar cell characteristics under illumination including the typical values: M_{PP}, U_{MPP}, U_{OC}, J_{MPP} and J_{SC}. 12

Figure 8: Schematic illustration of a p-i-n structured solar cell in the dark and under illumination. 13

Figure 9: Absorption coefficient as a function of the photon energy. Orange: c-Si, red: µc-Si:H and blue a-Si:H. The figure is adapted from Ref. [24] 15

Figure 10: Schematic drawing of a) a pn^+-Si single junction, b) a µc-Si:H p-i-n solar cell with glass window, TCO, front and back contact and c) an a-Si:H | a-Si:H | µc-Si:H solar cell with glass window, TCO, front and back contact. 16

Figure 11: JV-characteristics of a µc-Si:H and an a-Si:H | a-Si:H | µc-Si:H solar cell. This information originates from the A-LEAF project partner Forschungszentrum Jülich GmbH. 16

Figure 12: a) Schematic setup of a photoelectrochemical cell consisting of a front contact, a transparent conductive oxide (TCO), a µc-Si:H solar cell in pin-configuration with back contact which acts as CO_2 reduction catalyst (photocathode), the electrolyte solution and a catalyst for the oxygen evolution reaction which acts as anode. b) Schematic energy band diagram in the dark and c) under illumination. 20

Figure 13: Schematic drawing of the molecular reaction pathway of the chemical reduction of CO, which is suggested for the reaction mechanism on metallic Cu electrodes. With * denoted reaction pathways are rate determining steps. 23

Figure 14: Schematic set-up of an electron beam deposition process using crucible evaporation instead of rod or bar evaporation, which is suitable for a variety of materials such as Cu and Ag. 26

Figure 15: The inelastic mean free path of electrons in solid state materials vs. the kinetic energy according to.[92] 27

Figure 16: Schematic set-up of a photoelectron spectrometer, which shows its main parts: the monochromatic X-ray source, the hemispheric analyzer, the photo multiplier and the electrostatic lens system. 27

Figure 17: Band diagram, which schematically shows the energetically relationship between the measured kinetic energy and the binding energy of the electron in the sample during the photoelectron spectroscopy. 28

Figure 18: Three electrode configuration for photoelectrochemical measurements. Left: illumination with LED, right: illumination with solar simulator (special configuration for photoelectrochemical measurements of solar cells) 30

Figure 19: Schematic drawing of a SEM setup with the corresponding electron beam pathway. 31

Figure 20: Schematic set-up of the integrated vacuum system of the Technical University of Darmstadt DAISY-FUN (Darmstadt Integrated System for Fundamental research). The system contains different chambers for sample preparation as well as analysis units. 33

Figure 21: Omicron sample holder with different masks for Cu and Ag deposition. 35

Figure 22: a) Deposition of front and back contact (Cu or Ag) by using a mask, b) created front and back contact of an a-Si:H | a-Si:H | µc-Si:H solar cell. The back contact also serves as catalytic active layer. The same deposition technique can be used for µc-Si:H solar cells. 36

Figure 23: Development of the XP survey spectra of the p-Si | therm. SiO_2 | Cu contact during the interface experiment. The measurement of the bare p-Si | therm. SiO_2 substrate is displayed at the bottom of the diagram while the last deposition step at the top shows the final measurement of a relatively thick Cu layer. 42

Figure 24: Development of the Si 2p, O 1s and Cu 2p detail spectra of the p-Si | therm. SiO_2 | Cu contact during the interface experiment. The measurement of the bare p-Si | therm. SiO_2 substrate is displayed at the bottom of the diagram while the last deposition step at the top shows the final measurement of a relatively thick Cu layer. 44

Figure 25: Energy band diagrams before and after contact formation. a) p-Si | therm. SiO_2 before contact formation with pinned Fermi level and initial downward band bending of 0.4 eV and b) p-Si | therm. SiO_2 | Cu with a slightly reduced band bending of 0.3 eV. 44

Figure 26: Cyclic voltammetry measurement of the p-Si | therm. SiO_2 | Cu model system in 0.3 M $KHCO_3$ under chopped light conditions: 4 sec interval for the illumination of 180 W/m^2 with $\lambda = 625$ nm. 45

Figure 27: XP detail spectra of the p-Si | therm. SiO_2 | Cu sample showing the Cu 2p, O 1s, C 1s and Si 2p emission lines after performing cyclic voltammetry measurements. 47

Figure 28: XP survey spectra of the pn^+-Si substrates with different surface terminations: H-termination, native SiO_2 and thermal SiO_2. 48

Figure 29: Development of the XP survey spectra of the pn^+-Si | nat. SiO_2 | Cu contact during the interface experiment. The measurement of the bare pn^+-Si | nat. SiO_2 substrate is displayed at the bottom of the diagram while the last deposition step at the top shows the final measurement of a relatively thick Cu layer. 49

Figure 30: Development of the Si 2p, O 1s and Cu 2p detail spectra of the pn^+-Si | nat. SiO_2 | Cu contact during the interface experiment. The measurement of the bare pn^+-Si | nat. SiO_2 substrate is displayed at the bottom of the diagram while the last deposition step at the top shows the final measurement of a relatively thick Cu layer. 50

Figure 31: Development of the XP survey spectra of the pn^+-Si:H | Cu contact during the interface experiment. The measurement of the bare pn^+-Si:H substrate is displayed at the bottom of the diagram while the last deposition step at the top shows the final measurement of a relatively thick Cu layer. 51

Figure 32: Development of the Si 2p, O 1s and Cu 2p detail spectra of the pn^+-Si:H | Cu contact during the interface experiment. The measurement of the bare pn^+-Si:H | substrate is displayed at the bottom of the diagram while the last deposition step at the top shows the final measurement of a relatively thick Cu layer. 53

Figure 33: Development of the XP survey spectra of the pn^+-Si | therm. SiO_2 | Cu contact during the interface experiment. The measurement of the bare pn^+-Si | therm. SiO_2 substrate is displayed at the bottom of the diagram while the last deposition step at the top shows the final measurement of a relatively thick Cu layer. 54

Figure 34: Development of the Si 2p, O 1s and Cu 2p detail spectra of the pn^+-Si | therm. SiO_2 | Cu contact during the interface experiment. The measurement of the bare pn^+-Si | therm. SiO_2 substrate is displayed at the bottom of the diagram while the last deposition step at the top shows the final measurement of a relatively thick Cu layer. 55

Figure 35: Energy band diagrams before and after contact formation. a) pn^+-Si | SiO_2 before contact formation with flat band situation, b) pn^+-Si | nat. SiO_2 | Cu with an upward band bending of 0.35 eV, c) pn^+-Si | therm. SiO_2 | Cu with an upward band bending of 0.27 eV, d) pn^+-Si:H before contact formation with flat band situation and e) pn^+-Si:H | Cu with an upward band bending of 0.45 eV. 57

Figure 36: Comparison of the cyclic voltammetry behavior of the three different model systems: pn^+-Si | nat. SiO_2 | Cu (pink), pn^+-Si:H | Cu (cyan) and pn^+-Si | therm. SiO_2 | Cu (orange) in the dark and under an illumination of 180 W/m^2 with $\lambda = 625$ nm in 0.3 M $KHCO_3$. Solid lines: EC behavior under illumination. Dashed lines: EC behavior in the dark. As predicted from the interface investigations the samples show different behaviors depending on the surface barrier height. 59

Figure 37: XP detail spectra of the pn^+-Si | Cu samples with different surface terminations showing the Cu 2p, O 1s, C 1s and Si 2p emission lines after performing cyclic voltammetry measurements (orange: native SiO_2, blue: H-termination and pink: thermal SiO_2). 61

Figure 38: XP detail spectra of the pn^+-Si | nat. SiO_2 | Cu sample showing the effect of N_2 gas bubbling during performing cyclic voltammetry measurements. 62

Figure 39: SEM images of pn^+-Si | nat. SiO_2 | Cu samples with a magnification of 1000, a) before photoelectrochemistry and b) after photoelectrochemistry. 63

Figure 40: SEM images of the cross section of the pn^+-Si | nat. SiO_2 | Cu samples with a magnification of 25000, a) before photoelectrochemistry and b) after photoelectrochemistry. 64

Figure 41: XP survey spectra of the p-Si | µcn-Si substrates with different surface terminations: H-termination, native SiO_2 and thermal SiO_2 65

Figure 42: Development of the XP survey spectra of the p-Si | µcn-Si | nat. SiO_2 | Cu contact during the interface experiment. The measurement of the bare p-Si | µcn-Si | nat. SiO_2 substrate is displayed at the bottom of the diagram while the last deposition step at the top shows the final measurement of a relatively thick Cu layer. 66

Figure 43: Development of the Si 2p, O 1s and Cu 2p detail spectra of the p-Si | µcn-Si | nat. SiO_2 | Cu contact during the interface experiment. The measurement of the bare p-Si | µcn-Si | nat. SiO_2 substrate is displayed at the bottom of the diagram while the last deposition step at the top shows the final measurement of a relatively thick Cu layer. 68

Figure 44: Development of the XP survey spectra of the p-Si | µcn-Si:H | Cu contact during the interface experiment. The measurement of the bare p-Si | µcn-Si:H substrate is displayed at the bottom of the diagram while the last deposition step at the top shows the final measurement of a relatively thick Cu layer. 69

Figure 45: Development of the Si 2p, O 1s and Cu 2p detail spectra of the p-Si | µcn-Si:H | Cu contact during the interface experiment. The measurement of the bare p-Si | µcn-Si:H substrate is at the bottom of the diagram while the last deposition step at the top shows the final measurement of a relatively thick Cu layer. 71

Figure 46: Development of the XP survey spectra of the p-Si | µcn-Si | therm. SiO_2 | Cu contact during the interface experiment. The measurement of the bare p-Si | µcn-Si | therm. SiO_2 substrate is displayed at the bottom of the diagram while the last deposition step at the top shows the final measurement of a relatively thick Cu layer. 72

Figure 47: Development of the Si 2p, O 1s and Cu 2p detail spectra of the p-Si | µcn-Si | therm. SiO_2 | Cu contact during the interface experiment. The measurement of the bare p-Si | µcn-Si | therm. SiO_2 substrate is displayed at the bottom of the diagram while the last deposition step at the top shows the final measurement of a relatively thick Cu layer. 74

Figure 48: Energy band diagrams before and after contact formation. a) p-Si | µcn-Si | SiO_2 before contact formation with almost flat band situation, b) p-Si | µcn-Si | nat. SiO_2 | Cu with a slight downward band bending of 0.01 eV, c) p-Si | µcn-Si | therm. SiO_2 | Cu with an upward band bending of 0.02 eV, d) p-Si | µcn-Si:H before contact formation with almost flat band situation and e) p-Si | µcn-Si:H | Cu with a high upward band bending of 0.55 eV. 76

Figure 49: Comparison of the cyclic voltammetry behavior of the three different model systems: p-Si | µcn-Si | nat. SiO_2 | Cu (red), p-Si | µcn-Si:H | Cu (green) and p-Si | µcn-Si | therm. SiO_2 | Cu (purple) in the dark and under an illumination of 180 W/m^2 with λ = 625 nm in 0.3 M $KHCO_3$. Solid lines: EC behavior under illumination. Dashed lines: EC behavior in the dark. The measurements were performed without nitrogen gas bubbling. 78

Figure 50: XP detail spectra of the p-Si | µcn-Si | Cu samples with different surface terminations showing the Cu 2p, O 1s, C 1s and Si 2p emission lines after performing cyclic voltammetry measurements (red: native SiO_2, green: H-termination and purple: thermal SiO_2). 80

Figure 51: XP detail spectra of the p-Si | µcn-Si | nat. SiO_2 | Cu sample showing the effect of N_2 gas bubbling during performing cyclic voltammetry measurements. 82

Figure 52: SEM images of p-Si | µcn-Si | Cu samples with a magnification of 1000, a) before photoelectrochemistry and b) after photoelectrochemistry. 83

Figure 53: SEM images of the cross section of the p-Si | µcn-Si | Cu samples with a magnification of 10000, a) before photoelectrochemistry and b) after photoelectrochemistry. 83

Figure 54: Development of the XP survey spectra of the pin-Si | nat. SiO_2 | Cu contact during the interface experiment. The measurement of the bare pin-Si | nat. SiO_2 substrate is displayed at the bottom of the diagram while the last deposition step at the top shows the final measurement of a relatively thick Cu layer. 84

Figure 55: Development of the Si 2p, O 1s and Cu 2p detail spectra of the pin-Si | nat. SiO_2 | Cu contact during the interface experiment. The measurement of the bare pin-Si | nat. SiO_2 substrate is displayed at the bottom of the diagram while the last deposition step at the top shows the final measurement of a relatively thick Cu layer. 85

Figure 56: Energy band diagrams before and after contact formation. a) pin-Si | nat. SiO_2 before contact formation with flat band situation and b) pin-Si | nat. SiO_2 | Cu with an upward band bending of 0.13 eV. 87

Figure 57: Cyclic voltammetry behavior of the pin-Si | nat. SiO_2 | Cu sample in the dark and under an illumination of 180 W/m^2 with λ = 625 nm in 0.3 M $KHCO_3$. Solid line: EC behavior under illumination. Dashed line: EC behavior in the dark. 89

Figure 58: Cyclic voltammetry behavior of the pin-Si | nat. SiO_2 | Cu sample in the dark and under an illumination of AM 1.5 G (1000 W/m^2) in 0.3 M $KHCO_3$. Solid line: EC behavior under illumination. Dashed line: EC behavior in the dark. 90

Figure 59: XP detail spectra of the pin-Si | nat. SiO_2 | Cu sample showing the Cu 2p, O 1s, C 1s and Si 2p emission lines after performing cyclic voltammetry measurements. The photoelectrochemical measurement was performed while bubbling with N_2 gas. 92

Figure 60: SEM images of pin-Si | nat. SiO_2 | Cu samples with a magnification of 1000, a) before photoelectrochemistry and b) after photoelectrochemistry. 93

Figure 61: SEM images of the cross section of the pin-Si | nat. SiO_2 | Cu samples with a magnification of 10000, a) before photoelectrochemistry and b) after photoelectrochemistry. 93

Figure 62: Cyclic voltammetry behavior of the a-Si:H | a-Si:H | µc-Si:H | nat. SiO_2 | Cu sample (grey) in the dark and under an illumination of AM 1.5 G (1000 W/m^2) in 0.3 M $KHCO_3$ in comparison to the pin-Si | nat. SiO_2 | Cu sample (blue). Solid lines: EC behavior under illumination. Dashed lines: EC behavior in the dark. 95

Figure 63: Development of the XP survey spectra of the pn$^+$-Si | nat. SiO_2 | Ag contact during the interface experiment. The measurement of the bare pn$^+$-Si | nat. SiO_2 substrate is displayed at the bottom of the diagram while the last deposition step at the top shows the final measurement of a relatively thick Ag layer. 100

Figure 64: Development of the Si 2p, Ag 3d and O 1s detail spectra of the pn$^+$-Si | nat. SiO_2 | Ag contact during the interface experiment. The measurement of the bare pn$^+$-Si | nat. SiO_2 substrate is displayed at the bottom of the diagram while the last deposition step at the top shows the final measurement of a relatively thick Ag layer. The marked areas within the Ag 3d emission line show the loss features. 101

Figure 65: Energy band diagrams before and after contact formation. a) pn$^+$-Si | nat. SiO_2 before contact formation with an upward band bending of 0.13 eV and b) pn$^+$-Si | nat. SiO_2 | Ag with an upward band bending of 0.34 eV. 102

Figure 66: Comparison of the cyclic voltammetry behavior of the pn$^+$-Si | nat. SiO_2 | Ag sample (green) and the, pn$^+$-Si | nat. SiO_2 | Cu (orange) in the dark and under an illumination of 180 W/m^2 with $\lambda = 625$ nm in 0.3 M $KHCO_3$. Solid lines: EC behavior under illumination. Dashed lines: EC behavior in the dark. 104

Figure 67: Photograph of the pn$^+$-Si | nat. SiO_2 | Ag sample after performing photoelectrochemical measurements. The red marked areas show regions where the Ag film in partially removed. The whole Ag film seems to be damaged. 104

Figure 68: XP detail spectra of the pn$^+$-Si | nat. SiO_2 | Ag sample showing the O 1s, Ag 3d, C 1s and Si 2p emission lines after performing cyclic voltammetry measurements. 105

Figure 69: SEM images of the pn$^+$-Si | nat. SiO_2 | Ag sample after performing photoelectrochemical measurements with a magnification of a) 1000 and b) 10000. 106

Figure 70: Development of the XP survey spectra of the p-Si | µcn-Si |nat. SiO_2 | Ag contact during the interface experiment. The measurement of the bare p-Si | µcn-Si | nat. SiO_2 substrate is displayed at the bottom of the diagram while the last deposition step at the top shows the final measurement of a relatively thick Ag layer. 107

Figure 71: Development of the Si 2p, Ag 3d and O 1s detail spectra of the p-Si | µcn-Si | nat. SiO_2 | Ag contact during the interface experiment. The measurement of the bare p-Si | µcn-Si | nat. SiO_2 substrate is displayed at the bottom of the diagram while the last deposition step at the top shows the final measurement of a relatively thick Ag layer. The marked areas within the Ag 3d emission line show the loss features. 108

Figure 72: Energy band diagrams before and after contact formation. a) pn$^+$-Si | nat. SiO_2 before contact formation with an upward band bending of 0.05 eV and b) pn$^+$-Si | nat. SiO_2 | Ag with an upward band bending of 0.09 eV. 109

Figure 73: Comparison of the cyclic voltammetry behavior of the p-Si | µcn-Si | nat. SiO_2 | Ag sample (black) and the, p-Si | µcn-Si | nat. SiO_2 | Cu (red) in the dark and under an illumination of 180 W/m^2 with $\lambda = 625$ nm in 0.3 M $KHCO_3$. Solid lines: EC behavior under illumination. Dashed lines: EC behavior in the dark. 110

Figure 74: Photograph of the p-Si | µcn-Si | nat. SiO_2 | Ag sample after performing photoelectrochemical measurements. Only the outer edge of the Ag film seems to be preserved. 111

Figure 75: XP detail spectra of the p-Si | µcn-Si | nat. SiO_2 | Ag sample showing the O 1s, Ag 3d, C 1s and Si 2p emission lines after performing cyclic voltammetry measurements. 112

Figure 76: SEM images of a p-Si | µcn-Si | Ag sample after performing photoelectrochemical measurements with a magnification of a) 1000, showing an area where the Ag layer has been completely removed b) 1000, showing an area where the Ag layer is partially preserved and c) 10000, showing the edge of the sample. 113

Figure 77: Development of the XP survey spectra of the a-Si:H | a-Si:H | µcn-Si:H | nat. SiO_2 | Ag contact during the interface experiment. The measurement of the bare a-Si:H | a-Si:H | µcn-Si:H | nat. SiO_2 substrate is displayed at the bottom of the diagram while the last deposition step at the top shows the final measurement of a relatively thick Ag layer. 114

Figure 78: Development of the Si 2p, Ag 3d and O 1s detail spectra of the a-Si:H | a-Si:H | µcn-Si:H | nat. SiO_2 | Ag contact during the interface experiment. The measurement of the bare a-Si:H | a-Si:H | µcn-Si:H | nat. SiO_2 substrate is displayed at the bottom of the diagram while the last deposition

step at the top shows the final measurement of a relatively thick Ag layer. The marked areas within the Ag 3d emission line show the loss features. 115

Figure 79: Energy band diagrams before and after contact formation. a) a-Si:H | a-Si:H | µcn-Si:H | nat. SiO_2 before contact formation with an upward band bending of 0.02 eV and b) a-Si:H | a-Si:H | µcn-Si:H | nat. SiO_2 | Ag with an upward band bending of 0.12 eV. 116

Figure 80: Comparison of the cyclic voltammetry behavior of the a-Si:H | a-Si:H | µcn-Si:H | nat. SiO_2 | Ag sample (red) and the, a-Si:H | a-Si:H | µcn-Si:H | nat. SiO_2 | Cu (grey) in the dark and under solar simulation of AM 1.5 G (1000 W/m^2) in 0.3 M $KHCO_3$. Solid lines: EC behavior under illumination. Dashed lines: EC behavior in the dark....117

Figure 81: Photograph of the a-Si:H | a-Si:H | µcn-Si:H | nat. SiO_2 | Ag sample after performing photoelectrochemical measurements. From the first impression it seems that the Ag film is still intact. 118

Figure 82: XP detail spectra of the a-Si:H | a-Si:H | µcn-Si:H | nat. SiO_2 | Ag sample showing the O 1s, Ag 3d, C 1s and Si 2p emission lines after performing cyclic voltammetry measurements. The marked areas within the Ag 3d emission line show the loss features. 119

Figure 83: SEM images of an a-Si:H | a-Si:H | µcn-Si:H | Ag sample after performing photoelectrochemical measurements with a magnification of a) 1000 and b) 10000. 119

Bibliography

[1] Ashton, T. S. *The Industrial Revolution 1760-1830,* OUP Catalogue , Oxford University Press, number 9780192892898, 1997.

[2] N. Oreskes. *The Scientific Consensus on Climate Change*, In: Science 306.5702, pp. 1686–1686, no. 1, pp. 1–14, 2004.

[3] Ehleringer, J. R. and Cerling, T. E. Tree Physiology 15(2), 105–111, 1995.

[4] M. Mishra and D. M. Chun, *α-Fe2O3 as a photocatalytic material: A review*, Appl. Catal. A Gen., vol. 498, pp. 126–141, 2015.

[5] P. Bogdanoff et al., *Artificial Leaf for Water Splitting Based on a Triple-Junction Thin-Film Silicon Solar Cell and a PEDOT: PSS/Catalyst Blend*, Energy Technol., vol. 4, no. 1, pp. 230–241, 2016.

[6] R. van de Krol, M. Grätzel in Electronic Materials: Science and Technology (Ed.: H. L. Tuller), Springer, Heidelberg, 2012.

[7] B. D. James, G. N. Baum, J. Perez, and K. N. Baum, T*echnoeconomic Analysis of Photoelectrochemical (PEC) Hydrogen Production*, DOE Contract Number GS-10F-009J, vol. 22201, no. December, pp. 1–128, 2009.

[8] J. D. J. Olmos and J. Kargul, *Oxygenic photosynthesis: Translation to solar fuel technologies,* Acta Soc. Bot. Pol., vol. 83, no. 4, pp. 423–440, 2014.

[9] C. Kittel, *Einführung in die Festkörperphysik*. Oldenbourg, München, 2006.

[10] H. Ibach, *Solid-State Physics An Introduction to Principles of Materials Science*, 4th ed. 2009.

[11] G. H. and R. A. P. F. J. Himpsel, *Determination of the Fermi-level pinning position at Si(111) surfaces*, Phys. Rev. B, vol. 28, no. 12, pp. 7014–7018, 1983.

[12] M. Wanlass et al., *Monolithic, ultra-thin GalnP/GaAs/GalnAs tandem solar cells,* Conf. Rec. 2006 IEEE 4th World Conf. Photovolt. Energy Conversion, WCPEC-4, vol. 1, pp. 729–732, 2007.

[13] M. V. Fischetti and S. E. Laux, *Band structure, deformation potentials, and carrier mobility in strained Si Ge, and SiGe alloys,* J. Appl. Phys., vol. 80, no. 4, pp. 2234–2252, 1996.

[14] J. P. van der Ziel, T*wo-photon absorption spectra of GaAs with* $2\hbar\omega_1$ *near the direct band gap*,

Phys. Rev. B, vol. 16, pp. 2775–2780, 1977.

[15] S. M. Sze, *Physics of Semiconductor Devices*. Wiley-Interscience 2006.

[16] Sze, S. M. and Ng, K. K. *Physics of semiconductor devices*. Wiley-Interscience, Hoboken, N.J, 3rd edition, 2007.

[17] W. Shockley and H. J. Queisser, *Detailed balance limit of efficiency of p-n junction solar cells*, J. Appl. Phys., vol. 32, no. 3, pp. 510–519, 1961.

[18] P. Würfel, *Physics of solar cells: From principles to new concepts. Wiley-VCH, Weinheim*. 2005.

[19] R. A. Street, *Hydrogenated amporphous silicon*, Cambridge University Press, New York, USA, 1991.

[20] V. Smirnov, O. Astakhov, R. Carius, Y. Petrusenko, V. Borysenko, and F. Finger, *Variation in absorber layer defect density in amorphous and microcrystalline silicon thin film solar cells with 2MeV electron bombardment*, Jpn. J. Appl. Phys., vol. 51, no. 2 PART 1, 2012.

[21] L. Ley, *The Physics of Hydrogenated Amorphous Silicon II: Topics in Applied Physics - Photoemission and optical properties*, Springer Berlin / Heidelberg, Germany, 1984.

[22] B. Rech, *Solarzellen aus amorphem Silizium mit hohem stabilem Wirkungsgrad : zum Einfluß des p/i-Grenzflächenbereichs und der intrinsischen Absorberschicht*, Ph.D. thesis, Rheinisch Westfälische Technische Hochschule Aachen, Germany, 1997.

[23] O. Vetterl et al., *Intrinsic microcrystalline silicon: A new material for photovoltaics*, Sol. Energy Mater. Sol. Cells, vol. 62, no. 1, pp. 97–108, 2000.

[24] F. Urbain, *Light induced water splitting using multijunction thin film silicon solar cells*, Ph.D. thesis, Rheinisch Westfälische Technische Hochschule Aachen, Germany, 2016.

[25] R.E.I. Schropp, M. Zeman, *Amorphous and Microcrystalline Silicon Solar Cells, Modelling, Materials and Device Technology*, Kluwer Academic Publishers (1998), vol. 5, 1998.

[26] J. K. Rath, *Low temperature polycrystalline silicon: A review on deposition, physical properties and solar cell applications*, Sol. Energy Mater. Sol. Cells, vol. 76, no. 4, pp. 431–487, 2003.

[27] M. A. Green, A. W. Blakers, and C. R. Osterwald, *Characterization of high- efficiency silicon solar cells*, J. Appl. Phys. 58, 4402–4408, 1985.

[28] K. Tanaka, E. Maruyama, T. Shimada, and H. Okamoto, *Amorphous Silicon*, Wiley, New York, USA, 1999.

[29] A. Shah (ed.), *Thin-Film Silicon Solar Cells*, EPFL Press, Lausanne, Switzer- land, 2010.

[30] R. Memming, *Semiconductor electrochemistry*, Wiley-VCH, Weinheim, Germany, 2001.

[31] K. Rajeshwar, *Fundamentals of Semiconductor Electrochemistry and Photoelectrochemistry*, Wiley Online Library, 2007.

[32] C. A. Koval and J. N. Howard, *Electron transfer at semiconductor electrode- liquid electrolyte interfaces,* Chem. Rev. 92, 411 – 433, vol. 92, 1992.

[33] A.D. McNaught and A. Wilkinson, *IUPAC compendium of chemical terminology*, 2nd ed., (Eds.), Blackwell Sci. Publ. Oxford, UK, 1997.

[34] A. J. Bard and L. R. Faulkner, *Electrochemical methods: fundamentals and applications*, Wiley, New York, USA, 2001.

[35] K. Vetter, *Elektrochemische Kinetik*, Springer, Berlin / Heidelberg, Germany, 1961.

[36] P. G. Russell, N. Kovac, S. Srinivasan, and M. Steinberg, *The Electrochemical Reduction of Carbon Dioxide, Formic Acid, and Formaldehyde*, *J*. Electrochem. Soc., vol. 124, no. 9, pp. 1329–1338, 1977.

[37] Y. Hori, *Proceedings of the Symposium on Environmental Aspects of Electro- chemistry and Photoelectrochemistry*, The Electrochemical Society, Vol. 93-18 p. 1, 1993.

[38] J. A. Dean, McGraw-Hill, *Lange's Handbook of Chemistry*, 13th ed., p.6-2, p.9-4, p.9-107, 1985.

[39] K. J. Vetter, *Electrochemical Kinetics, Theoretical and Experimental Aspects*, Academic Press, New York, p.556, 1967.

[40] W. Paik, T. N. Andersen, and H. Eyring, Electrochem. Act. 14, 1217, 1969.

[41] Y. Hori and S. Suzuki, Bull. Chem. Soc. Jpn. 55, 660, 1982.

[42] H. Noda, S. Ikeda, Y. Oda, K. Imai, M. Maeda, and K. Ito, Bull. Chem. Soc. Jpn. 63, 2459, 1990.

[43] Y.Hori, K. Kikuchi and S. Suzuki, Chem. Lett. 1695, 1985.

[44] R. L.Cook, R. C. MacDuff, and A. F. Sammells, J. Electrochem. Soc. 134, 1873, 1987.

[45] R. L. Cook, R. C. MacDuff, and A. F. Sammells, J. Electrochem. Soc. 134, 2375, 1987.

[46] M. Azuma, K. Hashimoto, M. Hiramoto, M. Watanabe, and T. Sakata, J. Electroanal. Chem. 260, 441, 1989.

[47] Y. Hori, H. Wakebe T. Tsukamoto and O. Koga, Electrochim. Act. 39, 1833, 1994.

[48] K. Ito, T. Murata, and S. Ikeda, Bull. Nagoya Inst. Techn. 27, 209, 1975.

[49] M. Azuma, K. Hashimoto, M. Hiramoto, M. Watanabe, T. Sakata, J.Electrochem. Soc. 137, 1772, 1990.

[50] K. Ito, S. Ikeda, T. Iida, and H. Niwa, Denki Kagaku, 49, 106, 1981.

[51] F. Koleli, T. Atilan, N. Palamut, A. M. Gizir,R. Aydin, and C. H. Hamann, J. Appl. Electrochem. 33, 447, 2003.

[52] M. Todoroki, K. Hara, A. Kudo, and T. Sakata, J. Electroanal. Chem. 394, 199, 1995.

[53] Y. Hori, *Electrochemical CO_2 Reduction on Metal Electrodes*, Modern Aspects of Electrochemistry vol. 42, no. 42, pp. 89–189, 2008.

[54] T. E.Teeter, and P. Van Rysselberghe, J. Chem. Phys. 22, 1759, 1954.

[55] J. Jordan, and P. T.Smith, Proc. Chem. Soc. 246, 1960.

[56] B. R Eggins, E. M. Brown, E A. McNeil, and J. Grimshaw, Tetrahedron Letters 29, 945, 1988.

[57] A. Bewick, and G. P. Greener, Tetrahedron Letters No. 5 391, 1970.

[58] A. W. B. Aylmer-Kelly, A. Bewick, P. R. Cantrill and A. M. Tuxford, Faraday Disc. Chem. Soc. No. 56, 96, 1973.

[59] Y. Akahori, N.Iwanaga, Y. Kato, O. Hamamoto, and M. Ishii, Electrochemistry (Tokyo, Japan), 72, 266, 2004.

[60] M. Fujihira, T. Noguchi, Chem. Lett. 2043, 1992.

[61] P. Kedzierzawski and J. Augustynski, *Poisoning and Activation of the Gold Cathode during Electroreduction of CO_2*, J. Electrochem. Soc., vol. 141, no. 5, pp. L58–L60, 1994.

[62] H. Noda, S. Ikeda, A. Yamamoto, H. Einaga, and K. Ito, Bull. Chem. Soc. Jpn., 68, 1889, 1995.

[63] T. Ohmori, A. Nakayama, H. Mametsuka, and E. Suzuki, *Influence of sputtering parameters on electrochemical CO_2 reduction in sputtered Au electrode*, J. Electroanal. Chem., vol. 514, no. 1–2, pp. 51–55, 2001.

[64] R. Kostecki, and J. Augustynski, Ber. Bunsen-Ges. Phys. Chem. 98, 1510, 1994.

[65] N. Hoshi, M. Kato, and Y. Hori, *Electrochemical reduction of CO_2 on single crystal electrodes of silver*, J. Electroanal. Chem., vol. 440, no. 1–2, pp. 283–286, 1997.

[66] H. Yano, F. Shirai, M. Nakayama, and K. Ogura, *Efficient electrochemical conversion of CO_2 to CO, C_2H_4 and CH_4 at a three-phase interface on a Cu net electrode in acidic solution*, J. Electroanal. Chem., vol. 519, no. 1–2, pp. 93–100, 2002.

[67] S. Ikeda, T. Takagi, and K. Ito, Bull. Chem. Soc. Jpn. 60, 2517, 1987.

[68] W. M. Ayers and M. Farley, *Carbon Dioxide Reduction with an Electric Field Assisted Hydrogen Insertion Reaction*, American Chemical Society pp. 147–154, 1988.

[69] K. Ohkawa, Y. Noguchi, S. Nakayama, K. Hashimoto, and A. Fujishima, *Electrochemical reduction of carbon dioxide on hydrogen-storing materials. Part 3. The effect of the absorption of hydrogen on the palladium electrodes modified with copper*, J. Electroanal. Chem., vol. 367, no. 1–2, pp. 165–173, 1994.

[70] B. I. Podlovchenko, E. A. Kolyadko, and S. Lu, *Electroreduction of carbon dioxide on palladium electrodes at potentials higher than the reversible hydrogen potential*, J. Electroanal. Chem., vol. 373, no. 1–2, pp. 185–187, 1994.

[71] C. Iwakura, S. Takezawa, and H. Inoue, J. Electroanal. Chem. 459, 167, 1998.

[72] Y. Hori and A. Murata, Chem. Lett. 181, 1991.

[73] Y. Hori, *Electrochemical CO_2 reduction on metal electrodes*, in Modern aspects of electrochemistry, Springer, pp. 89–189, 2008.

[74] Y. Hori, K. Kikuchi, A. Murata, and S. Suzuki, Chem. Lett. 897, 1986.

[75] R. L. Cook, R. C. MacDuff, and A. F. Sammells, *On the electrochemical reduction of carbon dioxide at in situ electrodeposited copper*, J. Electrochem. Soc., vol. 135, no. 6, pp. 1320–1326, 1988.

[76] D. W. DeWulf, T. Jin, and A. J. Bard, *Electrochemical and Surface Studies of Carbon Dioxide Reduction to Methane and Ethylene at Copper Electrodes in Aqueous Solutions*, J. Electrochem. Soc., vol. 136, no. 6, pp. 1686–1691, 1989.

[77] S. Wasmus, E. Cattaneo, and W. Vielstich, *Reduction of carbon dioxide to methane and ethene-an on-line MS study with rotating electrodes,* Electrochem. Acta, vol. 35, no. 4, pp. 771–775, 1990.

[78] K. W. Frese, E*lectrochemical Reduction of CO_2 at Intentionally Oxidized Copper Electrodes*, J. Electrochem. Soc., vol. 138, no. 11, pp. 3338–3344, 1991.

[79] G. Kyriacou and A. Anagnostopoulos, *Electroreduction of CO2 on differently prepared copper electrodes. The influence of electrode treatment on the current efficiences*, J. Electroanal. Chem., vol. 322, no. 1–2, pp. 233–246, 1992.

[80] G. Z. Kyriacou and A. K. Anagnostopoulos, I*nfluence CO_2 partial pressure and the supporting electrolyte cation on the product distribution in CO2electroreduction,* J. Appl. Electrochem.,

vol. 23, no. 5, pp. 483–486, 1993.

[81] R. Shiratsuchi, Y. Aikoh, and G. Nogami, J. Electrochem. Soc. 140, 3479, 1993.

[82] B. Jermann and J. Augustynski, *Long-term activation of the copper cathode in the course of CO_2 reduction*, Electrochem. Acta, vol. 39, no. 11–12, pp. 1891–1896, 1994.

[83] P. Friebe, P. Bogdanoff, N. Alonso-Vante, and H. Tributsch, *A real-time mass spectroscopy study of the (electro)chemical factors affecting CO_2 reduction at copper*, J. Catal., vol. 168, no. 2, pp. 374–385, 1997.

[84] Y. Terunuma, A. Saitoh, and Y. Momose, *Relationship between hydrocarbon production in the electrochemical reduction of CO_2 and the characteristics of the Cu electrode,* J. Electroanal. Chem., vol. 434, no. 1–2, pp. 69–75, 1997.

[85] Y. Hori, A. Murata, S. Ito, Y. Yoshinami, and O. Koga, Chem. Lett. 1567, 1989.

[86] M. Watanabe, *Design of Alloy Electrocatalysts for CO_2 Reduction*, J. Electrochem. Soc., vol. 138, no. 11, p. 3382, 1991.

[87] S. Ishimaru, R. Shiratsuchi, and G. Nogami, *Pulsed electroreduction of CO_2 on Cu-Ag alloy electrodes*, J. Electrochem. Soc., vol. 147, no. 5, pp. 1864–1867, 2000.

[88] Y. Hori, A. Murata, and R. Takahashi, *Formation of hydrocarbons in the electrochemical reduction of carbon dioxide at a copper electrode in aqueous solution*, J. Chem. Soc. Faraday Trans. 1 Phys. Chem. Condens. Phases, vol. 85, no. 8, pp. 2309–2326, 1989.

[89] Y. Hori, O. Koga, H. Yamazaki, and T. Matsuo, *Infrared spectroscopy of adsorbed CO and intermediate species in electrochemical reduction of CO_2 to hydrocarbons on a Cu electrode*, Electrochim. Acta, vol. 40, no. 16, pp. 2617–2622, 1995.

[90] I. Oda, H. Ogasawara, and M. Ito, Langmuir 12, 1094, 1996.

[91] A. Einstein, *Über einen die Erzeugung und Verwandlung des Lichtes betreffenden heuristischen Gesichtspunkt*, Annalen der P. 1905.

[92] A. Klein, T. Mayer, A. Thissen, and W. Jaegermann, *Photoelectron Spectroscopy in Materials Science and Physical Chemistry,* Bunsen-Magazin, vol. 4, pp. 124–139, 2008.

[93] G. Lukowski, *Röntgen-Photoelektronenspektroskopie - Kapitel 3.6.*, Mod. Pharm. Technol., pp. 78–82, 2009.

[94] B. K. Moulder John, Stickle William, Sobol Peter, *Handbook of X-ray Photoelectron Spectroscopy*, Physical Electronics Inc., 1995.

[95] S. Tougaard and C. Jansson, *Background correction in XPS: Comparison of validity of different methods*, Surf. Interface Anal., vol. 19, no. 1–12, pp. 171–174, 1992.

[96] D. A. Shirley, Phys. Rev. B, vol. 5, no. 12, pp. 4709–4714, 1972.

[97] J. Goldstein, *Scanning electron microscopy and x-ray microanalysis.* Springer, NY 3.ed. 2003.

[98] W. Jaegermann, *Interface Engineering of Semiconductor Electrodes for Photoelectrochemical Water Splitting: Application of Surface Characterization with Photoelectron Spectroscopy*. Springer, 2016.

[99] W. Kern, *The Evolution of Silicon Wafer Cleaning Technology*, J. Electrochem. Soc., vol. 137, no. 6, p. 1887, 1990.

[100] F. Urbain et al., *A-Si:H/μc-Si:H tandem junction based photocathodes with high open-circuit voltage for efficient hydrogen production*, J. Mater. Res., vol. 29, no. 22, pp. 2605–2614, 2014.

[101] J. Ziegler, *Photoelektrosynthese von Wasserstoff mit Silizium-Dünnschicht-Tandemsolarzellen*, Ph.D. thesis, Technische Universität Darmstadt, Germany, 2015.

[102] C. Steinert, S. Tengeler, B. Kaiser, and W. Jaegermann, *The impact of different Si surface terminations in the (100) p-Si | n^+ -si | cu junction with respect to the photo electrochemical performance*, J. Electrochem. Soc., vol. 166, no. 5, 2019.

[103] S. Giménez, J. Bisquert, S. Tengeler, B. Kaiser, D. Chaussende, and W. Jaegermann, Applied Surface Science, 400, 6, 2016.

[104] S. Tengeler et al., *The Impact of Different Si Surface Terminations in the (001) n-Si/NiOx Heterojunction on the Oxygen Evolution Reaction (OER) by XPS and Electrochemical Methods*, J. Electrochem. Soc., vol. 165, no. 2, 2018.

[105] F. J. Grunthaner, P. J. Grunthaner, R. P. Vasquez, B. F. Lewis, J. Maserjian, and A. Madhukar, *Local atomic and electronic structure of oxide/GaAs and SiO_2/Si interfaces using high resolution XPS*, J. Vac. Sci. Technol., vol. 16, no. 5, pp. 1443–1453, 1979.

[106] M. C. Biesinger, L. W. M. Lau, A. R. Gerson, R. S. C. Smart, B. P. Payne, and A. P. Grosvenor, *Resolving surface chemical states in XPS analysis of first row transition metals, oxides and hydroxides: Cr, Mn, Fe, Co and Ni*, Appl. Surf. Sci., vol. 257, no. 3, pp. 887–898, 2010.

[107] R. Padiyath, J. Seth, S. V Babu, and L. J. Matienzo, *Deposition of copper films on silicon substrates: Film purity and silicide formation,* J. Appl. Phys., vol. 73, no. 5, pp. 2326–2332, 1993.

[108] M. Dai, J. Kwon, M. D. Halls, R. G. Gordon, and Y. J. Chabal, *Surface and interface processes*

during atomic layer deposition of copper on silicon oxide, Langmuir, vol. 26, no. 6, pp. 3911–3917, 2010.

[109] J. P. Espinós, J. Morales, A. Barranco, A. Caballero, J. P. Holgado, and A. R. González-Elipe, *Interface effects for Cu, CuO, and Cu_2O deposited on SiO_2 and ZrO_2. XPS determination of the valence state of copper in Cu/SiO_2 and Cu/ZrO_2 catalysts*, J. Phys. Chem. B, vol. 106, no. 27, pp. 6921–6929, 2002.

[110] R. T. Tung, Physical Review Letters, 84, 6078, 2000.

[111] C. C. Hobbs, L. R. C. Fonseca, A. Knizhnik, V. Dhandapani, S. B. Samavedam, W. J. Taylor, J. M. Grant, L. R. G. Dip, D. H. Triyoso, R. I. Hegde, D. C. Gilmer, R. Garcia, D. Roan, M. L. Lovejoy, R. S. Rai, E. A. Hebert, H. Tseng, S. G. H. Anderson, and B. E. White, IEEE Transactions on Electron Devices, Vol. 51, 6, 2004.

[112] O. F. Sankey, R. E. Allen, and J. D. Dow, Solid State Communications, vol. 49, no. 1, 1984.

[113] S. Tengeler, M. Fingerle, W. Calvet, C. Steinert, B. Kaiser, T. Mayer, and W. Jaegermann, Journal of the Electrochemical Society, 165(4), H3122, 2018.

[114] B. Vincent Crist, Vol 2 - XPS of Binary Oxides. 2005.

[115] Z. H. Lu, J. P. McCaffrey, B. Brar, G. D. Wilk, R. M. Wallace, L. C. Feldman and S. P. Tay, *SiO_2 film thickness metrology by x-ray photoelectron spectroscopy*, Appl. Phys. Lett., vol. 71, no. 19, pp. 2764–2766, 1997.

[116] K. B. C. and J. A. B. D. F. Mitchell, *Film thickness measurements of SiO_2 by XPS*, Surf. Interface Anal., vol. 21, no. 1, pp. 44–50, 1994.

[117] H. P. S.K. Chawla, N. Sankarraman, *Diagnostic spectra for XPS analysis of CuOSH compounds*, J. Electron Spectros. Relat. Phenomena, vol. 61, no. 1, pp. 1–18, 1992.

[118] Y. Teterin, K. Ivanov, A. Y. Teterin, A. Lebedev, I. Utkin, and L. Vukchevich, *Auger and X-ray photoelectron spectroscopy study of the density of oxygen states in bismuth, aluminium, silicon and uranium oxides*, J. Electron Spectros. Relat. Phenomena, vol. 101–103, pp. 401–405, 1999.

[119] J. P. Espinós, J. Morales, A. Barranco, A. Caballero, A. J. P. Holgado, and A. R. González-Elipe, *Interface effects for Cu, CuO, and Cu2O deposited on SiO2 and ZrO2. XPS determination of the valence state of copper in Cu/SiO2 and Cu/ZrO2 catalysts,* J. Phys. Chem. B, vol. 106, no. 27, pp. 6921–6929, 2002.

[120] B. Egert, *The Stability of CuO and Cu_2O surfaces sputtering*, Surf. Sci., vol. 151, pp. 400–408, 1985.

[121] J. Yu and J. Ran, *Facile preparation and enhanced photocatalytic H2-production activity of $Cu(OH)_2$ cluster modified TiO_2*, Energy Environ. Sci., vol. 4, no. 4, pp. 1364–1371, 2011.

[122] B. Gangaja, S. Chandrasekharan, S. Vadukumpully, S. V. Nair, and D. Santhanagopalan, *Surface chemical analysis of CuO nanofiber composite electrodes at different stages of lithiation/delithiation*, J. Power Sources, vol. 340, pp. 356–364, 2017.

[123] K. V. Gurav et al., *Room temperature chemical synthesis of $Cu(OH)_2$ thin films for supercapacitor application*, J. Alloys Compd., vol. 573, pp. 27–31, 2013.

[124] D. G. Georgiev, R. J. Baird, G. Newaz, G. Auner, R. Witte, and H. Herfurth, *An XPS study of laser-fabricated polyimide/titanium interfaces*, Appl. Surf. Sci., vol. 236, no. 1–4, pp. 71–76, 2004.

[125] K. Artyushkova, S. Levendosky, P. Atanassov, and J. Fulghum, *XPS Structural studies of nano-composite non-platinum electrocatalysts for polymer electrolyte fuel cells*, Top. Catal., vol. 46, no. 3–4, pp. 263–275, 2007.

[126] V. Datsyuk et al., *Chemical oxidation of multiwalled carbon nanotubes*, Carbon N. Y., vol. 46, no. 6, pp. 833–840, 2008.

[127] Y. Fu, H. Du, and S. Zhang, *Adhesion and interfacial structure of magnetron sputtered TiNi films on Si/SiO_2 substrate*, Thin Solid Films, vol. 444, no. 1–2, pp. 85–90, 2003.

[128] S. Libertino et al., *Layer uniformity in glucose oxidase immobilization on SiO_2 surfaces*, Appl. Surf. Sci., vol. 253, no. 23, pp. 9116–9123, 2007.

[129] M. Romand, M. Roubin, and J. P. Deloume, Elsevier Scientlfic Publishing Company vol. 13, pp. 229–242, 1978.

[130] M. C. Biesinger, *Advanced analysis of copper X-ray photoelectron spectra*, Surf. Interface Anal., vol. 49, no. 13, pp. 1325–1334, 2017.

[131] H. P. Boehm, *Surface oxides on carbon and their analysis: a critical assessment*, Carbon N. Y., vol. 40, pp. 145–149, 2002.

[132] K. Ding et al., *Characterization and simulation of a-Si:H/μc-Si:H tandem solar cells*, Sol. Energy Mater. Sol. Cells, vol. 95, no. 12, pp. 3318–3327, 2011.

[133] J. Fang et al., *Amorphous silicon/crystal silicon heterojunction double-junction tandem solar cell with open-circuit voltage above 1.5 V and high short-circuit current density*, Sol. Energy Mater. Sol. Cells, vol. 185, no. September 2017, pp. 307–311, 2018.

[134] B. Vincent Crist, Handbooks of Monochromatic XPS Spectra. 1999.

[135] E. W. J. Mitchell and J. W. Mitchell, *The work functions of copper, silver and aluminium*, Bourion 1949, pp. 70–84, 1951.

[136] H. J. Hagemann, W. Gudat, and C. Kunz, *Optical Constants from the Far Inftrared to the X-ray Region: Mg, Al, Cu, Ag, Au, Bi, C, and Al_2O_3*, J Opt Soc Am, vol. 65, no. 6, pp. 742–744, 1975.

Publications and Conference

Supervised Thesis

2019 John Mark Christian Dela Cruz

Investigation of Metallic Ag Films on Different Silicon Substrates as a Catalytic Active Layer for CO_2 Reduction.

Publications

2019 Sacha Corby, Miguel Garcia-Tecedor, Sven Tengeler, **Celine Steinert**, Benjamin Moss, Camilo A. Mesa1, Hany Heiba, Anna Wilson, Bernhard Kaiser, Andreas Kafizas, Wolfram Jaegermann, Laia Francàs, Sixto Gimenez, James R. Durrant

Separating Bulk and Surface Processes in NiOx Electrocatalysts for Water Oxidation.

ASC Energy Letters, submitted 11/2019

2019 **C. Steinert**, S. Tengeler, B. Kaiser, W. Jaegermann

The Impact of Different Si Surface Terminations in the (100) p-Si | n^+-Si | Cu Junction with respect to the Photo Electrochemical Performance.

Journal of the Electrochemical Society, vol. 166, no. 5, 2019

2018 S. Tengeler, M. Fingerle, W. Calvet, **C. Steinert**, B. Kaiser, T. Mayer, W. Jaegermann

The Impact of Different Si Surface Terminations in the (001) n-Si/NiOx Heterojunction on the Oxygen Evolution Reaction (OER) by XPS and Electrochemical Methods

Journal of the Electrochemical Society, 165(4), H3122. 2018

2018 C. Lohaus, **C. Steinert**, G. Deyu, J. Brötz, A. Klein

Enhancing Electrical Conductivity of Room Temperature Deposited Sn-doped In_2O_3 Thin Films by Hematite Seed Layers

Applied Physical Letters, 112, 152105. 2018

2017 C. Lohaus, **C. Steinert**, J. Brötz, A. Klein, W. Jaegermann

Systematic Investigation of the Electronic Structure of Hematite Thin Films.

Advanced Materials Interfaces, 4, 1700542. 2017

Conferences, Meetings and Exhibitions

2019 A-Leaf Project Meeting (London, United Kingdom)

Interface Investigations with Respect to the Photoelectrochemical Performance

2019 International Bunsen Discussion Meeting (Taormina, Italy)

Interface Investigations with respect to the Photoelectrochemical Performance of

pn^+-Si | Cu, p-Si | µcn-Si | Cu and p-i-n-Si | Cu Junctions

2018 Imagine Digital – Connect Europe, ICT (Vienna, Austria)

Represent A-LEAF project

2018 Nanoge Fall Meeting (Torremolinos, Spain)

The Impact of Different Si Surface Terminations in the (100) p-Si | n^+-Si | Cu Junction with respect to the Electrochemical Performance for the CO_2 Reduction Reaction.

2017 A-Leaf Project Meeting (Darmstadt, Germany)

Interface Investigations with respect to the Photoelectrochemical Performance of

pn^+-Si | Cu Contact with different Si Surface Terminations.

2017 A-Leaf Project Meeting (Leiden, Netherlands)

XPS Interface Investigations of the p-Si | Cu Contact with different Si Surface Terminations.

Résumé

Céline Schäfer

born 08.09.1992 in Miltenberg

Professional Experience	
04 / 2017 – today	**Research Assistant** TU Darmstadt, Surface Science Division Darmstadt, Germany
04 / 2015 – 07 / 2015	**Research Assistant** Fraunhofer Institute for Integrated Systems and Device Technology Erlangen, Germany
Education	
04 / 2017 – today	**Doctoral Studies** TU Darmstadt, Surface Science Division Darmstadt, Germany Title of Thesis: "Interface Investigations of the Si | Cu and Si | Ag Contact with Respect to the Photoelectrochemical Performance"
10 / 2015 – 03 / 2017	**Master's degree Materials Science** TU Darmstadt, Darmstadt Germany Title of Thesis: "Growth and Characterization of RF-magnetron Sputtered Epitaxial Hematite Thin Films"
08 / 2014 – 09 / 2014	**Stay Abroad** Internship, Khujand, Tajikistan
07 / 2013 – 12 / 2013	**Stay Abroad** Murdoch University, Perth, Australia

10 / 2012 – 08 / 2015	**Bachelor's degree Nanotechnology** FAU Erlangen-Nürnberg, Erlangen, Germany Title of Thesis: "Herstellung von TEM-Flüssigzellen mit elektronentransparenten Graphenmembranen"
10 / 2011 – 10 / 2012	**Bachelor studies Medical Engineering** FAU Erlangen-Nürnberg, Erlangen, Germany
09 / 2002 – 07 / 2011	**Maria-Ward-Gymnasium Aschaffenburg** Aschaffenburg, Germany Degree: Allgemeine Hochschulreife

Honorary Office

10 / 2017 – 12 / 2018	**Equal Opportunities Officer** TU Darmstadt, Department of Materials Science Darmstadt, Germany

Danksagung

An erster Stelle gilt mein Dank Prof. Dr. Wolfram Jaegermann für die Möglichkeit und Betreuung meiner Promotion in der Arbeitsgruppe Oberflächenforschung. Ich weiß das entgegengebrachte Vertrauen und die Freiheit das Thema selbstständig zu erforschen sehr zu schätzen.

Außerdem danke ich PD Dr. Bernhard Kaiser für die Unterstützung während der Bearbeitung des Projektes, sowie Marga Lang und Leslie Frotscher, die sich um alle bürokratischen Arbeiten gekümmert haben und immer ein offenes Ohr für meine Anliegen hatten.

Jun. Prof. Dr. Ulrike Kramm danke ich nicht nur für die Übernahme des Zweitgutachtens, sondern auch für die Zuversicht und die ermutigenden Worte während meiner Schwangerschaft. Prof. Dr. Rolf Schäfer und Prof. Dr. Wolfgang Ensinger danke ich dafür, dass sie als Prüfer agieren.

Ein besonderer Dank gilt dem Werkstattteam, das mich bei der Inbetriebnahme und Instandhaltung der Evaporatoren unterstützt hat, sowie Kerstin Lakus-Wollny, die für mich nicht nur zahlreiche REM Bilder aufgenommen hat, sondern auch immer eine nette Gesprächspartnerin war. Dr. Vladimir Smirnov danke ich für die Anfertigung der Solarzellen, sowie der Unterstützung bei sämtlichen Fragestellungen.

Ein herzliches Dankeschön gilt der Arbeitsgruppe Oberflächenforschung inklusive der heutigen Arbeitsgruppe Elektronenstruktur von Materialien. Nicht nur die zahlreichen wissenschaftlichen Diskussionen, sondern auch der freundschaftliche Umgang haben zum Erfolg dieser Arbeit beigetragen.

In besonderer Weise möchte ich mich bei den Wasserspaltern für die tolle Zusammenarbeit und eine wundervolle Zeit bedanken. Dabei gilt mein herzlicher Dank Paula Connor, die mich mit dem FUN vertraut gemacht hat und mich immer unterstützt hat, wenn ich Hilfe gebraucht habe. Außerdem danke ich Andreas Hajduk für die schöne gemeinsame Zeit im Büro mit vielen interessanten Gesprächen. Das freundschaftliche Verhältnis war maßgeblich an der Freude an meiner Arbeit beteiligt. Danke auch an Jona Schuch, Thorsten Cottre, Sven Tengeler und Dominik Moritz für die Zusammenarbeit.

Zuletzt, danke ich meiner tollen Mama, Holger, meinen Schwestern und Freunden, die nicht nur alle Höhen und Tiefen meiner Promotion miterlebt haben, sondern auch die, des gesamten Studiums. Ihr habt mich stets motiviert und mich auf besondere Weise unterstützt. Ein ganz besonderes Maß an Unterstützung habe ich von meinem wundervollen Mann Tobias erhalten, der mir immer zugehört hat, Freude und Sorgen mit mir geteilt hat und mich vor allem während der Schwangerschaft auf unglaubliche Weise entlastet hat, sodass ich meine Promotion erfolgreich beenden konnte. Vielen Dank dafür!

Erklärung zur Dissertation

Hiermit versichere ich die vorliegende Dissertation ohne Hilfe Dritter nur mit den angegebenen Quellen und Hilfsmitteln angefertigt zu haben. Alle Stellen, die aus Quellen entnommen wurden, sind als solche kenntlich gemacht. Diese Arbeit hat in gleicher oder ähnlicher Form noch keiner Prüfungsbehörde vorgelegen.

Darmstadt, den

(Céline Schäfer)